LHCb Hybrid Photon Detectors and Sensitivity to Flavour Specific Asymmetry in Neutral B-Meson Mixing

Robert William Lambert

Thesis submitted for the degree of Doctor of Philosophy

School of Physics & Astronomy

The University of Edinburgh

2008

"Science knows no country, because knowledge belongs to humanity, and is the torch which illuminates the world. Science is the highest personification of the nation because that nation will remain the first, which carries the furthest the works of thought and intelligence."

Louis Pasteur.
French biologist & bacteriologist (1822 - 1895).

"If you wish to be remembered, lest you die, you should either: write something worth reading; or, do something worth writing about."

Anon.

Abstract

The Large Hadron Collider started operation this year, 2008. LHCb is a precision heavy-flavour experiment at this collider. The precision of LHCb is greatly aided by the LHCb Ring Imaging Cherenkov system for the separation and identification of charged hadrons. This system uses pixel Hybrid Photon Detectors, an innovative new technology for single photon imaging. The simulation and testing of these photon detectors are reported and discussed. The photodetectors were measured to have reached or exceeded the specifications in key areas. In particular, the detector quantum efficiencies far exceed expectations, by a relative 27 %. The precision of LHCb will be used to examine CP-violation and rare decays of B-mesons. A key part of the physics programme will be a measurement of the CP-violating flavour specific asymmetry in neutral B-meson mixing. This asymmetry is expected to be very small in the Standard Model, of order 10^{-4}, however it is very sensitive to new physics, which can increase the asymmetry dramatically. We present an improved event selection and a novel method to control systematics. This will enable us to make a world-leading measurement of this parameter in one nominal year of data taking ($2\,\mathrm{fb}^{-1}$).

Declaration

This work represents the concerted effort of the LHCb collaboration. I have been privileged to be a contributing member of this international collaboration, based in CERN, Switzerland. Much of the work herein has been published elsewhere and/or presented to several audiences, as detailed later in this Thesis. To the best of my knowledge no significant parts of the work presented in this Thesis have been previously submitted for any degree or professional qualification. The writing of this Thesis has been entirely my own work.

Thesis Structure

Chapters 1, 2 and 3 introduce this Thesis. Chapter 1 is a theoretical introduction to particle physics, particularly the physics of CP-violation within the Standard Model. Chapter 2 introduces the Large Hadron Collider and its experiments, containing background information on accelerator/collider physics necessary for complete understanding of subsequent chapters. Chapter 3 is an introduction to the LHCb experiment, which began operation at the Large Hadron Collider, at CERN this year (2008).

Chapters 4, 5 and 6 contain the body of this Thesis and the work of the author. Chapter 4 describes the testing of 550 Hybrid Photon Detectors (HPDs) for use in the LHCb RICH system. This investigation has been published in two conference papers [1, 2], an LHCb internal note [3] and the LHCb detector paper [4], for which I was a contributing author. Chapter 5 introduces the LHCb Monte Carlo simulation, and describes improvements made to the simulation of the RICH HPDs. Chapter 6 contains an introduction to analysis within the LHCb framework, and an investigation of the measurement of flavour specific asymmetries by LHCb. Parts of this study were published as an LHCb public note [5] and an internal note [6].

Thesis Overview

The discovery of new phenomena should be considered the goal of physics. As will become clear in Chapter 1 we currently do not understand why the universe appears as we observe it. The Standard Model (SM) of particle physics, which we use to describe quantum interactions, has been very successful at predicting and describing experimental data. The success of the SM is a mixed blessing, as we know it to be incomplete. The SM does not explain gravity, dark matter or dark energy, neutrino oscillations, or the matter-antimatter asymmetry in the universe—requiring large CP-violation (CPV). In the LHC era we hope to discover new physics to deepen our understanding of the universe. To detect the subtle effects of new physics, which manifested during the first millionth of a second, requires us to push the boundaries of high energy physics. We are looking for new physics, be it hidden extra dimensions, supersymmetry, the graviton, or something even more strange.

To pin down new physics effects requires a precision experiment such as LHCb. LHCb will perform precision heavy-flavour tests of the SM and search for the signs of new physics. In the past precision flavour physics has been responsible for: the discovery of the charm quark; the discovery of CPV in the kaon sector–which lead to the prediction of the third generation of quarks; and predicting the mass of the top quark before it was directly measured. LHCb is *the* precision flavour-physics experiment in the LHC era. LHC and LHCb are described in detail in Chapters 2 and 3. One of the key features of LHCb is the RICH system, which uses Cherenkov light to determine the velocity of charged particles and hence allows us to determine their mass. To detect the Cherenkov photons requires a

fast low-noise photodetector. The Hybrid Photon Detectors chosen are described in Chapter 4. The detectors underwent a rigorous testing protocol for which the results are presented. In Chapter 5 the Monte Carlo simulation of these detectors is improved and the expected performance of the RICH system is discussed.

Now that LHCb is ready for data-taking, the question then arises as to where to look for the signs of new physics. When searching for something new, it is best to start looking where signs are the most obvious. A key place to look for new particle physics is in loop diagrams, which are a small contribution to Standard Model processes, but also where very heavy new physics particles can enter to change the result substantially. As is further discussed in Chapter 1, loop-level processes are able to probe high energy physics at much higher than the energy of the LHC beam. Neutral B-meson mixing is a loop-level process in which CPV is expected. The CPV is parameterised by the flavour specific symmetry, a_{fs}, which can be directly measured in $B^0_{s,d} \to D^{\mp}_{(s)}\mu^{\pm}\nu_{\mu}X^0$ and $B^0_s \to D^{\mp}_s\pi^{\pm}$. The technical issues relevant to the measurement at LHCb including a decision-tree-inspired trigger, are investigated in Chapter 6.

The measurement of a_{fs} by LHCb is complicated by systematic issues which were not present at previous colliders. In this Thesis a method is proposed which eliminates these systematic effects. More statistics can be taken with LHCb in two days of running at design luminosity than were taken in total over 6 years for the current world-leading measurement by DØ. With these statistics CP-violation in B^0_q-mixing will be probed to a higher precision than ever before; possibly revealing the first signs of new physics beyond the Standard Model.

Acknowledgements

There are far too many people to thank individually for their help, but special acknowledgements go out to: Franz Muheim, my supervisor; Nick Austin who kept me sane while at CERN; and Helen my fiancée who put up with me throughout. Thanks and best wishes to the attendees of the CERN-JINR summer school 2007, and UK GRAD Girton 2007 Team V!

Work within the Chapters 4 and 5 is jointly acknowledged to the LHCb-RICH collaboration. Many thanks to Neville Harnew, Thierry Gys, Stephan Eisenhardt, the PDTF and RICH-HPD groups, for their collaboration in Chapter 4, and Sajan Easo, Antonis Papanestis and Chris Jones for their collaboration in Chapter 5.

The analysis in Chapter 6 was aided greatly by collaborators with Bristol university, joint authors of Ref. [5]. The theoretical framework is attributed to the many theorists whose papers I enjoyed reading. I thank the Production and Decays working group and the Ganga and Dirac teams for their support through the study of production asymmetry. Thanks go out to G. Corti, N. Brook, P. Robbe and K. Harrison for their advice with generator study issues. Special thanks to T. Sjöstrand for helping to understand PYTHIA, B. Webber, A. Sherstnev and P. Richardson for helping to understand HERWIG; and further thanks to these groups for explaining the differences between the two.

Selected chapters of this Thesis were proof-read by Lindsay Ashford, Sajan Easo, Stephan Eisenhardt, Thierry Gys, Helen McLaughlin, Colin McLean, Nick Styles and Yuehong Xie.

Contents

List of Figures

List of Tables

Chapter 1

Theoretical Introduction

The cosmic microwave background which permeates the cosmos is an echo of the cataclysmic beginning of our universe around 14 billion years ago, known as the 'Big Bang'. The universe was most likely created in an explosion of energy and space-time; creating all the space, matter and energy we observe today. However, to the best of our understanding, the astronomically large quantities of matter produced must have been matched exactly by the production of an equally large quantity of antimatter. The majority of the matter and antimatter annihilated each other in the initial expansion phase of the universe but, curiously, a small quantity of matter has survived, from which all galaxies, and ourselves, are made. For this residual matter to survive there must be some very small difference between matter and antimatter, and the way they behave in the universe.

There is such an absence of antimatter that it remained unobserved and unexpected until Dirac proposed a particular solution of relativistic quantum mechanics. It was still a surprise when, in 1933, Anderson discovered the positron with equal and opposite properties to the electron [7]. Following the discovery of antimatter, its role in the physics of elementary particles was not well understood, leading to much speculation. The interpretation of Feynman and Stueckelberg [8] was two-fold: antiparticles may be considered a duplicate set of physically different species, or the same species evolving/travelling in a reversed arrow of time. Under this postulate,

a universe which is symmetric under the reversal of the arrow of time, i.e. obeys T-symmetry, would also be matter-antimatter symmetric. In our universe, therefore, T-symmetry must be broken.

In the Standard Model (SM) of particle physics, T forms a part of the larger CPT-symmetry, which is obeyed by the theory as a whole.[1] T-symmetry may be broken, if and only if it is compensated by an equal and opposite breaking of CP-symmetry, i.e. CP-violation (CPV). As proposed by Andrei Sakharov in 1967 [10], CP-violation is one of three conditions necessary to reproduce the asymmetry we observe in the universe. These are:

1. Baryon number violation,
2. CPV,
3. Interactions out of thermal equilibrium (in the early universe).

CPV has consequences at the scale of elementary particle interactions as described by the SM. Curiously, the level of CPV possible within the SM could never provide the level of symmetry breaking we observe in the universe today. Therefore we can be sure there must be some CP-violating new physics waiting to be discovered.

B-hadrons, particles containing bottom quarks (b and $\bar{b}$), possessing the quantum number called Beauty, $\tilde{B}$, exhibit the largest presently observable CP-violation [11]. This is the most interesting place to examine this phenomenon. At the Large Hadron Collider (LHC) the LHCb experiment will measure CPV and rare decays of B-hadrons more precisely than the combined power of all other experiments to date: searching for new sources of CPV, and new physics.

We rely on the discovery of new phenomena to explain how the universe began, what forces controlled the development of the early universe and, ultimately, to understand why our existence is even possible.

[1] For further reading on the operators of C, P, T, and CPT symmetry, see Ref. [9].

1.1 The Standard Model

The SM is a collection of theories, joined together in an attempt to construct a single mathematical equation to describe fundamental particle physics. As classical physics is a macroscopic extreme of the quantum, the SM represents our attempts at a single equation—a theory of everything [12].

Last century with cosmic ray experiments through to the development of the first colliders many subatomic particles were discovered. The majority of these were not present in 'normal' matter and were highly unstable. The numerous particles are categorised into leptons, hadrons and gauge bosons. Leptons are spin 1/2 point-like particles, like the electron. Hadrons are half-integer spin non-point-like particles like the neutron. Gauge bosons are force carriers such as the massless photon. Hadrons presented the largest mystery, a seemingly limitless number of particles and resonances, each with different properties. A small selection of these are presented in Table 1.1. The particles were grouped together and empirically assigned quantum numbers without explanation to describe their behaviour. The SM brings order, explanation, and reveals the beauty of elementary particle physics.

1.1.1 A renormalisable Lagrangian quantum field theory

The SM is a relativistic quantized Lagrangian field theory. A quantized field theory differs from a Schrödinger-style quantized theory in that it invokes second quantization. This is the quantization of the field itself (and conversely a field description of particles), on top of the quantization of permitted energy states

Table 1.1: A selection of hadrons and some of their associated quantum numbers [13].

Hadron	Mass, M_X	Charge	Quantum numbers				Lifetime	Quark
X	/ GeVc^{-2}	Q_X / e+	Spin, s	Charm, C	Strange, S	Beauty, $\tilde{B}$	τ_X / s	content[a]
π^+	0.140	+1	0	0	0	0	2.6×10^{-8}	$u\bar{d}$
K^-	0.494	-1	0	0	-1	0	1.2×10^{-8}	$s\bar{u}$
D_s^-	1.968	-1	0	-1	-1	1	5.0×10^{-13}	$s\bar{c}$
B_s^0	5.297	0	0	0	-1	1	1.4×10^{-12}	$s\bar{b}$
Λ_b^0	5.624	0	1/2	0	0	-1	1.2×10^{-12}	udb

[a] from the quark model as discussed in Sec. 1.1.2.

as described by the Schrödinger equation.[2] The SM is an effective field theory, constructed at the energy regime accessible in modern particle physics, as the simplest Lagrangian that reproduces the observed physics. Consequently the SM does not include the cosmological-scale effects of gravity and general relativity.

Symmetries are imposed upon the SM Lagrangian as required to obey the observed conservation laws.[3] A crucial symmetry we impose is Lorentz invariance. We want the SM to be invariant under the transformations of special relativity.

The SM has been very successful, due to its renormalizability. This is crucial for it to describe the physical universe. When a basic SM is constructed, which we call a "bare" SM, there are many situations where observable values are discovered to be infinite, for example the energy density of the elementary vacuum, often leading to violation of unitarity. These infinities are unphysical, despite us having started with an empirical set of equations. In the SM we reconcile this by renormalising the theory, which requires absorbing infinities within physical observables. We avoid each infinity by choosing a normalisation scheme, in which we redefine integrals, dimensions or constants with an observable that must be measured experimentally.

At first glance this process seems clumsy and obtuse. However, infinities in the mathematics indicate an unknown or unpredictable quantity. It is as if the theory is insisting that there are some constants that are not predictable, that to construct the universe you must define and measure some physical parameters.

1.1.2 The form of the Standard Model

The SM is an amalgamation of: quantum electrodynamics (QED), quantum chromodynamics (QCD) and the theory of the weak interaction. QED predicts the interaction of electrically charged particles with photons. QCD describes the interaction of particles holding colour charge. The weak interaction describes flavour dynamics: the interactions of quarks and leptons with $W^{\pm}$ and Z^0 gauge bosons.

[2] For further reading on quantum field theory, see Ref. [14].
[3] For example see Sec. 7.5 in Ref. [15].

Table 1.2: Four fundamental forces, and their appearance in the SM [13].

force	charge	acts on	associated boson(s)	length scale / m	relative strength[a]
EM	electric charge	all charged	photon, γ	∞	1
Weak	flavour	quarks, leptons	$W^{\pm}$, Z^0	10^{-18}	10^{-4}
Strong	colour	quarks, gluons	gluon, g	10^{-15}	25
Gravitational[b]	mass-energy	all	(graviton)	∞	10^{-41}

[a] on the typical scale of a nucleus, between experiencing particles (quarks or nucleons), relative to the electromagnetic force. [b] A quantum theory of gravity is not yet part of the SM.

Table 1.3: Bosons, the force mediators of the SM [13].

boson	associated force	electric charge /e+	mass /GeVc^{-2}	spin	lifetime /s
Photon, γ	electro-magnetic	$<5\times10^{-30}$ [a]	$<6\times10^{-26}$ [b]	1	∞
$W^{\pm}$	weak	$\pm$ 1	80.4	1	3×10^{-25}
Z^0	weak	0	91.2	1	3×10^{-25}
gluon, g	strong	0	0	1	–
Higgs, H	electro-weak	0	>114.4 [c]	0	–

[a] zero charge in the SM. [b] zero mass in the SM. [c] to a 95 % confidence level.

The four fundamental interactions are compared in Table 1.2. The corresponding exchange particles for each force are listed in Table 1.3. All known fundamental fermions are present in the SM, including quarks and leptons, which are described in Tables 1.4 and 1.5 . The SM has 19 free parameters which must be determined experimentally. Commonly adopted possible sets are given in Table 1.6.

Quarks were introduced as the building blocks of hadrons. It was noticed protons and neutrons were not point like, and that all hadrons belonged to symmetric sets of particles. The symmetry grouping was known as the eight-fold-way [16]. This implied hadrons were not fundamental particles in themselves. Just as electrons and protons were introduced following the construction of the periodic table, quarks followed the discovery of the eight-fold-way.[4] The observation of the Δ^{++} state, which has three u quarks in the same spin state made it necessary to introduce a new unobservable quantum number (colour), carried by quarks, with three values (red, green, blue), to preserve the Pauli-exclusion principle. QCD is the theory of the dynamics of exchange of colour, mediated by eight gluons. QCD is a non-Abelian

[4]For further reading on the construction of the quark model, see Chapter 10 in Ref. [17].

Table 1.4: Observed leptons and their properties [13]. Leptons carry weak charge and lepton number, they do not carry colour charge. The heavy leptons are electrically charged. No violation of lepton number has so far been directly observed. Three generations of leptons have been observed, and significant experimental data are consistent with there only being three generations in existence.

$$\begin{pmatrix} e \\ \nu_e \end{pmatrix} \begin{pmatrix} \mu \\ \nu_\mu \end{pmatrix} \begin{pmatrix} \tau \\ \nu_\tau \end{pmatrix}$$

lepton, l	mass, m_l / MeVc^{-2}	electric charge, Q_l / e+	mean lifetime, τ_l / s
e	0.511	$\pm$ 1	$> 1.45 \times 10^{34}$ [a,b]
μ	105.66	$\pm$ 1	2.20×10^{-6}
τ	1776.99	$\pm$ 1	2.91×10^{-10}
ν_e	$< 2 \times 10^{-6}$ [a,c]	$< 2 \times 10^{-14}$ [d]	>300 $\times m_{\nu_e}$ [a,b]
ν_μ	<0.19 [a,c]	$< 2 \times 10^{-14}$ [d]	$> 15.4 \times m_{\nu_\mu}$ [a,b]
ν_τ	< 18.2 [e,c]	$< 2 \times 10^{-14}$ [d]	– [b]

[a] to a 90 % confidence level. [b] stable in the SM. [c] usually assigned zero mass in the SM. [d] zero charge in the SM. [e] to a 95 % confidence level.

Table 1.5: Known quarks and their properties [13]. Quarks carry weak charge, colour charge, and a quantum number associated with their quark flavour. Weak interactions can violate quark number. Quarks have not been observed in isolation, a fact explained within the SM by asymptotic freedom and gluon self-coupling.

$$\begin{pmatrix} u \\ d \end{pmatrix} \begin{pmatrix} c \\ s \end{pmatrix} \begin{pmatrix} t \\ b \end{pmatrix}$$

quark, q	mass, m_q / MeVc^{-2}	electric charge, Q_q / e+	name	associated quantum number
u	1.5 to 3.0	$+\frac{2}{3}$	up	Number of up, N_u
d	3 to 7	$-\frac{1}{3}$	down	Number of down, N_d
s	95 $\pm$ 25	$+\frac{2}{3}$	strange	Strangeness, S
c	1250 $\pm$ 90	$-\frac{1}{3}$	charm	Charm, C
t	174200 $\pm$ 3300	$+\frac{2}{3}$	top	Truth, T
b	4200 $\pm$ 70	$-\frac{1}{3}$	bottom	Beauty, $\tilde{B}$

gauge theory, meaning the mediating particle, the gluon, is charged/coloured and interacts with itself. As the exchange particle interacts strongly with itself, isolation of colour charge is not energetically favourable. Consequently, quarks bind strongly together to form colour-neutral hadronic states.

Table 1.6: Example possible complete sets of 19 observable parameters for the SM [12].

type	free parameters	symbol(s)	name(s)
Yukawa couplings	9	m_e, m_μ, m_τ	lepton masses
		m_u, m_c, m_t	quark masses
		m_d, m_s, m_b	
CKM-parameters	4	$[V_{CKM}]_{ii}$	weak mixing of quarks
		ρ, η, λ, A	Wolfenstein parameters
QED†	1	α	fine structure constant
		$(= e^2)$	(electron charge ^{2})
Weak parameters†	2	θ_W	Weak mixing angle
		G_F	The Fermi constant
		M_W, M_Z	Weak boson masses
		g_W, g'_W	Weak coupling constants
Higgs sector†	1	m_H, λ	Higgs boson mass
		$\langle v \rangle$	Higgs vev
QCD	2	α_s	Strong coupling constant
		Θ_{QCD}	Strong CP-phase

† written such that in the electro-weak sector there are 4 free parameters.

1.1.3 Perturbation theory and Feynman rules

Within the field theory of the SM it is possible to calculate probabilities and cross-sections from first principles, integrating over all possible field configurations. This is computationally expensive so, wherever possible, perturbation theory is used to simplify the calculation. One of the great beauties of the SM is that perturbations performed around the coupling constant can be represented diagrammatically. These Feynman diagrams encode all relevant information and can be translated into mathematical equations using Feynman rules [8]. Where perturbation theory fails other methods must be attempted, e.g. when the coupling constant of low-energy QCD approaches unity, Lattice QCD is used [18].

1.2 CP-violation in the Standard Model

CPT symmetry is a good symmetry of the SM Lagrangian.[5] Parity, P, is maximally violated by the weak interaction, which separates states with left-handed and right-handed helicity. CP is also violated in the SM, to a much lesser extent. In the SM CP-violation (CPV) could be present in the quark sector, or the weak sector. Curiously CPV in the strong interaction is not observed, leading to what is commonly called the "Strong CP problem"[19].[6] If we assume neutrinos are massless, lepton mixing cannot occur, and so CPV is confined to the weak mixing of quarks.

Weak quark mixing is linked to the Higgs mechanism, which allows the fundamental particles of the SM to obtain mass. To allow for a simple mass term, i.e. to find mass-decay eigenstates, the off-diagonal elements of Higgs sector couplings are absorbed in the unitary weak mixing matrix. This requires a rotation of the set of basis states away from the weak eigenstates $(d, s, b) \rightarrow (d', s', b')$. It is apparent that the weak eigenstates (q') are not the mass-decay eigenstates (q).[7] Additionally, in the presence of CP-violation, the weak and mass-decay eigenstates are also both distinct from the CP eigenstates. The strong force is unnafected by the rotation, however production and decay of hadrons through the weak force then also involves this basis rotation. In lay terms: observed hadrons with a given lifetime and mass are a mixture of the particle and antiparticle state, and CPV produces differences in behaviour between the hadrons and their associated antihadrons.

A generic example of a hadronic initial state i decaying to a final state f is given in Fig. 1.1, which also defines some key parameters: production and decay amplitudes A and $\bar{A}$, eigenvalues q, p, and propagation operators $g_{\pm}$. CPV is usually separated into three categories for the purposes of measurement. These are: CPV in production or decay, also known as direct CP-violation; CPV in mixing; and CPV

[5] For further reading on the operators of C, P, T, and CPT symmetry, see Ref. [9].

[6] For more information on the Strong CP problem, and possible solutions see Refs. [20] and [21].

[7] The mass-decay eigenstates are the quark-flavour eigenstates, the 'physical' particle-like eigenstates.

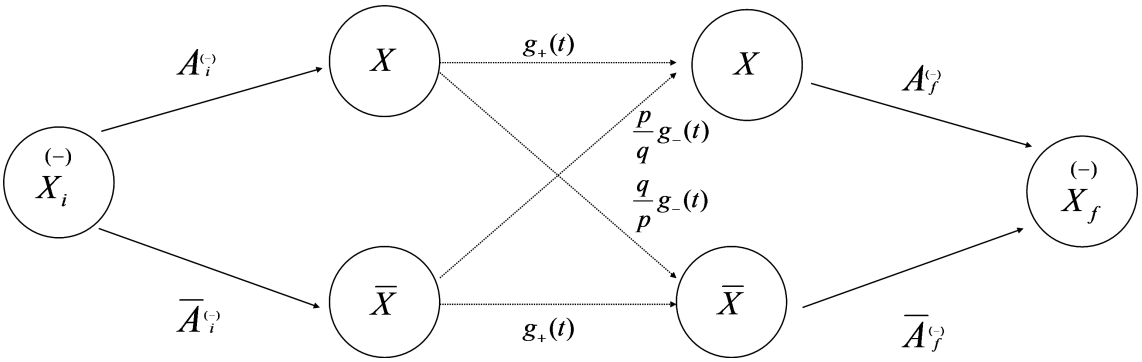

Figure 1.1: Production, interference, mixing and decay. Generally the propagation and decay of the physical hadron $X_{i,f}$ are described via the quark eigenstates X through a few terms: amplitudes A, eigenvalues q, p, and propagation operators $g_\pm$. The eigenstates of central box diagram $|X_m\rangle = q|X\rangle \pm p|\bar{X}\rangle$ can be considered the propagating mass-decay eigenstates.

in the interference between mixing and decay. These are characterised by:

$$\text{Direct CPV} \quad : \quad |A_j| \neq |\bar{A}_{\bar{j}}| \tag{1.1}$$

$$\text{CPV in mixing} \quad : \quad \left|\frac{q}{p}\right| \neq 1 \tag{1.2}$$

$$\text{CPV in interference} : \quad \arg\lambda_f \neq 0 \text{ where } \lambda_f = \frac{q}{p}\frac{\bar{A}_f}{A_f} \tag{1.3}$$

If a state X is neutral, i.e. B_s^0 or K^0, it can mix with its antipartner ($g_-(t)\times q/p \neq 0$). A formalism for neutral meson mixing is presented in Sec. 1.3. Firstly we will discuss the SM mechanism which is responsible for CP-violation, and the measurements currently constraining its parameters.

1.2.1 The CKM matrix

The unitary mixing matrix between quark flavours in the SM is responsible for all flavour-changing processes at the quark level, mediated by the charged $W^\pm$ weak bosons. The mixing matrix is referred to as the Cabbibo-Kobayashi-Maskawa (CKM) matrix, $\underline{\underline{V}}$, after the three physicists who originally proposed its form and identified its relevance to CP-violation [22, 23]. In the SM $\underline{\underline{V}}$ is a unitary complex 3×3 matrix. The element $\left[\underline{\underline{V}}\right]_{ij}$ is the coupling constant for a $q_i q_j W$ vertex (normalised to the Fermi constant $\sqrt{G_F}$) and also the component of down-type

quark q_j in the weak eigenstate of q'_i [24]:

$$\begin{pmatrix} d' \\ s' \\ b' \end{pmatrix} = \begin{pmatrix} V_{ud} & V_{us} & V_{ub} \\ V_{cd} & V_{cs} & V_{cb} \\ V_{td} & V_{ts} & V_{tb} \end{pmatrix} \begin{pmatrix} d \\ s \\ b \end{pmatrix} = \underline{\underline{V}} \begin{pmatrix} d \\ s \\ b \end{pmatrix} \tag{1.4}$$

A complex 3×3 matrix has 18 free parameters. The CKM matrix is unitary, which applies nine constraints to this matrix. Additionally, overall phases in the Lagrangian are not observables. They can be arbitrarily absorbed into the quark fields. Five of the six remaining phases and phase-differences can be absorbed, leaving a single observable relative phase difference. The CKM matrix has four free parameters, three mixing angles and one complex phase. This complex phase is the only source of CP-violation in the SM. When Cabbibo first proposed a mixing angle in 1963 only three quarks were expected [22]. For four quarks the 2×2 mixing matrix has no CP-violation and only one free parameter, the "Cabbibo mixing angle". The surprising discovery of CP-violation in the kaon sector (1964 [25]) led Kobayashi and Maskawa to propose a third generation of quarks (1972 [23]), as was proven with the discovery of the bottom quark in 1977 [26]. Kobayashi and Maskawa were awarded the Nobel prize for physics this year (2008).

The CKM matrix is observed to be hierarchical, with diagonal elements of order 1. This is reflected in the most common parameterisation of the CKM matrix known as the Wolfenstein parameterisation [27, 28]. The most appropriate application of this parameterisation is presented as adapted from Refs. [29] and [30]:

$$\underline{\underline{V}} = \begin{pmatrix} \bar{c} & \lambda & A\lambda^3(\rho - i\eta) \\ -\lambda + A^2\lambda^5(\frac{1}{2} - \rho - i\eta) & \bar{c} - \frac{1}{2}A^2\lambda^4 & A\lambda^2 \\ A\lambda^3(1 - \bar{\rho} - i\bar{\eta}) & -A\lambda^2 + A\lambda^4(\frac{1}{2} - \rho - i\eta) & 1 - \frac{1}{2}A^2\lambda^4 \end{pmatrix} + O(\lambda^6) \tag{1.5}$$

where:

$$\bar{c} = \sqrt{1 - \lambda^2} = \left(1 - \frac{\lambda^2}{2} - \frac{\lambda^4}{8} \ldots\right) \quad , \quad \bar{\rho} = \rho\, \bar{c} \quad , \quad \bar{\eta} = \eta\, \bar{c} \tag{1.6}$$

here the four free parameters, A, η, λ, and ρ are real constants. $\lambda{\sim}0.23$ is the sine of the Cabbibo angle with $\bar{c}{\sim}0.97$ as the cosine, and η parameterises the complex phase and level of CPV.

We have stated that the SM CKM matrix is unitary. In extended models outside of the SM the new physics (NP) could change the form of the CKM matrix. For example, with additional generations the 3×3 matrix in the SM, would be part of a larger matrix; or with additional fields and couplings there would be additional terms in the Feynman diagrams, not arising from the SM CKM. In this case in a fit of the SM CKM to experiment unitarity would be superficially violated. Examining the validity of the unitarity of the 3×3 matrix is a search for new physics. There are nine unitarity relations, which take the form $\sum_k V_{ik}V_{jk}^* = \delta_{ij}$. Examining the Wolfenstein parameterisation there are two unitarity relations which contain large CPV and apply to the b-system:

$$V_{ud}V_{ub}^* + V_{cd}V_{cb}^* + V_{td}V_{tb}^* = 0 \tag{1.7}$$

$$V_{td}V_{ub}^* + V_{ts}V_{us}^* + V_{tb}V_{ud}^* = 0 \tag{1.8}$$

The unitarity relations can be plotted on an Argand diagram, forming triangles in the complex plane. These are known as unitarity triangles (UTs), of which the above two are plotted in Fig. 1.2. As there are only four free parameters, with only one complex phase it is usual to normalise with respect to the magnitude of $V_{cd}V_{cb}^*$. The parameters of the UT, as shown in Fig. 1.2 can be written as:

$$\alpha = \arg\left(-\frac{V_{td}V_{tb}^*}{V_{ud}V_{ub}^*}\right) (= \pi - \beta - \gamma) \tag{1.9}$$

$$\beta = \arg\left(-\frac{V_{cd}V_{cb}^*}{V_{td}V_{tb}^*}\right) \tag{1.10}$$

$$\gamma = \arg\left(-\frac{V_{ud}V_{ub}^*}{V_{cd}V_{cb}^*}\right) \tag{1.11}$$

$$\chi = \arg\left(-\frac{V_{ts}V_{us}^*}{V_{cd}V_{cb}^*}\right) \tag{1.12}$$

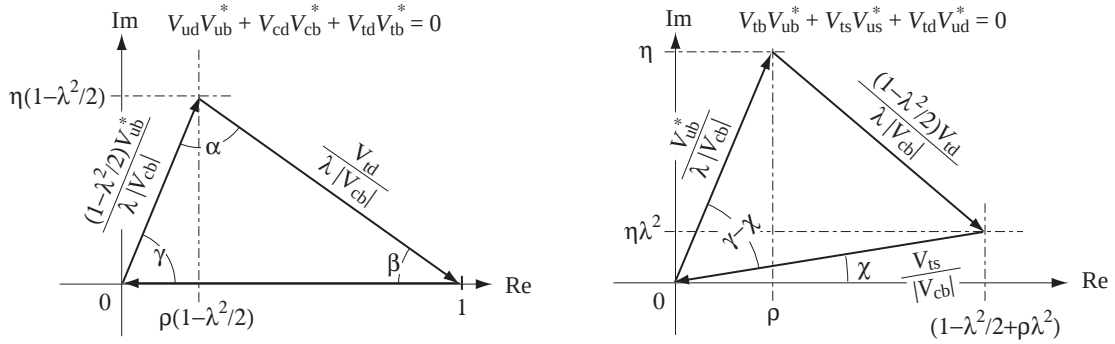

Figure 1.2: Two unitarity triangles with standard LHCb paramaterisation, after [31]. Left, for Eqn. 1.7. Right, for Eqn. 1.8.

and it is useful to define the equivalent of β in the B_s^0-system:

$$\beta_s = \arg\left(-\frac{V_{ts}V_{tb}^*}{V_{cs}V_{cb}^*}\right) \quad (\equiv \chi) \tag{1.13}$$

In the SM these triangles are closed, there are only two degrees of freedom for the UT in Fig. 1.2, left, and three for the UT in Fig. 1.2, right. There are many observables that can be measured to over-constrain the sides and angles individually.

1.2.2 Observables in CP-violation

Observables can be formed taking $|V_{ij}|$ or from combinations of four CKM matrix elements, such that they are real and invariant under the arbitrary rephasing of the quark fields.[8] Measurements are usually couplings and decay rates to constrain the magnitude of CKM elements, and asymmetries to constrain the relative phases.

The current direct experimental constraints on the magnitudes of the CKM matrix elements are [13]:

$$\begin{pmatrix} 0.97418 \pm 0.00027 & 0.2255 \pm 0.0019 & 0.00393 \pm 0.00036 \\ 0.230 \pm 0.011 & 1.04 \pm 0.06 & 0.0416 \pm 0.0011 \\ 0.0081 \pm 0.0006 & 0.0387 \pm 0.0023 & > 0.78(95\,\%CL) \end{pmatrix} \tag{1.14}$$

[8] For example, the Jarskog invariant [9] and the angles $\alpha, \beta, \gamma, \chi, \beta_s$.

The hierarchy here affirms the Wolfenstein parameterisation. These magnitudes may be seen as coupling constants, which are extractable through decay-rate or Branching Ratio (BR) measurements, such as $K^{\pm} \to \pi^0 l^{\pm} \nu_l$ to measure $|V_{us}|$ [32].

CP-violation in the SM is produced by the single phase in the CKM matrix. This phase is convention-dependent and can be probed through interference techniques. The three angles of the UT, α, β, γ can be probed individually to measure the single free phase in the CKM matrix. Current measurements [13] constrain:

$$\alpha = (88^{+6}_{-5})^{\circ} \tag{1.15}$$

$$\sin 2\beta = 0.681 \pm 0.025 \tag{1.16}$$

$$\gamma = (77^{+30}_{-32})^{\circ} \tag{1.17}$$

The angles of the UT are the phases of combinations of four CKM elements which are usually probed through interference measurements. For example β is the relative phase of $V_{td}V_{tb}^*$, which is the main coupling involved in B_d^0-mixing. Decays to a CP-eigenstate, B_d^0 or $\bar{B}_d^0 \to f$ and $B_d^0 \to \bar{B}_d^0 \to f$ then provide interference terms in the observable widths, and probe the phases. At the B-factories, BABAR and BELLE, $B_d^0 \to J/\Psi K_s$ is used, which is theoretically clean and dominates the world average measurement quoted [33, 34].

A global SM fit can further constrain the CKM matrix as is demonstrated in Ref. [13]. The multitude of measurements that constrain the UT are best plotted in the $\bar{\rho} - \bar{\eta}$ plane, as is performed by the CKM Fitter collaboration in Fig. 1.3. Arguably, the measurements which could benefit most from improvement are of the angle γ and the measurement of CPV in mixing[9], which are both orthogonal to the most precise measurement of $\sin 2\beta$ from the B-factories. The measurement of these parameters will play a key part in the physics programme of LHCb.

Currently measurements in the B_d^0-system are consistent with the SM. Interestingly and controversially, however, the UTfit collaboration have claimed in Ref. [36] that the current measurements of β_s are 3.7σ away from the SM prediction.

[9] through a_{fs}^q, as will be discussed in Sec. 1.3 and Chapter 6

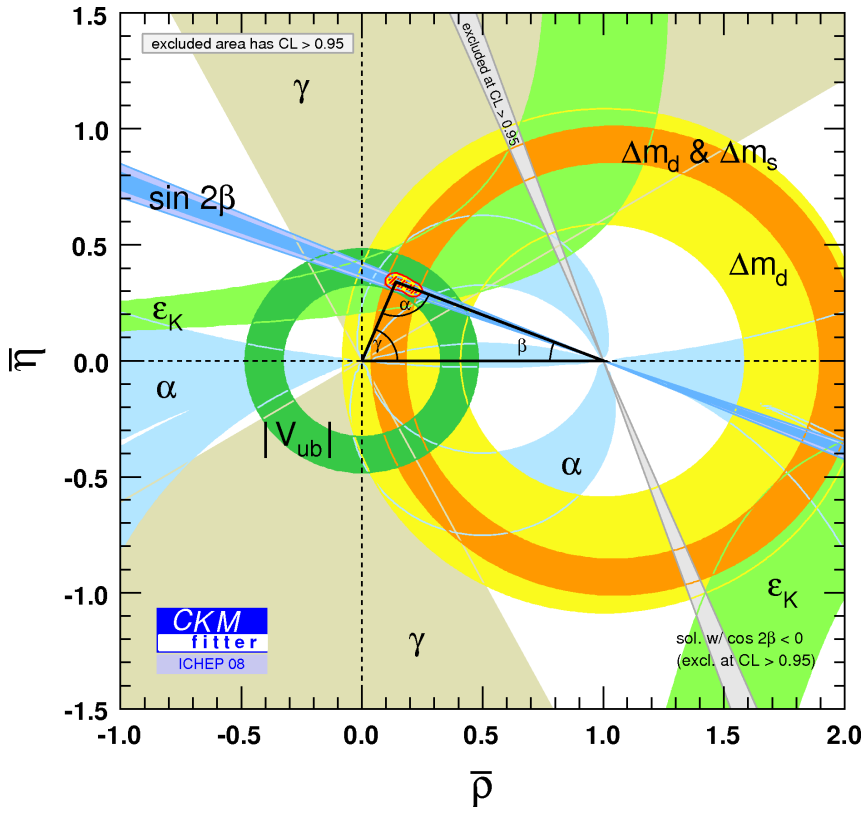

Figure 1.3: The global fit for $\bar{\rho}$ and $\bar{\eta}$, from the CKM Fitter group [35]. An example Unitarity Triangle is superimposed. The coloured bands correspond to the constraints on $\bar{\rho}$ and $\bar{\eta}$ from different measurements. Δm_s and Δm_d are mass differences from $B^0_{s,d}$-meson mixing and will be discussed in Sec. 1.3. ε_K is a mixing parameter in the kaon sector [13].

1.3 Mixing of neutral mesons

CP-violation in the mixing of neutral mesons was discovered in the mixing of the neutral kaons in 1964 [25]. We will focus on the case of neutral mesons containing b-quarks [11]. We start with eigenstates in two bases, the mass-decay bases ($|B^0_L\rangle$, $|B^0_H\rangle$) and the quark basis ($|B^0_q\rangle$, $|\bar{B}^0_q\rangle$).

In the SM the mixing of neutral mesons is described by a box diagram of the form given in Fig. 1.4 [30]. As this is a loop-level process it is sensitive to new physics. New particles may enter into the loop with different couplings and new quantum numbers. Furthermore, these include virtual particles, which may be far from their mass shell. Loop contributions from new particles of much higher mass can be probed indirectly through mixing; theoretically up to 10^4 TeV at the LHC.

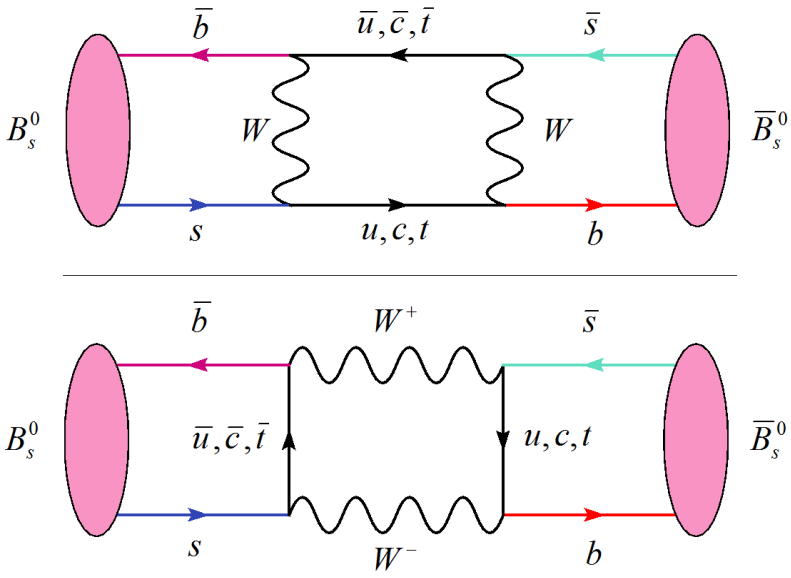

Figure 1.4: $\bar{B}_s^0$-B_s^0 mixing in the SM. The box diagram is mediated by W-boson exchange and dominated by the top quark contribution. The CKM elements V_{tb} and V_{ts} are important.

Considering the quark eigenstates, one can construct a Hamiltonian describing the propagation of B-mesons in the most general, pseudo model-independent case:

$$i\frac{d}{dt}\begin{pmatrix}|B_q^0(t)\rangle\\|\bar{B}_q^0(t)\rangle\end{pmatrix} = \left(\underline{\underline{M_q}} - \frac{i}{2}\underline{\underline{\Gamma_q}}\right)\begin{pmatrix}|B_q^0(t)\rangle\\|\bar{B}_q^0(t)\rangle\end{pmatrix} \tag{1.18}$$

Where $\underline{\underline{M_q}}$ and $\underline{\underline{\Gamma_q}}$ are the mass matrix and the decay matrix, and are Hermitian. As usual, given the matrices are Hermition we define:

$$\left[\underline{\underline{\Gamma^q}}\right]_{12} = \Gamma_{12}^q = \Gamma_{21}^{q\,*} \qquad \text{and} \qquad \left[\underline{\underline{M^q}}\right]_{12} = M_{12}^q = M_{21}^{q\,*} \tag{1.19}$$

As mixing of neutral mesons has been observed Γ_{12}^q and M_{12}^q are non-zero. Diagonalising Eqn. 1.18 one extracts propagating states of the meson in a mass-decay basis, i.e. the mass/decay eigenstates, which are not equal to the quark eigenstates. We define the light and heavy eigenstates $|B_L^q\rangle$ and $|B_H^q\rangle$ with masses M_L^q, M_H^q, and widths Γ_L^q, Γ_H^q, respectively:

$$|B_L^q\rangle = p|B_q^0(t)\rangle + q|\bar{B}_q^0(t)\rangle \tag{1.20}$$

$$|B_H^q\rangle = p|B_q^0(t)\rangle - q|\bar{B}_q^0(t)\rangle \tag{1.21}$$

where p and q are taken from the eigenvalues of the Hamiltonian in Eqn. 1.18, $|p|^2 + |q|^2 = 1$. In the absence of CPV $|p/q| = 1$. Now we define some parameters for the mixing [37]:

$$\Delta m_q = M_H^q - M_L^q = 2\,|M_{12}^q| \tag{1.22}$$

$$\Delta\Gamma_q = \Gamma_H^q - \Gamma_L^q = 2\,|\Gamma_{12}^q|\cos\Phi_q \tag{1.23}$$

Where Φ_q is a physical CP-violating phase difference:

$$\Phi_q = \arg(\Gamma_{12}^q) - \arg(M_{12}^q) \tag{1.24}$$

A system produced in a pure $|B_q^0\rangle$ or $|\bar{B}_q^0\rangle$ state at time zero will oscillate through the antiparticle state, evolving with time, t, according to:

$$|B_q^0(t)\rangle = g_+|B_q^0(t)\rangle + \frac{q}{p}g_-|\bar{B}_q^0(t)\rangle \tag{1.25}$$

$$|\bar{B}_q^0(t)\rangle = g_+|\bar{B}_q^0(t)\rangle + \frac{p}{q}g_-|B_q^0(t)\rangle \tag{1.26}$$

Where $g_\pm$ are time-dependant probabilities proportional to:

$$|g_\pm(t)|^2 = \frac{e^{-\Gamma_q t}}{2}\left[\cosh\left(\frac{\Delta\Gamma_q t}{2}\right) \pm \cos(\Delta m_q t)\right] \tag{1.27}$$

It can be seen in this equation that the oscillations are cosinusoidal with a frequency given by the mass difference. The oscillations of B_s^0 and B_d^0 are compared in Fig. 1.5, with central SM values for the mixing parameters.

1.3.1 CPV in mixing through a_{fs}^q

Three parameters are required to determine the mixing matrix in Eqn. 1.18, $\Delta\Gamma_q, \Delta m_q$ and a measurement of the CP-violating phase Φ_q. $\Delta\Gamma_q, \Delta m_q$ are mixing parameters that quantify the difference between the mass-decay eigenstates and the quark eigenstates. The CP-violating phase can be directly determined by measuring

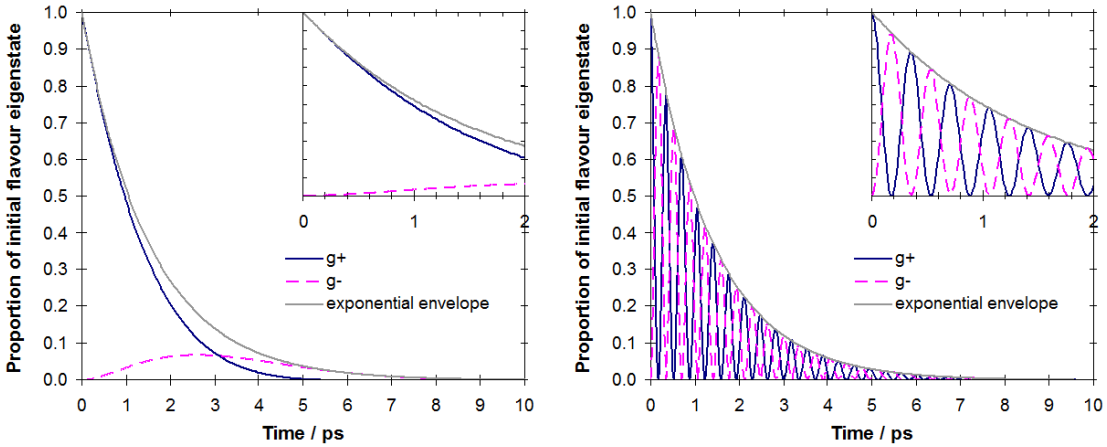

Figure 1.5: $\bar{B}^0_q$-B^0_q oscillations. Beginning with a pure sample of either B^0_q or $\bar{B}^0_q$ the proportion of the quark eigenstates are plotted against time. Left, the case for B^0_d, right, the equivalent for B^0_s, using the current SM predictions and measurements as appear in Refs. [38] and [13]. The solid dark line represents the proportion of the original quark eigenstate, the dashed light line represents the anti-quark state and the solid grey line represents the overall exponential decay of the particle. Inset into each is an expanded image of the first two picoseconds.

a^q_{fs}, the flavour-specific asymmetry in B^0_q-decays. a^q_{fs} quantifies the difference between the mass-decay eigenstates and the CP eigenstates and is complimentary to the measurement of the phase in, for example, $B^0_s \to J/\Psi\phi$ decays.

$$a^q_{fs} = \mathsf{Im}\left\{\frac{\Gamma^q_{12}}{M^q_{12}}\right\} \tag{1.28}$$

which is related to the mixing parameters [39, 40, 41, 42]:

$$a^q_{fs} \approx 2 - 2\left|\frac{p}{q}\right| \tag{1.29}$$

$$a^q_{fs} = \left|\frac{\Gamma^q_{12}}{M^q_{12}}\right| \sin\Phi_q = \frac{\Delta\Gamma_q}{\Delta m_q}\tan\Phi_q = 4 * \frac{\mathsf{Re}\{\varepsilon_{B^0_q}\}}{1 + \left|\varepsilon_{B^0_q}\right|^2} \tag{1.30}$$

where $\varepsilon_{B^0_q} = (1 + q/p)/(1 - q/p)$ is the mixing parameter for B-mesons.[10] We can see from Eqn. 1.29 and 1.2 that a non-zero value of a^q_{fs} is a measurement of CPV in mixing. The measurement of a^q_{fs} is discussed in Chapter 6.

[10] $\varepsilon_{B^0_q}$ is the equivalent of the kaon mixing parameter, $\bar{\varepsilon}_K$.

1.3.2 CPV in mixing in the Standard Model

M_{12}^q and Γ_{12}^q are predicted in the SM and related to other CKM parameters [30]:

$$M_{12}^q = -\frac{G_F^2 m_W^2 \eta_B m_{B_q} B_{B_q} f_{B_q}^2}{12\pi^2} S_o\left(\frac{m_t^2}{m_W^2}\right)(V_{tq}^* V_{tb})^2 \tag{1.31}$$

$$\Gamma_{12}^q = \frac{G_F^2 m_b^2 \eta_B' m_{B_q} B_{B_q} f_{B_q}^2}{8\pi^2}\left[(V_{tq}^* V_{tb})^2 + V_{tq}^* V_{tb} V_{cq}^* V_{cb}\mathcal{O}\left(\frac{m_c^2}{m_b^2}\right) + (V_{cq}^* V_{cb})^2 \mathcal{O}\left(\frac{m_c^2}{m_b^2}\right)\right] \tag{1.32}$$

where G_F is the Fermi constant, m_W the W boson mass, and m_i the mass of quark i; m_{B_q}, f_{B_q} and B_{B_q} are the B_q^0 mass, decay constant and bag parameter.[11] $S_0(x)$ is a known Inami-Lin function approximated very well by $0.784\ x^{0.76}$, V_{ij} are the elements of the CKM matrix, η_B and η_B' are QCD corrections of order unity.[12]

Within the SM a_{fs}^q is small [44], but non-zero:

$$\left|\frac{\Gamma_{12}^q}{M_{12}^q}\right| = \mathcal{O}\left(\frac{m_b^2}{m_t^2}\right) \ll 1 \tag{1.33}$$

$$\arg\left(-\frac{\Gamma_{12}^q}{M_{12}^q}\right) = \mathcal{O}\left(\frac{m_c^2}{m_b^2}\right) \ll 1 \tag{1.34}$$

$$a_{fs}^q \propto -\mathsf{Im}\left(\frac{V_{cq}^* V_{cb}}{V_{tq}^* V_{tb}}\right) \tag{1.35}$$

Including next-to-leading order QCD corrections, using an operator basis reducing α_s and $1/m_b$ errors [37, 38]:

$$a_{fs}^d = -(4.8_{-1.2}^{+1.0}) \times 10^{-4} \tag{1.36}$$

$$a_{fs}^s = +(2.06 \pm 0.57) \times 10^{-5} \tag{1.37}$$

Current measurements of a_{fs} do not constrain the UT[13] [44, 45], which would require a measurement error of at most 0.5 %. To make this precision measurement requires the full exploitation of higher luminosity and large $b\bar{b}$-cross section only available from the LHC, with the LHCb experiment.

[11] f_{B_q} and B_{B_q} are from lattice calculations of $\langle \bar{B}_q^0 | (\bar{b}q)_{V-A}(\bar{b}q)_{V-A} | B_q^0 \rangle = 8 m_{B_q} B_{B_q} f_{B_q}^2/3$ [43].
[12] The complicated relationship to the Wolfenstien parameterisation is discussed in Refs. [39, 44].
[13] Current measurements will be discussed in Sec. 6.1.2

Chapter 2

The Large Hadron Collider

The Large Hadron Collider (LHC) is the latest particle accelerator built at CERN, the European Council for Nuclear Research, straddling the border between France and Switzerland, close to Geneva. The LHC ring, nominally 100 m underground, is shown in Fig. 2.1. It is a proton synchrotron, a 27 km-long double-ring of vacuum vessel, superconducting dipole and triplet focusing magnets, radio-frequency accelerating cavities and cryogenic cooling. The LHC replaces the Large Electron-Positron collider (LEP), which was particularly successful in confirming the SM between 1989 and 2000. The LHC is the world's largest subatomic-microscope.

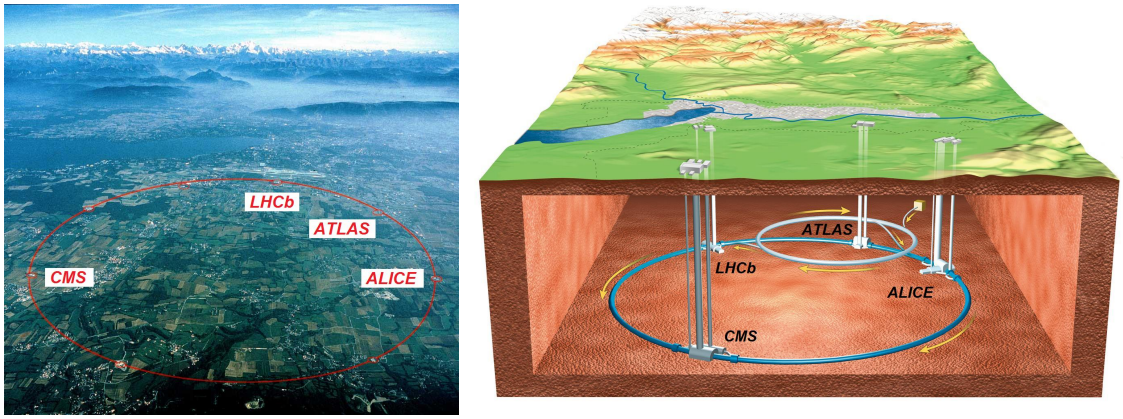

Figure 2.1: The LHC accelerator, courtesy of the CERN photography service. Left, an aerial view towards Geneva. Right, an underground schematic, showing the SPS and LHC. The four main LHC experiments are shown.

2.1 Accelerator physics

Particle accelerators are constructed with two parameters in mind: energy and luminosity. The centre-of-mass energy, $\sqrt{s}$, of the collisions determines the energy available to produce new particles. To increase the energy is analogous to increasing the resolution of the microscope. The luminosity, L, is a measure of the particle flux, the rate of an interaction is proportional to the luminosity. To increase the luminosity is analogous to increasing the brightness of the microscope image.

The energy of the particles is increased through acceleration by an electromagnetic field. Commonly low-loss resonant microwave cavities are used to obtain the high field energies required. Either the particles can make a single pass through many of these cavities (a linac, like SLAC), or can be bent using magnetic fields to facilitate many passes through the same cavities (a synchrotron, like the LHC). In either case additional cavities and higher field-strengths are required to increase the energy.

The luminosity of a collider with bunches of n_1 and n_2 particles colliding at a frequency f is given by:

$$L = \frac{1}{A} f n_1 n_2 \tag{2.1}$$

where A is the beam cross-sectional area. The rate of a given interaction is easily explained with an analogy. Imagine two colliding sets of solid spherical balls. The number of observed collisions, N, is proportional to the cross-sectional area of the balls, σ, the flux of colliding balls (the luminosity), and the length of time it is observed, t. When we replace the solid spheres with quantum mechanical wavefunctions, the 'cross-section', σ_i, is an observable probability which can be predicted from the Feynman rules of the given process, i:

$$N_i(t) = \int_0^t L \sigma_i dt \tag{2.2}$$

The cross-section of a given process is a function of the centre-of-mass energy. Measuring the event rate measures the cross-section. As the cross-sections are typically measured in barns ($1\,\mathrm{b} \equiv 10^{-28}\,\mathrm{m}^2$), integrated luminosities are typically measured in inverse barns, b^{-1}, which is a measure of the sample size collected.

$10\,\text{fb}^{-1}$ of data are expected to be collected by LHCb over its lifetime.

In the case of a hadronic mode, k, in a detector with a real detection efficiency, ϵ_k, where hadronisation through an intermediate state j occurs, Eqn. 2.2 becomes:

$$S_k(t) = \int_0^t L\sigma_i f_{ij} BR_{jk} \epsilon_k dt \tag{2.3}$$

where S_k is the number of observed signal decays of type k, f_{ij} is the fraction of N_i which hadronise to state j and BR_{jk} is the probability that a state j decays to the signal k – known as the Branching Ratio (BR).

To gather more signal, higher luminosity or longer observation time is required. It is more useful to increase the luminosity by a factor of ten, rather than increasing the observation time by the same factor. Eqn. 2.1 can be re-written in terms of two beam parameters: β, the amplitude function; and ϵ, the transverse emittance:

$$L = \frac{1}{4\pi\sqrt{\epsilon\beta^*}} f n_1 n_2 \tag{2.4}$$

Where β^* is the value of β at the collision point. These parameters describe the beam in transverse coordinates. The emittance is a conserved quantity of the beam, provided no damping is employed.[1] A larger ϵ indicates more particles with high transverse energy, also known as high beam 'temperature'. A smaller ϵ indicates a more parallel beam of more highly contained particles; a low beam temperature. β is a function of position: a larger β describes a beam whose particles are spaced far apart, but travelling more parallel; a small beta decribes a beam diverging from, or converging onto, a point. To increase luminosity one can do any of the following:

1. Increase beam currents, by increasing f, n_1, n_2,
2. Decrease β^*, using powerful focussing magnets near the IP,
3. Decrease ϵ, through damping or stochastic cooling.

All these techniques are employed together in the LHC, which is at the cutting edge of accelerator technology. The LHC design parameters are given in the next section.

[1] Conservation of ϵ is a manifestation of Liouville's theorem [46].

2.2 LHC design parameters

Two counter-rotating beams of protons are injected into the LHC by the Super Proton Synchrotron, SPS, at 450 GeV and are accelerated by the LHC to provide two beams of protons at 7 TeV each, colliding at a rate of 40 MHz. 1,232 dipole magnets with magnetic fields of up to 8.33 T are used to store the particles at high energy for up to 20 hours. A cross-section of a typical magnet is shown in Fig. 2.2. The total energy stored in the beam is around 725 MJ, which is equivalent to the energy released in the detonation of 157 kg of TNT. The LHC design parameters for proton–proton collisions are given in Table 2.1. Besides proton–proton collisions, both proton–nucleus (proton–lead) and nucleus–nucleus (lead–lead) collisions are foreseen as part of the initial experimental programme at the LHC. The LHC is capable of accelerating lead nuclei to a kinetic energy 2.76 TeV, which will correspond to a centre-of-mass energy of 1.15 PeV [47, 48, 49].

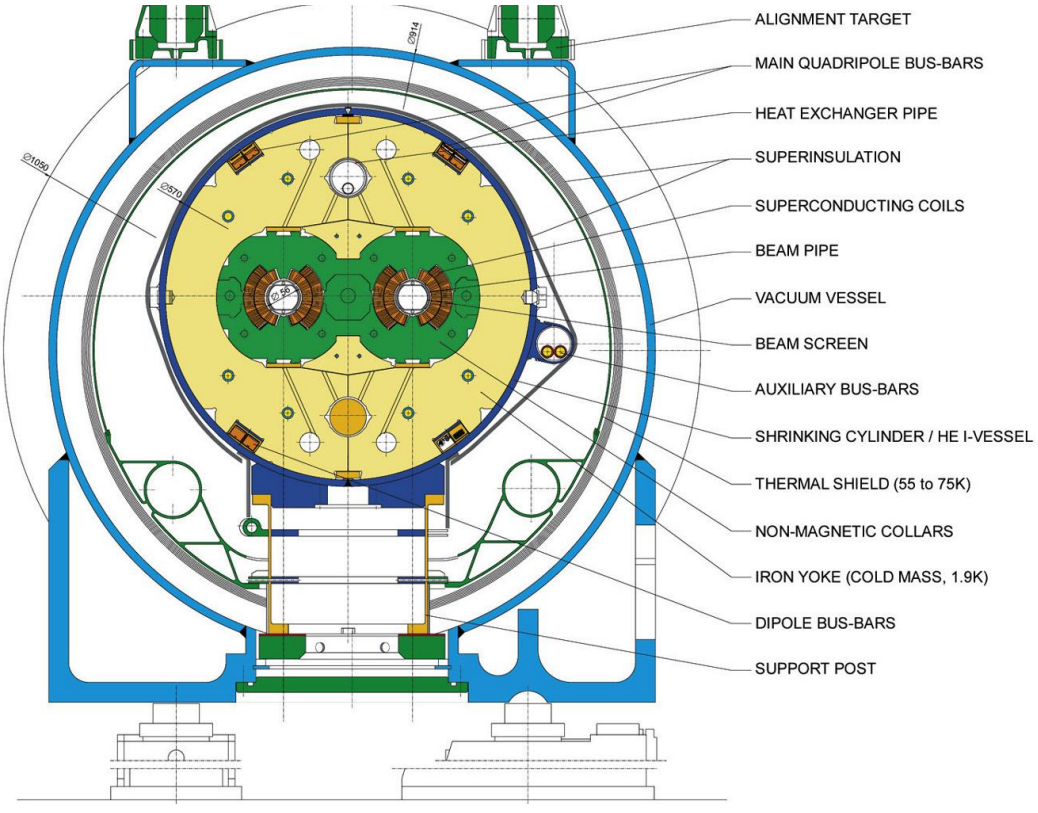

Figure 2.2: A cross-section of a typical superconducting LHC dipole magnet.

Table 2.1: The LHC design beam parameters, after [47].

Parameter	Injection	Collision	Unit
Beam Data:			
Proton Energy	450	7000	GeV
Relativistic Gamma	479.6	7461	–
Number of Particles per Bunch	1.15×10^{11}	1.15×10^{11}	
Number of Bunches	2808	2808	–
Longitudinal Emittance (4σ)	1.0	2.5	eVs
Transverse Normalised Emittance	3.5	3.75	μm rad
Circulating Beam Current	0.582	0.582	A
Stored Energy Per Beam	23.3	362	MJ
At Peak Luminosity:			
RMS bunch Length	11.24	7.55	cm
RMS Beam Size at IP1 and IP5	375.2	16.7[a]	μm
RMS Beam Size at IP2 and IP8	279.6	70.9[b]	μm
Peak Luminosity in IP1 and IP5	–	1.00×10^{34}	$\mathrm{cm}^{-2}\mathrm{s}^{-1}$
Luminosity in IP8[c]	–	$\sim 2.00\times 10^{32}$	$\mathrm{cm}^{-2}\mathrm{s}^{-1}$

[a] $\beta^* = 0.55\,\mathrm{m}$, [b] $\beta^* = 10\,\mathrm{m}$, [c] the luminosity at IP8 is tuneable

2.3 The LHC experiments

The LHC began operation this year (2008). LHC and its experiments are described in detail in Ref. [50]. Four large-scale experiments are ready to capitalise on the first data [51]: "A Large Ion Collider Experiment" – ALICE [48, 52], "A Toroidal LHC ApparatuS" – ATLAS [53, 54], the "Compact Muon Solenoid" – CMS [55, 56], and the "LHC Beauty" Experiment – LHCb [4, 31].

ALICE, described in Sec. 2.4, will investigate heavy-ion collisions. ATLAS, described in Sec. 2.5, and CMS, Sec. 2.6, are complimentary experiments, designed to cover 4π-steradians, which will concentrate on discovering the Higgs boson. LHCb will investigate the physics of b-quarks examining CP-violation and rare decays.

There are also several smaller experiments, including: the "LHC Forward" experiment – LHCf [57, 58], and "Total Cross Section, Elastic Scattering and Diffraction Dissociation at the LHC" – TOTEM [59, 60]. TOTEM is described in Sec. 2.7.

LHCb is a precision heavy flavour experiment and is described in Chapter 3. LHCb and ATLAS/CMS are entirely complimentary. To discover new physics requires the generic resonance searches made by ATLAS/CMS at the LHC centre-of-mass energy and the precision measurements of LHCb able to constrain much higher energy scales. This allows us to capitalise on the new luminosity and energy frontier.

2.4 ALICE

The ALICE detector as shown in Fig. 2.3 will measure the properties of the quark gluon plasma (QGP). The QGP is a state of matter with freely deconfined quarks and gluons proposed to have occupied the early high-temperature universe before the creation of the first baryons; between $\sim 10^{-12}$ and $\sim 10^{-6}$ s after the big bang. The QGP was officially designated as a state of matter in 2000. The QGP has been seen to act as an almost perfect liquid, and validation of this property will be one of ALICE's avenues of research. To observe the QGP, very high temperature, high density quark matter must be produced, for which the LHC will be the ideal research environment. ALICE will be capitalising on the high-energy proton-Pb and Pb-Pb collisions produced at the LHC. The central detector sits within the L3 magnet, a remnant of the earlier L3 experiment. The key feature of the QGP is the dissociation of hadrons, particularly those which are only loosely bound, such as the J/Ψ meson. As J/Ψ can be well identified by its decay to two muons, with a branching ratio of $\sim 6\,\%$, a forward muon spectrometer/detector was incorporated.

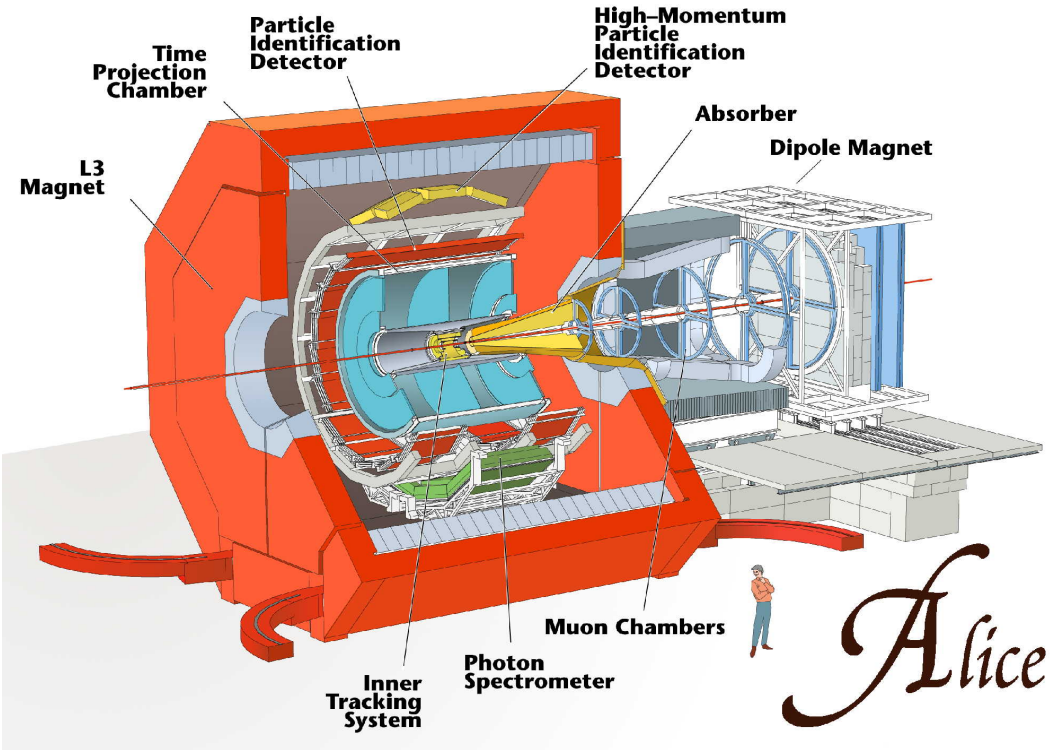

Figure 2.3: The ALICE detector, after [48].

2.5 ATLAS

ATLAS [53] will capitalise on the highest luminosities delivered by the LHC, aiming to illuminate the mechanism for electro-weak symmetry breaking in the SM, assumed to be due to the Higgs mechanism. At maximum luminosity, the ATLAS detector, shown in Fig. 2.4, will have to handle events with a mean of around 20 inelastic interactions in each interesting event. ATLAS has been designed to provide: very good electromagnetic calorimetry, high-precision muon momentum measurements, efficient tracking at high luminosity, large acceptance in solid angle, both in pseudorapidity (η) and with almost full azimuthal angle (ϕ) coverage, triggering and measurements of particles at $\sim 6\,\mathrm{GeV}c^{-1}$ transverse momentum. The ATLAS central barrel region extends to $|\eta| \leq 3.2$ and is fitted with high-granularity liquid-argon calorimeters. The endcaps also feature liquid-argon technology extending the calorimetry to $|\eta| \leq 4.9$. ATLAS uses three sets of magnets to provide up to 8 Tm bending power, for precise momentum resolution. There is an inner solenoidal magnet of 2 T, an outer toroidal air-core magnet of up to 4.1 T, and smaller end-cap toroids. The muon chambers are the most recognisable features of the ATLAS detector, surrounding the calorimetry with four wheels on either side of the detector, the largest of which is over 22 m in radius.

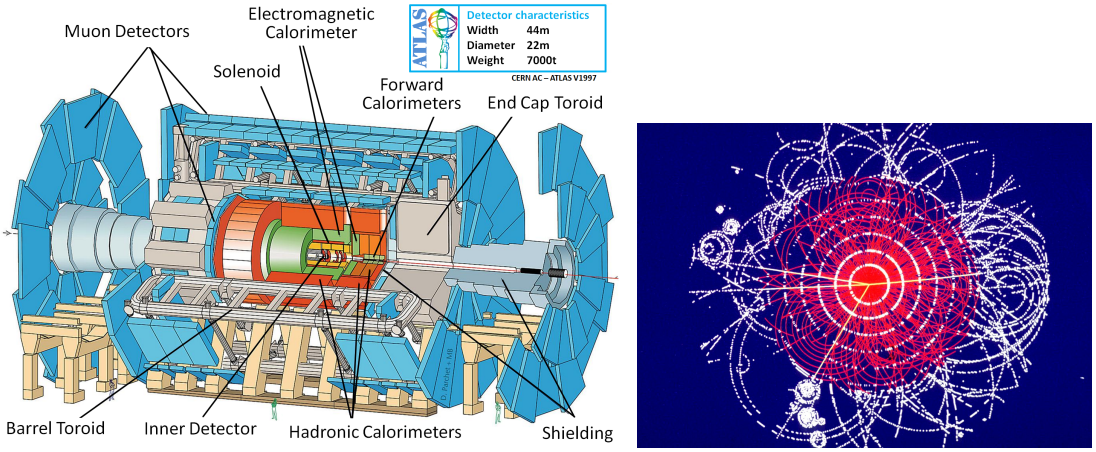

Figure 2.4: The ATLAS detector, after [53]. Left, an exploded view of ATLAS. Right, an example simulated Higgs to four muon event in the ATLAS inner detector.

2.6 CMS

CMS and ATLAS are complimentary detectors for LHC. CMS has the same general goals as ATLAS. In addition CMS plays host to the TOTEM experiment which is further described in Sec. 2.7. The CMS detector is drawn in Fig. 2.5. It has been designed to provide: coverage of the central rapidity region out to $|\eta| \leq 2.5$, good muon identification and momentum resolution over a wide range of momenta, good charged particle momentum resolution and reconstruction efficiency, efficient triggering and offline tagging of τs and b-jets, dimuon, diphoton and dielectron mass resolution $\approx 1\,\%$ at $100\,\mathrm{GeV}c^{-2}$, good E_T^{miss} and dijet mass resolution. The final item requires coarse hadron calorimetry out to high values of $|\eta| \leq 5$. CMS is therefore realised with several barrel regions covering the central rapidities, and endcaps covering the larger η ranges.

The key feature of CMS, and the reason behind the name, is the 12,000 tonne, 4 T superconducting magnet solenoid. The CMS solenoid alone weighs more than the whole ATLAS detector. The solenoid provides the charge discrimination and momentum resolution of CMS and is surrounded by the muon tracking stations. In the centre of CMS is a $1\,\mathrm{m}^2$ pixel vertex detector system with 40 million channels and a silicon strip tracker with close to $200\,\mathrm{m}^2$ of silicon and 5.4 million channels.

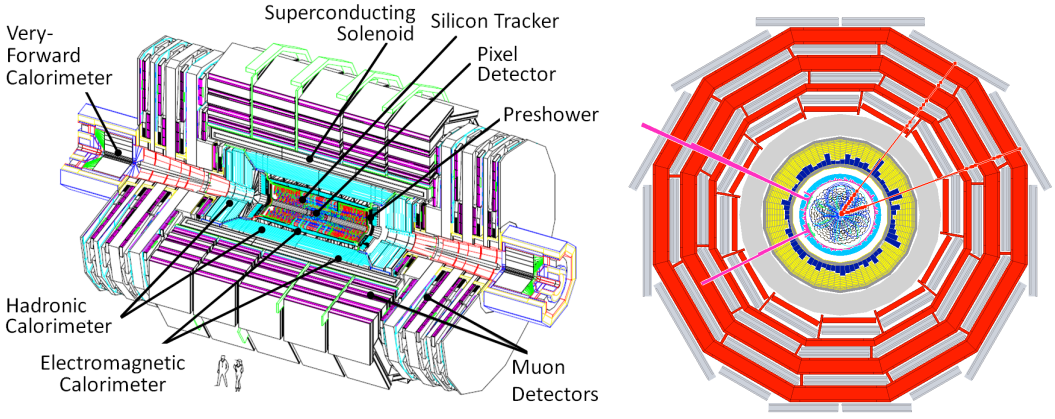

Figure 2.5: The CMS detector, courtesy of the CERN photography service. Left, an exploded view of CMS. Right, an example simulated Higgs event in CMS.

2.7 TOTEM

TOTEM is a far-forward experiment operating alongside the CMS experiment, as shown in Fig. 2.6. Independently TOTEM will measure: the total cross-section in the LHC proton collisions, with a luminosity-independent method; soft diffraction; elastic proton scattering in the range of polar angle, θ, and momentum, p, given by $10^{-3}\,\mathrm{GeV}^2c^{-2} < t = (p\theta)^2 < 10\,\mathrm{GeV}^2c^{-2}$. Working together with CMS, TOTEM will measure: hard diffraction; central, exclusive particle production; physics at low Bjorken x; $\gamma\gamma$ and $p\gamma$ physics; particle and energy flow in the forward direction; and leading particles. TOTEM is divided into a 'left' and 'right' section, down the respective sides of the beam line. Each section has two near tracking detectors T1-T2 and three far detectors RP1-RP3 on each side. The T-detectors track inelastically scattered particles, with pseudorapidities up to $\eta = 5$ for T1 and $\eta = 7$ for T2. T1 is a cathode-strip chamber and is within the CMS endcap. T2 uses Gas Electron Multipliers (GEM, [61]). The far detectors are located between 147 m and 220 m down the beamline to detect the total elastic cross-section. Due to the gradual curvature of the ring, these are offset slightly from the beam line, and are placed in the shadow of LHC collimators to reduce background. These are silicon microstrip detectors encapsulated in their own vacuum and cooled to -15°C, so-called "Roman pots". The data gathered by TOTEM will be very useful for LHCb, due to the overlap of rapidity ranges. It may be used for the tuning of our overall Monte Carlo, to model the underlying event and normalize luminosity measurements.

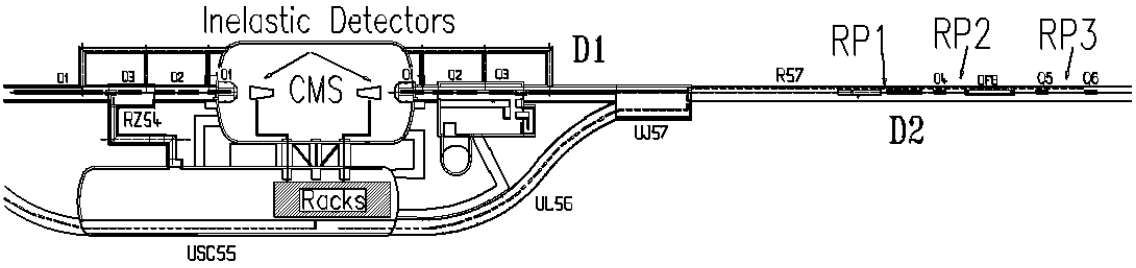

Figure 2.6: The TOTEM detector, after [59]. The near detectors are placed inside the CMS experimental hall. One set of far detectors is shown, RP1-3.

Chapter 3

The LHCb Experiment

This Chapter describes the LHC Beauty experiment, LHCb, which will investigate CP-violation and rare decays of hadrons containing b-quarks[31].

The LHCb detector is shown in Fig. 3.1 [4]. To measure and identify b-hadrons from their decay products the LHCb detector must determine the momentum (vector) $\underline{p}$, electric charge, q, and mass m, of the daughter particles. To improve the resolution of each of these parameters data from many specialised subdetectors are combined.

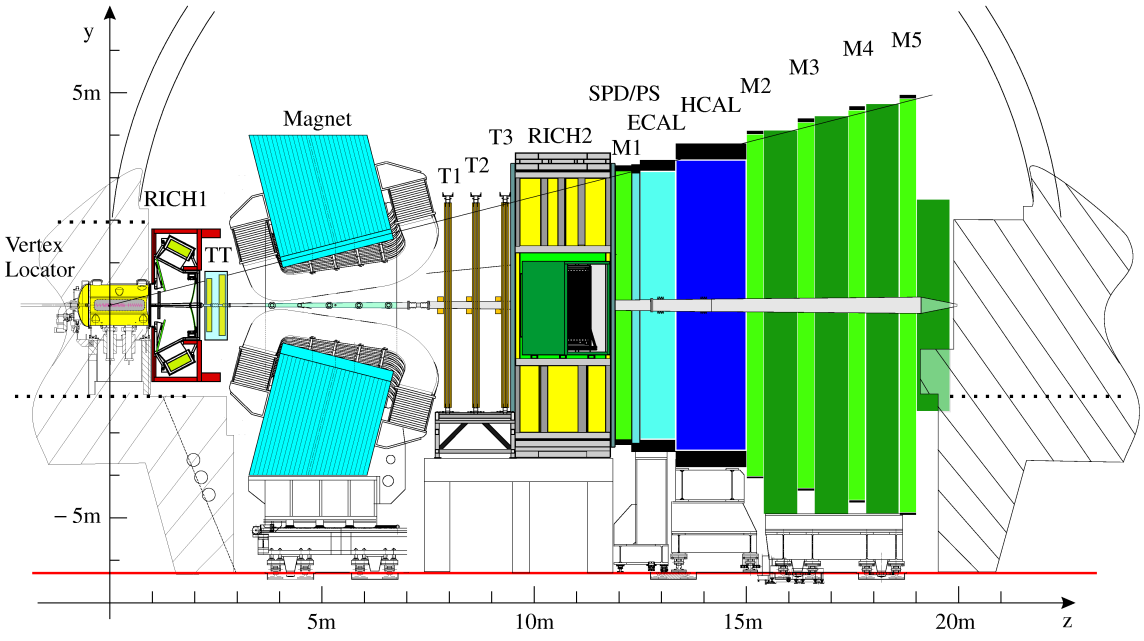

Figure 3.1: The LHCb detector, after [31]. Acronyms used are defined later in this Section.

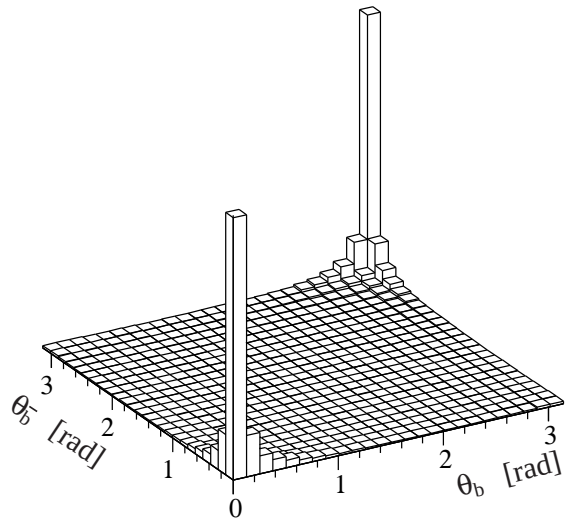

Figure 3.2: Polar production angles for b and $\bar{b}$-containing mesons at the LHC, after [62]. Calculated by the PYTHIA event generator. Angle in the centre of mass frame of the colliding protons w.r.t. the beam axis.

The LHCb detector is centred about the LHC beampipe, 100 m underground. The detector is a forward-arm spectrometer. LHCb measures particles which appear within its angular acceptance of 10 mrad to 250 mrad vertically, and 10 mrad to 300 mrad horizontally [62]. This is less than 1 % of all solid angles, however, LHCb covers 34 % of the produced b-quarks. This is because the production of b-quarks, peaks in the forward and backward directions at the LHC, as shown in Fig. 3.2.

3.1 An overview of LHCb

To understand the LHCb detector, we will consider an interesting interaction, producing b-quarks. At the interaction point, a proton-proton deep inelastic scattering occurs, producing a highly boosted virtual gluon and breaking up the incoming protons at a primary vertex. In this case the virtual gluon decays instantly to a $b\bar{b}$ pair. The quarks are quickly separated due to their high momentum and hadronise separately into b-hadrons; e.g. a B_s^0-meson ($\bar{b}$) and an 'opposite-side' b-hadron. Around 40 other tracked particles are also produced at the primary-vertex. The b-hadrons are highly boosted in the lab frame. They are unstable and decay after travelling typically 10 mm in the lab frame.

As an example we will take the semileptonic decay $B_s^0 \to D_s^- \mu^+ \nu_\mu$, producing the hadron and muon tracks shown in Fig. 3.3. The neutrino passes right through LHCb, and on through the earth, without interacting. The D_s^- travels a few mm and decays, producing a tertiary vertex, $D_s^- \to K^+ K^- \pi^-$. Within tens of nanoseconds the final state particles have travelled through our detector.

The charged particles deposit energy in the Vertex Locator (VELO), Turicensis Tracker (TT), and T1-T3 tracking stations. The hits are used to reconstruct each particle's trajectory. The curvature of the particles through the magnetic field reveals their momentum and charge. In the Ring Imaging Cherenkov detectors, RICH 1 and RICH 2, the charged particles emit Cherenkov radiation, which is used to identify the kaons and pions. The energies of the hadrons are measured with the Hadron Calorimeter (HCAL). As the muon is a minimum-ionising particle (MIP) it passes through the HCAL, producing hits in the muon stations.

The subdetectors and subsystems are summarised in more detail in the remainder of this Chapter, starting with the LHCb VELO, finishing with an in-depth discussion of the LHCb RICH and an overview of the trigger system.

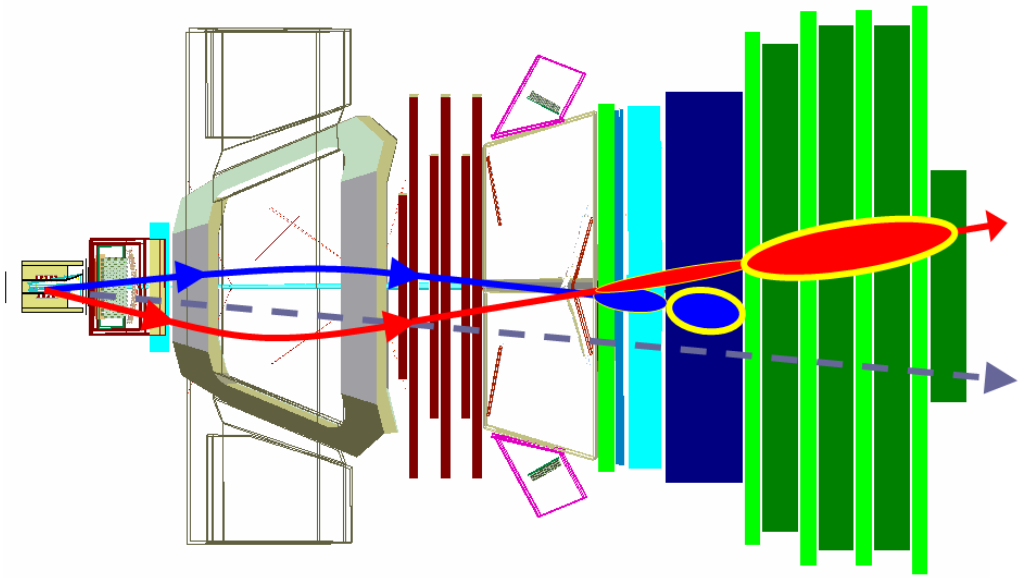

Figure 3.3: Top view of the LHCb detector. Example particle tracks are given typical of: a neutrino (dashed grey, which does not interact with the detector) a muon (red) and a hadron (blue). The measured particles deposit the majority of their energy in the detectors indicated with the ovals.

3.2 The VErtex LOcator

The VErtex LOcator (VELO) is one of the crucial LHCb subdetectors. The VELO, as shown in Fig. 3.4, is composed of 21 detector stations, covering a pseudorapidity range of $1.6 < \eta < 4.9$. Each station is split into two semicircular sections, left and right of the beam pipe. The layout of these stations is given in Fig. 3.5.

The sections each hold two semicircular silicon sensors, which are 300 μm thick, coming as close as 7 mm from the beam line, with a 1 mm inactive area of guard ring material closest to the beam [63]. The sensors are silicon strip detectors, alternating between having strips orientated in R and Φ. Each R and Φ sensor has 2,048 strips with variable pitch to ensure approximately equal occupancy for all readout channels. A simplified schematic of the readout sensors is given in Fig. 3.4, right. The VELO sensors and readout chain have a typical signal-to-noise ratio of 21.5, and are radiation hard.[1] In usual operation the semicircular detector halves overlap slightly, to provide full angular coverage and permit relative alignment. During commissioning, changing the magnetic field, filling and acceleration of the LHC, the sensors can be retracted by up to 6 cm to prevent damage.

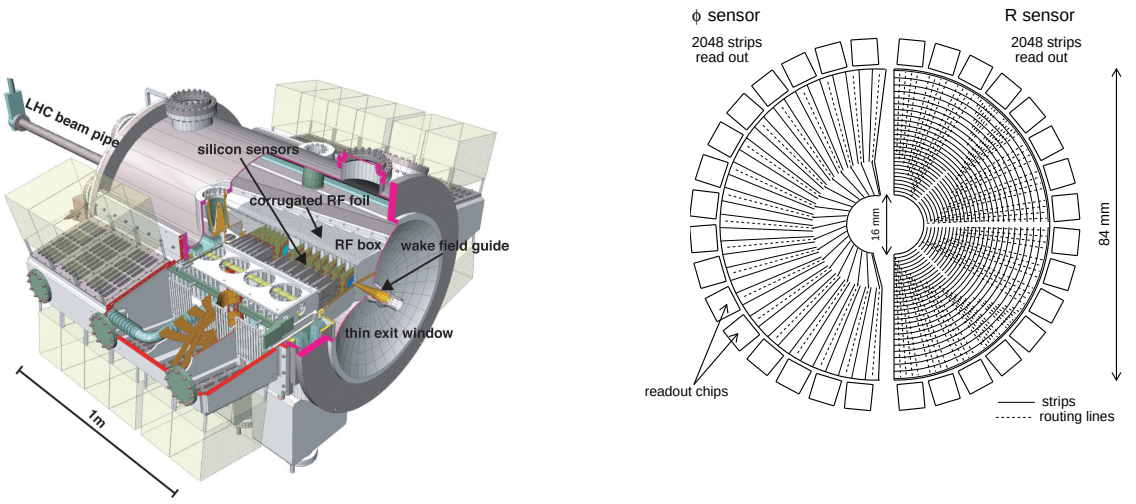

Figure 3.4: The LHCb VELO, after [63] and [31]. Left, a slightly simplified schematic. Cut away shows sensors. Right, simplified R/Φ sensors in comparison.

[1] Negligible degradation was observed under irradiation by 24 GeV protons, 4.1×10^{14} protons per square centimetre, which is the equivalent of approximately 6 fb^{-1} of integrated luminosity.

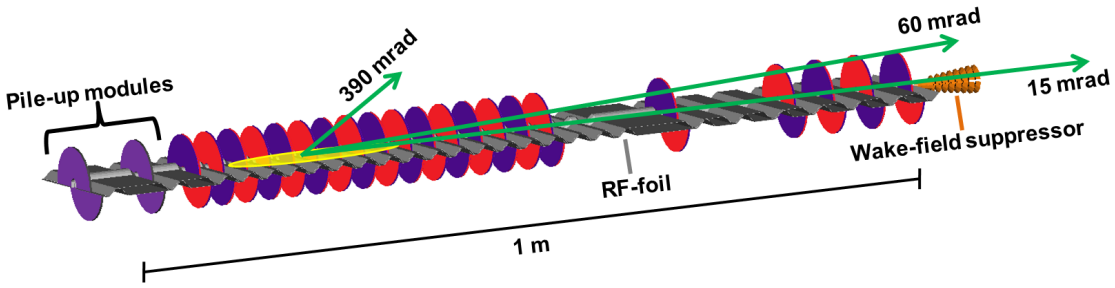

Figure 3.5: The LHCb VELO detector stations, after [63] and [31]. The limits of the VELO acceptance in the forward direction are shown.

To reduce the distance and the material between the interaction point and the VELO sensors, the sensors are encapsulated within their own vacuum vessel, enabling the beam pipe to be thinned in the interaction region. Thinning the beam pipe requires the use of an RF foil and a wake field suppressor foil, which are shown in Fig. 3.5. As well as covering the full LHCb angular acceptance in the forward direction, two stations cover a little of the backward direction. Primarily these two stations are used to provide a pileup veto: a triggering veto whenever more than one major interaction has occurred during the event. They have a faster readout system to accommodate inclusion in the Level-0 trigger (see Sec. 3.8) at 40 MHz.

A typical ionising track between pseudorapidities of $1.6 < \eta < 4.9$ produces at least three hits in the VELO. These are reconstructed with a typical resolution of $7\,\mu$m, which varies with the strip pitch, as measured in various testbeams [4]. The distance of closest approach between a track and a reconstructed primary vertex is known as the impact parameter (ip, or b). The ip can be reconstructed with a resolution as low as $10.3\,\mu$m, dependent on the transverse momentum, p_T, through $\sigma(b) = [10.3 + (17.4\,\text{GeV}c^{-1})/p_T]\,\mu$m.

3.3 Tracking

Tracking of charged particles is provided by multiple stations situated along the detector, the VELO, Turicensis Tracker station (TT), and the three main tracking stations – T1-T3, as shown in Figs. 3.1 and 3.6.

The TT is located downstream of RICH 1 and in front of the entrance of the LHCb magnet. The TT is comprised entirely from silicon micro-strip detectors, with a total area of $8.3\,\mathrm{m}^2$. The two TT stations have two silicon layers each, in '$xuvx$' format to provide 2D-reconstruction. In this format the first and last detector layers are vertical (0°, x-layers), and that the second and third layers have readout strips rotated by a stereo angle of $+5°$ and $-5°$ (u and v layers). The TT is constructed in ladders of $410\,\mu$m-thick silicon sensors. Over 180k channels, from strips of pitch $198\,\mu$m, are read out in analogue with custom-designed 'Beetle' chips. The signals are digitised and serialised close to the detector before being relayed to the counting room for possible use in the trigger system.

T1 to T3 are shown on the right in Fig. 3.6. Each station, T1-T3, is divided into the Inner Tracker, closest to the beam pipe and the Outer Tracker. The Inner Tracker

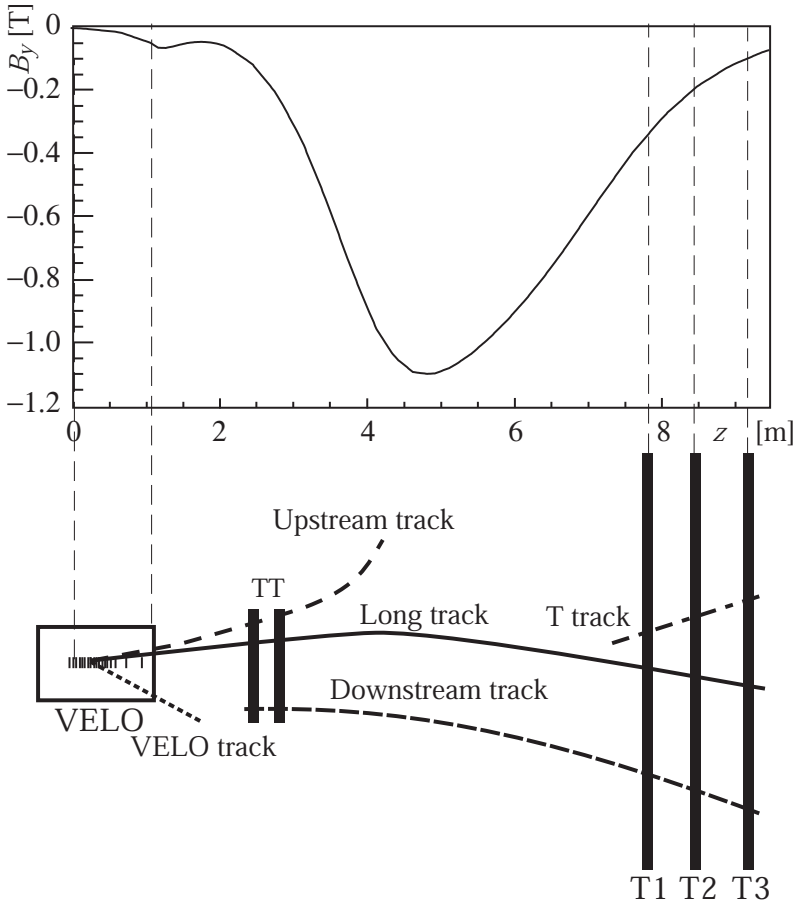

Figure 3.6: A schematic of the tracking system within LHCb, including a description of the track types, after [31]. The horizontal B-field from the magnet is also plotted.

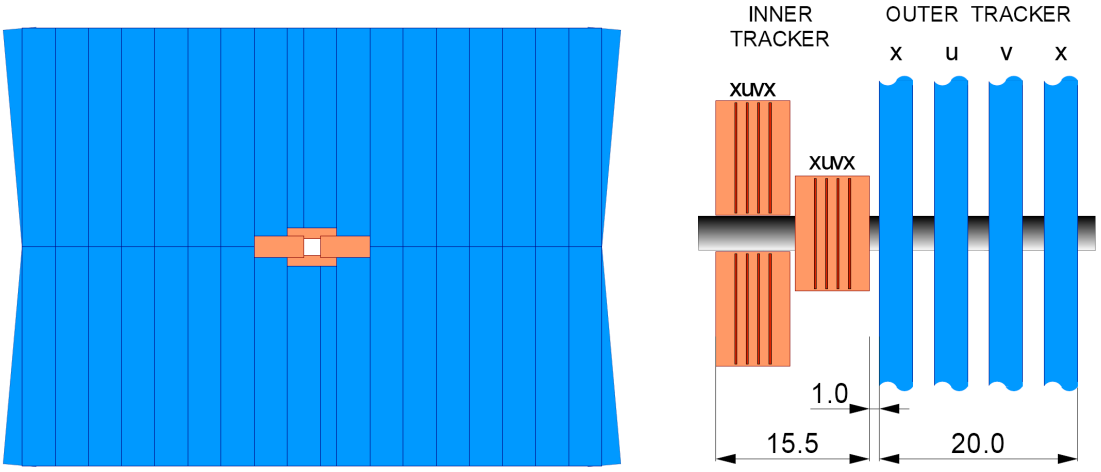

Figure 3.7: The tracking station subdetectors. Left, a front view of a tracking station. Right, a cut-away top view of the tracking stations displaying the IT-OT offset in cm. The Outer Tracker in blue, the Inner Tracker in peach, after [64].

(IT) is composed of silicon micro-strip detectors [64], the same as the TT stations, whereas the Outer Tracker (OT) is composed of straw drift-tube modules [65]. The IT and OT are built as complimentary shapes and slightly offset in z-position as demonstrated in Fig. 3.7. The OT is constructed from 5 mm-diameter straws at a pitch of 6 mm. Electrons within the tubes drift under a 1.55 kV field in an Ar(75 %)-CF_4(15 %)-CO_2(10 %) gas mixture. The expected momentum resolution from the tracking system is $\delta p/p = 0.4\,\%$ (for daughters of a typical B-meson decay).[2]

3.4 Magnet

The LHCb magnet [66] was the first detector element to be installed in the LHCb pit. The magnet provides the dipole field which enables the spectrometry in our experiment. The LHCb magnet is a conventional (warm) conductor, water-cooled, with an overall bending power of $\int Bdl = 4\,\mathrm{Tm}$. The magnet weighs 1,600 tonnes with an excitation current NI of 2.6 MA. The y-component of the B-field is given as a function of the z-position in Fig. 3.6.

[2]The complicated global minimisation technique for track reconstruction is not discussed in this Thesis. For further information the reader should consult Refs. [31] and [4].

3.5 Calorimetry

Calorimetric information is a key part of the LHCb triggering system (Sec. 3.8). Multiple calorimeter stations, shown in Fig. 3.8, measure the energy of electrons, photons, and hadrons, and perform particle identification [67]. The calorimeter subsystems are summarized in Table 3.1.

The electromagnetic and hadronic calorimeters (ECAL and HCAL) are the main calorimeter subdetectors. Scintillators are sandwiched between layers of absorber. The energy of the particles is sampled by collecting photons from showers of secondary particles. We adopt a shashlik design, each detector section is "skewered" by its own read-out fibres. Scintillation light is transmitted to sensitive detectors by wavelength shifting (WLS) fibres. To improve resolution, both spatially and in terms of energy, we require additional subsystems: the Scintillating Pad Detector (SPD) and PreShower (PS). The scintillation light is detected with PMTs in the ECAL and HCAL. Multi-anode photomultiplier tubes (MAPMTs) are used for the SPD and PS.

The SPD and PS are planes of polystyrene scintillating tiles located just before, and just after, a 12 mm-thick Lead wall, placed in front of the main calorimeters.

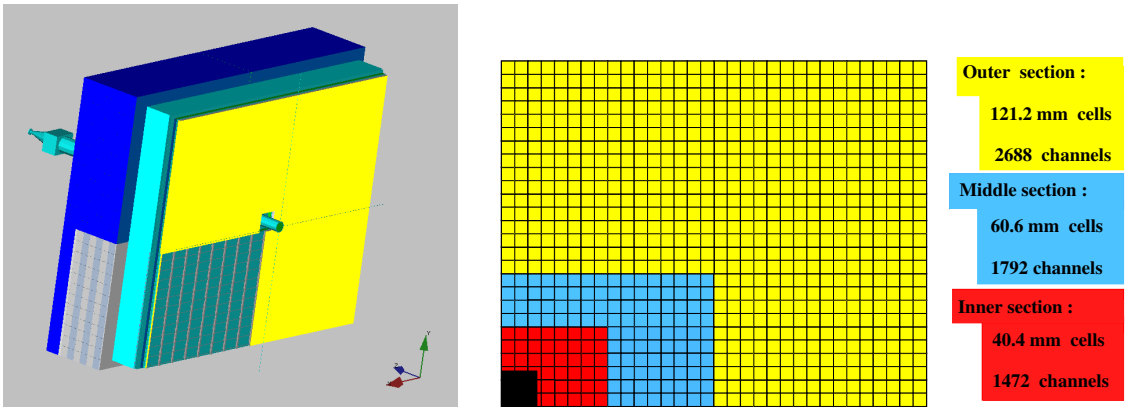

Figure 3.8: LHCb calorimeters. Left, isometric view of the calorimeters, with cutaway. From left to right, in royal blue the HCAL, light blue the ECAL, dark blue the PS, in yellow the SPD. Right, the granularity of the SPD/PS and ECAL, one quarter of the detector is shown, after [67]. Dimensions for ECAL are given, reduce by ≈1.5 % for SPD/PS.

Table 3.1: The LHCb calorimeter parameters, after [67].

Parameter	SPD/PS	ECAL	HCAL	Unit
Channels	11904	5952	1468	–
Dimension ($x \times y$)	6.2×7.6	6.3×7.8	6.8×8.4	m^2
Dimension z	180	835	1655	mm
Radiation lengths	2	25	–	X_0
Interaction lengths	0.1	1.1	5.6	λ_I
Layers (Scint. + Lead)	2+1	67+66	3+3	
Dynamic range:				
–MIPs	0-100	–	–	MIPs
$-E_T$	–	0-10	0-10	GeV
Resolution:				
–Photons	20-30	–	–	per MIP
–Energy	–	$10\,\%/\sqrt{E}$ $\oplus 1.5\,\%$	$80\,\%/\sqrt{E}$ $\oplus 10\,\%$	$\sigma(E)/E$

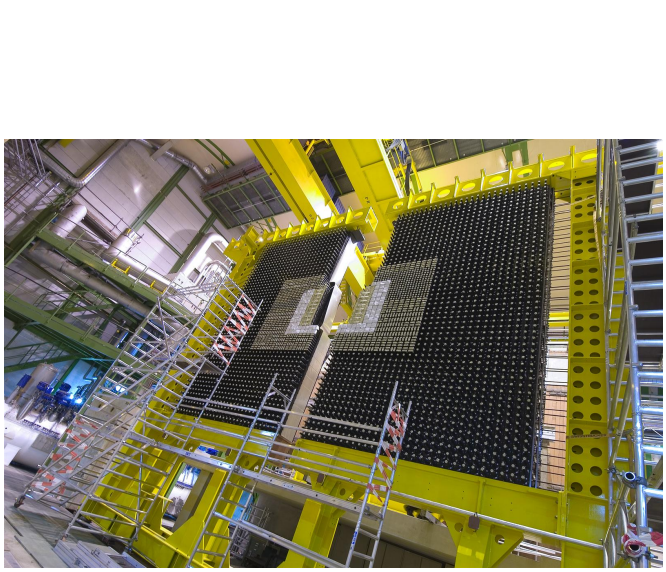

Figure 3.9: The LHCb Calorimeters ready for commissioning. Left, the ECAL. Right, the HCAL. Courtesy of the CERN photography service.

The Electromagnetic CALorimeter, ECAL, is primarily used for the identification and calorimetry electrons and photons. The ECAL is shown in Fig. 3.9 and consists of cell-partitioned 2 mm Lead and 4 mm-thick scintillator pads.

The Hadronic CALorimeter, HCAL (Fig. 3.9), is similar to the ECAL in design. It consists of 16 mm-thick iron sheets, interspersed with ∼4 mm-thick scintillator regions. Almost all hadrons interact with the HCAL, however, muons continue through the HCAL to the muon chambers.

3.6 Muon chambers

The muon system is used to identify and measure the energy of muons within the LHCb acceptance [68]. Muons are highly penetrating minimum ionising particles, within the typical energy range from a b-decay, of order $\mathrm{GeV}c^{-2}$. To identify muons we place all but one of the muon chambers after the ECAL and HCAL, which provide a screen, absorbing almost all photons, electrons and hadrons. The five muon stations, see Fig. 3.1, provide excellent identification of muons with momentum larger than $5\,\mathrm{GeV}c^{-1}$. The total system comprises 1392 chambers with a total area of $435\,\mathrm{m}^2$. Honeycomb-structure multi-wire proportional chambers (MWPC) are used for all but the central regions of M1, which have high particle fluxes, requiring more radiation hard triple-GEM[3] detectors [4].

3.7 The RICH system

The RICH system is crucial for the particle identification of charged kaons and pions within the LHCb experiment [69]. As will be demonstrated in this section, the separation of kaons and pions is required to separate a given decay of interest from similar hadronic backgrounds. There are two Ring Imaging CHerenkov, RICH, subdetectors, which are shown in Fig. 3.10.

3.7.1 Introduction to RICH systems

To unambiguously determine the identity of a particular particle one requires knowledge of how it interacts, its mass and its charge. We can measure the momentum and energy of a particle with calorimeters and tracking, however, we must also determine its velocity to recover the mass. It is especially difficult to determine the velocity of a particle observed within a particle physics experiment. Typically the velocity is a large fraction of the speed of light and time-of-flight

[3] Gas electron multiplier [61].

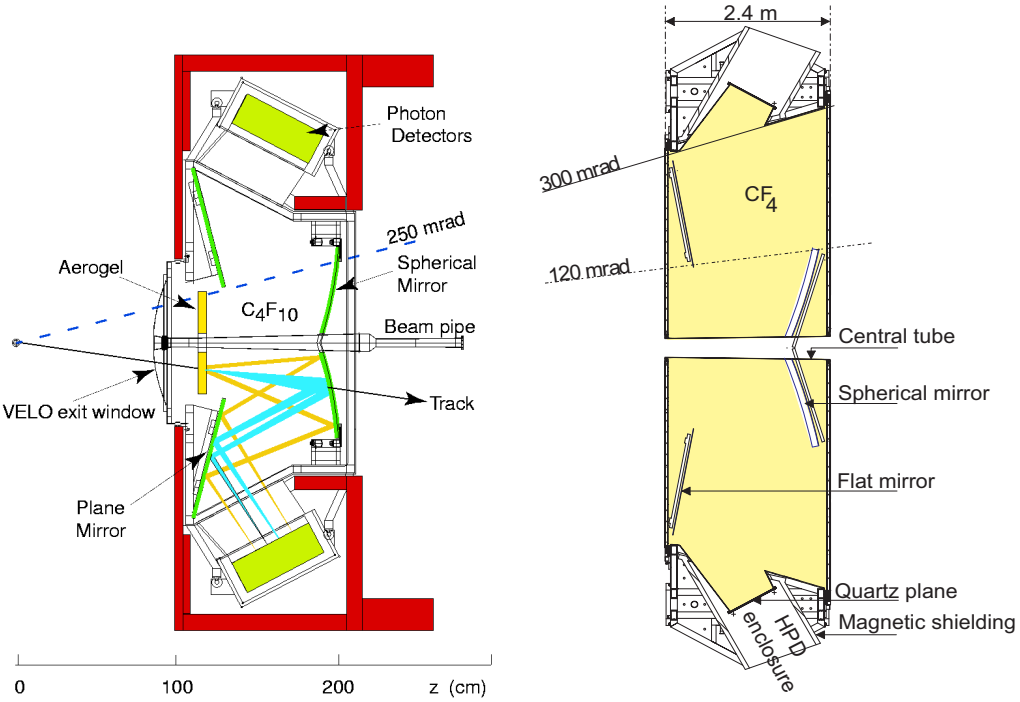

Figure 3.10: The LHCb RICH detectors. Left, the RICH 1 detector seen in the vertical plane, after [31]. Right, the RICH 2 detector seen in the horizontal plane, after [69].

measurements would require sub-nanosecond time resolutions. Instead Cherenkov methods are used.

As a charged particle traverses a dielectric (insulating) medium, it perturbs the local electric field. The particle deposits energy into the field, displacing local electric charge, which may relax by the emission of photons. From relativity, a particle may never travel faster than the speed of light, c. However, in a medium with a refractive index higher than 1, the particle may exceed the local phase velocity of light in the medium. When a charged particle exceeds this velocity coherent interference effects occur, the particle's transition results in emission of a cone of Cherenkov light, the optical equivalent of a sonic boom. The cone half-angle, θ, is dictated by the velocity of the particle, $v = \beta c$, and the refractive index of the material, n:

$$\cos(\theta) = \frac{1}{n\beta} \tag{3.1}$$

Considering Huygen's theorem (see Fig. 3.11), one can construct this result in an elementary manner. This angle is notably independent of wavelength, position,

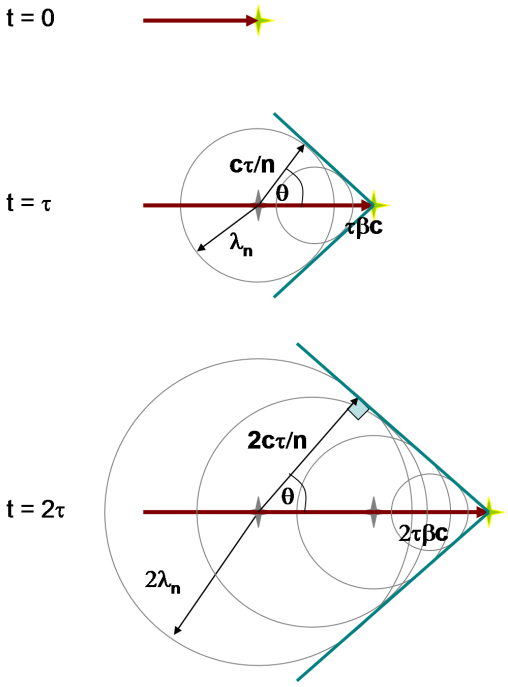

Figure 3.11: Schematic of Cherenkov radiation in the Huygen's approximation. Consider wavelets with wavelength λ_n and period τ emitted continuously along the path of the particle. Wavefronts coherently superpose along the plane in which the wavefronts all lie, to form a cone whose angle, θ, is dictated by the refractive index of the medium, n, and the particle velocity, $v = \beta c$. $cos(\theta) = 1/n\beta$, as in Eqn. 3.1. At all other cone angles the waves interfere destructively.

time, or particle type. Radiation of any frequency is possible, along the same angle.

To demonstrate this effect more fully a derivation with Maxwell's equations is given in Ref. [70]. The number of Cherenkov photons detected, N_c, is given by:

$$N_c = L\frac{\alpha z^2}{\hbar c}\int \eta(E)\sin^2(\theta_c(E))dE \tag{3.2}$$

where L is the length of the radiator, α is the fine-structure constant, z is the particle charge, E the Cherenkov photon energy, which has a probability of being detected given by $\eta(E)$. As the dependence of the refractive index on the photon energy is typically weak, one can factor out the energy dependencies into a figure of merit, N_0, which qualifies any Cherenkov system:

$$\begin{aligned} N_c &= LN_0\langle\sin^2(\theta_c)\rangle \\ N_0 &= \frac{\alpha z^2}{\hbar c}\int \eta(E)dE \\ N_0 &= \frac{\alpha z^2}{\hbar c}\eta_g \int \eta_{pde}(E)dE \end{aligned} \tag{3.3}$$

where $\alpha/\hbar c \approx 370\,\mathrm{cm}^{-1}\mathrm{eV}^{-1}$, η_g is the geometric coverage of the photon detectors and η_{pde} their photon detection efficiency, which is usually the product of the detector

quantum efficiency η_q and a collection efficiency η_c, which should incorporate losses from other optical elements in the system. N_0 is usually expressed in cm^{-1} or m^{-1}.

Ring Imaging Cherenkov (RICH) detectors use spherical mirrors to focus this cone emission onto a plane of photosensitive detectors, forming a ring, whose diameter is therefore a measure of the velocity of the particle. Gas radiators and other materials with refractive indices close to 1 are typically chosen to minimise the material added and to ensure the ring falls within the sensor plane such that it can be adequately reconstructed.

3.7.2 The LHCb RICH

Using two RICH detectors, LHCb can cover the full momentum range in the acceptance regions applicable to kaons and pions from a typical b-decay. The complimentary regions covered by RICH 1 and RICH 2 are shown in Fig. 3.12.

RICH 1 is upstream of the magnet, directly after the VELO, and RICH 2 is after

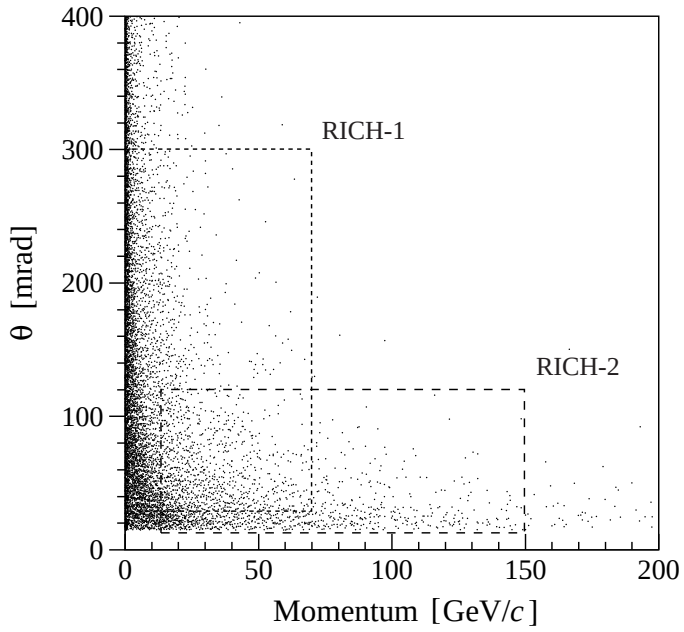

Figure 3.12: The complimentary coverage of the two RICH detectors is shown in the plane of Polar angle, θ, versus momentum, p. On the same graph is plotted the distribution of tracks in simulated $B_d^0 \to \pi^+\pi^-$-events, after [69].

Table 3.2: Properties of RICH 1 and RICH 2, after [4].

Feature	Comment	RICH 1		RICH 2	Unit
Mass	total M_T	16		30	tons
	shield M_S	15		12	tons
Dimension	$x \times y \times z$	$1.95 \times 4.0 \times 1.175$		$9.8 \times 7.2 \times 2.4$	m^3
Radiator	material	Aerogel	C_4F_{10}	CF_4	–
	index	1.030	≈ 1.0014	≈ 1.0005	–
	θ_c	242	53	32	mrad
	π threshold	0.6	2.6	32	GeVc^{-1}
	K threshold	2.0	9.3	15.6	GeVc^{-1}
	volume	$<$0.1	3.5	95	m^3
Spherical mirror	material	carbon-fibre		SIMEX	–
	curvature	2.7		8.6	m
Photon detectors	HPDs	196		288	–
	channels	201		295	10^3
Radiation length	total	8		15	$\% X_0$

the magnet, before the first muon chamber [69]. The RICH detectors are compared in Table 3.2. Three radiator materials were selected to cover complimentary regions in refractive index. RICH 1 employs Aerogel ($n \approx 1.030$) and C_4F_{10} ($n \approx 1.0014$) radiators to determine the velocity of particles with low momenta, from $\sim$2 GeVc^{-1} up to 60 GeVc^{-1}. RICH 2 employs CF_4 ($n \approx 1.0005$) and determines the velocity of particles with higher momenta, from $\sim$15 GeVc^{-1} to $\sim$100 GeVc^{-1}.

Aerogel is a colloidal form of quartz and is a very useful radiator, able to cover the gap in refractive indices between liquid radiators and gas radiators [71]. The density of Aerogel is low and tuneable, providing a range of refractive indices, 1.01-1.10. Due to Rayleigh scattering Aerogel is an optically lossy material. The level of Rayleigh scattering is characterised by the clarity coefficient C. The transmission, T, is related to the wavelength, λ, thickness, x, and C, through the Hunt formula $T = e^{-Cx/\lambda^4}$ [71]. The LHCb Aerogel tiles have a refractive index of 1.030 at 400 nm and an excellent clarity of below $C = 0.0054\,\mu\text{m}^4\,\text{cm}^{-1}$. We use a 300 μm-thick glass filter to remove photons of energy above 3.5 eV, which will be scattered off the Cherenkov cone. The RICH1 Aerogel can be compared to the other RICH radiators given in Table 3.2. The momentum threshold for Cherenkov radiation is 0.6 GeVc^{-1} for pions and 2.0 GeVc^{-1} for kaons, which extends the separating power of the RICH system down to the required 2.0 GeVc^{-1} in momentum.

To reduce the material in the LHCb acceptance, RICH 1 and RICH 2 both employ a combination of spherical and flat mirrors allowing the photon detector planes to be placed outside of the acceptance. To further minimise the material, the RICH 1 spherical mirrors are constructed of coated carbon-fibre composite and the gas enclosure is mounted directly on the VELO exit window.

The expected number of photons detected from a charged track with $\beta \simeq 1$ is ~ 16 from the C_4F_{10} radiator in RICH 1, ~ 5 from the Aerogel, and ~ 14 from the CF_4 radiator in RICH 2. We require single-photon sensitive devices, whose active areas cover a large fraction of the $3.3\,m^2$ photon-detector plane. The chosen photodetector technology, Hybrid Photon Detectors (HPDs), are discussed in Sec. 4.1. The HPDs are stored under a helium-free atmosphere, separated from the radiator-gas volume by quartz windows, which are anti-reflection coated.

Soft iron shielding is required to reduce the magnetic field in the region of the RICH 1 photon detector planes from $\sim$60 mT to below 5 mT in order to operate the HPDs.

The RICH system was amongst the first LHCb subdetectors to be commissioned. The majority of RICH 1 was assembled in situ. The RICH 2 superstructure, complete with mirrors, was the largest complete LHCb component to be lowered into the pit. The upper HPD plane in RICH 1 is shown in Fig. 3.13, top, and an image is projected on the RICH 2 plane in Fig. 3.13, bottom.

3.7.3 Particle identification

Neutral particles ($\pi^0, \gamma,\ n^0,\ K_L^0$) are trackless and are identified solely from their interactions in the calorimeters. Muons are identified primarily by the muon system, electrons are separated from hadrons by the combination of calorimeter information. Separation of final state hadrons, ($\pi^\pm, K^\pm, p^\pm$), is reliant on the RICH.

As discussed in Sec. 3.7.1 measurement of Cherenkov angle is a measurement of the velocity of the particle. Combined with a measurement of the momentum, a mass hypothesis is made. For each hypothesis information from RICH and the

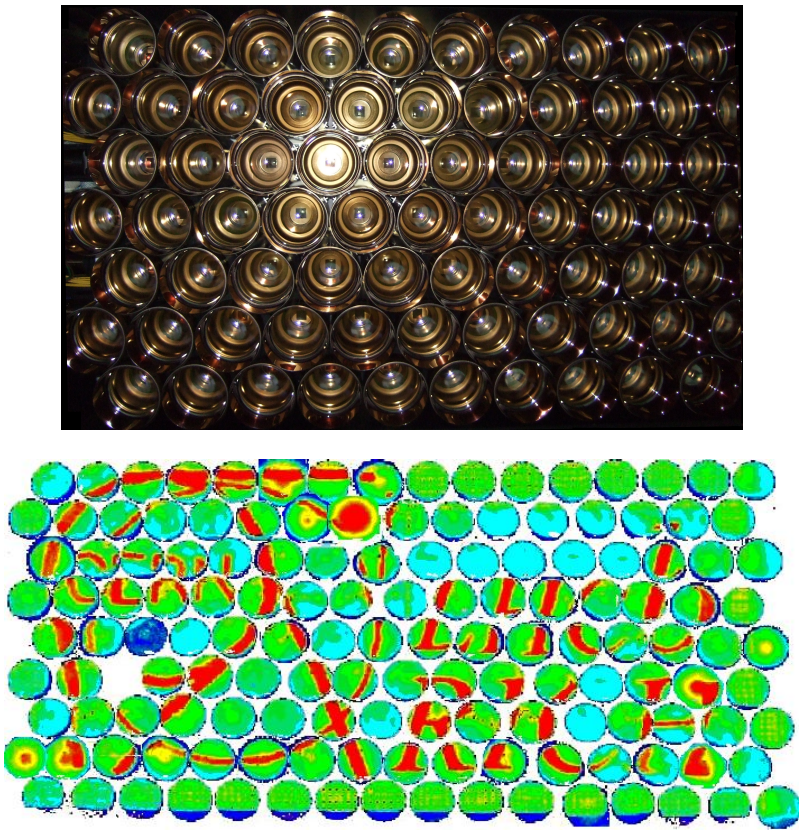

Figure 3.13: The commissioned RICH HPDs. Top, HPDs in the RICH 1 upper plane, ready for insertion. Bottom, the LHCb RICH logo projected with single photons onto the RICH 2 HPD plane and recorded by the photon detectors. Courtesy of the CERN photography service.

calorimeters is combined by summing the log likelihoods.[4]

The possibilities that a hit is background from secondaries, trackless particles or a noise hit are accounted for probabilistically. A cut on the log likelihood difference between different hypotheses is used to separate particle types. The resultant PID performance from MC-truth information for kaons is shown in Fig. 3.14. The efficiency of the algorithm is typically $> 90\,\%$ with a mis-ID rate of $< 10\,\%$.

The separation of hadronic final states using the RICH information can be demonstrated in several channels, for example[5] $B^0 \to h^+h^-$ [72], from Monte Carlo simulation (See Sec. 5.1). The invariant mass of the dihadrons, $M(h^+h^-)$, i.e. of the B^0-candidates, is given in Fig. 3.15, left, for selected candidates without using

[4]The complicated global log likelihood minimisation technique is only briefly discussed in this Thesis. For further information the reader should consult Refs. [4] and [31].

[5]Also see Sec. 6.2.

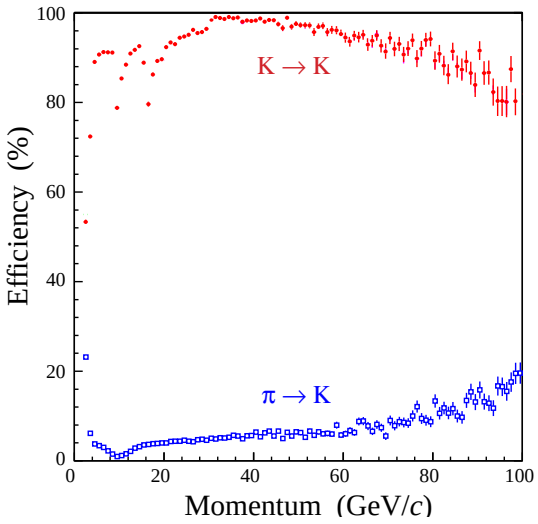

Figure 3.14: RICH PID performance. Kaon ID efficiency and pion misidentification rate as a function of momentum, resulting from the delta-log-likelihood (Δ_{LL}) comparison.

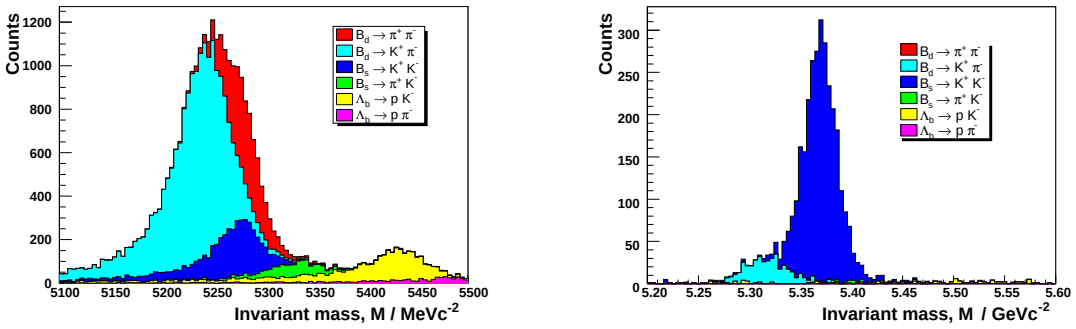

Figure 3.15: Invariant mass distributions of simulated $B^0 \to h^+h^-$-candidates, after [72]. Left, without employing RICH information, all tracks are hypothesised to be pions. Right, cutting on the RICH information allows us to separate the $B_s^0 \to K^+K^-$-mode clearly. On the right tracks are given the kaon hypothesis, which also makes the B^0 invariant mass slightly larger.

RICH information. Individual modes, such as $B_s^0 \to K^+K^-$, can be efficiently selected utilising the RICH information as is demonstrated in Fig. 3.15, right.

3.8 The LHCb trigger

For LHCb the visible event rate is 10 MHz.[6] We use a two-tiered triggering system online to select events of interest [73]. Data are collected from a few key subsystems at the LHC clock frequency of 40 MHz. These data are processed by the Level-0 trigger (L0), shown schematically in Fig. 3.16. The L0 trigger reduces the data output to 1 MHz, which is then passed to the High-Level-Trigger (HLT).

L0 Trigger: The primary task of the L0 trigger is to reduce the data rate from the bunch-crossing frequency of 40 MHz to 1 MHz, at which frequency it is possible to read out the entire detector, while retaining as many interesting events with b-hadrons (b-events) as possible. The L0 examines the overall multiplicity and event energy from the calorimeters. A fast reconstruction is performed of the highest E_T clusters in the calorimeters typical of hadrons, electrons and photons, and the two highest-p_T muon candidates in the muon chambers.

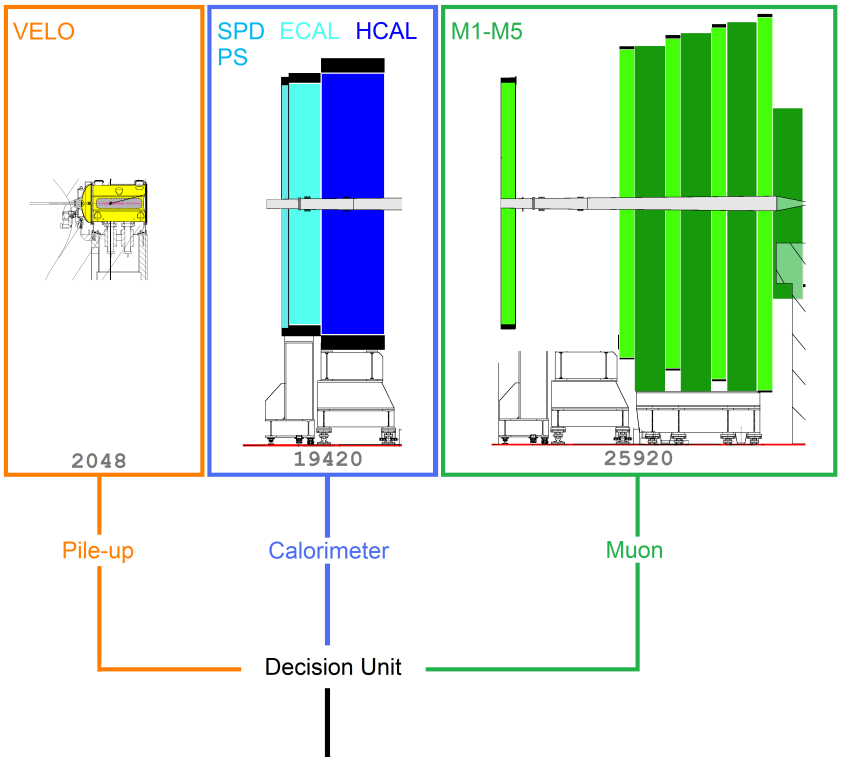

Figure 3.16: Schematic of the L0 trigger system, after [4], the number of channels are shown.

[6] This is the rate of events with at least one ineleastic $p-p$ interaction, causing tracks in LHCb.

Table 3.3: The L0 trigger cuts, example parameters from Monte Carlo tuning.

Name	Subdet.	Particle	Parameter	Condition	Value	Unit
PuMult	Pile-up	all	multiplicity	$<$	112	–
PuPeak2	Pile-up	all	peak [a]	$<$	3	–
SPDMult	SPD	All	multiplicity	$<$	280	–
$\sum E_T(X)$	Calo	all hadrons	$\sum E_T$	$>$	5	GeV
$E_T(e)$	ECAL	electron	E_T	$>$	2.14	GeV
$E_T(\gamma)$	ECAL	photon	E_T	$>$	1.96	GeV
$E_T(X)$	HCAL	hadron	E_T	$>$	3.98	GeV
$E_T(\pi^0)$	Calo	π^0	E_T	$>$	3.98	GeV
$p_T(\mu)$	Muon	muon	p_T	$>$	0.84	GeV
$p_T(\mu\mu)$	Muon	di-muon	p_T	$>$	0.84	GeV

[a] height of second peak from the pile-up processor

Table 3.4: The L0 trigger streams, with the parameters from Table 3.3.

Name	Applied Cuts
Global event cut (GEC)	PuMult & PuPeak & SPDMult & $\sum E_T(X)$
Electron	$E_T(e)$ & GEC
Photon	$E_T(\gamma)$ & GEC
Hadron	$E_T(X)$ & GEC
Pi-zero	$E_T(\pi^0)$ & GEC
Muon	$p_T(\mu)$ & GEC
Di-muon	$p_T(\mu\mu)$ & $\sum E_T(X)$

Additionally there is a dedicated pile-up system, provided to identify events with multiple primary vertices. This information is extracted from the first two VELO modules. Example cuts and trigger streams are given in Tables 3.3 and 3.3. Typically the L0 is $>80\,\%$ efficient for events containing a muon from a B-decay, $\sim 50\,\%$ efficient for events containing a hadron from a B-decay, and typically around $30\,\%$ for events with electrons from a B-decay [73, 47].

HLT: The HLT is a C++ program operated on the event filter farm, which is expected to have up to 2,000 CPUs. The HLT can in principle access the entire event. However, the first stage, HLT1, aims to refine the L0 decision, outputting at 30 kHz. In the HLT1 basic reconstruction using multiple subdetectors is performed. Firstly the HLT1 attempts to confirm the L0 decision. The remaining HLT1 is organised into alleys, with each event being tested against specific partial reconstruction algorithms as shown in Fig. 3.17. To further improve the purity of the event sample

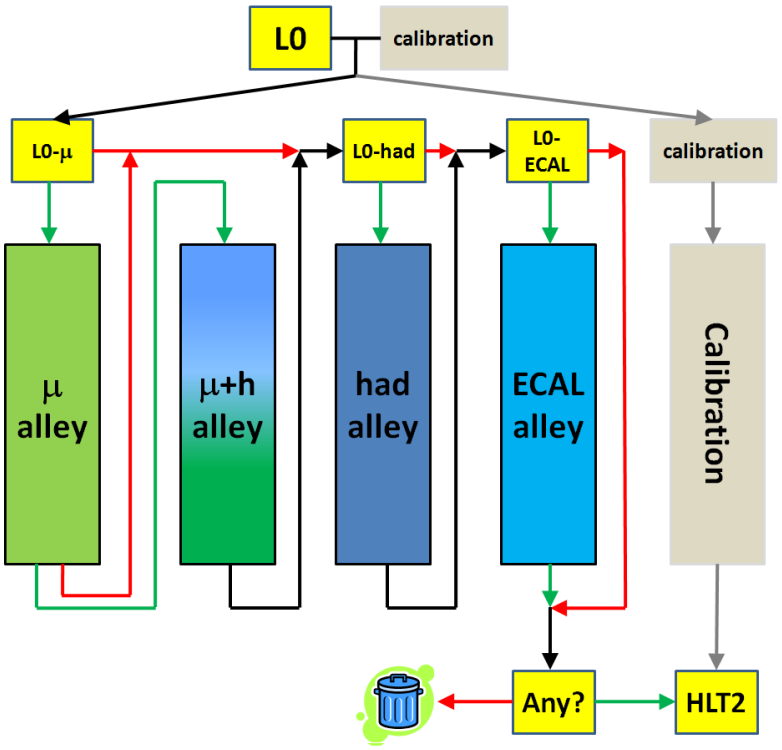

Figure 3.17: Schematic of the high-level trigger system, after [4]. The HLT1 is organised into alleys each with their own specialised C++ algorithms. Green arrows represent a positive result, red arrows represent a negative result.

inclusive and exclusive triggers specific to event types are implemented in a separate stage, HLT2. The HLT2 takes the output from HLT1 and reduces the rate to 2 kHz, suitable for writing to disk. The HLT is fully software-implemented and highly configurable. Initially the HLT will be tuned on Monte Carlo signal events, however, the specifics will be dictated by the early data.

Chapter 4

Hybrid Photon Detectors for the LHCb RICH

The LHCb RICH system contributes greatly to the precision of LHCb physics. As was detailed in Sec. 3.7.2, the RICH detectors measure the velocity of charged particles through the Cherenkov light they emit. The RICH system relies on its photodetectors to provide a fast, high efficiency, low noise, detection of Cherenkov photons, across four detector planes covering a total area of $\simeq 3.3\,\mathrm{m}^2$. Hybrid Photon Detectors (HPDs) which are described in Sec. 4.1 were chosen. The HPDs were developed specifically for the purpose by LHCb RICH, in collaboration with ALICE (see Sec. 2.4) and with industry. The HPDs were rigorously tested before being installed in LHCb. In Sec. 4.2 the programme of testing is presented. The quantum efficiencies of $\sim$10 % of the HPDs were measured in a dedicated setup confirming the measurements by the manufacturer. The quantum efficiency measurement is discussed in more detail in Sec. 4.3 and a selection of test results for the entire HPD sample is given in Sec. 4.4.1. Altogether the production yield is $> 97.5\,\%$, and an impressive increase in quantum efficiency of a relative 27 % has been observed. The improvement in HPD performance as a result is investigated in Chapter 5.

4.1 Hybrid Photon Detectors

To perform accurate particle identification within the LHCb RICH over the lifetime of the experiment, the single-photon sensitive detectors must exhibit the requirements listed in Table 4.1.

HPDs are a technology exploiting the advantages of vacuum photon detector tubes with pixelated silicon detectors and read out with integrated circuit technology [74]. A broad wavelength range of incident light, extending into the UV[1], is transmitted by a 7 mm-thick quartz window (QW) and falls upon a multi-alkali photocathode (PC). The PC is biased to $-20\,\mathrm{kV}$ relative to the silicon chip. Through the photoelectric effect in the PC, incident photons are converted to photoelectrons which travel within the HPD vacuum and are accelerated toward the pixelated silicon detector. Fig. 4.1 presents example schematics. The PC is imaged with an electrostatic field onto the encapsulated silicon sensor with a demagnification factor of $\sim$5. Around 85 % of all photoelectrons are detected as hits. Each photoelectron produces $\sim 5,000\,\mathrm{e}^-$ in the sensor. These may be shared across more than one pixel, producing multiple adjacent hits. The p-n pixelated sensor[2] is over-depleted with a reverse bias of 80 V under operation. The silicon sensor is bump-bonded [75] to a pixelised readout chip. The chip is also encapsulated within the vacuum

Table 4.1: Selected requirements and parameters for the RICH photon detectors.

Feature	Comment	Value	Unit
Active area fraction	- -	80	%
Detection range	wavelength	200-600	nm
Lifetime	at least	10	years
Hit rate	maximum	50	MHz cm^{-2}
Dark count rate	maximum	5	MHz cm^{-2}
Afterpulse probability	maximum	1	%
Granularity	- -	2.5x2.5	mm^2
Clock frequency	LHC clock	40	MHz
Internal buffering	trigger latency	4	μs
Radiation tolerance	- -	30	krad
B-field conditions	maximum	5	mT
	direction	any	

[1] To $\sim$200 nm.

[2] p-type pixels in an n-type sensor substrate.

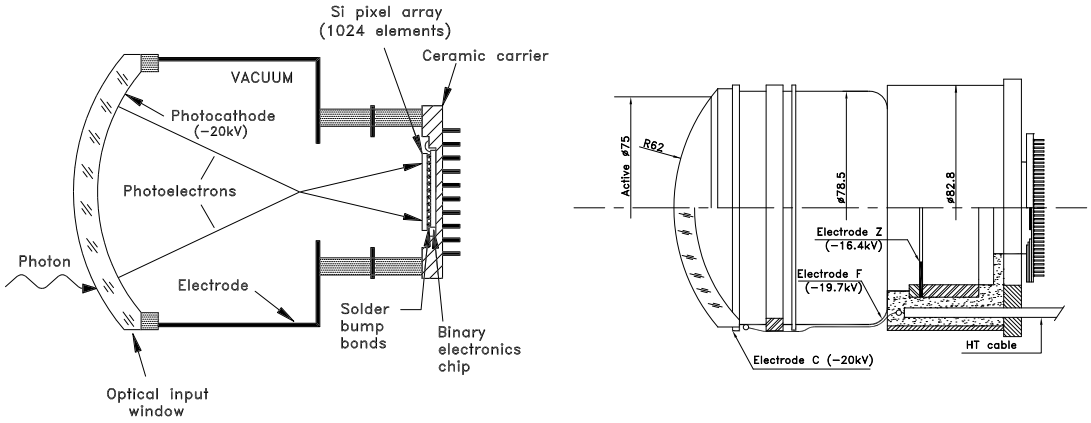

Figure 4.1: HPDs for the LHCb RICH [69]. Left, HPD schematic with electron optics highlighted. Right, more technical description of a complete HPD.

of the HPD. This results in low capacitive load to the front-end electronics and hence a high signal-to-noise ratio. The HPD pixel chip was a joint development between the LHCb and ALICE collaborations [76].[3] The detection and readout chain within each HPD is pixelated to 8,192 pixels, 500.0 μm by 62.5 μm in dimension. To meet the latency and readout requirements of the triggering system in LHCb pixels are actively ORed together in sets of eight to effectively form 1024 'super-pixels', or LHCb-pixels, of dimension 500 μm by 500 μm. Each of the 8,192 pixels consists of sensor, pre-amplifier, shaper, a discriminator with individually configurable threshold, 16-cell data buffer and readout electronics. A selection of the specifications for HPDs is given in Table 4.2. These are based on the parameters from Table 4.1 and the performance of prototype HPDs.

The HPDs are manufactured in several stages in an international effort in close collaboration with industry. LHCb was involved at all stages in the design and testing of the components. The details of the procedure are reported in Ref. [74]. The final stage of encapsulation of the HPD, PC deposition, vacuum sealing and potting was performed by Photonis-DEP.[4] We require 484 HPDs to equip both RICH detectors. The manufacture of HPDs began in mid 2005 and the entire sample of 550 production HPDs, which includes spares, was completed in 2007.

[3] 96 chips were also used in the NA60 tracking telescope [77].

[4] Photonis Netherlands B.V., Dwazziewegen 2, P.O. Box 60, NL-9300 AB Roden, The Netherlands. Formerly Delft Electronic Products (DEP).

Table 4.2: Selected specifications for final assembled HPDs [78].

Feature	Comment	Lower	Typical	Upper	Unit
QW Transmission	200 nm	–	35	–	%
	240 nm	–	75	–	%
	>280 nm	–	92	–	%
Quantum efficiency	270 nm	20.0	23.3	–	%
(QE) (η_q)	400 nm	15.7	19.3	–	%
	520 nm	8.3	10.7	–	%
Dark count	- -	–	5.0	–	kHz cm^{-2}
Sensor leakage current	At 80 V at 50 °C	–	1.0	–	μA
Afterpulsing	Ion feedback rate	–	–	1	%
Lifetime	≤10 % deviation	10	–	–	yrs
Radiation hardness	- -	30	–	–	krad
Pixel threshold	- -	–	–	1500	electrons
Pixel noise	- -	–	145	250	electrons
Photoelectron efficiency	–	–	85	–	%
Working channels	- -	95	–	–	%

4.2 Photo-Detector Test Facilities

Photonis-DEP tested each manufactured HPD including a full QE measurement. LHCb also verifies that manufactured HPDs are within specifications. Two Photo-Detector Test Facilities (PDTFs) located at Edinburgh and Glasgow were commissioned by LHCb, each with two test stations. Testing includes a confirmation measurement of the QE performed at seven wavelengths on a subsample of 10 % of HPDs. Fig. 4.2 shows a test station constructed at Edinburgh.

Figure 4.2: PDTF station 1 at Edinburgh. From left to right: dark box with fibre-delivered light source, distortion mask and mounting point for the HPD, readout and data acquisition electronics, HV box, power supplies and measurement instruments, DAQ PC.

4.2.1 Methodology

At the PDTF a comprehensive programme tests all functionality and specifications unique to each HPD. Configuration, monitoring and data taking are fully automated with LabVIEW [79]. Post-test analysis of test data provides a comprehensive electronic record and printable summary. A clustering algorithm is used to identify and remove adjacent hits due to charge sharing.

On arrival the HPD is inspected for defects and its mechanical dimensions are determined using a custom mechanical jig. The anode functionality, including thresholding, noise, DAC functionality and supply current requirements are determined. This includes a current-voltage (IV) curve measurement of the silicon sensor. The leakage current of the HPD modifies the voltage dropped across the sensor. This in turn changes the drift time of the deposited electrons. The leakage current, therefore, influences the timing response of the HPD. A larger leakage current corresponds to a longer drift time. The average pixel threshold is optimised to eliminate electronic noise, save that from specifically noisy pixels, which are identified and removed from later analyses. High voltage is then gradually applied to the HPD and the stability (at 20 kV) is monitored throughout the test procedure. The dark count is allowed to settle and is monitored for at least 30 mins. The response to light is determined with pulses from an LED coupled into a single-mode fibre.[5] The LED intensity is tuned to give 2-6 hits per event, simulating a typical RICH 2 occupancy. The PC image quality, its size, position and uniformity, along with the number of unresponsive (dead) pixels are determined (see Fig. 4.3).

Once fully settled, the dark count is determined from a dark run of 5M-triggers with the HPD biased to operating potential (-20 kV). A typical dark photocathode image is reproduced in Fig. 4.4. Due to the very low level of inherent dark count, noisy pixels can also be identified in this high-statistics run.

The afterpulse rate from ion-feedback is determined from a timing scan. As

[5] 15 ns FWHM pulses of wavelength 470 nm, 10 nm-FWHM, into a fibre of 0.11NA. The fibre is positioned within the box ∼43 cm from the quartz window (QW).

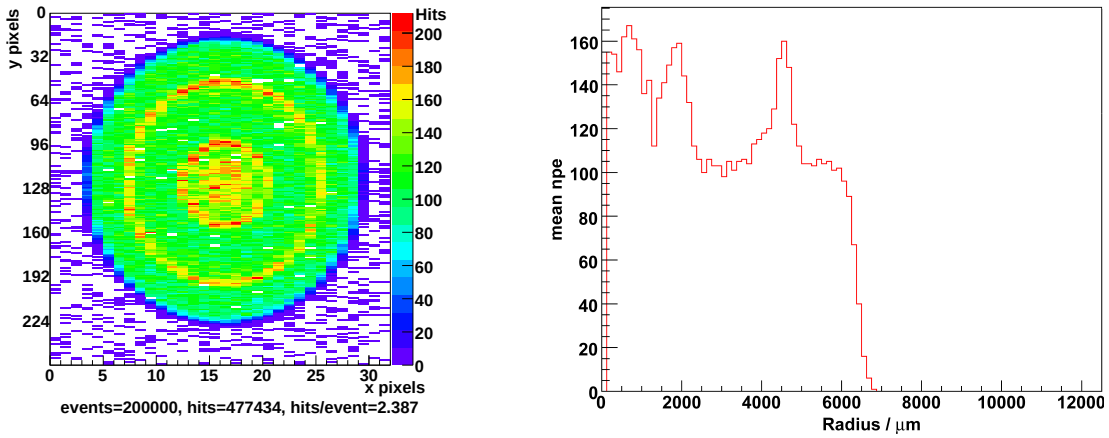

Figure 4.3: Photocathode image analysis from test PDTF data. Long LED run, 200,000 triggers, 2.387 hits per event with HPD H602003. Left, a histogram of total hits for each pixel. Right, pixel occupancy as a function of radius. Three reflections from the chromium coating at the edge of the QW give the concentric rings seen above. npe is the number of photoelectrons.

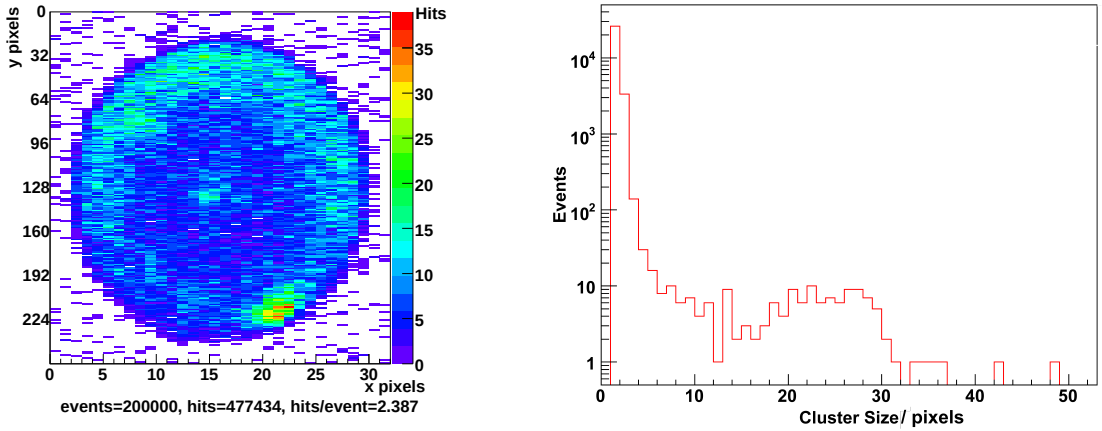

Figure 4.4: Dark count of a typical production HPD, H606002, from 5M trigger dark run. Left, the hit distribution. Right, a histogram of cluster sizes per event. This HPD was measured to have a dark count of 2.57 kHz cm^{-2}, and no noisy pixels.

photoelectrons ejected from the PC travel through the vacuum of the tube they may ionise residual gas molecules. The positive ions produced are accelerated towards the PC. When the ions impact they deposit their energy and result in multiple electron emission. The electrons are then accelerated back to the anode, forming a large cluster of hits on the anode, typically 10-30 adjacent pixels. Due to the cross-focusing of the HPD the highest electron density is close to the longitudinal centre, and in the lateral centre, of the HPD (demonstrated in Fig. 4.1). Ion feedback has a characteristic delay resulting from the drift time of the ions. A timing scan, such as

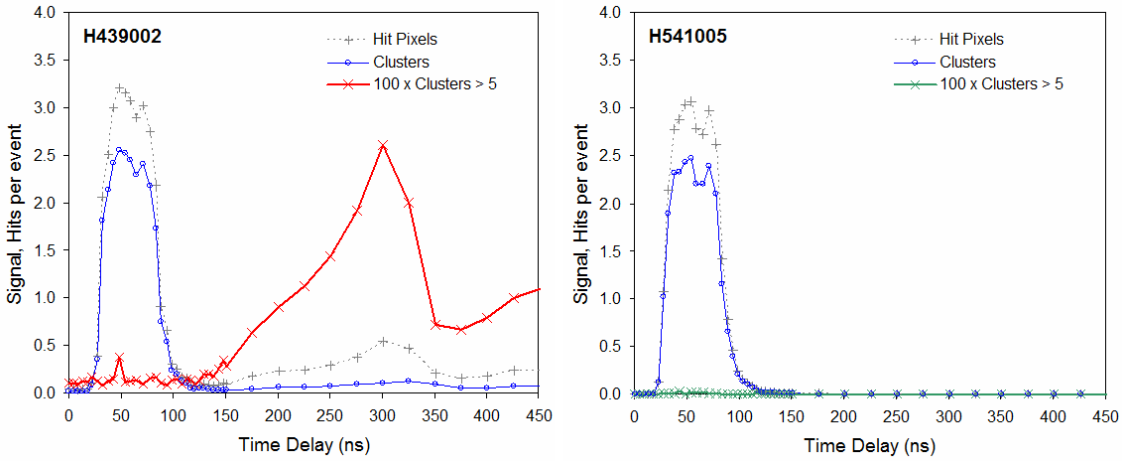

Figure 4.5: A timing scan (strobe-scan) measured at PDTF. The hit rate, cluster rate and large cluster rate are plotted versus the delay time of the signal gate. Left, for an atypical pre-series HPD with large delayed IFB. Right, for a typical production HPD with excellent vacuum quality.

is shown in Fig. 4.5, is used to study the ion feedback clusters. The ratio of the peak in delayed clusters, larger than five pixels, to the initial prompt signal, at the peak of the LED pulse, gives the ion feedback probability. This measures the vacuum quality of the HPD, which is expected to degrade slowly over time. Mechanisms for the introduction of residual gas involve diffusion through the QW, diffusion through imperfections in the tube body or the vacuum seal, and outgassing of the HPD internally. Ion feedback is further discussed in Appendix A.

4.3 Quantum efficiency measurements

A high HPD photocathode quantum efficiency (QE), η_q, is important for a high photon detection efficiency and a high photon yield in the RICHes [80]. The QE of all HPDs are measured by Photonis-DEP, before shipping to the test centres in Scotland [78]. Independent QE measurements were made possible at the LHCb RICH Photo Detector Test Facilities (PDTFs) through the development of a measurement setup working in concert with the already established tests.

This section brings together test results from LHCb facilities at CERN, the manufacturer's quality assurance tests and the LHCb Photo Detector Test Facilities (PDTFs) to provide a complete picture of the quantum efficiencies of the HPDs, as is described in Ref. [3].

4.3.1 Quantum efficiency

The QE, η_q, of a material represents the probability of liberating an electron by any given photon falling on the material. It dictates the ratio of the number of photoelectrons produced to the number of incident photons. Absorbed within this ratio are the material properties, such as absorption and work function, which result in a wavelength dependence. Absorption occurs within the bulk material, so electron transport properties and scattering along with thermal and bulk effects are included in the QE [81]. For a metal, absorption occurs within a thin layer on the surface, penetrating to the electromagnetic skin depth of the material, dictated by its refractive index. Additionally, reflection at the surface reduces the available light in the bulk. To determine the QE of a material one measures the following quantities [82]: the current drawn by the material in response to a given stable light source (the photocurrent) and the intensity of that light source. From knowledge of the intensity one can deduce the photon arrival rate, and from knowledge of the drawn current the rate of photoelectron production can be deduced. To measure the photocurrent, photoelectrons must be drawn to a collection surface through an electrostatic potential. The bias of the photocathode must be negative, or below the threshold of the photoelectric effect.

For the HPDs we do not directly measure the QE of the photocathode. We perform measurements which fold in reflective losses at the Air-Quartz window interface and the Quartz-Photocathode interface, back-reflections and interference at the photocathode-vacuum interface. Gain from reflections, scattering effects within the bulk photocathode material and feedback from ionisation of residual tube gasses may also exist; however, the number which is important for physics, and to qualify the performance of any photon-sensitive system is precisely this overall QE of the HPD, folding in all effects. We should exclude parasitic gain features, such as ion feedback, which produce new emission at an unrelated point in space and/or delayed in time within the HPD. These would cause a systematic bias to the measured QE.

4.3.2 Measurements by LHCb RICH at CERN

A pre-series of nine pixel Hybrid Photon Detectors (HPDs) were manufactured over the period September-December 2004. These HPDs have undergone extensive testing in the laboratory [74, 80] and in test beams [83]. Their QE has been measured by the manufacturer DEP, and was measured again by LHCb at CERN for comparison purposes. In addition, one of these pre-series tube has been subjected to an accelerated ageing test, with a QE measurement performed before and after.

The results are given in Ref. [84] and briefly summarised here for the nine pre-series HPDs measured. Good agreement is obtained with the DEP measurements over the full wavelength range, as demonstrated by Fig. 4.6.[6] From the measurements of these preseries HPDs, and the prototype HPDs, an expected (average) QE spectrum was extracted. This spectrum was used as the input to the LHCb Monte Carlo simulation. Photon yield, Cherenkov angle resolution, and PID performance figures for LHCb RICH are based on this QE, which serves as a benchmark for comparison of the production HPDs.

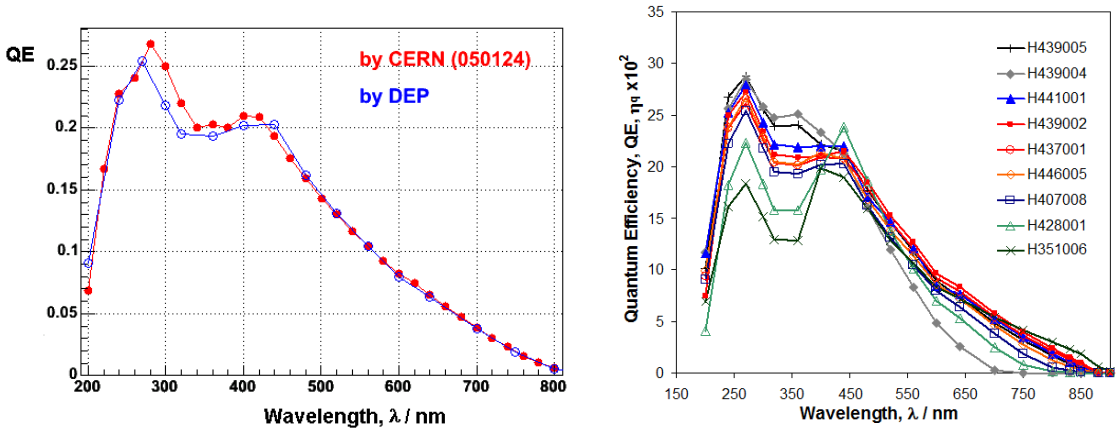

Figure 4.6: Quantum efficiency vs. wavelength of pre-series HPDs measured by DEP and LHCb at CERN. Left, for an example HPD, H407008. The CERN measurements in red agree well with the DEP measurements in blue. Right QE vs wavelength of the 9 preseries HPDs as measured by DEP. The DEP measurements technique is discussed in Sec. 4.3.3.

[6] A single HPD falls below the specifications at 270 nm as given in Table 4.2.

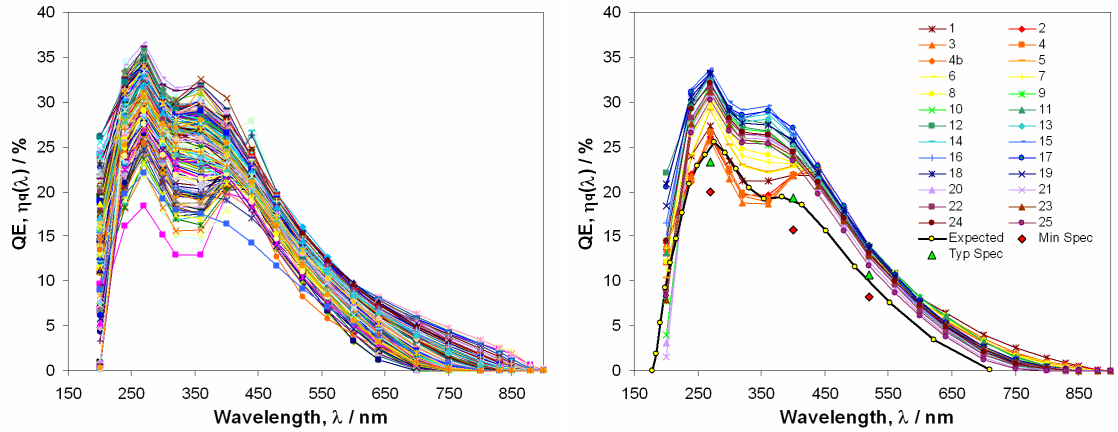

Figure 4.7: Quantum efficiency measurements performed by DEP as a function of wavelength. Left, one third of all measurements are shown. Right, average QE per batch. The expectations arise from initial tests on preseries HPDs, see Sec. 4.3.2.

4.3.3 DEP measurements

In a similar technique to that reported in Sec. 4.3.4, DEP measures the QE over wavelengths of 200 – 900 nm with 10 nm band-pass filters. They use white light sources to illuminate the centre of the photocathode up to 25 mm in diameter, and compare to a calibrated reference measurement. The QE is measured with the HPD photocathode at −900 V and all other electrodes at ground. Two separate measurement setups are employed for wavelengths up to 400 nm and for wavelengths beyond 400 nm. No infra-red blocking filters are used.

The resultant QE curves for a third of the sample are plotted against wavelength in Fig. 4.7, and the summary of all results is presented in Table 4.3. DEP have demonstrated an ability to consistently produce HPDs with higher QE than the

Table 4.3: QE summary for all production HPDs.

Detail	Typ. Spec.	Mean	R.M.S. width	Unit	Increase
270 nm	23.3	30.8	3.4	%	32 %
400 nm	19.3	24.2	2.4	%	25 %
520 nm	10.7	13.4	1.3	%	25 %
Σ QE δE	0.762†	0.967	0.113	eV	27 %
Σ QE(Aerogel) δE ‡	0.076†	0.108	0.011	eV	41 %

Errors are not included. †Expectations from pre-series and prototype HPDs.
‡Weighted for Aerogel performance. See Sec. 4.3.5.2

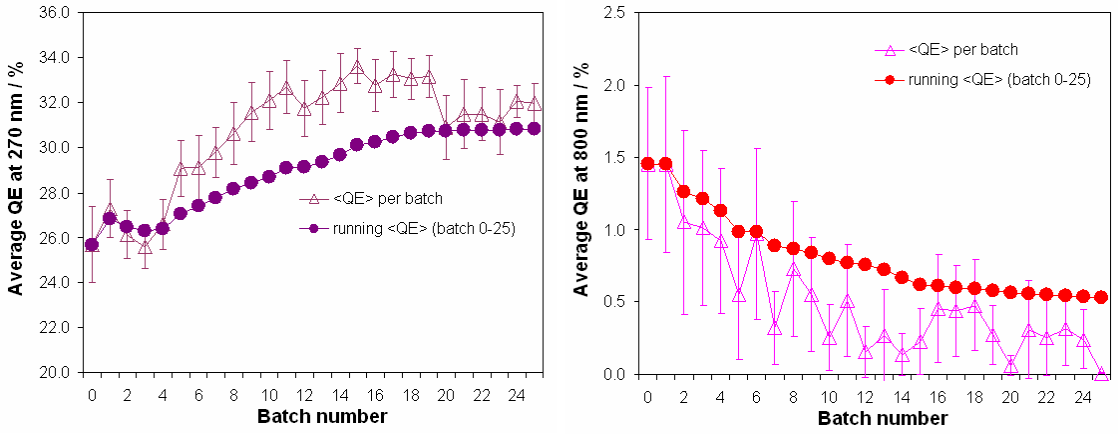

Figure 4.8: Systematic improvements to HPD QE as measured by DEP. Left, at 270 nm an increase is seen over the production time. Right, at 800 nm a decrease is seen over the production time. The vertical bars are the standard deviation of the compared samples.

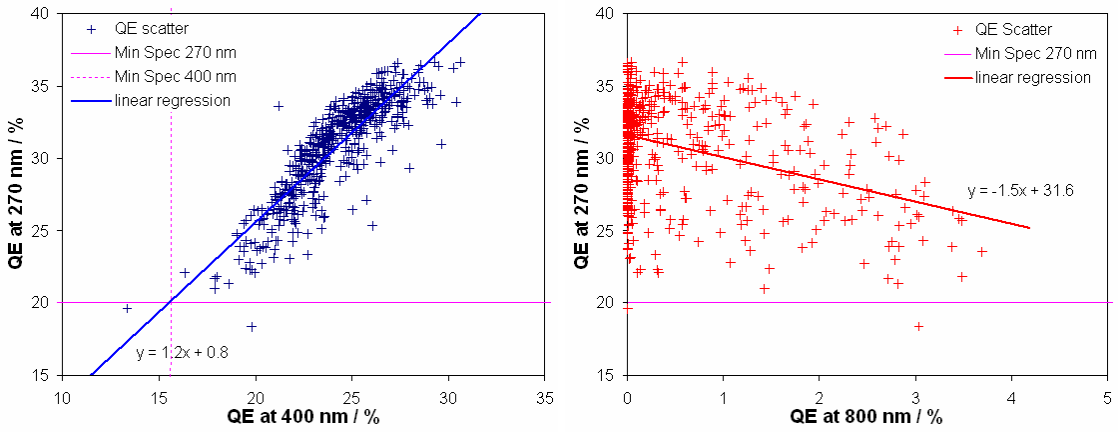

Figure 4.9: Correlations between QE at different wavelengths as measured by DEP. Left, at 270 nm vs. 400 nm, one can see a positive correlation. Right, at 270 nm vs. 800 nm, one can see a negative correlation. The trendlines plotted are linear regressions to guide the eye.

expectations from the pre-series HPDs (Fig. 4.7, right). DEP report they have been able to systematically improve the QE in the blue and UV, while reducing the QE in the red, as demonstrated in Fig. 4.8. From Fig. 4.7 we also see that DEP have reduced the effect of the dip [81] in QE at 300 - 400 nm. Sensitivity to light at or beyond 800 nm will increase the background counts resulting from thermal emission from the environment. One finds the QE at 270 nm is positively correlated with the QE at 400 nm and anti-correlated with the QE at 800 nm from Fig. 4.9.

4.3.4 Measurements by LHCb RICH at PDTF

4.3.4.1 Methodology

We have adopted a self-calibrating test method, similar to that presented by previous authors [82], also used by LHCb at CERN and by DEP. We aim to provide reliable, repeatable, results. For simplicity we use a white-light source, namely a Quartz-Tungsten-Halogen (QTH) bulb, with an emission range from $\approx 220\,\mathrm{nm}$ to $> 2\,\mu\mathrm{m}$. We then select light within a 10 nm region employing specific reflection-absorption filters – 10 nm bandpass (BP) filters. We use a picowatt-sensitive photodiode (PD) of calibrated and well-known QE, $\eta_q^{(PD)}$, to measure the light output through measurement of the PD photocurrent, I_{PD}. Combining this with measurement of the current drawn by the HPD, I_{HPD}, allows for calculation[7] of the HPD QE, $\eta_q^{(HPD)}$:

$$\eta_q^{(HPD)}(\lambda) = \eta_q^{(PD)}(\lambda)\frac{I_{HPD}(\lambda)}{I_{PD}(\lambda)} \tag{4.1}$$

Fig. 4.10 gives the realised design schematic. The HPD photocathode is protected with a series resistor of $1\,\mathrm{G}\Omega$ which ensures that the current drawn by the HPD is always less than 100 nA under 100 V bias.[8] The bias line was interlocked to the dark box and the picoampere meter was protected with parallel diodes. Filters were selected for several wavelengths (270 nm, 340 nm, 400 nm, 440 nm, 520 nm, 640 nm and 800 nm). With such filters, any transmission of thermal infrared emission will provide a highly fluctuating background, as the lamp at PDTF is not temperature controlled. The PD is more responsive to infrared and visible radiation than the HPD, and therefore various combinations of visible and infrared blocking filters were employed to eliminate systematic effects. The lamp was stabilised by operating in a constant current mode and allowing thermal equilibrium to be reached before commencing measurements. This lengthens the time requirements of the tests significantly. Two current values are used for the measurements: $(2691 \pm 2)\,\mathrm{mA}$ ($\sim 6\,\mathrm{V}$) for visible and infra-red light, $(3941 \pm 2)\,\mathrm{mA}$ ($\sim 12\,\mathrm{V}$) for UV light. The

[7] Note the HPD and PD dark current are subtracted in the measurement of I_{HPD} and I_{PD}

[8] An acceptable instantaneous current which will prevent immediate photocathode damage

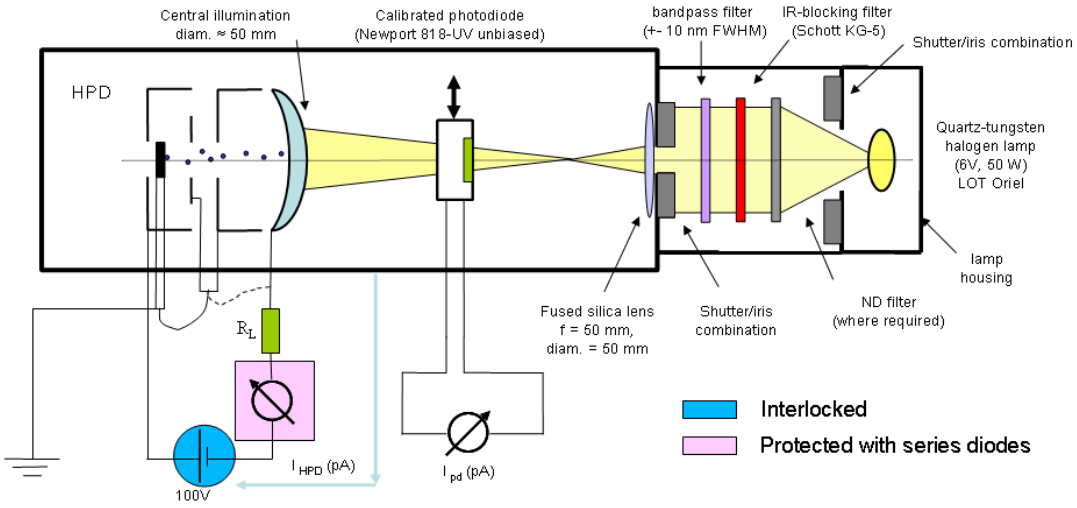

Figure 4.10: Quantum efficiency design schematic. I_{HPD} and I_{PD} are the currents determined using the picoampere meter for the HPD and the reference PD respectively.

HPD and PD are placed on axis, in a light-tight box, illuminated centrally. All the light must hit the receptor area of the PD and the HPD, though it might be slightly off-centre of the PD or HPD with no systematic effect. The PD has a small active area, of 8 mm diameter, of which as large a proportion as possible (~ 5 mm) is illuminated. The HPD has an active area of 78 mm in diameter of which a ~ 50 mm-diameter circle is illuminated at the approximate centre of the HPD.

Two sets of calibration measurements are done with the PD: one before and one after the HPD measurements. The PD is fitted and/or removed by hand and must be removed during the HPD measurements. The PD is placed aside and the HPD photocathode is gradually biased. The HPD may be negatively biased up to 500 V.[9] The collection efficiency is improved by increasing this potential difference, and reaches a plateau at around 20 V for our geometry (Fig. 4.11). Typically 100 V is used for the QE test. In the cases of HPDs with high ion-feedback 22 V is used to eliminate the gas gain.[10]

The picoampere meter is configured to its most accurate region, ± 1 pA. A long integration time is required to eliminate fluctuations from RF interference. Readings

[9] A limit of the Kiethley 6985 picoammeter used.

[10] See the discussion in Sec. 4.3.5.3 and Appendix A. Low voltages are equally useful in extracting the QE due to the nature of the photoelectric effect. As a reminder, to prevent any photocurrent it is necessary to positively bias the photocathode. Even if earthed under illumination the photocathode current will be significant.

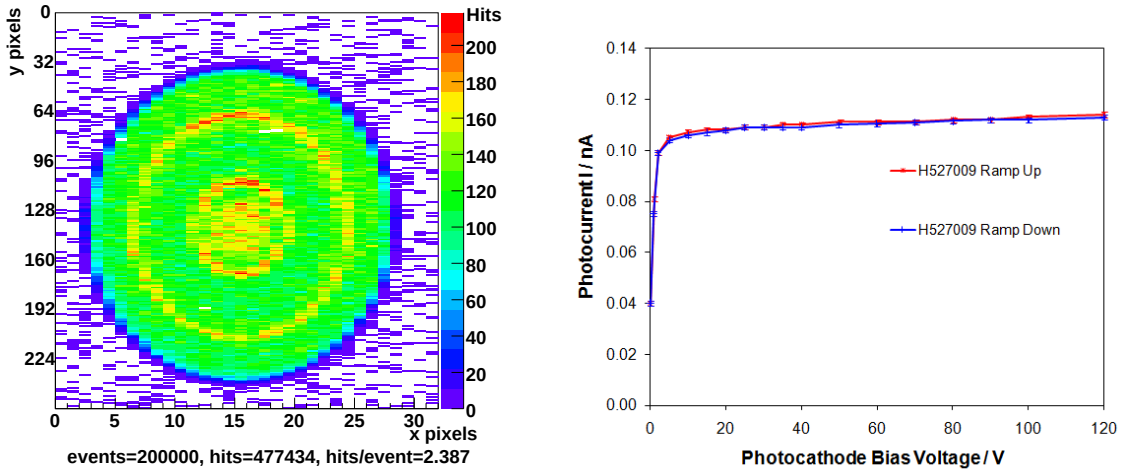

Figure 4.11: Left, Photocathode image produced by uniform LED illumination at PDTF on H527009 at -20 kV. Right, measuring the photocurrent as a function of potential difference with 270 nm illumination at PDTF. For a typical production HPD, e.g. H527009, one observes only a small rise in current between the plateau region at ∼20 V and 500 V.

are repeated at five minute intervals and the lamp housing temperature is recorded along with the photocurrent and dark current.

4.3.4.2 Error Calculation

We obtain an accurate estimate for the experimental error as follows. We sum quadratically the following errors: measurement error, resulting from the precision of the picoampere meter used, typically 0.5 %; the calibration error, from our knowledge of the QE of the reference PD, typically 2 %; the temperature error, resulting from thermal fluctuations between tests, typically 2 % in high-power mode, and 1 % in low-power mode. In order to assess the temperature error we investigated the systematic variations as a result of changing lamp temperature. Unfortunately, a temperature monitor could not be connected to the lamp directly, but the temperature of the lamp housing is constantly monitored. Temperature variation can be large, as demonstrated in Fig. 4.12, left. We can assess the systematic error induced, however, by determining the variation of lamp intensity with temperature. The relative lamp intensity as a function of temperature is plotted in Fig. 4.12, right. The relative thermal error is determined to be $0.2\,\% \,\mathrm{K}^{-1}$, for low-voltage operation

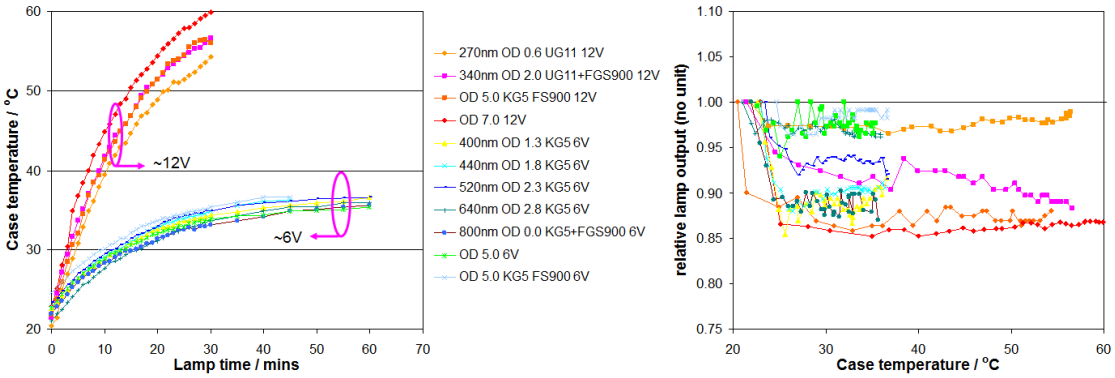

Figure 4.12: Thermal effects on the lamp intensity at PDTF. Left, the temperature of the lamp housing and was monitored over time. Right, by calculating the change in intensity as a function of the measured temperature an estimate of the systematic error is produced.

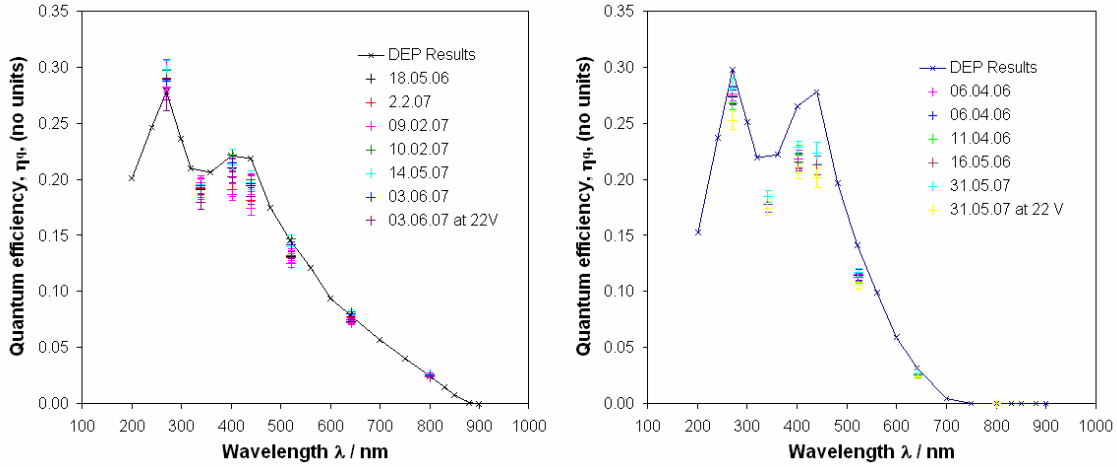

Figure 4.13: Quantum efficiency repeatability at PDTF. Measurements were repeated over a period of a year. Left, for H527009. No disagreement is observed outwith the measurement error. Right for H516002, an atypical case where PDTF disagree with DEP's measurement, as confirmed with repeated tests (which are consistent within errors).

and $0.5\,\%\,\mathrm{K}^{-1}$ for high-voltage operation. This systematic error has been seen to encompass any observed variation between readings, see, for example Fig. 4.13.

4.3.4.3 Results for HPD subsample

We have measured the QE of 60 production HPDs, which is $>10\,\%$ of the total number of 550 Production HPDs. We have also measured the QE of nine preseries HPDs, whose performance will be discussed in Sec. 4.3.5, and the QE of 'recovered' HPDs, which have gone through an additional process at DEP to correct a chip

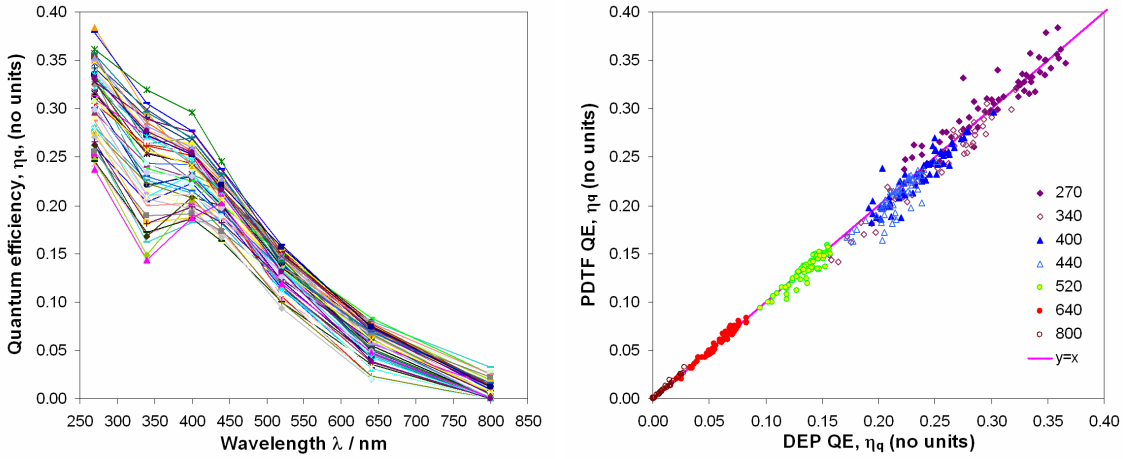

Figure 4.14: Quantum efficiency of HPDs measured by PDTF. 60 production HPDs are shown. Left, the overlaid measurements by PDTF. The lines connect the measured points to guide the eye, they do not reflect the real shape of the QE curve. Right the comparison with measurements performed by DEP.

error and are treated as a separate dataset in this study. The repeatability of our measurements is demonstrated in Fig. 4.13. The overlay of all the (unique) measured QE curves is given in Fig. 4.14. The measured subsample is valid representation of the production HPDs. In a few atypical cases the PDTF and DEP measurements are seen to clearly disagree. We consider these to be bookkeeping errors and are very pleased with the overall agreement shown in Fig. 4.14.

4.3.5 Discussion

In this section we discuss and analyse the results, comparing across the measurements, and examining the overall implication of the results on the performance of the HPDs.

4.3.5.1 DEP and PDTF comparisons

A scatter plot of QE for all HPDs measured at PDTF versus that at DEP is shown in Fig. 4.14. The summary of the sample distributions at each measurement wavelength are given in Fig. 4.15, left. The curves are very similar, it is clear that the average values agree. To quantify the agreement with respect to the measurement error we

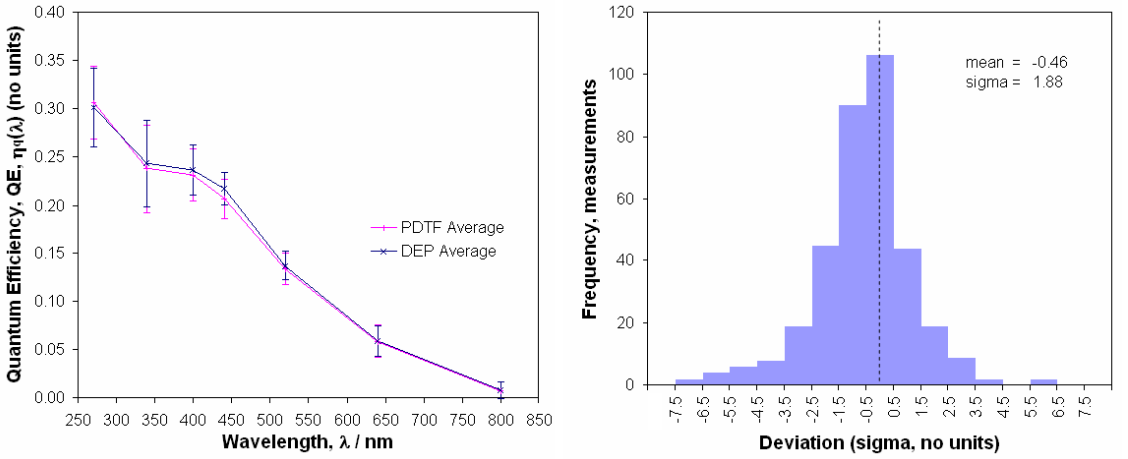

Figure 4.15: Quantum efficiency distributions, PDTF vs. DEP. Left, summary of measurements on production HPDs, a profile histogram, plotted against wavelength. The vertical bars are the standard deviation of the compared samples. Right, data pull distribution w.r.t. DEP. This is not a true pull test as the DEP error is unknown. The distribution shown is the difference in DEP and PDTF measurements of QE divided by the measurement error at PDTF.

subtract each DEP measurement from the corresponding PDTF measurement and divide the result by the error in the PDTF measurement. This is not a true pull distribution as the DEP errors are unknown. A histogram of this pull distribution in Fig. 4.15. The width of $1.88\,\sigma_{PDTF}$ suggests that the unknown measurement error from DEP is $\sigma_{DEP} \approx 1.6 \times \sigma_{PDTF}$ on average. This is a reasonable error, considering the differences in the two setups. The negative bias suggests that on average PDTF measurements are lower than DEP measurements. This is likely to be partially due to ion feedback, which will be discussed in Sec. 4.3.5.3. The different measurement voltages ($-100\,\mathrm{V}$ for PDTF vs. $-900\,\mathrm{V}$ for DEP) systematically enhance the ion feedback contribution and collection efficiency within DEP measurements. This could also be a slight difference in the calibrations of the PDTF and DEP reference photodiodes. DEP do not use any IR-blocking filter in their measurements, and PDTF measurements at IR wavelengths are seen to be more accurate. Overall we verify DEP's results and are very pleased with the level of agreement. This implies uniformity of QE with collection voltage as expected, and uniformity of QE across the photocathode for this sample of HPDs –DEP measures with a much smaller spot size than we do at PDTF. We have been able to independently confirm the very impressive quantum efficiencies reported by DEP.

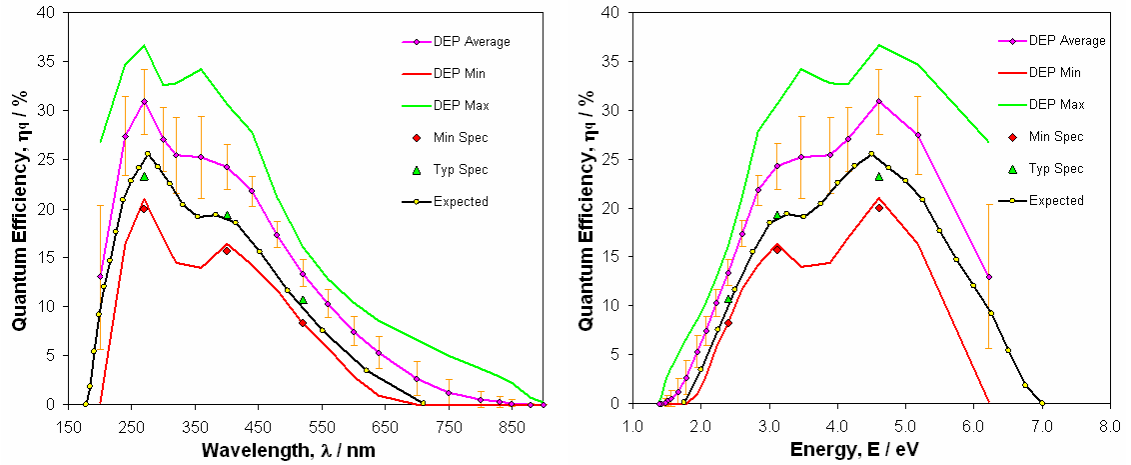

Figure 4.16: Summary of HPD QE performance as measured by DEP for the entire sample compared with expectations from pre-series and prototype HPDs, as used in the 2006 Monte Carlo (DC06, see Chapter 5). Left, QE with wavelength. Right, variation of QE with photon energy. The vertical bars are the standard deviation of the samples. The red and green curves are extrema, envelopes of all data points, no single HPD exhibits these curves.

One can compare the production sample in its entirety to the expectations. We plot the key features of the QE distributions with in Fig. 4.16. The majority of the HPD sample is measured to be above the expectation at all wavelengths.

4.3.5.2 Integrated QE improvement

To quantify the increase in measured QE, and how it affects the number of photons we expect to detect in the LHCb RICHes, several factors must be taken into account. The correct way of performing such a study is to examine the full range of effects in a full Monte Carlo simulation, including distributions of the photons across the detector, distributions of QE across the detector, folding in the transmission, absorption and emission spectra of the various radiators, windows, and filters.

To first approximation the Cherenkov emission is flat in energy and HPDs are assumed to be placed at random. The QE integrated over energy provides a multiplicative factor on the number of photons detected. We have not measured a continuous QE spectrum at DEP or PDTF and hence perform a sum of areas using a trapezoid method. We call this value $\Sigma \mathrm{QE}\,\delta \mathrm{E}$ and a histogram is presented from the DEP measurements in Fig. 4.17. We can see from Fig. 4.17 that the sample

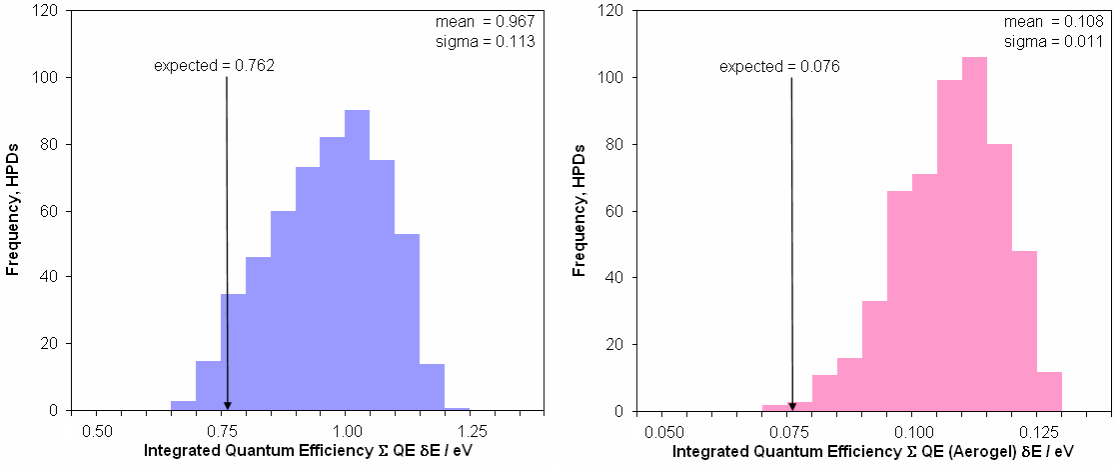

Figure 4.17: ΣQE δE from the entire HPD population calculated from the DEP measurements. Left, integrated over entire energy spectrum. The mean is 27 % higher than the expectation from preseries and prototype HPDs. Right, weighted for the photon distribution of the Aerogel radiator; the mean is 41 % higher than expectations.

of produced HPDs performs much better than the expectation, which is taken from initial measurements on preseries and prototype HPDs (See Sec. 4.3.2). On average the increase in ΣQEδE is 27 %.

To the second approximation we should consider the dispersion of the radiator media, which provide an energy dependence on the number of photons. The RICH system also includes an Aerogel radiator, within which photons are Rayleigh scattered, leading to a large dependence of photon yield with energy. The dispersion in Aerogel is also larger and would result in a significant chromatic error in the Cherenkov angle resolution. To reduce the chromatic error a filter of known spectrum is used after the Aerogel. To calculate the relative increase in the expected number of photons from this radiator, we must take this into account and fold into the integral the transmission of the Aerogel filter, T, and the emission spectra, A, as a function of energy. The considered effects for the calculation of A are the refractive index distribution and the λ^4-effects from Rayleigh scattering. These are given in Fig. 4.18, left, as a function of energy, with the average QE measurement from DEP given as a reference. $T \times A$ forms a weighting factor in the integral calculation. The weighted QE distribution of the entire HPD sample are given in Fig. 4.18, right. The weighted integral is $\Sigma\text{QE} \times T \times A\, \delta\text{E}$. In Fig. 4.17, right, we plot a histogram of the integral. We anticipate an increase in Aerogel photon yield over our expectations of 41 %.

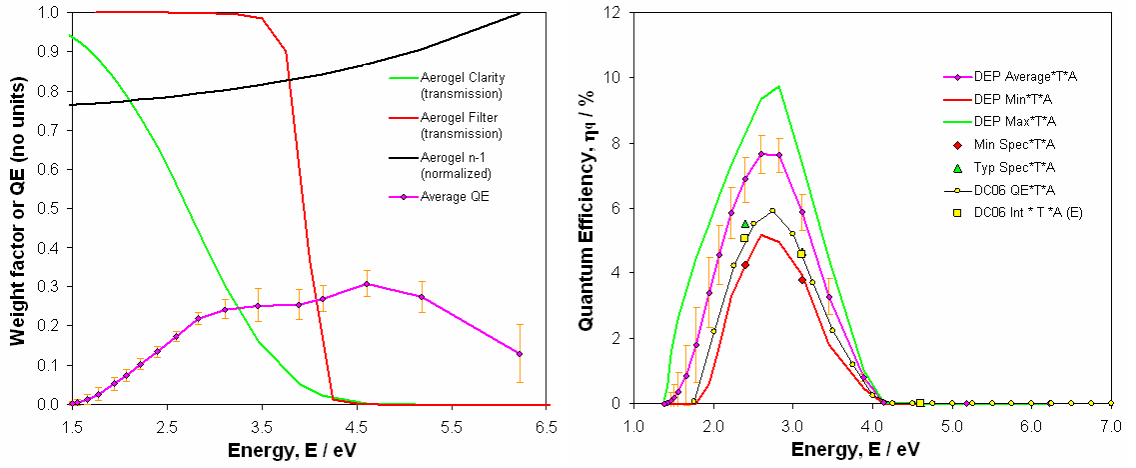

Figure 4.18: Calculation of Aerogel photon yields performed over energy. Left, considered effects for Aerogel radiator in terms of the weighting factors they impose on the calculation of the QE. In green the transmission factor from the λ^4-effects of Rayleigh scattering, in red T, the transmission of the Aerogel filter, in black the weighting factor from the dispersion in n. The average QE curve from Fig. 4.16 is shown in pink for comparison. Right, resultant quantum efficiency summary, weighting the DEP results. The vertical bars are the standard deviation of the compared samples. The red and green curves are extrema, envelopes of all data points, no single HPD exhibits these curves.

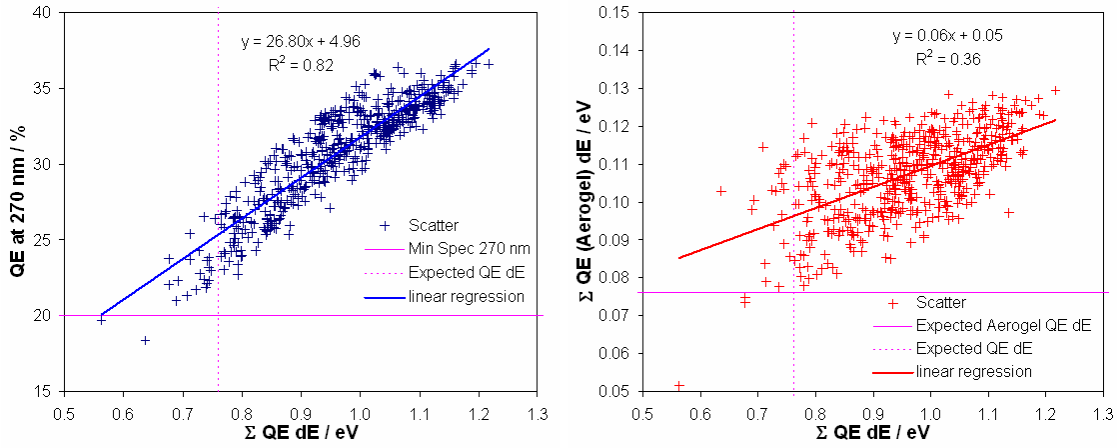

Figure 4.19: Correlations between QEs measured by DEP. Left, QE at 270 nm vs. ΣQE δE, one can see a strong positive correlation. Right, ΣQE δE, for Aerogel, vs. overall ΣQE δE, one can see a weak positive correlation. Errors are not included. The trendlines plotted are linear regressions to guide the eye.

As expected the ΣQE δE is highly positively correlated with the QE at 270 nm or 400 nm, as shown in Fig. 4.19, left. The correlation is weak between ΣQE δE and the integral weighted for Aerogel performance. This has implications on the placement of HPDs in the LHCb RICHes as discussed in Sec. 4.3.6 and Appendix B.

The gradual increase in the QE during the production time can be seen in the

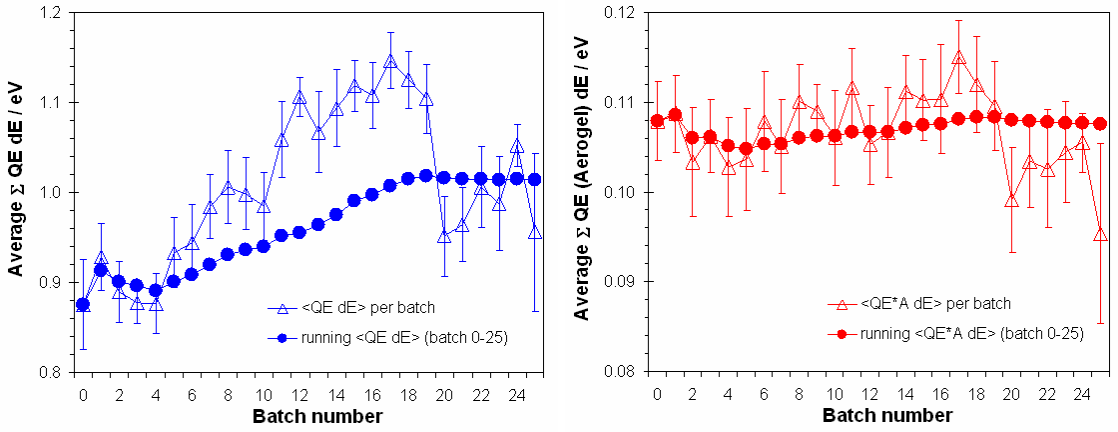

Figure 4.20: Systematic improvements to integrated HPD QE as calculated from DEP measurements. Left, over the entire spectrum an increase is seen over the production time. Right, when weighted for the distribution of photons from Aerogel no significant change is seen over the production time. The small drop towards the end of production results from recovered HPDs. The vertical bars are the standard deviation of the compared samples.

integrated quantum efficiency of each batch in Fig. 4.20. The dip in integrated QE toward the end of production is partially due to the presence of recovered HPDs, as the photocathodes of these tubes were deposited more than a year before the delivery time. One can see the Aerogel performance does not increase strongly over the batches, however, it is on average 41 % higher than the expectation.

For the gas radiators we define a parameter, the 'HPD goodness', which is a relative measure of the overall efficiency of each HPD relative to the expectations. We take the integrated quantum efficiency (across the full wavelength range), the number of dead channels and (to a much smaller extent) the HPD dark count as measured by the PDTFs [1] weighted to the effect on the overall hit rate. Due to the excellent HPD quality, this is highly dominated by the HPD QE. We find the overall increase in HPD Goodness to be 27 %.

4.3.5.3 Ion feedback, vacuum quality and QE

Ion feedback (IFB) increases the drawn photocurrent to a given light signal, i.e. it produces a gas gain. For the majority of production HPDs we have shown that our QE values agree with that of DEP (who perform the measurement at

a higher voltage) and we know independently that the average ion feedback rate is low from extensive PDTF testing [1], indicating good initial vacuum in the majority of production HPDs.

The gain that results from the additional IFB can be measured as a function of voltage at PDTF using the QE measurement system at low voltages (0-500 V). This is an independent measurement of the vacuum quality, and/or vacuum degradation over time. The observed effects of ion feedback on photocurrent measurements are discussed fully in Appendix A. It is shown that observations are consistent with helium as the main residual gas, and it is demonstrated that the effects of IFB on the photocurrent measurement are understood and can be modelled.

In the few cases where residual gas has been observed to increase the photocurrent measurements performed by DEP we have obtained a correction factor from PDTF measurements at 22 V which we have then applied to the DEP measurements.

4.3.5.4 Ageing effects on quantum efficiency

Accelerated ageing tests were carried out by LHCb at CERN on pre-series tube H407008 that showed the largest initial rate of ion feedback. As is reported in Ref. [84] the tube was exposed to a light-intensity level a factor of 120 larger than the average light level expected in the LHCb-RICH detectors. In order to enhance any possible outgassing effect, the tube was surrounded by a heating jacket increasing the temperature to $\sim$50°C. The tube performance was monitored at regular time intervals over a period equivalent to 2000 days (10 years) of LHCb operation.

The corresponding QE curve as measured by LHCb at CERN at -100 V is reproduced in Fig. 4.21, together with the original DEP measurements, and the CERN measurement before ageing. There is no significant difference between the QE before and after ageing.

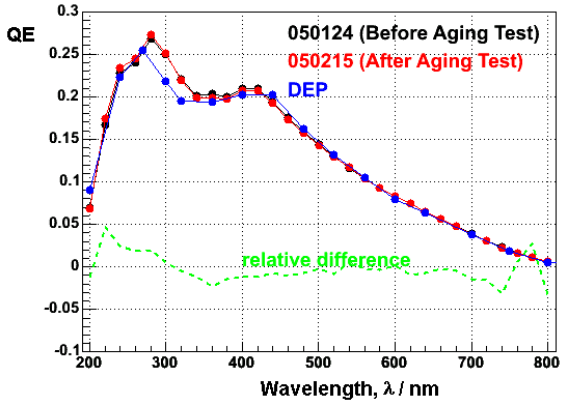

Figure 4.21: Quantum efficiency of H407008, before and after ageing tests, as a function of wavelength. The black and red curves are from before and after accelerated ageing and show no significant difference.

4.3.6 Anticipated improvement in RICH photon yields

To further quantify the expected photon yield improvement the distribution of quantum efficiencies across the baseline RICHes, and the distribution of Cherenkov photons from the gas radiators is taken into account, as is described in Appendix B.3.

We convolute the HPD goodness with the overall occupancy of HPDs, in terms of the average photon distribution within each HPD column or ladder.[11] We obtain a further estimate of the improvement in performance. We estimate the increase in the number of recovered photons in RICH 2 to be 22 % and the increase in the number of photons in RICH 1 to be 36 % for the gas radiators compared to the estimates from preseries and prototype HPDs. These numbers are seen to differ from the overall 27 % increase quoted earlier as RICH 2 is mainly populated by earlier HPDs with a relatively lower QE and RICH 1 was populated later with a relatively higher QE, and arranged specifically to place the highest QE HPDs in the highest occupancy regions.

Clearly there are many other factors which must be taken into account, e.g. the variation in occupancy between different columns and ladders. These factors are most easily tackled with a full Monte Carlo simulation, as is detailed in Sec. 5.3.2.

[11] Columns are vertical in RICH 2 and ladders are horizontal in RICH 1. The position conventions are defined further in Appendix B and Refs. [85, 86, 87, 88].

4.4 Measured HPD parameters

We have tested and qualified all production HPDs at the PDTFs, and have measured only 12 HPDs which fail our selection criteria (Table 4.2), such that they are unusable in the RICH. This corresponds to a production yield of >97.5 %.

4.4.1 HPD test results

The summary of results is presented in Table 4.4. Selected histograms of these measurements are given in Figs. 4.22 to 4.25. The dark count and ion feedback rate are given in Fig. 4.22. The distribution of dark count drops off over the typical specification of 5 kHz cm^{-2}. The distribution of ion feedback is centred much lower than the specified 1 %.

The PC image is evidently well-centred and uniform in size across the production sample as shown in Fig. 4.23. The bump-bonding technique and encapsulation of the silicon sensor and readout electronics has been very successful, providing large signal:noise ratios and a small number of faulty channels, as is demonstrated in Fig. 4.24. The spread in leakage current of the silicon sensor is large, Fig. 4.25. The variation of timing with respect to leakage current was discussed earlier. The

Table 4.4: Selected results for production HPDs.

Measurement	Comment	Mean	R.M.S. width	Unit
PC image	Radius	6615	122	μm
	offset	386	207	μm
Threshold	average per HPD	1064	101	e-
Noise	average per HPD	145	12	e-
Dead pixels	out of 8192	12	32	pixels
Noisy pixels	out of 8192	2	14	e-
Leakage current	Si sensor	1492	2660	nA
Dark count rate	5M triggers	2.54	5.98	kHz cm^{-2}
Afterpulse probability	ion feedback	0.03	0.14	%
Quantum	270 nm	30.8	3.4	%
efficiency†	400 nm	24.2	2.4	%
(QE) (η_q)	520 nm	13.4	1.3	%
Integrated QE†	Σ QE δE	0.967	0.113	eV

PDTF measurements, except for † which are Photonis-DEP measurements.
Errors are not included.

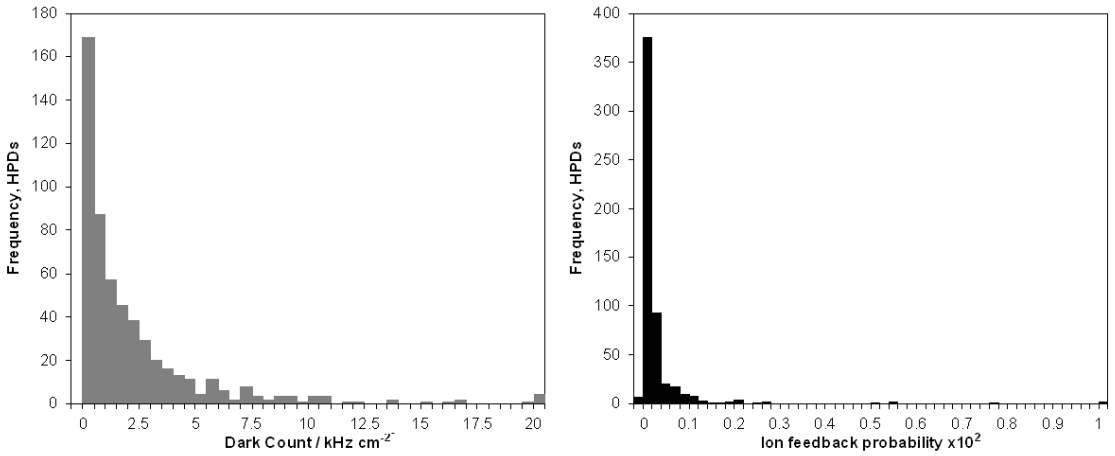

Figure 4.22: Noise and afterpulse results from production HPDs. Left, Dark count from 5M trigger samples. Right, ion-feedback probability ($\times 10^2$) from timing scans.

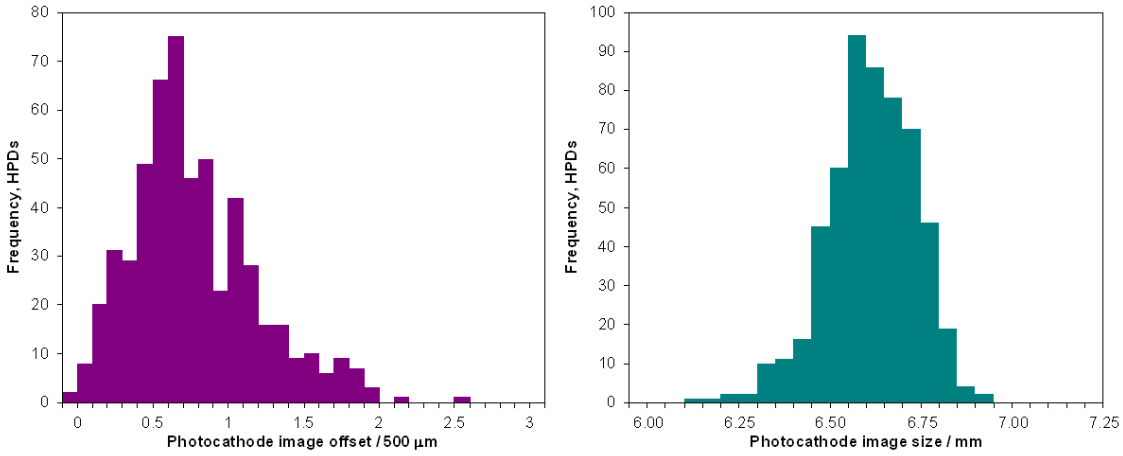

Figure 4.23: Electron optics of HPDs. Left, the deviation of the image centre from the centre of the chip. These units are used as 1 LHCb pixel is 500 μm in X or Y dimension. Right, radius of the demagnified image on the silicon sensor.

leakage current distribution will be reflected in the optimum timing of HPD read-out across the RICH, however, timing scans of the HPDs in situ will be used to optimise the timing for each pair of HPDs. As the timing can only be optimised per pair of HPDs, high-leakage-current HPDs were grouped into pairs for mounting in the RICH system. The read-out chip operating parameters in Fig. 4.25 are as expected. QE results from the whole sample are given in Sec. 4.3.

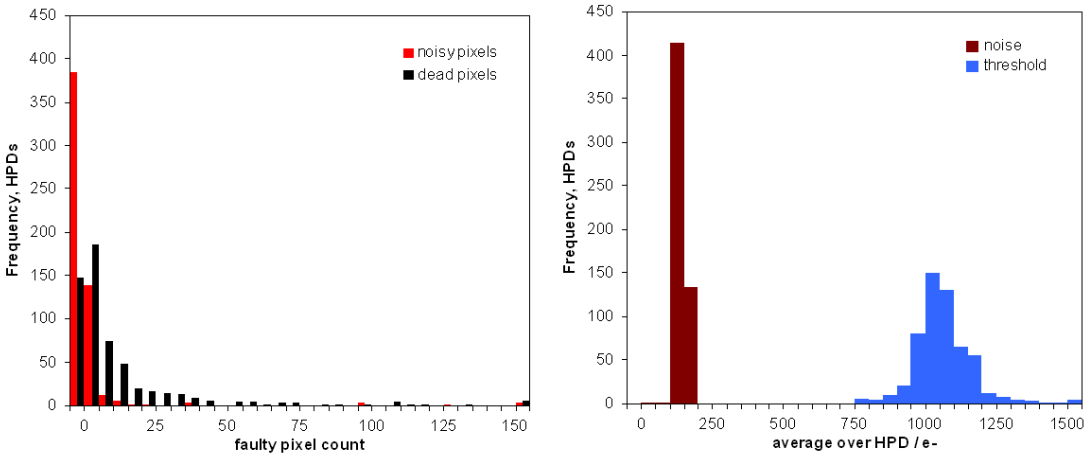

Figure 4.24: Pixel chip operation results from production HPDs. Left, the number of dead and noisy channels out of 8192. Right, the average pixel thresholds and noise per HPD, c.f. the typical signal of 5000 e- per hit.

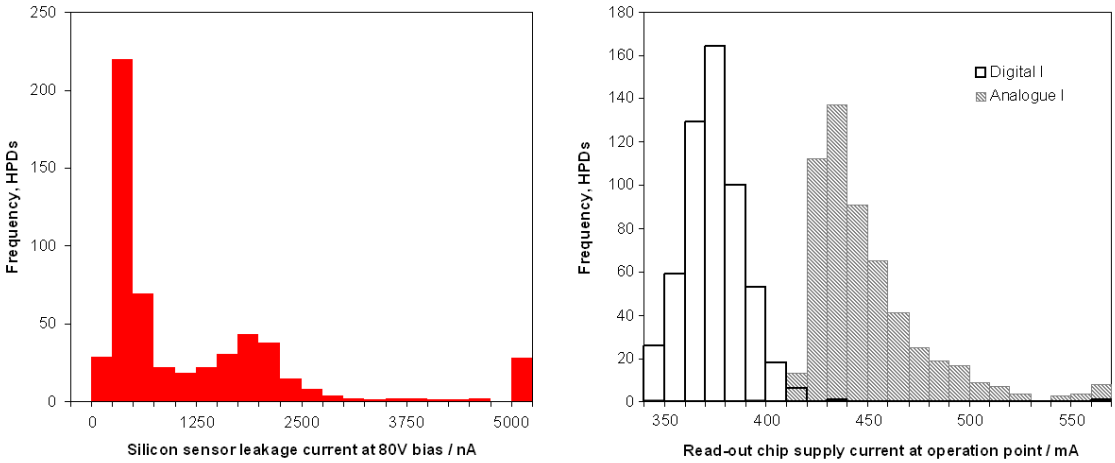

Figure 4.25: Anode operation results from production HPDs. Left, the sensor leakage currents at 80 V bias. Right, the read-out chip supply currents at 1.8 V supply voltage with the silicon sensor on and biased to 80 V.

4.4.2 Discussion

We adopt a categorisation scheme to qualify HPDs as shown in Table 4.5. Categories were defined in reference to the specifications and requirements (Tables 4.2 and 4.1). The distribution of HPD amongst the categories is shown in Fig. 4.26. The majority of HPDs pass with an 'A$^+$' or 'A' categorisation, indicating excellent overall performance.

Due to the distribution of Cherenkov photons as shown in Appendix B, category

Table 4.5: Categorisation of HPDs by PDTF.

Cat.	Explanation	Key Specifications					
		QE @ 270 nm $\times 10^2$	Faulty channels	PC offset / mm	I_{leak} / μA	Dark count / kHz cm^{-2}	IFB $\times 10^2$
A+	Specifically recommended	> 30	< 20	< 0.5 mm	< 3	No features, max pixel noise $< 2 \times 10^{-5}$	< 1
A	Meets specifications	≥ 20	< 80	< 1 mm	< 5	< 5	< 1
B	May fail specifications, still perfectly usable.	≥ 20	< 200	< 1 mm	< 5	< 100	< 1
E	Flagged with an issue. Still fully usable.	≥ 20	< 400	< 2 mm	< 20	< 100	< 1
F	Fails specifications, unusable.	< 20	≥ 400	≥ 2 mm	≥ 20	≥ 100	≥ 1

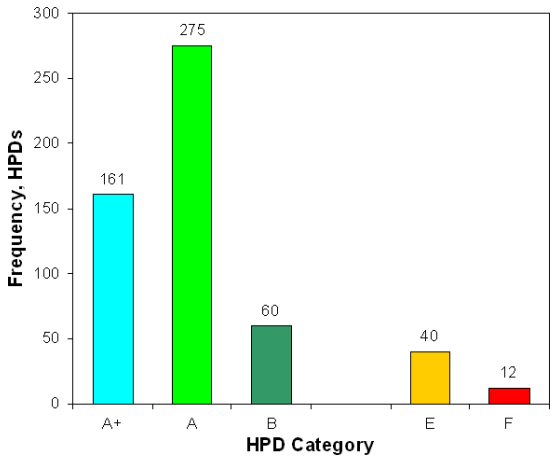

Figure 4.26: Categorisation of 548 HPDs. Category types are defined in Table 4.5.

'A+' HPDs were preferentially mounted in the central region of RICH 1, where the occupancy is highest, capitalising on the benefits from the highly recommended, low noise, high QE, HPDs. Category 'E' HPDs have been grouped in pairs at the edges of columns when mounted. This has moved lower-quality HPDs out of the high-occupancy central regions, and paired together high leakage current HPDs, as is necessary to correct the timing differences discussed earlier. The distributions of measured parameters and HPD categories across the baseline detectors are given in Appendix B.

The HPDs rated as 'B' are mostly those whose dark count exceeds the 5 kHz cm^{-2} specification (Table 4.2). Increased dark count significantly over the specification will not be a problem for the RICH. The pattern recognition can cope with 1 % noise *per LHCb pixel* before the erroneous rings and ghost rings overwhelm the

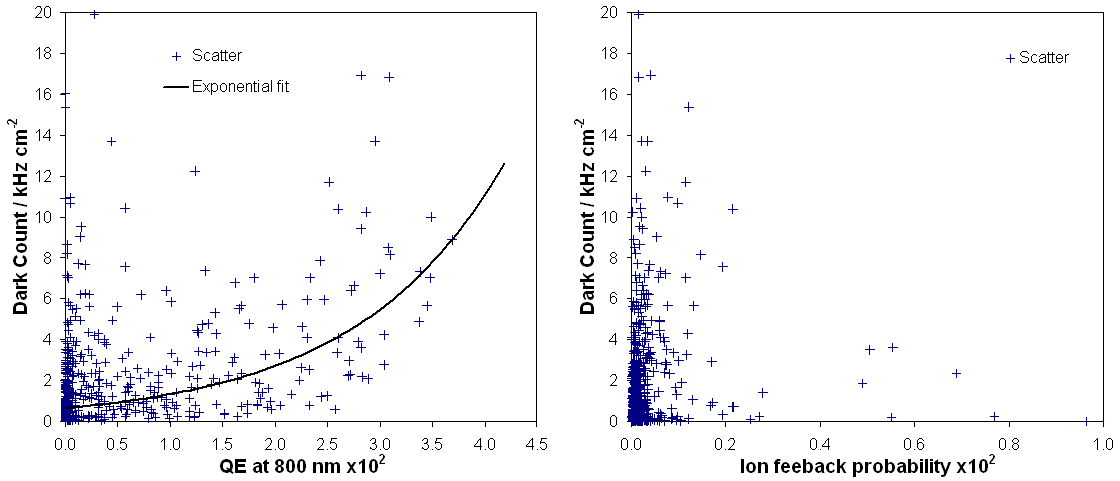

Figure 4.27: Noise sources in production HPDs. Left, dark count from 5M trigger samples vs. QE at 800 nm. The exponential curve plotted is a trendline to guide the eye. Right, the dark count vs. ion-feedback probability, where no trend is apparent.

reconstruction software. A value of $5\,\mathrm{kHz\,cm^{-2}}$ corresponds to 1 % noise *per HPD*. There is at least a 1024-fold safety margin on this specification. Despite this very stringent specification the majority of HPDs are below $5\,\mathrm{kHz\,cm^{-2}}$. The HPD dark count may be caused by electronic noise, field effect emission, thermionic emission, and absorption of thermal IR light emitted elsewhere in the environment (e.g. by the walls of the RICH or the PDTF test station). Fig. 4.27, left, demonstrates the effect of IR absorption, low QE at 800 nm correlates with low dark count ($< 1\,\mathrm{kHz\,cm^{-2}}$). In Fig. 4.27, right, the dark count rate is plotted against the ion feedback rate. It is clear there is no correlation.

The HPDs rated as 'E' are mostly those whose leakage current exceeds 5.0 μA leakage at 80 V. A histogram of leakage currents was given as Fig. 4.25. Two HPDs with high image offsets, >2 LHCb pixels have been observed and are also categorised as type 'E'. The PC image offset is important in the presence of the fringe magnetic field in RICH 1. The electron optics are distorted by the fringe field and could produce an additional offset which would place the edge of the PC image outside of the chip active area. The position of the image centres are shown in Fig. 4.28, left. The cross-focussing optics reduce the image size in the presence of a physical offset, as is clear from the correlation in Fig. 4.28, right.

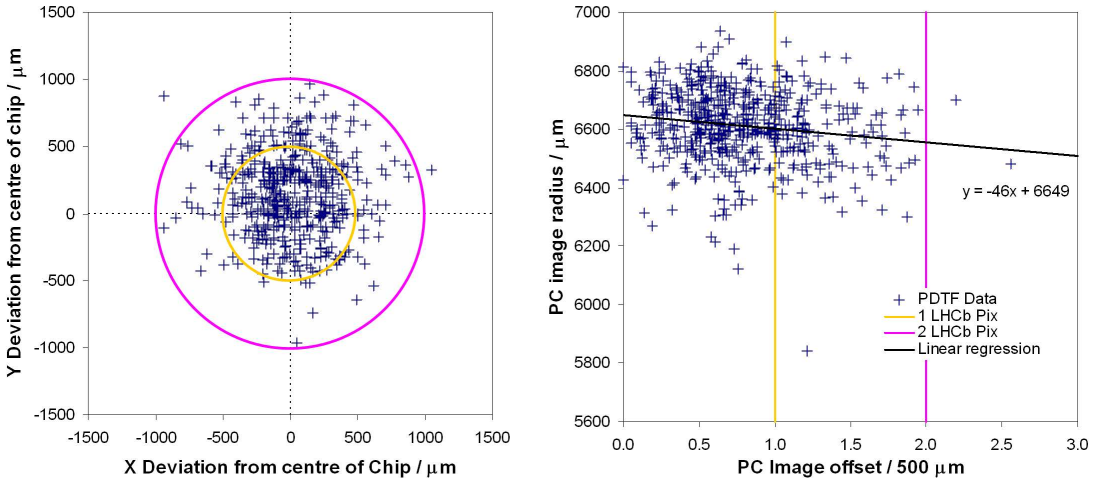

Figure 4.28: Electron optics of HPDs. Left, the X-Y deviation of the image centre from the centre of the chip. The concentric circles represent an offset of 1 LHCb pixel and 2 LHCb pixels, the cut-off values used for classification. Right, the radius of the demagnified image vs. the total offset on the silicon sensor, a trendline is plotted to indicate the negative correlation, the vertical lines represent an offset of 1 LHCb pixel and 2 LHCb pixels. 1 LHCb pixel is 500 μm in X or Y dimension.

Overall the production HPDs are excellent, meeting or exceeding the specifications and the requirements.

4.5 Summary

The full sample of 550 pixel hybrid photon detectors required for the LHCb RICHes, including spares and replacements, have been produced. The HPDs have been thoroughly tested by the LHCb collaboration at two purpose-built photo-detector test facilities. We report an accepted yield exceeding 97.5 %, with the majority of HPDs exceeding the requirements and/or the specifications in key areas, including the vacuum quality, the dark noise, the pixel chip quality and in particular the QE.

The QE has been measured both by the manufacturer and by LHCb, at CERN and/or at dedicated PDTFs. We observe an impressive improvement in the QE over the production time. Integrated across the energy spectrum the QE is 27 % (relative) above our expectations from preseries and prototype HPDs, which were used in the LHCb Monte Carlo, as will be discussed in Chapter 5. This will directly

enhance the performance of the LHCb RICH detectors.

The expected increase in the photons detected by the RICH 1 or RICH 2 baseline detector has been investigated. An increase in recovered Aerogel photons for RICH 1 of 41 % is expected. Taking into account the expected distribution of gas photons within the RICH columns/ladders, we expect the increase in the number of detected gas photons in RICH 2 to be 22 % and the increase in the number of gas photons in RICH 1 to be 36 % compared with the DC06 estimates. For a more realistic photon yield estimate a full Monte Carlo simulation is required, as will be performed in Sec. 5.3.

Chapter 5

Simulation of the LHCb RICH

An accurate simulation of the LHCb detector is extremely useful for several reasons. Firstly, it will allow us to understand the detector and quantify our level of understanding. Secondly, with a sufficiently accurate simulation we may predict the performance of LHCb and optimise physics analysis. The LHCb simulation software is described in Sec. 5.1.

Predicting the performance of the RICH detectors requires an accurate simulation of the HPDs. This Chapter describes the improvements made to the HPD description based on the manufactured HPDs. Measurements of the optical properties of the HPD materiel, and the electron-scattering properties of the Silicon sensor were used to tune the simulation, as is documented in Secs. 5.2.1 to 5.2.3.

To develop and verify the improvements a simulation of the PDTF test stations was designed, as is discussed in Sec. 5.2.4. The improvements were then implemented in the full LHCb simulation, resulting in an $11 - 15\,\%$ increase in the level of signal-correlated background (Sec. 5.2.5). The particle-ID performance, presented in Sec. 5.3, was reassuringly found to be robust under this increased background. We show that including the measured HPD QE, which is much higher than the DC06 expectation (as discussed in Chapter 4) improves the RICH performance significantly. This will directly improve background supression in hadronic channels.

5.1 LHCb software environment

During operation LHCb is expected to collect data at a rate of 40 TB every minute [89]. It is currently not feasible to record and store all these data. The trigger, as described in Sec. 3.8, will reduce the 40 MHz bunch-crossing rate down to 2 kHz [73] of events to be recorded. This will require a very large bandwidth of 60 MB/s. This is roughly the equivalent of one DVD of data every minute.

The software environment was carefully designed to cope with such high data flows. LHCb software [89] uses the Gaudi framework against which applications are built, Gaudi is described fully in Ref. [90]. Gaudi is a specific particle physics framework, developed in C++, within LHCb, and now adopted by other experiments. The separation of "data" and "algorithms" is one of Gaudi's key features. Gaudi simplifies data storage, and provides an inheritance structure such that algorithms may exploit common interfaces to centralised data stores.

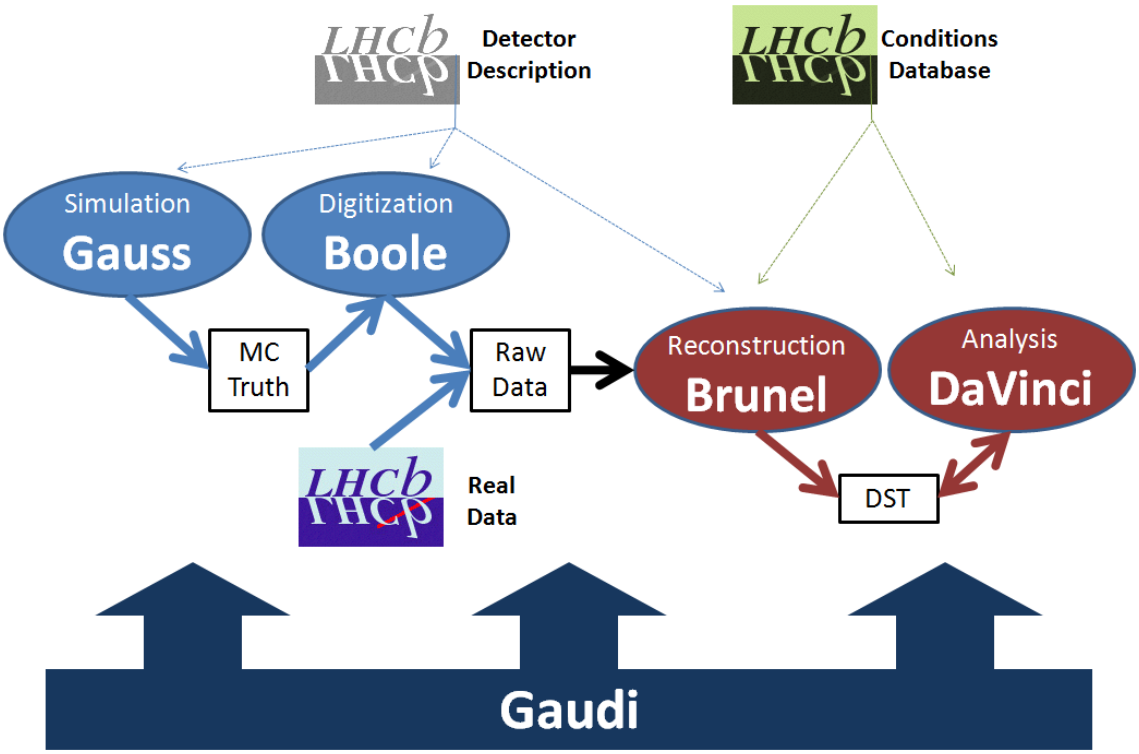

Figure 5.1: The LHCb computing model. Using the flexibility of the Gaudi framework LHCb programs run as algorithms, detached from each other, obtaining information on the state of the detector through centralised databases, after [89].

The simulation, digitisation, reconstruction, analysis and visualisation of events are delegated to their own Gaudi applications, namely: Gauss [91], Boole [92], Brunel [93], DaVinci [94] and Panoramix [95], respectively. The model for this architecture appears in Fig. 5.1. Gauss and Boole are used for Monte Carlo generation, simulating the detector and its electronics. The subsequent programs can equally well operate on Monte Carlo or real LHCb event data. A centralised description of the detector geometry and running conditions are used, realised as XML databases.

The simulation of the detector is handled by Gauss. Gauss is a set of Gaudi algorithms utilising external event generators (e.g. PYTHIA [96], EvtGen [97]) and Geant4 [98, 99] for detector simulation.

Geant4 is a freely available physics toolkit and can be used to simulate many macroscopic physical processes, including the hadronic and electromagnetic interactions of relativistic particles with matter. A description of the theoretical formulation of the Geant4 physics processes can be found in Ref. [100].

Since the re-optimisation of LHCb [47] there have been three main Monte Carlo studies. For DC02/03, Data Challenge 2002/2003 a FORTRAN simulation with Geant3, 40 million events were generated. DC04, Data Challenge 2004, was the first fully C++ simulation using Geant4, $\sim$210 million events were generated. DC06 is the latest data challenge involving a more accurate detector description along with improved physics libraries [89]. More than 150 million events have been generated so far, and the generation is continuing.

The RICH-specific code, such as Cherenkov emission and other optical effects reside in the package GaussRICH [101]. The Cherenkov effect, optical propagation of Cherenkov light, the photoelectric conversion in the HPDs, and the hits produced are all simulated with Geant4. The detector description closely follows what is described in Sec. 3.7.2.

5.2 HPD Simulation

Despite being the most recent major simulation study, the description of the HPDs within the LHCb Monte Carlo for DC06 is heavily simplified [69, 89]. There are several differences between the manufactured HPDs and those simulated, as described in Table 5.1. The assumptions made to justify these approximations have in most cases not been fully tested with regards to their effects on RICH performance. While validating this simplified description with testbeam studies, the need for higher accuracy was recognised [102]. In this section the DC06 simulation of HPDs is tested and improved.

A simulation of the PDTF test configuration was used to develop and verify the changes to the simulation, as detailed in Sec. 5.2.4. The changes were then implemented in GaussRICH as described in Sec. 5.2.5.

5.2.1 Geometrical changes

The geometry of the HPD QW in the DC06 RICH simulation is simplified as shown on the left in Fig. 5.2. The simulation was improved as shown in Fig. 5.2, right. The

Table 5.1: Simplifications in the LHCb RICH HPD simulation for DC06.

Detail	DC06 Simulation	Real HPD	Comment
Quartz window (QW)			
– n	1.47	Fig. 5.4	Contained in measured QE
– T	100 %	Fig. 5.4	Transmission contained in measured QE
– radius	37.5 mm	40.3 mm	Refraction limited input radius= 37.5 mm
– geometry	Fig. 5.2	Fig. 5.2	if T =100 %, geometry outside PC has no effect
Photocathode (PC)			
– n	1.47	Fig. 5.5	Prevents TIR at QW-PC interface
– T at QW	100 %	Fig. 5.5	T contained in measured QE
– Effective QE	Prototype curve	Fig. 4.16	
Kovar			
– Geometry	Envelope only	Fig. 4.1	
– R	0 %	60 %	
Chromium			
– Geometry	None see Fig. 5.2	36.0–40.3 mm	Assumed outside PC acceptance
Silicon Chip			
– Efficiency	85 %	~ 87 %	Estimate from testbeam analyses
– Backscatter	0 %	2.9 %	
– R	30 %	Fig. 5.3	

n is a refractive index. T an optical transmission, R an optical reflectivity.

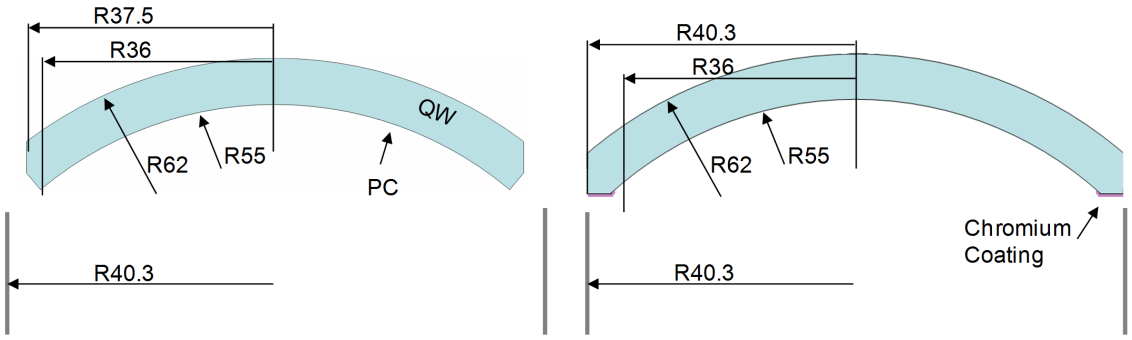

Figure 5.2: The Gauss description of the HPD quartz windows (QW). Left, simplified schematic of the QW as used in the GaussRICH simulation for DC06 [89]. Right, schematic for the improved simulation, as for the manufactured HPDs. Note: the omission of the Chromium coating in the left. Any chamfering at the edge of the window is not considered. All dimensions are in millimetres.

extent of the QW was increased to its actual vertical and radial extent of 21 mm and 40.3 mm, and a Chromium coating on the underside of the photocathode at its edges was added. Comparing both these schematics with Fig. 4.1 demonstrates the improvements made. In the real HPD the chromium coating provides the electrical connection to the PC, but also reflects light back into the QW.

5.2.2 Reflective effects

The reflectivity of the Kovar, Kapton[1], silicon, quartz-window and PC, were investigated. Kovar is a metal, it is a diffuse reflector, with an inherently high reflectivity, similar to that of steel [103]. As no integrating sphere, or similar apparatus, was available to measure the diffuse reflectivity of Kovar directly, the abundant data [103] on similar alloys was used and an approximation of 60 % was applied. The reflectivity of Kapton and the silicon chip were measured using a reflectometer. These reflectivities are plotted in Fig. 5.3. The Fresnel reflectivity of the air-quartz interface was applied as expected from a typical variation in the refractive index of quartz. The reflectivities and refractive index used are plotted in Fig. 5.4 as a function of wavelength. Note that in DC06 the reflectivity of the quartz window is artificially set to zero as it is included in the measured quantum efficiency. The PC itself is composed of several very thin layers of alkali metal.

[1]Kapton is used as the insulator for the HPD magnetic shields.

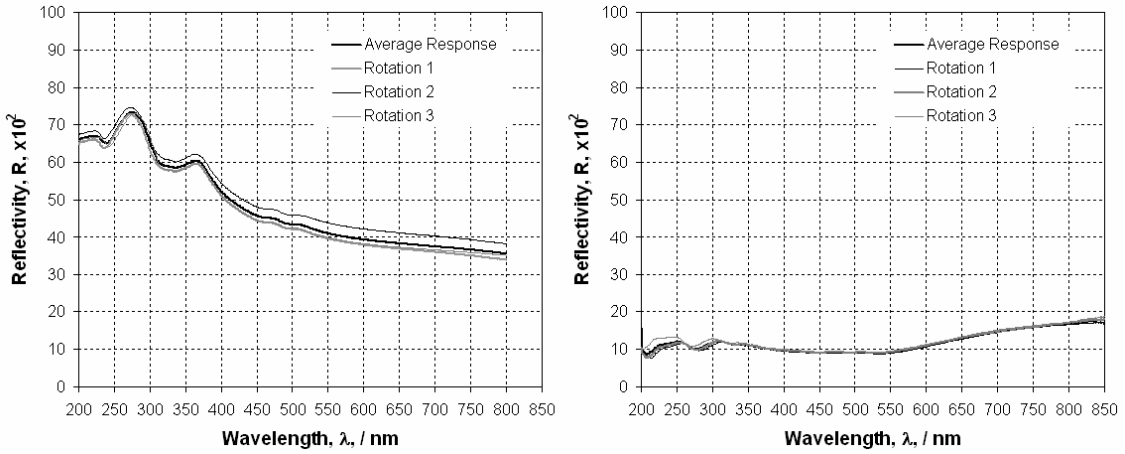

Figure 5.3: Measured reflectivities as a function of wavelength. Left, the HPD silicon sensor. Right, the HPD Kapton. A wide-range reflectometer was used, each sample was rotated and remeasured to average out polarisation-sensitive effects.

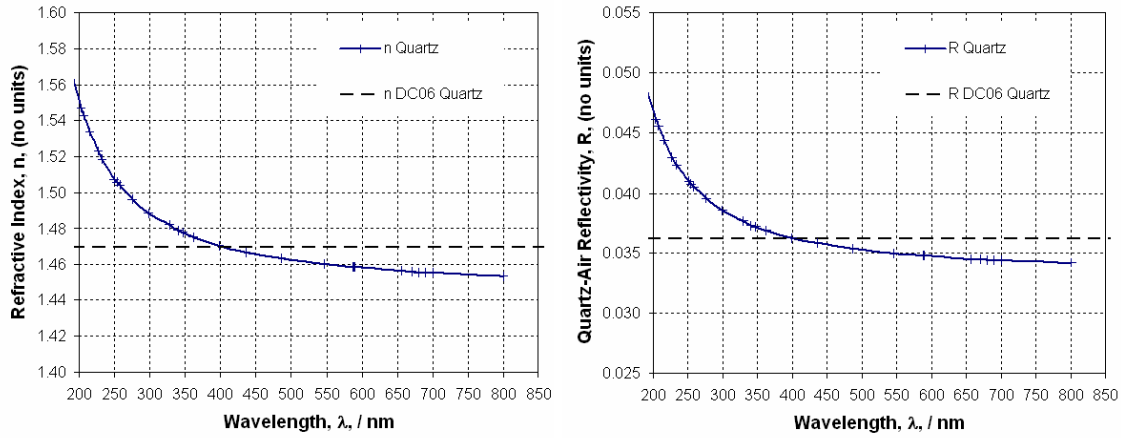

Figure 5.4: Expected reflectivity of the HPD quartz window. Left, the expected refractive index versus wavelength, compared to that in DC06. Right, the resultant reflectivity in air versus wavelength. In DC06 GaussRICH no reflectivity is used as this is included in the measured quantum efficiency.

Its total thickness is smaller than the typical wavelengths of light used. The overall reflectivity will be altered by interference effects, which are not modeled by Geant4. It would be inappropriate to allow two separate reflective surfaces for this thin a material.[2] Additionally any absorber possesses a complex refractive index[3], $n_c = n_R + ik$. The imaginary part of the refractive index[4] describes absorption within the material. Below the plasma frequency the imaginary refractive index of

[2]The simulation time would also greatly increase, as the step size in Geant4 would have to be reduced from a few mm, to 100 nm or less.

[3]n_R and k are real and usually positive.

[4]Also called the extinction ratio or k-value.

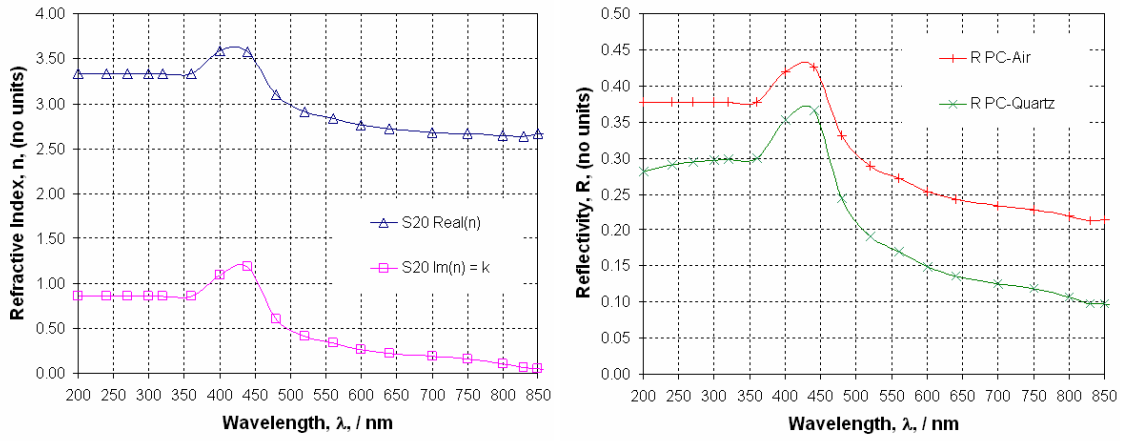

Figure 5.5: Optical properties of the HPD photocathode as used in the revised simulation. Left, the expected refractive index variation with wavelength, from Ref. [104]. The refractive index applied in the simulation is the sum of the real and imaginary parts, resulting in the reflectivities given on the right as a function of wavelength. In DC06 GaussRICH no reflectivity is used as this is included in the measured quantum efficiency.

a metal is significant. The Fresnel reflectivity, R, of a metal, for example where $n_R = 1$, in vacuum, is:

$$R = |r|^2 = \left|\frac{1 - n_c}{1 + n_c}\right|^2 \approx \left|\frac{-ik}{1 + n_c}\right|^2 = \frac{k^2}{4 + k^2} \tag{5.1}$$

Absorption is already included in our simulation as part of the photoelectric processes, which use the measured QE. It would be inappropriate to apply a second absorption step in the simulation. The measured refractive indices for an S20-type PC are given in Fig. 5.5. To approximate the magnitude of the reflectivity and give the correct variation with wavelength, we take the sum of the real and imaginary parts of the refractive index, $n_{applied} = n_R + k$, to calculate the reflectivity, resulting in the reflectivities shown in Fig. 5.5, right. To compensate for the additional losses at these interfaces, the effective QE was increased by a small amount for each HPD.

The addition of the chromium ring in the geometry causes a significant increase in the effective active area of the PC. Light incident at the edge of the PC can be reflected producing hits elsewhere in the HPD[5] as is demonstrated with simple ray-tracing in Fig. 5.6.

[5]Through total-internal reflection.

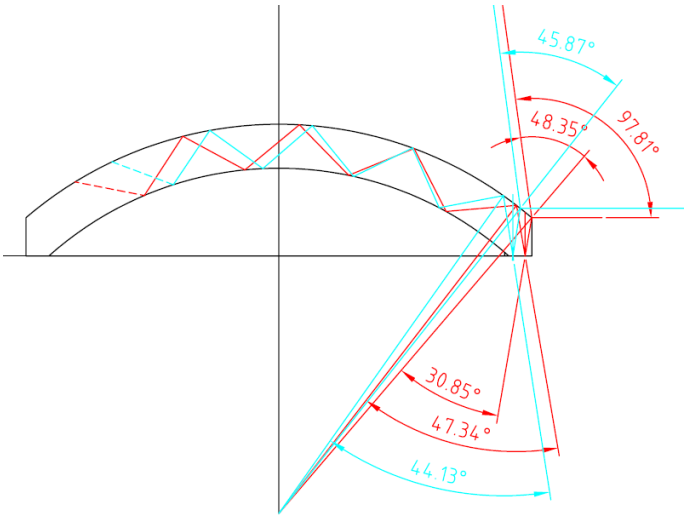

Figure 5.6: Ray-tracing of reflected light from chromium ring at the edge of the photocathode quartz window. Compare with Fig. 5.8. T. Gys, reproduced with permission.

With a point source as used in the long LED run at PDTF these reflections are clearly visible as concentric circular perturbations in the uniformity of the photocathode image as was shown in Fig. 4.3. In the RICH detectors these reflections will result in additional signal-correlated background and higher occupancy.

5.2.3 Backscattering

The silicon chip in DC06 is assigned a photoelectron detection efficiency, A, of 85 %. This represents the number of digital hits recorded by the pixel chip, as a percentage of the number of photoelelectrons produced at the PC [69]. The overall photon detection efficiency is an experimentally determinable parameter, provided that the HPD quantum efficiency is known and the analogue and digital responses of the chip can be determined independently. This 15 % loss includes threshold effects, thermal recombination effects, noise effects in the readout chip and backscatter from the interaction of the electrons with the surface of the silicon detector, i.e. a reflection of the electrons. It has been assumed for DC06 that the majority of the back-scattered electrons produce no hits.

It is possible to calculate the proportion of backscattered electrons along with their trajectory and their deposited energy from direct measurements, such as those in

Ref. [105], using the geometry, and the field description of the HPD, therefore one can calculate the noise contributions from first principles. From a computational point of view, adding this to the simulation is extremely costly as a full field description is required, which would affect all simulated photoelectrons. From an experimental point of view, the full field distribution inside the HPD in the residual magnetic field of the LHCb magnet cannot be measured. Therefore, to simulate the relatively small proportion of hits which result from backscatter, a simpler model is required. We make the following assumptions: a) backscattered hits are produced by electrons which did not already produce a hit, b) the hit locations from backscattered electrons are distributed randomly across the silicon chip, c) the secondary hit probability is low (less than $1 - A$).

Backscattered electrons are visible at PDTF, as they cause hits outside of the PC image. Along with backscatter, hits outside of the PC image may result from thermal and field-effect emission or electronic noise in the HPD read-out, i.e. a dark-count. Backscatter is the only one of these to scale with the intensity of signal light.

Taking the hits outside the PC image, one can define a noise occupancy. Scaling the occupancy to the total number of pixels on the HPD gives an estimate for the total noise, N, across the HPD due to dark count, D and backscatter B. $N = D + B$. The probability of a backscattered hit, P_b, is then related to the total number of signal electrons E through:

$$B = P_b \times E \tag{5.2}$$

$$H = E \times A + N \tag{5.3}$$

With a total number of hits H and an anode efficiency A. Letting $P_a = P_b/A$:

$$B = P_b \times (H - N) \div A = P_a \times (H - N) \tag{5.4}$$

The total number of noise hits can be re-written in terms of the total number of

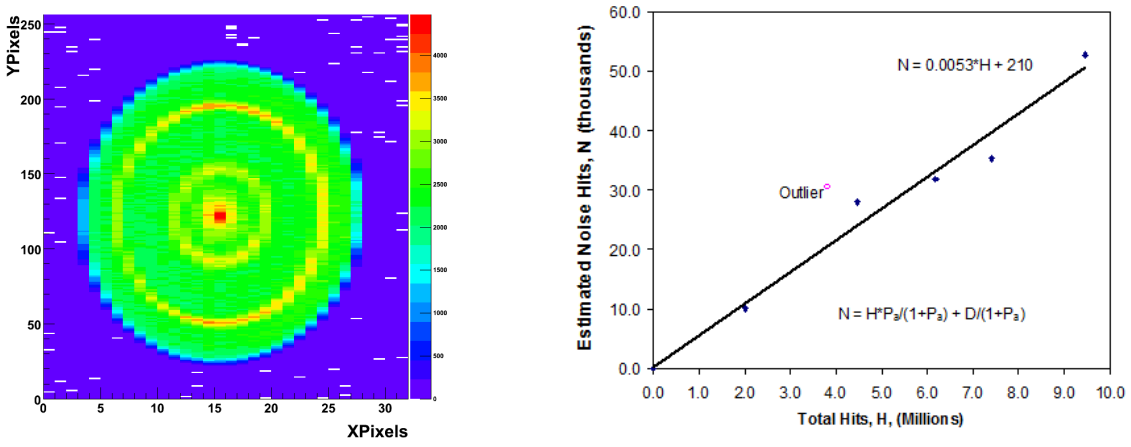

Figure 5.7: Backscatter measurements at PDTF. Left, the photocathode image of HPD H612020 from a 200k LED run. Right, the estimated noise contribution to the hit count as a function of total hits, from 200k events, where only the signal light intensity was varied. The linear regression measures the noise contribution from backscattered electrons.

measured hits H:

$$N = D + P_a \times (H - N)$$

Which re-arranges to give:

$$N = H\frac{P_a}{1+P_a} + \frac{D}{1+P_a} \tag{5.5}$$

A graph of H against N should be a straight line with a gradient related to the backscatter probability, and y-intercept proportional to the dark count.

To determine the probability of backscatter an HPD was chosen with an inherently low noise, zero dead and zero noisy pixels, H612020. Several LED runs with the same number of triggers, varying the light intensity only, were taken. The hits outside the PC image were used to estimate the overall noise contributions across the HPD and the backscatter probability extracted as shown in Fig. 5.7. The measured backscatter P_a, extracted from the linear regression is 5.3×10^{-3}. With $A \sim 85\,\%$ this requires a fraction of 3.4×10^{-2} of the initially lost electrons to be recreated in the simulation at a random point above the chip.

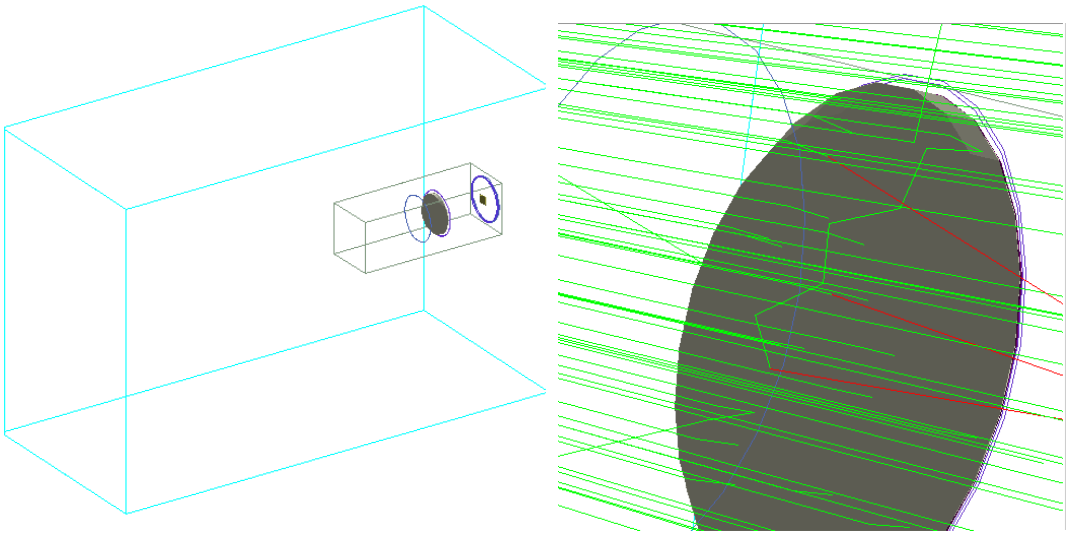

Figure 5.8: PDTF simulation geometry. Left, the HPD geometry as used in DC06. Right, close-up of the HPD, where the QW geometry has been improved and a chromium coating has been added. Green tracks are photons, red tracks are photoelectrons. Reflections from the Chromium ring can be clearly seen.

5.2.4 Simulation of PDTF

A version of the stand-alone Geant4 simulation used for testbeam simulation and analysis was obtained [71, 83]. The geometry of the setup was altered, to match that of the PDTF test facilities. The resulting geometry is illustrated in Fig. 5.8. Photons were injected mimicking the output of a 470 nm (10 nm FWHM) LED coupled into a fibre[6] delivering ∼3 hits per event. This simulation was then used to verify the changes listed previously. The geometry of the QW itself was altered. An example internal reflection from the simulation in shown in Fig. 5.8. These reflections agree qualitatively with those predicted by simple ray-tracing as shown in Fig. 5.6.

The model used for backscatter was validated across a range of input values. As demonstrated in Fig. 5.9 the input value is recovered well across this range. An example event demonstrating the backscatter model is given as Fig. 5.10, right.

The resulting hit distributions from a 1.5M event sample are given in Fig. 5.11. In Fig. 5.12 the influence of the reflections can be seen as peaks in the radial distribution

[6] A Gaussian distribution 0.11 radian half-angle HWHM was used to simulate the 0.11 NA single-mode fibre, located 429 mm from the HPD QW.

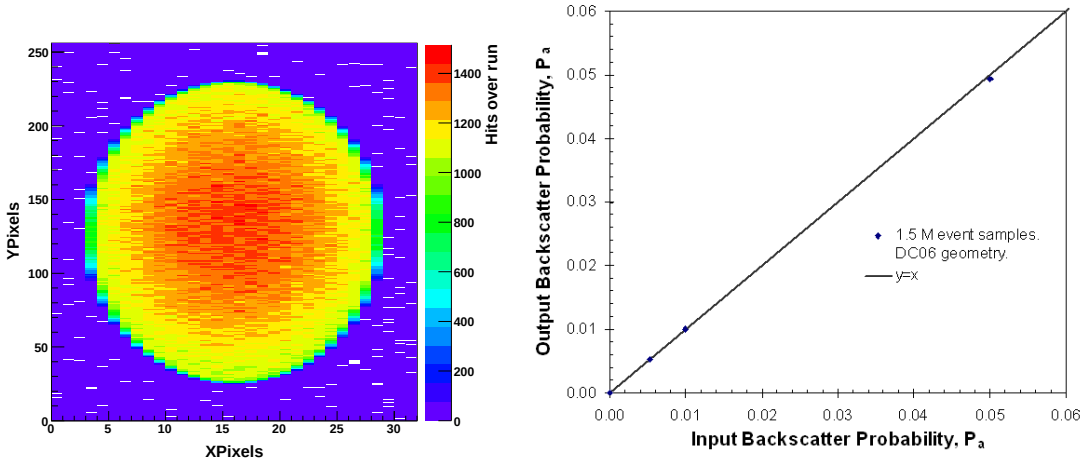

Figure 5.9: Backscatter modelling. Left, 2D hit distribution for an HPD described by DC06-like geometry with the backscatter model. Right, the extracted noise contribution from backscatter from 1.5M-event simulations, varying the backscatter probability.

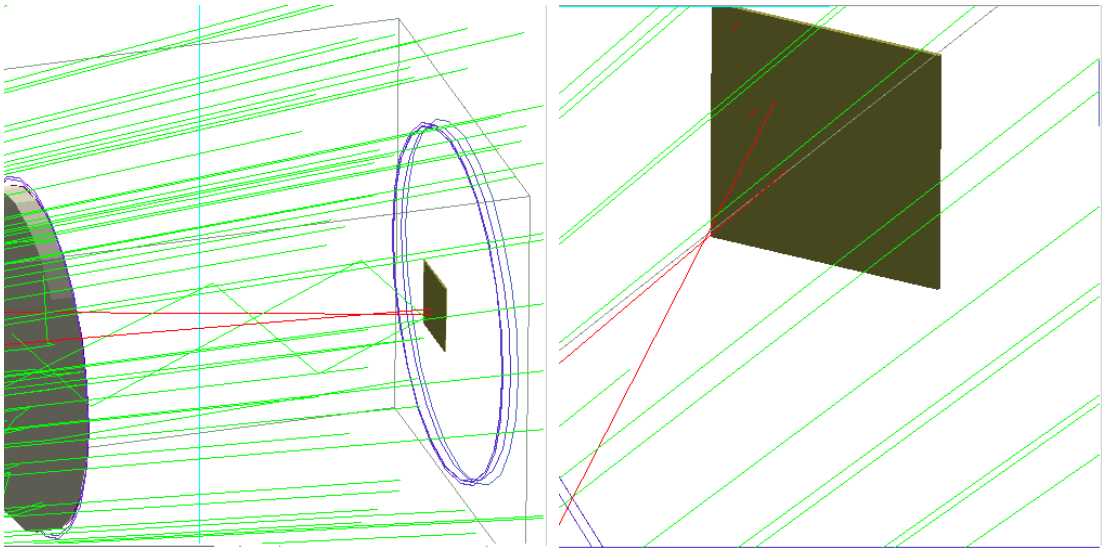

Figure 5.10: Other HPD background effects. Green tracks are photons, red tracks are photo-electrons. Left, reflections from the walls of the HPD and the Silicon chip. Right, tracks created at a random point on the silicon sensor to simulate backscatter.

of hits. In Fig. 5.12, left, it can be seen that the QE correction applied corrects well for the reflections at the quartz-air and quartz-photocathode interfaces. In Fig. 5.12, right, the central peak in the PDTF data corresponds to the contribution from ion feedback, which is not simulated. The gradual drop in occupancy towards the edge of the HPD in the simulation, Fig. 5.12, left, is not seen in the PDTF data 5.12, right. This suggests the light distribution from the fibre source does not fall away as fast as expected in the central region, this does not influence the conclusions

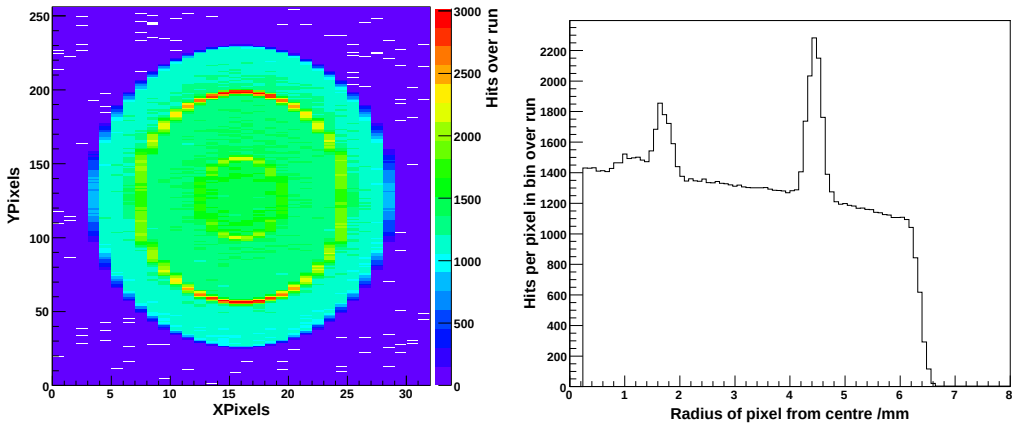

Figure 5.11: PDTF simulation with single HPD in black-out box. 1.5M events, improved QW geometry, with reflections and backscatter. Left, the resulting 2D hit distribution. Right, hits per pixel as a function of the radius from the centre of the PC image.

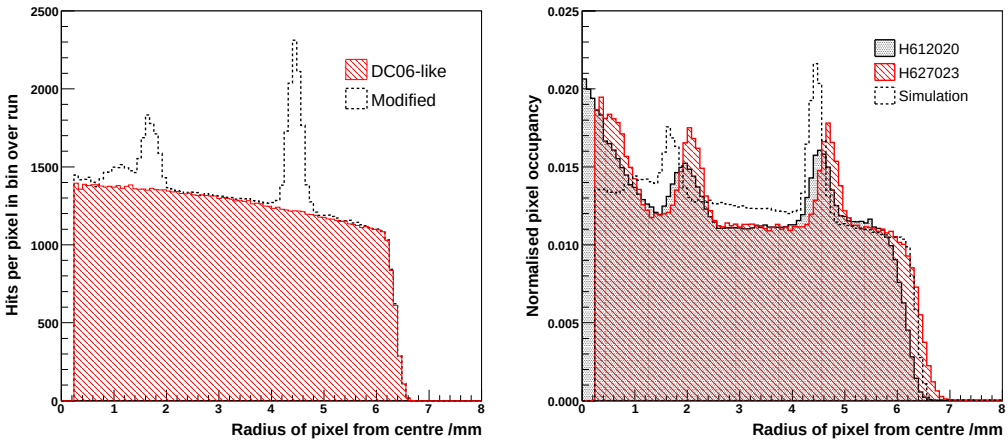

Figure 5.12: Comparison of Monte Carlo and PDTF data. The resulting occupancy as a function of radius is plotted. Left, the comparison of the Monte Carlo simulations in the DC06-like geometry (red, shaded) without reflective effects, and the modified geometry (black, dotted) with reflective effects, the QE is well-corrected. Right, the comparison of two example HPDs with the simulation including reflections and backscatter.

from this study. The position of the concentric chromium reflections correspond well to the reflections observed with the PDTF tests. The remaining difference in relative amplitude of the two peaks suggests that the improved quartz-photocathode reflectivity is still an underestimate. The slight positional difference suggests that chamfering at the outer edge of the HPD, which is not included in the simulation, modifies the angular distribution of the reflected photons.

The relative number of hits per event with each modification is listed in Table 5.2.

Table 5.2: Increased hit rates due to added background effects in the PDTF simulation.

Description	Hits per event	Relative
DC06-like geometry	3.314 ± 0.001	100 %
Improved geometry	3.316 ± 0.001	100.1 %
Added kovar reflections	3.342 ± 0.001	100.8 %
Kovar and silicon reflections	3.341 ± 0.001	100.8 %
Kovar, silicon, quartz and PC reflections	3.595 ± 0.001	108.5 %
Back scatter model	3.331 ± 0.001	100.5 %
All effects	3.616 ± 0.001	109.1 %

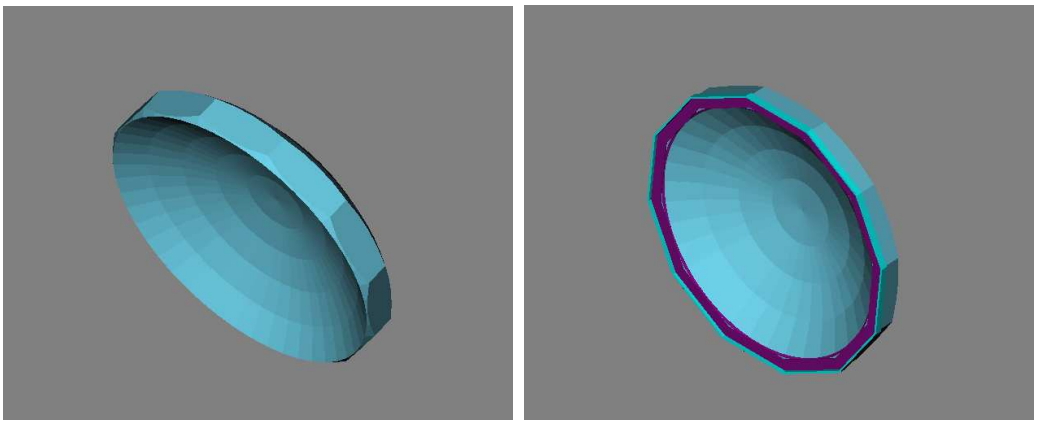

Figure 5.13: Geometrical changes to HPD quartz window description in Gauss, as visualised with panoramix. Left, the original quartz window. Right, modified window with added chromium coating (highlighted in purple).

An increase of 9.1 % signal-correlated background is found.

5.2.5 Improvements to the Gauss v30 series

Having verified the changes in geometry and reflectivities with a stand-alone Geant4 simulation, these were implimented in the description of the RICH detector.[7] The geometrical changes to the QW are shown in Figs. 5.13. Additional tags carried through the simulation were integrated to allow the identification of the various backgrounds from the Monte Carlo truth information. Samples of 5,000 events from the simulation with a "particle gun" event generator were used to verify the changes in the overall hit rates. Pions ($\pi^{\pm}$) with momenta of 80 GeVc^{-1} in the angular range

[7] In SQLDDDB v2r3 and GaussRICH v7r2, for Gauss v30r4.

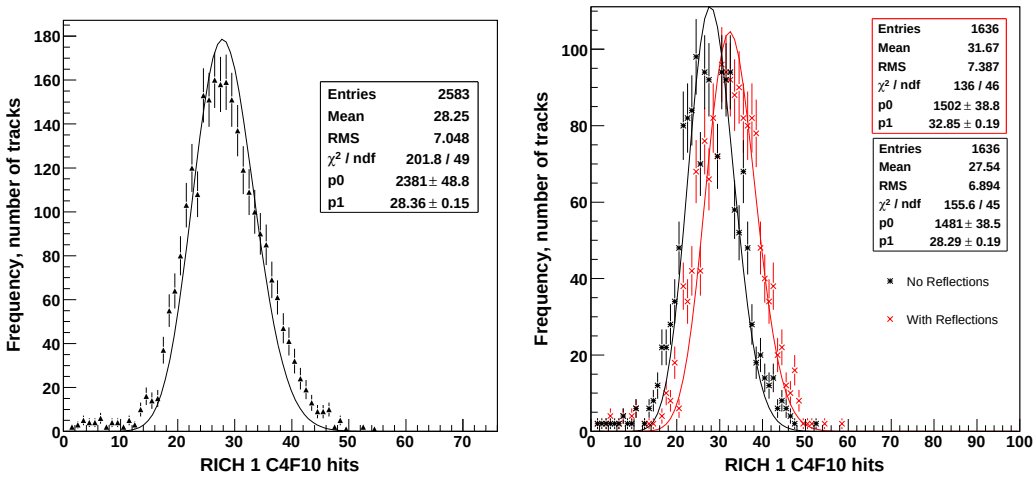

Figure 5.14: Effect of reflective backgrounds in RICH 1 C_4F_{10} radiator. The number of hits per saturated track are plotted and a Poisson distribution is fitted. Left, for C_4F_{10} before the changes to the simulation. Right, for C_4F_{10} after the changes, where the black points and fit represent the number of hits from this track that have not been reflected within the HPD, and the red points are for all hits associated to this track including the reflections. p0 is the fit parameter corresponding to the normalisation of the Poisson, p1 is the fit parameter corresponding to the mean of the Poisson.

$0.0 < \Phi < 2\pi$ and $0.01 < \theta < 0.35$ radians representing the full RICH 1 acceptance were generated. To obtain realistic measures of the increase in the number of hits, the hits from saturated tracks ($\beta \rightarrow 1$) from the three radiator materials were initially compared. An example is plotted for the RICH 1 C_4F_{10} radiator in Fig. 5.14. A Poisson distribution is fitted to the hits to extract each mean. The mean of the black curve on the left (DC06) is lower than that on the right (modified description). This is due to the correction of the HPD QE for multiply reflected photons within the QW. The mean of the red curve on the right (modified description) is larger than both black curves as it includes all the background effects.

A table of the background effects seen, from 10k of such "particle gun" events, is given as Table 5.3. In both RICHes the background is slightly larger than the 9.1 % expected from the PDTF simulation (Table 5.2).

The effect of the additional backgrounds (relative to the DC06 simulation) on the pattern recognition performance in RICH is the subject of the next section, 5.3.

Table 5.3: Increased hit rates due to added HPD backgrounds in GaussRICH.

Description	RICH 1 gas		RICH 2 gas	
	Hits per event	Relative	Hits per event	Relative
Signal	23.7 ± 0.1	100 %	17.4 ± 0.1	100 %
HPD Background	3.5 ± 0.1	14.7 %	2.0 ± 0.1	11.5 %
Total	27.2 ± 0.1	115 %	19.4 ± 0.2	112 %
Backscatter[a]	0.150 ± 0.003	0.6 %	0.049 ± 0.002	0.3 %
PC reflections[a]	0.97 ± 0.01	4.1 %	0.29 ± 0.01	1.6 %
chromium reflections[a]	2.85 ± 0.02	12 %	0.75 ± 0.02	4.3 %

[a] inclusive and correlated in some cases, also this is not an exhaustive list. The three background categories here should not be added simply.

5.3 Particle ID with improved simulation

We have seen that there are several areas in which DC06 is imperfect for the simulation of the RICH HPDs. In Sec. 4.3 we have demonstrated that the HPD QE is considerably above the level expected from the pre-series and prototype HPDs and that the value used in the simulation is an underestimate. It is expected that this increase will improve the RICH performance. It is also noted in Sec. 5.2 that the DC06 simulation does not include signal-correlated background contributions from reflections and backscatter within the HPDs, which would be expected to degrade the pattern recognition and mitigate the improvements from the higher QE. In this section the PID performance with each contribution is discussed.

5.3.1 PID with increased HPD background

A simulation was performed with the GaussRICH changes implemented.[8] By artificially removing the additional background hits using Monte Carlo truth information a direct comparison of the particle identification performance has been made.

In Fig. 5.15 the kaon efficiency and pion mis-ID rate are plotted as a function of momentum. With the added backgrounds the kaon efficiency is only slightly reduced, by (0.62 ± 0.21) %, and the pion mis-ID rate is only slightly increased, by

[8] Gauss v30r4.

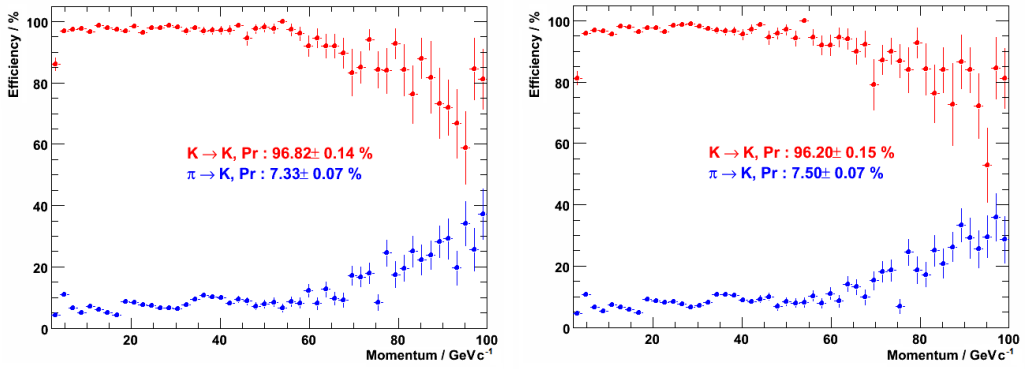

Figure 5.15: RICH kaon ID performance with HPD backgrounds as a function of momentum. The kaon ID efficiency in red, the pion mis-ID rate in blue. Left, the simulation with HPD background hits artificially removed. Right, the simulation with HPD backgrounds included. These plots were generated with Gauss v30r4, courtesy of C. Jones.

$(0.17\pm0.10)\,\%$. This is a reassuring result and emphasises the stability of the log likelihood approach, which compensates for the additional background. These plots were generated with a particular Δ_{LL} cut to demonstrate the improvement.[9]

5.3.2 PID with increased QE

The measured QE values have been included in the most recent version of the full simulation.[10] We observe the number of photons per saturated track has increased, as tabulated in Table 5.4. The observed increase is compared with the estimation from the QE study in Sec. 4.3.6. The observed increase is consistent with the expected increase for the two gas radiators. The Aerogel yield is lower than expected. This is attributed to the spatial distribution of Aerogel photons in RICH 1, which was not accounted for in this estimate.[11] The PID performance with and without the QE increase are compared in Fig. 5.16. The kaon ID is the same with increased HPD QE, but the pion mis-ID is reduced by $(4.43\pm0.12)\,\%$. These plots were once again generated with a particular Δ_{LL} cut to demonstrate the improvement.

[9] The likelihood method was briefly discussed in Sec. 3.7.2. Variation in the cut may increase the efficiency, but will also increase the mis-ID rate. An optimum is found for each analysis, such as the analysis presented in the next Chapter. The value used for this cut at this stage does not affect the conclusions drawn.

[10] Gauss v35r1.

[11] The spatial distribution is given in Appendix B, for reference.

Table 5.4: Increased hit rates due to improved QE in GaussRICH.

Radiator	Hits per saturated track			
	Original QE	Improved QE	Increase	Expected Increase[a]
Aerogel	6.1 ± 0.2	8.2 ± 0.2	$(34.4 \pm 3.4)\,\%$	41 %
C_4F_{10}	27.6 ± 0.4	37.4 ± 0.5	$(35.5 \pm 1.9)\,\%$	36 %
CF_4	20.0 ± 0.6	24.2 ± 0.7	$(21.0 \pm 3.6)\,\%$	22 %

[a] taken from Sec. 4.3.

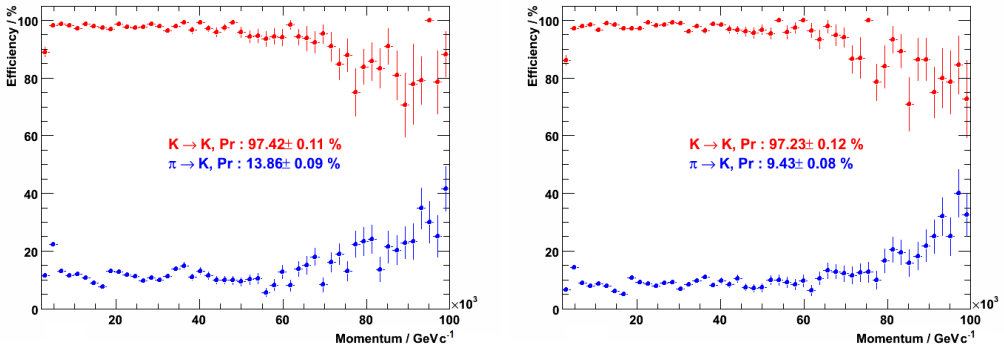

Figure 5.16: RICH kaon ID performance with baseline HPD QE as a function of momentum. The kaon ID efficiency in red, the pion mis-ID rate in blue. Left, the simulation with the standard DC06 QE. Right, the simulation with QE information from the DEP tests. These are preliminary results, generated with Gauss v35r1, courtesy of C. Jones.

5.4 Summary

The HPD geometry in the LHCb Monte Carlo simulation has been made more realistic, which has generated up to an extra 15 % signal-correlated background. This produced only a small degradation in the RICH performance, which was far outweighed by the improvements from the better than expected QE of the production HPDs. The final efficiency and mis-ID rate in a given channel is tunable in a user analysis, by varying the Δ_{LL} cut, usually to maximise the signal significance $S/\sqrt{S+B}$. The tuning of RICH PID cuts is presented in the next Chapter, for the selection of $D^{\pm} \to K^+K^-\pi^{\pm}$ decays in a semileptonic B_q^0 decay. The above improvement in RICH performance will help to reduce backgrounds from $D^{\pm} \to K^{\mp}\pi^{\pm}\pi^{\pm}$ decays, a dangerous source of peaking background. Similar improvements may be expected in other hadronic channels, although these preliminary results will require a further large-scale Monte Carlo production to verify (e.g. DC09).

Chapter 6

Determining Flavour Specific Asymmetries in LHCb

The flavour-specific asymmetry a^q_{fs} measures the CP-violating phase, Φ_q in the model-independent Hamiltonian for B^0_q mixing. A range of current measurements are discussed in Sec. 6.1.2, with a typical null result consistent with zero, to 1 % precision. In this Chapter it is shown that a^q_{fs} is a key place to look for new physics and that LHCb can improve upon current measurements substantially.

In order to make this measurement a clean sample of $B^0_s \to D^\mp_s \mu^\pm \nu_\mu X^0$ and $B^0_d \to D^\mp \mu^\pm \nu_\mu X^0$ decays needs to be obtained. In Sec. 6.2 we will show that it is possible to improve upon the previous expected yields by at least a factor of two with improved offline event selection and a decision-tree inspired HLT2 selection.

Detector and production asymmetries are expected to pollute the measurement, as discussed at length in Secs. 6.1.4, 6.1.5, 6.3, 6.4 and 6.5. Dedicated MC studies were made of these asymmetries, which appear in detail in Appendices C and D.

In Sec. 6.6 we propose a method to remove these pollutants through a simultaneous measurement in the channels $B^0_s \to D^\mp_s \mu^\pm \nu_\mu$ and $B^0_d \to D^\mp \mu^\pm \nu_\mu$. This 'subtraction' method is demonstrated to mitigate the background and production asymmetries, eliminate the detector asymmetry, and measure $\Delta A^{s,d}_{fs} \approx (a^s_{fs} - a^d_{fs})/2$.

6.1 Flavour specific asymmetries

A formalism for neutral meson mixing and decay was presented in Chapter 1. We now consider the decay of B mesons to a final state f, where f refers to a final state particle, or a collection of particles. $\bar{B}$ and $\bar{f}$ are the charge conjugate states.

The term flavour-specific refers to a decay such as $B \to f$ and/or $\bar{B} \to \bar{f}$ that is allowed at tree level, when the decay to the charge conjugate state $B \to \bar{f}$ and/or $\bar{B} \to f$ is not allowed directly. Flavour specific channels include $B_q^0 \to D_q^{\mp}\mu^{\pm}\nu_\mu$ and $B_s^0 \to D_s^{\mp}\pi^{\pm}$ (e.g. $f = D_s^-\pi^+$). The mixing of neutral mesons allows the 'forbidden' decays as the propagating state is a superposition of the two quark eigenstates [106].

The allowed decay is often called the Right-Sign (RS) decay, and the forbidden decay is often called the Wrong Sign (WS) decay. To uniquely identify or "tag" the initial state is complicated. As both states can potentially decay to f, the flavour of f no longer tags the initial state of the meson, i.e. this decay is not self-tagging. It is often possible to tag the flavour of the B produced through other means, e.g. by collecting information on the associated light hadrons produced, or measuring the flavour of the opposite-side $\bar{B}$-hadron. We will show, however, that tagging is not necessary to perform this analysis, and that it is, in fact, undesirable. The only information we then use in this untagged analysis is the kinematics and flavour of the final state f, which could have arisen from either a produced B or $\bar{B}$.

Sec. 1.3 introduced the phenomena of neutral meson oscillations. The reader saw that the complex phase in the CKM matrix allows B_q^0 and $\bar{B}_q^0$ to behave differently, violating CP. The flavour-specific asymmetry a_{fs}^q, introduced in Sec. 1.3.1, parameterises CPV in mixing. In the SM a_{fs}^q is small: $a_{fs}^d = -(4.8^{+1.0}_{-1.2}) \times 10^{-4}$, $a_{fs}^s = +(2.06 \pm 0.57) \times 10^{-5}$ [37, 38]. LHCb will measure a_{fs}^q in an untagged sample, by measuring the time-dependent rates of f and $\bar{f}$ production, which could have decayed from either an intial B_q^0 or $\bar{B}_q^0$:

$$A_{fs}^{unt,q}(t) = \frac{\Gamma(B_q^0 \text{ or } \bar{B}_q^0 \to f) - \Gamma(B_q^0 \text{ or } \bar{B}_q^0 \to \bar{f})}{\Gamma(B_q^0 \text{ or } \bar{B}_q^0 \to f) + \Gamma(B_q^0 \text{ or } \bar{B}_q^0 \to \bar{f})} \sim \frac{a_{fs}^q}{2} \tag{6.1}$$

6.1.1 Decay rates with a^q_{fs}

In decays with no direct CP-violation, the decay amplitudes are equal, as are the widths of the tree-level Right-Sign (RS) decays. The flavour-specific asymmetry then manifests in the previously 'forbidden' or Wrong-Sign (WS) decays:

$$\Gamma^{RS} = \Gamma(B^0_q \to f) = \Gamma(\bar{B}^0_q \to \bar{f}) = \bar{\Gamma}^{RS} \tag{6.2}$$

$$\Gamma^{WS} = \Gamma(B^0_q \to \bar{B}^0_q \to \bar{f}) \neq \Gamma(\bar{B}^0_q \to B^0_q \to f) = \bar{\Gamma}^{WS} \tag{6.3}$$

$$\frac{\Gamma^{WS}_q - \bar{\Gamma}^{WS}_q}{\Gamma^{WS}_q + \bar{\Gamma}^{WS}_q} = a^q_{fs} \tag{6.4}$$

With a_{fs} included, the RS and WS decay widths can be written as:

$$\Gamma^{RS} = e^{-\Gamma t}|A|^2 F^+(t) = \bar{\Gamma}^{RS} \tag{6.5}$$

$$\Gamma^{WS} = e^{-\Gamma t}|A|^2 F^-(t)(1 + a_{fs}) \tag{6.6}$$

$$\bar{\Gamma}^{WS} = e^{-\Gamma t}|A|^2 F^-(t)(1 - a_{fs}) \tag{6.7}$$

Where $\Delta\Gamma$ and Δm are the width and mass differences, as defined in Eqn. 1.23:

$$F^{\pm}(t) = \cosh\left(\frac{\Delta\Gamma t}{2}\right) \pm \cos(\Delta m t) \tag{6.8}$$

6.1.2 Current measurements of A_{SL}

All previous experimental measurements are in the semileptonic channel, where the asymmetry measured is often called the semileptonic asymmetry, A_{SL}. At hadron colliders A_{SL} is a linear combination of A^s_{SL} and A^d_{SL}, the flavour-specific asymmetries which are extracted. These are in most cases equivalent to $a^{s,d}_{fs}$. All measurements to date have been made untagged and time-integrated. Most measurements have been made of the dimuon asymmetry, apart from the most recent DØ measurement, which is similar to the measurement proposed for LHCb.

The BABAR [107], BELLE [108], CLEO [109, 110], DØ [111] and CDF [112] experiments studied events where two b-mesons of anti-correlated flavour were

produced. Where both these mesons decay to leptons with the same charge, one of the two mesons must have oscillated into its partner. The dilepton asymmetry $A_{\mu\mu}$ is given by:

$$\begin{aligned}\Gamma^{\pm\pm} &= \Gamma(b\bar{b} \to \mu^{\pm}\mu^{\pm}X) \\ A_{\mu\mu} &= \frac{\Gamma^{++} - \Gamma^{--}}{\Gamma^{++} + \Gamma^{--}} \qquad (6.9) \\ &= \frac{\Gamma^{WS}\bar{\Gamma}^{RS} - \bar{\Gamma}^{WS}\Gamma^{RS}}{\Gamma^{WS}\bar{\Gamma}^{RS} + \bar{\Gamma}^{WS}\Gamma^{RS}} = F_d\, A^d_{SL} + F_s\, A^s_{SL} \qquad (6.10)\end{aligned}$$

F_q is the linear coefficient of A^q_{SL} and is given by $F_q = f_q Z_q/(f_d Z_d + f_s Z_s)$. f_q is the fraction of B^0_q in the sample, and Z_q, relates the mixing and decay times.[1] f_q and Z_q are determined experimentally [13, 113] [114].

At the $\Upsilon(4S)$ resonance, i.e. for the BABAR, BELLE and CLEO experiments, only pairs of B^0_d-$\bar{B}^0_d$ and B^--B^+ mesons are produced, therefore $f_s = 0$, $A_{\mu\mu} \to A^d_{SL}$ [107, 110]. Calculating the naive average of $\Upsilon(4S)$ results, Ref. [114] finds:

$$A^d_{SL} = +(1.1 \pm 5.5) \times 10^{-3} \qquad (6.11)$$

For DØ and CDF, the di-muon sample contains a mixture of B^0_s and B^0_d decays [38]:

$$A^{TeV}_{\mu\mu} = (0.582 \pm 0.030) A^d_{SL} + (0.418 \pm 0.047) A^s_{SL} \qquad (6.12)$$

The overall asymmetry is measured to be [112, 115, 116]:

$$A^{D\emptyset}_{\mu\mu} = -(9.2 \pm 4.4(stat) \pm 3.2(syst)) \times 10^{-3} \div \left[1 + \frac{f_s Z_s}{f_d Z_d}\right] \qquad (6.13)$$

$$A^{CDF}_{\mu\mu} = +(8.0 \pm 9.0(stat) \pm 6.8(syst)) \times 10^{-3} \qquad (6.14)$$

Note: the definition of $A^{D\emptyset}_{\mu\mu}$ differs by a scale factor.[2] To obtain the measured flavour-specific asymmetry A^s_{SL}, A^d_{SL} must be taken from elsewhere. Either from B-factory measurements, or the SM. Combining the measured A_{SL} values from the Tevatron with the average A^d_{SL} value from the B-factories allows an indirect determination of

[1] Strictly speaking this is a prediction using the SU(3)-flavour approximation that $\Gamma^s_{SL} = \Gamma^d_{SL}$.

[2] We thank Guennadi Borissov for explaining this feature of the DØ analysis.

A^s_{SL} [112, 116]:

$$\text{DØ-indirect:} \quad A^s_{SL} = -(6.4 \pm 10.1) \times 10^{-3} \tag{6.15}$$

$$\text{CDF-indirect:} \quad A^s_{SL} = -(20 \pm 21(stat) \pm 16(syst) \pm 9(inputs)) \times 10^{-3} \tag{6.16}$$

Alternatively using the SM value for a^d_{fs} one finds from Ref. [38]:

$$\text{Given } a^{d,SM}_{fs}\text{:} \quad A^s_{SL} = -(5.2 \pm 3.9) \times 10^{-3} \tag{6.17}$$

In a method more similar to that proposed for LHCb, DØ has also made a direct measurement of A^s_{SL} in the channel $B^0_s \to D^{\mp}_s \mu^{\pm} \nu_{\mu}$ [115]. They measure:

$$A_{D_s\mu} = \frac{N(\mu^+ D^-_s) - N(\mu^- D^+_s)}{N(\mu^+ D^-_s) + N(\mu^- D^+_s)} \approx \frac{A^s_{SL}}{2} \tag{6.18}$$

For 27K events recorded in $1.3\,\text{fb}^{-1}$, with a B/S ~ 0.2, DØ obtain [116]:

$$\text{DØ-direct:} \quad A^s_{SL} = (2.45 \pm 1.93(\text{stat}) \pm 0.35(\text{syst})) \times 10^{-2} \tag{6.19}$$

Typically the current results are all consistent with zero, to a 1 % precision. The substantially larger sample of B-decays obtained by LHCb will provide a more precise measurement of these asymmetries, allowing us to search for NP contributions.

6.1.3 a^q_{fs} with new physics

a_{fs} is very small in the SM, but it is highly sensitive to new physics (NP) in the mixing. Mixing is a loop-level process, and therefore it is sensitive to new virtual particle contributions, at much higher energy scales than can be directly observed. Theoretically a_{fs} is sensitive to NP at energy scales up to $10^4\,\text{TeV}$ at the LHC. Furthermore a^q_{fs} will be affected by new CP-violating phases, illuminating possible NP explanations for the matter-antimatter asymmetry in the universe.

The untagged measurement of A^q_{fs} is difficult at LHCb due to the environment, which offsets the measured asymmetry. We say that the environment contributes "pollutants," which will be discussed shortly. However, the measurement of A^q_{fs} is well motivated due to the much higher statistics LHCb can obtain in flavour specific channels and the fact a precise measurement of A^q_{fs} can illuminate/constrain wide avenues of possible NP.

Much of the parameter space of the numerous proposed new physics models has already been explored, however it is difficult to constrain models whose physics differs only slightly from the SM at LHC energies.

Refs. [44] and [114] demonstrate that knowledge of the flavour-specific asymmetry can constrain NP models even if :

1. They have no new flavour structure
2. They maintain a unitary SM CKM matrix
3. Tree level processes are still SM dominated
4. New CPV enters only in the mixing terms

In many new models significant departures from the SM are predicted for a^q_{fs} [40, 42] with up to two orders of magnitude enhancement in the B^0_s system [117]. Under the above constraints, the most general model-independent form parameterising NP in $B^0_{d,s}$ mixing is as follows, adopting the notations used in Refs. [38, 114, 117]:

$$\left(\Gamma^q_{12}\right)^{NP} = \left(\Gamma^q_{12}\right)^{SM} \tag{6.20}$$

$$\left(M^q_{12}\right)^{NP} = \Delta_q \cdot \left(M^q_{12}\right)^{SM} = r_q^2 e^{2i\theta_q} \left(M^q_{12}\right)^{SM} = \left(1 + h_q e^{2i\sigma_q}\right) \left(M^q_{12}\right)^{SM} \tag{6.21}$$

where r_q^2 and h_q are real parameters representing the magnitude of new physics, σ_q and θ_q are real angles representing the phase of new physics and Δ_q is a complex parameter encompassing information on the real and imaginary new physics contribution. The reader will recall the definitions of the matrix elements Γ_{12} and M_{12} from the mixing Hamiltonian in Sec. 1.3, Eqn. 1.19, and how they relate to observables in the mixing and decay rates. Note that Eqn. 6.20 is the direct

equivalent of bullet point 3. The mixing parameters become:

$$(\Delta m_s)^{NP} = (\Delta m_s)^{SM} r_s^2 \tag{6.22}$$

$$(\Delta \Gamma_s)^{NP} = (\Delta \Gamma_s)^{SM} \cos(2\theta_s) \tag{6.23}$$

$$\left(a_{fs}^s\right)^{NP} = \mathsf{Im}\left\{\frac{\Gamma_{12}^s}{M_{12}^s}\right\}^{SM} \frac{\cos(2\theta_s)}{r_s^2} - \mathsf{Re}\left\{\frac{\Gamma_{12}^s}{M_{12}^s}\right\}^{SM} \frac{\sin(2\theta_s)}{r_s^2} \tag{6.24}$$

The other new physics parameters can be derived geometrically using Eqn. 6.21. There are three necessary conditions in order that a measurement of the flavour specific asymmetry a_{fs}^s should constrain the NP phase [114]:

1. The experimental error on a_{fs}^s should be at or below$|\Gamma_{12}^s/M_{12}^s|$ $(\approx 5 \times 10^{-3})$
2. An upper bound on r_s^2 should be available
3. An independent upper bound on a_{fs}^d should be available

Ref. [114] uses the $A_{SL}^{s,d}$ from present data given in Sec. 6.1.2, and an early Δm_s value from the CDF collaboration [118] to constrain $2\theta_s$:

$$\Delta m_s = (17.33^{+0.42}_{-0.21} \pm 0.07)\ \mathrm{ps}^{-1} \tag{6.25}$$

$$r_s^2 = \frac{\Delta m_s^{expt}}{\Delta m_s^{SM}} = (0.97 \pm 0.26) \tag{6.26}$$

$$\sin(2\theta_s) \approx -\frac{A_{SL}^s}{[\mathsf{Re}\{\Gamma_{12}^s/M_{12}^s\}]^{SM}} \frac{\Delta m_s^{expt}}{\Delta m_s^{SM}} = -(1.9 \pm 2.8) \tag{6.27}$$

which is the limit assuming NP-dominance in A_{SL}^s. Evidently there is currently no significant constraint on the CP-violating NP phase $2\theta_s$ from current measurements.

A significant improvement is possible at LHCb, due to the higher luminosity and high $b\bar{b}$ cross-section at the LHC, however this measurement and other similar studies are complicated by polluting asymmetries.

6.1.4 Pollutants in asymmetry measurements at LHCb

The remit of the LHCb experiment is to investigate CP-violation [31]. However, the LHC provides proton-proton collisions which are not charge-symmetric. As we

begin with a beam containing more particles than anti-particles, the overall number of particles produced must be on average higher than the number of antiparticles.[3] This manifests as a non-zero production asymmetry, δ_p^i, for each particle type, i :

$$\delta_p^i = \frac{\bar{I}}{I} - 1 \tag{6.28}$$

where I and $\bar{I}$ refer to the number of particles and antiparticles produced.[4] The LHCb detector is, by necessity, constructed from matter, and also not charge-symmetric (or CP symmetric) [47]. The reconstruction efficiency, ε, of a particle is expected to differ slightly from its antipartner, particularly for hadrons. This is quantified by the detector asymmetry δ_c^i:

$$\delta_c^i = \frac{\varepsilon(\bar{f}^i)}{\varepsilon(f^i)} - 1 \tag{6.29}$$

here once again f and $\bar{f}$ refer to final state particles and antiparticles respectively, or a collection of particles and the collection of their charge conjugates.

These two asymmetries, the production and detection asymmetry, apply also to backgrounds, resulting in a background asymmetry, δ_b^i:

$$\begin{aligned} \delta_b^i &= \frac{N(\text{Bg in } \bar{f}^i)}{N(\text{Bg in } f^i)} - 1 = \frac{\bar{b}^i}{b^i} - 1 \\ (1+\delta_b^i) &= (1+\delta_{c,b}^i)(1+\delta_{p,b}^i) \end{aligned} \tag{6.30}$$

The background asymmetry from different sources will also differ. The asymmetries can be parameterised in terms of the δ parameters given above, or equally in terms of more conventional asymmetries, A, which are equivalent:

$$A_p = \frac{I - \bar{I}}{I + \bar{I}} = \frac{-\delta_p}{2 + \delta_p} \quad \text{similarly:} \quad A_i = \frac{-\delta_i}{2 + \delta_i} \tag{6.31}$$

Any of the three asymmetries, $\delta_{c,p,b}$, could mimic CPV within signal channels, particularly in untagged studies, time-independent studies and direct CPV searches.

[3] In all cases we adopt the particle-antiparticle convention used by the PDG.
[4] We adopt the convention of Nierste from Ref. [37].

All three terms contribute to the measurement of a^q_{fs} at LHCb.

6.1.5 Flavour specific asymmetry at LHCb

The event topology for a b-event containing information on A_{fs} at LHCb is given in Fig. 6.1. LHCb will measure A_{fs} in an untagged sample:

$$A^{unt,q}_{fs} = \frac{\Gamma(B^0_q \text{ or } \bar{B}^0_q \to f) - \Gamma(B^0_q \text{ or } \bar{B}^0_q \to \bar{f})}{\Gamma(B^0_q \text{or} \bar{B}^0_q \to f) + \Gamma(B^0_q \text{ or } \bar{B}^0_q \to \bar{f})} \tag{6.32}$$

$$= \frac{\Gamma^{RS} + \bar{\Gamma}^{WS} - \bar{\Gamma}^{RS} - \Gamma^{WS}}{\Gamma^{RS} + \bar{\Gamma}^{WS} + \bar{\Gamma}^{RS} + \Gamma^{WS}} \sim \frac{a^q_{fs}}{2} \tag{6.33}$$

In an untagged study δ^q_c, δ^q_p, and δ^q_b are included.[5] The measured decay widths are different from the ideal decay widths by factors of the pollutants. We add a subscript 'e' for the experimentally measured widths, which take the form:

$$\begin{aligned}
\Gamma^{RS}_e &= \Gamma^{RS} \\
\Gamma^{WS}_e &= (1+\delta_c)\Gamma^{WS} \\
\bar{\Gamma}^{RS}_e &= (1+\delta_p)(1+\delta_c)\bar{\Gamma}^{RS} \\
\bar{\Gamma}^{WS}_e &= (1+\delta_p)\bar{\Gamma}^{WS}
\end{aligned} \tag{6.34}$$

From Eqns. 6.34 and 6.7:

$$A^{e,q}_{fs,unt}(t) = \frac{2a^q_{fs} - \delta_c\left[2+\delta^q_p\right]}{4 + 2\delta^q_p + \delta_c\left[2+\delta^q_p\right]} - \left(\frac{2a^q_{fs} + \delta^q_p\left[2+\delta_c\right]}{4 + 2\delta_c + \delta^q_p\left[2+\delta_c\right]}\right)\frac{\cos(\Delta m_q t)}{\cosh(\Delta\Gamma_q t/2)} \tag{6.35}$$

where terms of order δ^3_i, a^2_{fs}, $a_{fs}\delta_i$ and higher have been ignored. Ignoring all second-order terms gives:

$$A^{e,q}_{fs,unt}(t) \approx \frac{\delta^q_c}{2} + \frac{a^q_{fs}}{2} + \left(\frac{\delta^q_p}{2} - \frac{a^q_{fs}}{2}\right)\frac{\cos(\Delta m_q t)}{\cosh(\Delta\Gamma_q t/2)} \tag{6.36}$$

Allowing for an asymmetric background adds a term in the overall widths. This

[5] The possibility of using tagging information is described in Sec. 6.1.5.1.

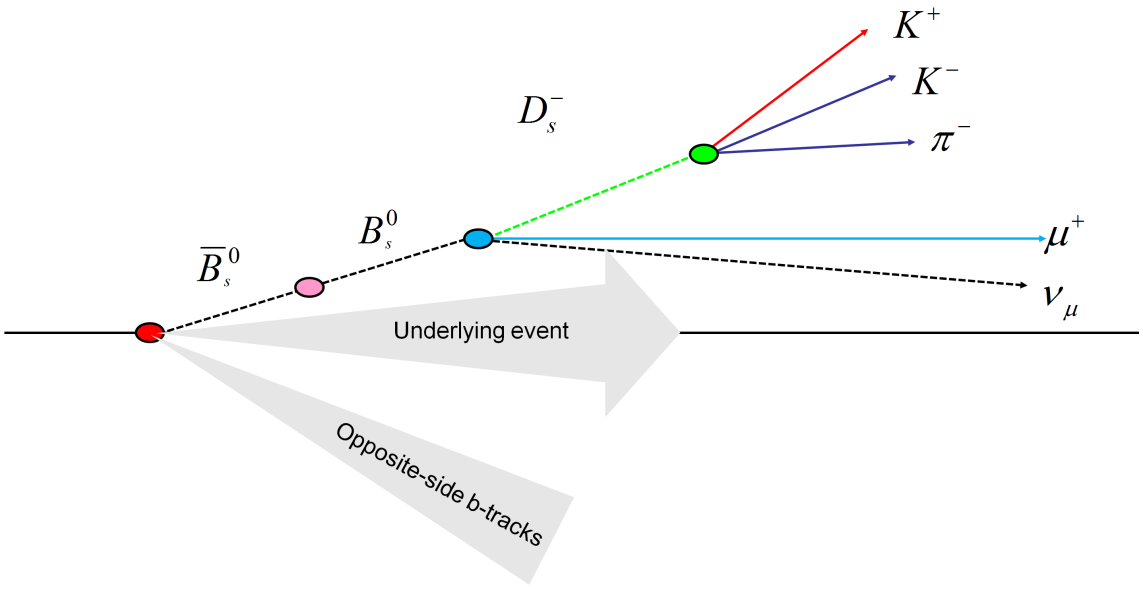

Figure 6.1: Topology of an example semi-leptonic event involving A_{fs} at LHCb.

adds a time-independent term in the expression for a_{fs}, which is easiest expressed when prescaled by $(1 + B/S)$:

$$(1 + B/S)\ A^{b,q}_{fs,unt}(t) = \frac{\delta^q_c}{2} + \frac{a^q_{fs}}{2} + \left(\frac{\delta^q_p}{2} - \frac{a^q_{fs}}{2}\right) \frac{\cos(\Delta m_q t)}{\cosh(\Delta\Gamma_q t/2)} + A^q_B \tag{6.37}$$

where we let:

$$A^q_B = \frac{\delta^q_b}{2} \left(\frac{B}{S}\right)^q \tag{6.38}$$

Finally, in the presence of a finite proper-time resolution σ_t[106]:

$$\begin{aligned}(1 + B/S)\ A^q_{fs}(t) = \frac{\delta^q_c}{2} + \frac{a^q_{fs}}{2} + A^q_B \\ + e^{-\frac{1}{2}\sigma_t^2\left[(\Delta m_q)^2 + (\Delta\Gamma_q)^2\right]} \left(\frac{\delta^q_p}{2} - \frac{a^q_{fs}}{2}\right) \frac{\cos(\Delta m_q(t - \sigma_t^2\Gamma_q))}{\cosh(\frac{1}{2}\Delta\Gamma_q(t - \sigma_t^2\Gamma_q))}\end{aligned} \tag{6.39}$$

This equation has a time dependent and a time-independent part, which contain different linear combinations of a_{fs} and the polluting asymmetries. Any two of the asymmetries can be fitted, if the others are known. None of the polluting asymmetries are trivial to measure. As will be discussed in Secs. 6.3 to 6.5, they are expected to be many orders of magnitude larger than a_{fs}. The pollutants could in

principle be separated by performing a tagged analysis; however, tagging introduces additional complications, discussed below. Instead we will propose a method to cancel or fit for the polluting asymmetries and measure $\Delta A_{fs}^{s,d} \approx (a_{fs}^{s} - a_{fs}^{d})/2$.

6.1.5.1 A side note on tagged analysis

A measurement of a_{fs} with tagging is also possible at LHCb. With tagging we can directly measure:

$$\Gamma_{tag}^{RS} = \epsilon_T \Gamma_e^{RS} + \omega \bar{\Gamma}_e^{WS} \propto \epsilon_T \Gamma^{RS} + \omega(1+\delta_p)\bar{\Gamma}^{WS} \quad (6.40)$$

$$\Gamma_{tag}^{WS} = \epsilon_T \Gamma_e^{WS} + \omega \bar{\Gamma}_e^{RS} \propto \epsilon_T (1+\delta_c)\Gamma^{WS} + \omega(1+\delta_p)(1+\delta_c)\bar{\Gamma}^{RS} \quad (6.41)$$

$$\bar{\Gamma}_{tag}^{RS} = \bar{\epsilon}_T \bar{\Gamma}_e^{RS} + \bar{\omega} \Gamma_e^{WS} \propto \bar{\epsilon}_T (1+\delta_p)(1+\delta_c)\bar{\Gamma}^{RS} + \bar{\omega}(1+\delta_c)\Gamma^{WS} \quad (6.42)$$

$$\bar{\Gamma}_{tag}^{WS} = \bar{\epsilon}_T \bar{\Gamma}_e^{WS} + \bar{\omega} \Gamma_e^{RS} \propto \bar{\epsilon}_T (1+\delta_p)\bar{\Gamma}^{WS} + \bar{\omega}\Gamma^{RS} \quad (6.43)$$

With tagging efficiencies of ϵ_T and $\bar{\epsilon_T}$ and mistag probabilities of ω, $\bar{\omega}$, for the charge conjugate states, which we do not expect to be equal.

There are four additional equations, and four additional unknowns. If ϵ and ω were extracted from control channels with sufficient precision the addition of these four equations would allow for the simultaneous extraction of δ_p^q, δ_c^q and a_{fs}^q. In the presence of an uncertainty in these values comparable to the precision on a_{fs} and a high tagging power $P = \epsilon(1-2\omega)^2 \rightarrow 1$, a small systematic error would be added. However, typically the tagging power is small, around 0.1, and a precise enough measurement of the tagging efficiency is very difficult. In this case the additional tagging information would further increase systematic errors, so it is not used.

6.1.6 Summary

We have demonstrated that the flavour specific asymmetry is an interesting physics parameter to investigate, however, the measurement at LHCb is polluted by the detection, production and background asymmetries. To understand the origin and

expected level of these pollutants Monte Carlo studies are performed in Sec. 6.3, Sec. 6.4 and Sec. 6.5, once the event selection has been established.

6.2 Event selections

Event selection at LHCb is employed to provide a data sample of reasonable purity for a given analysis. Events are selected which contain one or more decay candidates. Selections reduce the number of events by discarding candidate decays which fall outside of a given range in kinematic variables or PID information. This process is known as cutting. Cuts are chosen in variables where the signal and background distributions differ such that they can be separated.

Altogether selected events must pass the L0 trigger, HLT, a preselection and a final offline selection. The hardware and implementation of L0 and HLT are described in Sec. 3.8. Offline event selection is tuned first, to the most recent Monte Carlo samples available, then offline-selected events are used to tune the HLT.

The preselection is a loose selection of events, to reduce the number of events required for full offline analysis. In the current computing model, the preselections are limited to a rate of $\sim 20\,\mathrm{Hz}$ and user analysis is limited to these preselected data. The preselection is a starting point for the optimal offline event selection, which is a tighter selection of signal events, aiming to achieve a background over signal ratio, B/S of ~ 1, and/or optimise the signal significance $S/\sqrt{(S+B)}$. The offline selection and the HLT2 selection have been reoptimised, as in Secs. 6.2.1 and 6.2.4. The L0 trigger and HLT1 performance is discussed in Secs. 6.2.2 and 6.2.3.

6.2.1 Combined offline selection of $B_q^0 \to D_q^{\mp}\mu^{\pm}\nu_\mu X^0$

In order to ensure the same detector asymmetry in different channels a simultaneous selection is required. A combined selection has been developed for $B_s^0 \to D_s^{\mp}\mu^{\pm}\nu_\mu X^0$ and $B_d^0 \to D^{\mp}\mu^{\pm}\nu_\mu X^0$, where X^0 is a group of undetected particles with an overall

Table 6.1: Monte Carlo event samples used for selection tuning.

Name	Identifier*	Gauss	Boole	Brunel	Events	Time† /s
Cocktail $B_s^0 \to D_s^{\mp}\mu^{\pm}\nu_\mu X^0$	13774001	v25r8	v12r10	v30r14	380k	$\sim 2.3 \times 10^4$
Cocktail $B_d^0 \to D^{\mp}\mu^{\pm}\nu_\mu X^0$	11874011	v26r0	v14r6	v31r12	400k	$\sim 4.3 \times 10^4$
Inclusive $b\bar{b}$	10000000	v25r10	v12r10	v30r17	800k‡	~ 512
Minimum bias	30000000	v25r10	v12r10	v30r17	2.9 M**	3.3
Inclusive $b\bar{b} \to \mu\mu X$	10012000	v25r10	v12r10	v30r17	3.3 M‡	$\sim 2.5 \times 10^4$

The software versions are given for the reference of experts. Gauss, Boole and Brunel were discussed in Chapter 5.

* numerical event type as defined in Ref. [119]. † seconds at nominal luminosity required to produce this number of events, multiply by $0.2\,\text{nb}^{-1}s^{-1}$ to get the relative integrated luminosity.

‡ preselection already applied ** L0 trigger already applied

charge of zero (including π^0, γ, ν_l), and both $D^{\mp}$ and $D_s^{\mp}$ decay to $K^+K^-\pi^{\mp}$.

Here we present the full list of cuts after optimisation. The cut efficiency and the relevant signal and background distributions are given in Appendix E. For the reference of experts, this selection was developed and optimised with DaVinci v19r11.

6.2.1.1 Event Samples

The signal and background samples used for this investigation are given in Table 6.1. The two cocktail samples were generated with several possible intermediate resonances[6], and several possible X^0-states. The proportion of the different final states, and the total visible branching ratios are given in Tables 6.2 and 6.3. In these tables the branching ratios $D_s^{\pm} \to K^+K^-\pi^{\pm} = (5.2 \pm 0.9)\%$ and $D^{\pm} \to K^+K^-\pi^{\pm} = (1.00 \pm 0.04)\%$ have been included.

It is worth noting that the branching ratios of B_d^0 to the excited $D^{*\pm}$ states have been measured at the B-factories [120, 121], and are in general agreement with the inclusive semileptonic branching fraction [122]. Although the inclusive semileptonic B_s^0 branching ratio has been measured [24], the branching ratios to the exclusive $D_s^{(*)\pm}$ states have not. The total branching ratio used here is normalized to the measured inclusive semileptonic B_s^0 branching ratio. However the proportion of

[6]The B_d^0-sample was compiled and generated personally. The B_s^0-sample was generated as part of DC06, but reprocessed personally with Brunel v31.

Table 6.2: Proportion of events in B_s^0 cocktail samples.

decay mode	BR $\times 10^3$	proportion
$B_s^0 \to D_s^- \mu^+ \nu_\mu$	1.09	0.254
$B_s^0 \to D_s^{*-} \mu^+ \nu_\mu \to D_s^- \mu^+ \nu_\mu X^0$	2.55	0.592
$B_s^0 \to D_{s1}^{'-} \mu^+ \nu_\mu \to D_s^- \mu^+ \nu_\mu X^0$	0.21	0.048
$B_s^0 \to D_{s0}^{*-} \mu^+ \nu_\mu \to D_s^- \mu^+ \nu_\mu X^0$	0.21	0.048
$B_s^0 \to D_s^- \tau^+ \nu_\tau \to D_s^- \mu^+ \nu_\mu X^0$	0.07	0.017
$B_s^0 \to D_s^{*-} \tau^+ \nu_\tau \to D_s^- \mu^+ \nu_\mu X^0$	0.14	0.033
$B_s^0 \to D_{s1}^{'-} \tau^+ \nu_\tau \to D_s^- \mu^+ \nu_\mu X^0$	0.016	0.004
$B_s^0 \to D_{s0}^{*-} \tau^+ \nu_\tau \to D_s^- \mu^+ \nu_\mu X^0$	0.016	0.004
Total	4.304	1.00

Table 6.3: Proportion of events in B_d^0 cocktail samples.

decay mode	BR $\times 10^3$	proportion
$B_d^0 \to D^- \mu^+ \nu_\mu$	0.2236	0.364
$B_d^0 \to D^{*-} \mu^+ \nu_\mu \to D^- \mu^+ \nu_\mu X^0$	0.1951	0.318
$B_d^0 \to D_1^- \mu^+ \nu_\mu \to D^- \mu^+ \nu_\mu X^0$	0.0073	0.012
$B_d^0 \to D_0^{*-} \mu^+ \nu_\mu \to D^- \mu^+ \nu_\mu X^0$	0.0162	0.026
$B_d^0 \to D_1^{'-} \mu^+ \nu_\mu \to D^- \mu^+ \nu_\mu X^0$	0.0118	0.019
$B_d^0 \to D_2^{*-} \mu^+ \nu_\mu \to D^- \mu^+ \nu_\mu X^0$	0.0065	0.011
$B_d^0 \to D^- \mu^+ \pi^0 \nu_\mu$	0.00002	0.00003
$B_d^0 \to D^{*-} \mu^+ \pi^0 \nu_\mu \to D^- \mu^+ \nu_\mu X^0$	0.0108	0.018
$B_d^0 \to D^- \tau^+ \nu_\tau \to D^- \mu^+ \nu_\mu X^0$	0.1309	0.213
$B_d^0 \to D^{*-} \tau^+ \nu_\tau \to D^- \mu^+ \nu_\mu X^0$	0.0095	0.015
$B_d^0 \to D_1^- \tau^+ \nu_\tau \to D^- \mu^+ \nu_\mu X^0$	0.0003	0.0005
$B_d^0 \to D_0^{*-} \tau^+ \nu_\tau \to D^- \mu^+ \nu_\mu X^0$	0.0008	0.0013
$B_d^0 \to D_1^{'-} \tau^+ \nu_\tau \to D^- \mu^+ \nu_\mu X^0$	0.0005	0.0081
$B_d^0 \to D_2^{*-} \tau^+ \nu_\tau \to D^- \mu^+ \nu_\mu X^0$	0.0010	0.0016
Total	0.614	1.00

the different $D_s^{(*)\pm}$ states are taken from isospin-symmetry arguments. Given the assumptions required, some of which are already in disagreement with the results in the B_d^0 system [123], a generous theory uncertainty should be allowed [124]. We use the measured value and uncertainty for the inclusive leptonic branching fraction. We allow a 50 % theory uncertainty in the exclusive $D_s^\pm$ branching fractions, and a 100 % uncertainty in the excited $D_s^{*\pm}$ exclusive fractions. We perform our analysis of A_{fs} on the full sample of all decays. The statistics are increased and the branching ratio error is reduced. The total branching ratios to these states, i.e. the visible branching ratios, used are:

$BR_{vis}(B_s^0) = (4.3 \pm 1.5)\times10^{-3}$, $BR_{vis}(B_d^0) = (6.14 \pm 0.62)\times10^{-4}$.

$b\bar{b}$-inclusive events have been generated with the constraint that the two b-quarks must point within the LHCb acceptance. For signal samples, $D_q^{\pm}$ and $\mu^{\pm}$ must point within the LHCb acceptance. This corresponds to a geometric cut at the generator level, ϵ_{geom}, which is (43.7±0.1) % efficient for the $b\bar{b}$-events and (18.95±0.03) % efficient for signal. Similarly the $b\bar{b} \to \mu\mu$ is constrained such that the two muons must be in the LHCb acceptance, which occurs in (2.21 ± 0.001) % of inclusive $b\bar{b}$ events. The preselection was applied to all samples before optimisation. For the background samples in Table 6.1 a logical OR of all preselections was applied centrally in the 'stripping' of events. The stripping retained 13.6 % of all $b\bar{b} \to \mu\mu$ events and 3.6 % of inclusive-$b\bar{b}$ events. These are used as scaling factors to calculate the equivalent luminosity in Table 6.1.

6.2.1.2 Event weighting

To calculate overall B/S fractions and other discriminants for optimisation, the selection results from the samples in Table 6.1 were weighted to the expected yield in 5×10^4 s (about two days) and summed. Signal was taken from the signal samples only, and backgrounds were inclusively added from all available $b\bar{b}$ samples. From now on this will be referred to as the weighted dataset. This dataset was used for optimisation of offline selection cuts. Optimisation was performed to maximise $S/\sqrt{S+B}$ after applying the preselection. The final optimised cuts are reported here, and the details of efficiency and background suppression are given in Appendix E.

6.2.1.3 Selection of charged tracks

The abbreviations used and the full list of cuts from selection and preselection are defined in Table E.2 of the Appendix. A sample of pions, kaons and muons are selected from long charged tracks using kinematic cuts and PID information. PID

information is compiled as described in Sec. 3.7.2, although the details of the log-likelihood approach are discussed elsewhere [4]. The difference in log likelihood of two hypotheses, μ and e, say, is denoted by $\Delta_{LL}(\mu - e)$. The global minimisation algorithms that perform track reconstruction are not discussed in this Thesis, they are also discussed elsewhere [65]. A measure of the $\chi^2/n.d.f.$, the track goodness-of-fit, is assigned to each track. This does not necessarily form a true χ^2 distribution, but it is still a very useful parameter to cut on to reduce ghost tracks reconstructed from disparate hits in the detector. The tracking goodness-of-fit χ^2 is propagated through the vertex fitting tools used to obtain a goodness-of-fit for each vertex χ^2_{vtx}.

Hadrons: $P > 2\,\mathrm{GeV}c^{-1}$, P_t >500 $\mathrm{MeV}c^{-1}$, ips> $3\,\sigma$, where RICH information about the track is available.

Pions: charged hadrons $\Delta_{LL}(\pi - K) > -5$.

Kaons: charged hadrons $\Delta_{LL}(K - \pi) > 1$, $\Delta_{LL}(K - \mu) > 0$, $\Delta_{LL}(K - p) > -3$.

Muons: charged tracks with hits in the muon system, P_t >1 $\mathrm{GeV}c^{-1}$, ips> 2σ, $\Delta_{LL}(\mu - K) > 0$, $\Delta_{LL}(\mu - \pi) > 0$, $\Delta_{LL}(\mu - p) > 0$.

Four cuts were specifically re-optimised. These were the generic cut on the track goodness-of-fit $\chi^2_{tr}/n.d.f$, muon transverse momentum $P_t(\mu)$, kaon particle ID $\Delta_{LL}(K - \pi)$, and muon impact parameter significance ips(μ).

The track goodness-of-fit is useful in identifying ghosts. In Fig. 6.2, left, the distribution of track fit quality for the negative kaon sample is given as an example. A cut was selected to optimise the signal discriminant $S/\sqrt{S+B}$, which is plotted against the cut value in Fig. 6.2.

$P_t(\mu)$ is known to be very useful in the HLT to remove combinatorial background. However, with the full offline track reconstruction and once other selection cuts are included the majority of the background muons are true muons from b-decays, which have the same kinematic distribution as the signal. This can be seen in the distribution plotted in Fig. 6.3, left, from preselected candidates. A signal discriminant, $S/\sqrt{S+B}$ is plotted in Fig. 6.4 left, against the value of this cut. 600 $\mathrm{MeV}c^{-1}$ is the value used in the preselection. As can be seen lower cuts on the

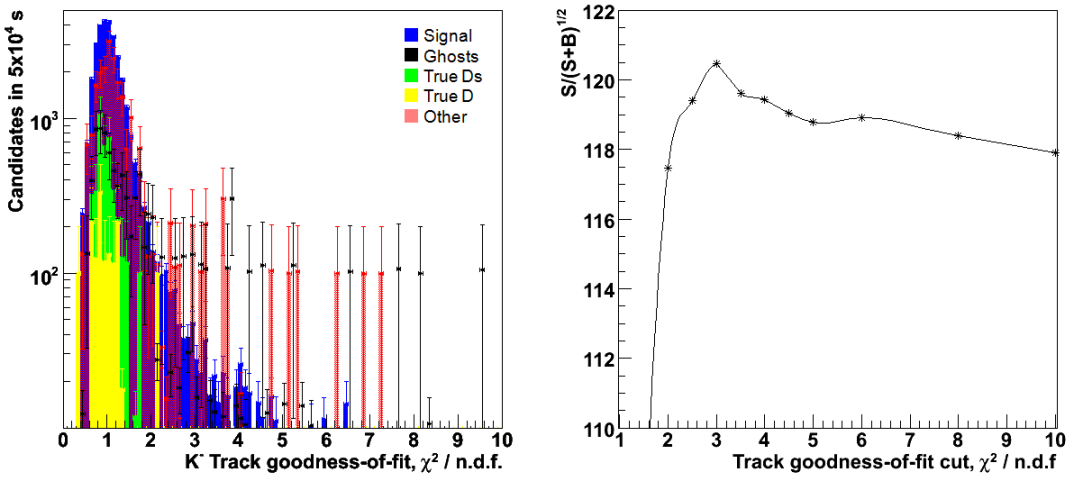

Figure 6.2: Background suppression through track cuts. On the left is plotted the distribution of the track $\chi^2_{tr}/n.d.f.$ for the negative kaon after preselection. Signal is shown in blue and different background types in other colors scaled to 5×10^4 seconds. On the right is given the value of the discriminator $S/(S+B)^{1/2}$ as a function of the cut applied in selection, with all other selection cuts applied and wide $D^{\pm}$-mass windows. The optimal cut value is $\chi^2_{tr}/n.d.f. < 3.0$.

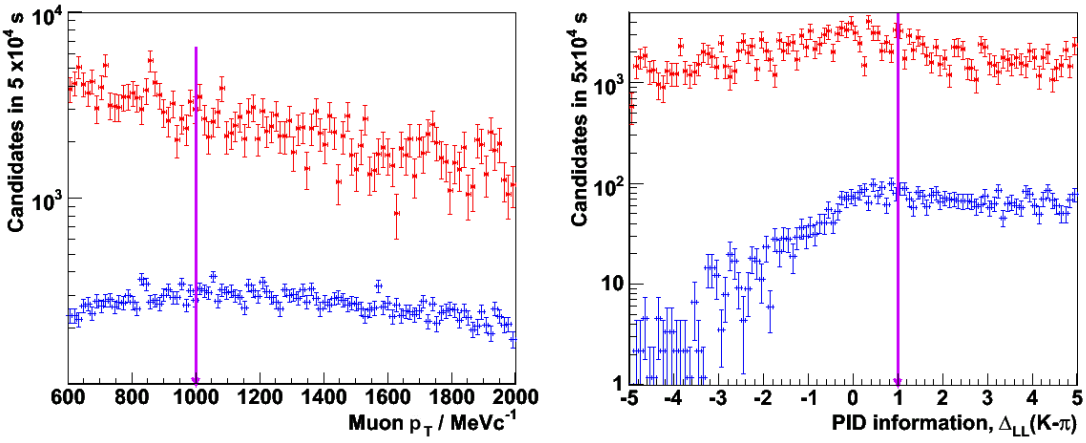

Figure 6.3: Distribution of muon transverse momentum, p_T, and kaon PID information, $\Delta_{LL}(K-\pi)$, in preselected samples, signal in blue and background in red. The optimal offline cut is shown as the purple arrow. The b-event samples are listed in Table 6.1.

muon transverse momentum are preferred. A tight cut at $1\,\mathrm{GeV}c^{-1}$ is chosen.

In the $D^{\pm}$-mass window, separation of the decay $D^{\pm} \to K^+K^-\pi^{\pm}$ from $D^{\pm} \to K^{\mp}\pi^{\pm}\pi^{\pm}$ is improved drastically by the tightening of cuts on the kaon PID. The distributions of $\Delta_{LL}(K-\pi)$ are plotted in Fig. 6.3, right, from preselected candidates. $S/\sqrt{S+B}$ is plotted in Fig. 6.4 right, against the value of this cut. A cut of $\Delta_{LL}(K-\pi) > 1$ is chosen.

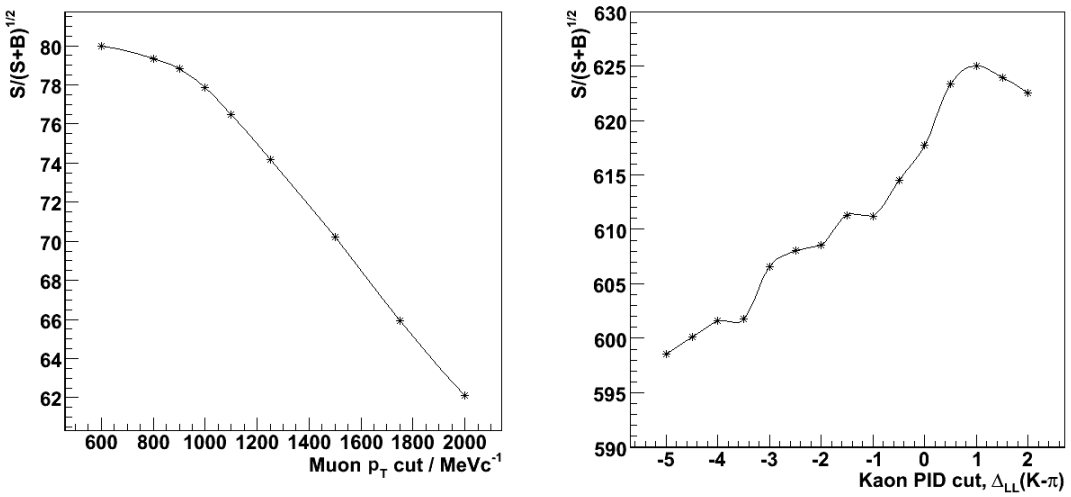

Figure 6.4: $S/(S+B)^{1/2}$ as a function of the muon p_T and kaon PID cuts. Left, the muon P_T cut with all other selection cuts applied. Right, the kaon PID cuts with all other selection cuts applied. S/B is calculated from the b-event samples in Table 6.1.

The muon impact parameter significance (ips) is shown for preselected events in Fig. 6.5, left. There is a significant dip at a significance of $4\,\sigma$ which is produced by a biased primary vertex position. When averaging a primary vertex position initially all tracks in the event are used, including the tracks from the signal decay. Tracks are assigned to the PV whose impact parameter is less than $4\,\sigma$ in significance. The position of the PV is biased by signal tracks, which did not originate from the PV. Refitting the primary vertex removing the tracks from signal candidates reduces this bias considerably as shown in Fig. 6.5, right. However, there is no advantage to further cuts on the ips or refitted ips beyond the preselection cut of $2\,\sigma$. $S/\sqrt{S+B}$ against values of this cut is plotted in Fig. 6.6.

6.2.1.4 Selection of charmed mesons

A $D^{\pm}_{(s)}$ vertex is formed from two opposite charged kaons and one charged pion, which form a vertex with a fit $\chi^2_{vtx} < 10$. Candidate mesons are selected with:

- p_T >1.5 GeVc^{-1}, ips> 3σ.
- Mass from $-200\,\mathrm{MeV}c^{-2}$ to $+100\,\mathrm{MeV}c^{-2}$ of the nominal PDG mass.[7]

[7] $1768.49\,\mathrm{MeV}c^{-2}$ – $2068.49\,\mathrm{MeV}c^{-2}$.

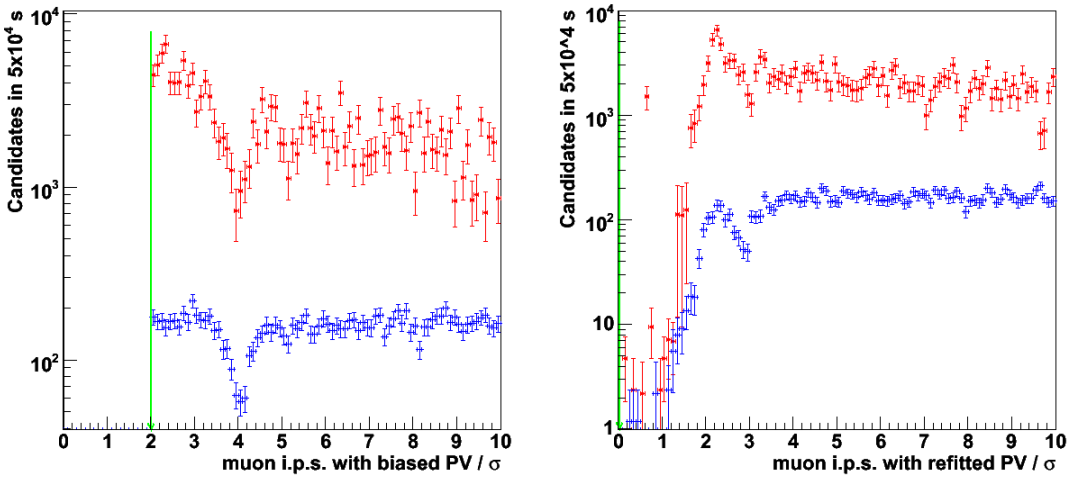

Figure 6.5: Distribution of muon impact parameter significance in preselected samples, signal in blue and background in red. Left, the biased impact parameter significance shows a large dip at a value of $4\,\sigma$. Right, the significance following a refit of the primary vertex shows a much reduced dip at a value of $3\,\sigma$. The b-event samples are listed in Table 6.1.

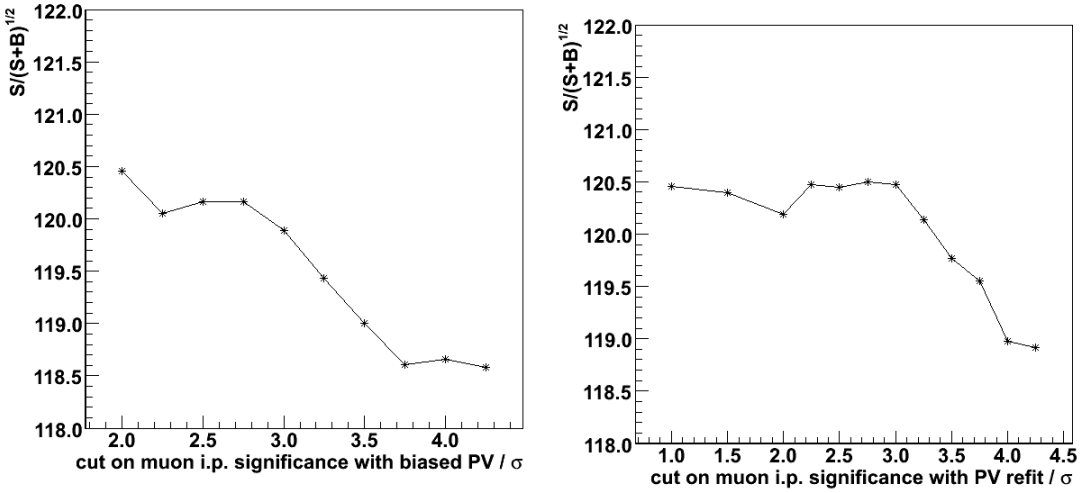

Figure 6.6: $S/(S+B)^{1/2}$ for preselected candidates as a function of cuts on the muon ips Left, for the biased impact parameter significance. Right, for the significance following a refit of the primary vertex. No significant improvement can be made, even taking the loose preselection. The shape of the two plots are very similar as these two calculations are highly correlated. The b-event samples are listed in Table 6.1.

The upper mass window has been reduced relative to the preselection, in order to agree with the current HLT trigger implementation for $D_s^{\pm}$-decays. This also equalizes the upper and lower sidebands. Roughly $100\,\mathrm{MeV}c^{-2}$ of the mass window is below the $D^{\pm}$ mass, $100\,\mathrm{MeV}c^{-2}$ is between the two mass peaks and $100\,\mathrm{MeV}c^{-2}$

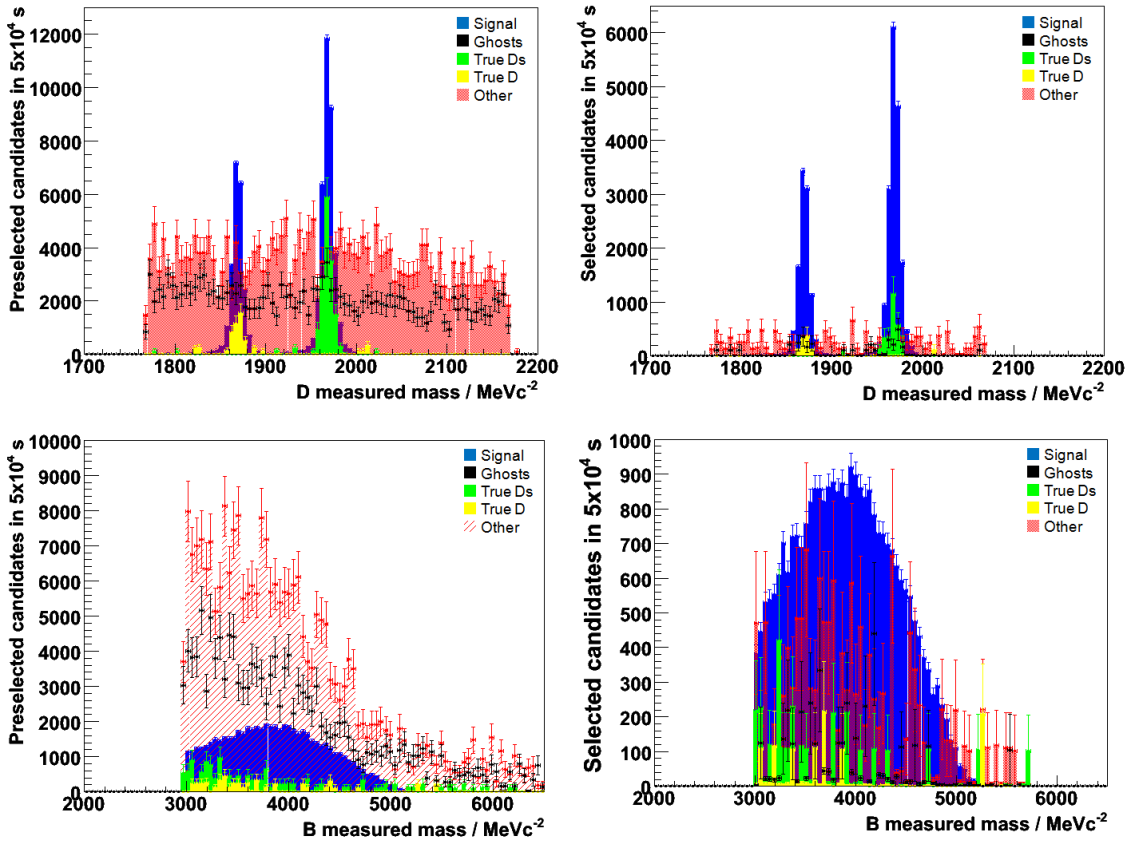

Figure 6.7: Distribution of reconstructed $D_q^{\pm}$ and $B_q^{\pm}$ masses in selected samples. On top, the $D_q^{\pm}$ distributions, on the bottom the B_q^0 distributions. On the left, the distribution in the preselected data, on the right, the distribution with the full selection. Signal distributions are in blue and backgrounds in other colours. The b-event samples are listed in Table 6.1.

is above the $D_s^{\pm}$ mass. A tight mass window of $\pm 20\,\mathrm{MeV}c^{-2}$ about the $D^{\pm}$ or $D_s^{\pm}$ nominal masses may be subsequently imposed to select the $D_{(s)}^{\pm}$ peaks. We use this later to report on the proportion of background under these two peaks. The distributions of $D_{(s)}^{\pm}$ masses from opposite-charge combinations are given Fig. 6.7.

6.2.1.5 Selection of B_q^0 candidates

The B_q^0 is not fully reconstructed due to the missing neutrino and possible missing X^0. A candidate particle is instead formed from the $D_{(s)}^{\pm}$ and $\mu^{\pm}$ pair. For simplicity we refer to this as the B_q^0-candidate from now on. A B_q^0 vertex is formed from a $D_{(s)}^{\pm}$ and $\mu^{\pm}$ candidate, which form a vertex $\chi^2_{vtx} < 5$ and:

- mass from $3.0\,\mathrm{GeV}c^{-2}$ to $5.7\,\mathrm{GeV}c^{-2}$.
- $\cos\theta_p^r$ >0.999, $\Delta z_{D_{(s)}^{\pm}} > 1\,\mathrm{mm}$.

θ_p^r is the pointing angle, the angle between the reconstructed B_q^0 momentum (p) and its flight direction (r). All same and opposite charge combinations of $D_{(s)}^{\pm}\mu^{\pm}$ are taken. The distribution of B_q^0 masses selected is given in the bottom two plots of Fig. 6.7. The upper-mass limit is chosen to allow possible fitting for the peaking background distribution, and hence the background asymmetry, which will be discussed in Sec. 6.5.

6.2.1.6 Selection results

The number of events passing the selection cuts from each sample is given in Table 6.4. The efficiency on signal is equal within errors for the two decay channels considered and is $(2.19 \pm 0.02)\,\%$ on average. The number of signal candidates in the Min Bias sample is consistent with the expected yield of ~ 2.3, assuming Poissonian statistics.

The expected B/S is calculated from the selected candidates in the weighted dataset, using MC truth information, ignoring wrong charge combinations. Normalising to a running time of $5 \times 10^4\,\mathrm{s}$ we expect:

$$\frac{B}{S}(\text{preselection}) = \frac{483183 \pm 2576}{58877 \pm 312} = 8.21 \pm 0.06 \tag{6.44}$$

$$\frac{B}{S}(\text{selection}) = \frac{22024 \pm 468}{28159 \pm 149} = 0.782 \pm 0.018 \tag{6.45}$$

Table 6.4: Results of selection on several event types.

Events	B_s^0-cocktail	B_d^0-cocktail	$bb \to \mu\mu$	bb-inclusive	Min Bias*
Total	371858	393707	3238848	792707	2873772
Preselected	18110	19974	34956	5018	82
Selected	8035	8702	2734	368	6
Efficiency	(2.16± 0.02) %	(2.21± 0.02) %	(0.084± 0.002) %	(0.046± 0.003) %	(2.1±0.9) $\times 10^{-6}$
Candidates	8292	8987	2950	397	6
Signal	8006	8715	892	176	4
Background	252	226	1524	177	2
Wrong charge	34	46	534	44	0

* L0 trigger already applied

for wide mass windows. Tightening the mass windows to $\pm 20\,\mathrm{MeV}c^{-2}$ about the nominal $D^{\pm}$ and $D_s^{\pm}$ masses gives:

$$\frac{B}{S}(B_s^0) = \frac{5889 \pm 248}{17299 \pm 92} = 0.340 \pm 0.015 \tag{6.46}$$

$$\frac{B}{S}(B_d^0) = \frac{3753 \pm 171}{10200 \pm 54} = 0.368 \pm 0.017 \tag{6.47}$$

The B/S of these two modes is consistent given the statistical errors. The statistical errors given above are increased if we also consider the error in the signal branching ratios (BR), which results in:

$$\frac{B}{S}(\text{preselection}) = 8.2 \pm 0.06(stat) \pm 3.0(BR) \tag{6.48}$$

$$\frac{B}{S}(\text{selection}) = 0.78 \pm 0.02(stat) \pm 0.34(BR) \tag{6.49}$$

for wide mass windows. With tight mass windows:

$$\frac{B}{S}(B_s^0) = 0.34 \pm 0.01(stat) \pm 0.12(BR) \tag{6.50}$$

$$\frac{B}{S}(B_d^0) = 0.368 \pm 0.022(stat) \pm 0.038(BR) \tag{6.51}$$

The peaking backgrounds are the most dangerous backgrounds, and are usually from true B-decays. There are two main sources. $B_q \to D_{(s)}^{(*)\mp} X$ where the $D_{(s)}^{(*)\mp}$ decays to $K^+K^-\pi^\mp$ and the hadron X decays semileptonically. Also tracks from two B-decays may be combined; i.e. a muon from a semileptonic B-decay, and a $D_{(s)}^{(*)\pm}$ from the decay of the other B-hadron in the event.

6.2.2 L0 trigger efficiency

The L0 trigger efficiency on this channel is quite high. This is attributed to the high transverse momentum of the selected muons. The L0 efficiency of the two signal

channels is equal within errors and averages to be:

$$\epsilon_{sig}(L0|\text{preselection}) = (78.2 \pm 0.2)\,\% \tag{6.52}$$

$$\epsilon_{sig}(L0|\text{selection}) = (84.7 \pm 0.3)\,\% \tag{6.53}$$

6.2.3 HLT1 summary

In the High Level Trigger (HLT), a fast reconstruction is performed to confirm and refine the L0 decision, see Sec. 3.8.

At the time of this study, the HLT1 trigger performance was very poor, with efficiencies at the level of $30 - 40\,\%$. However, it has been shown that with optimisation, the HLT1 efficiency, given L0, can exceed $98\,\%$. In Refs. [125, 126] the typical efficiency of HLT1 is between $93\,\%$ and $99\,\%$ after this optimisation.

Assuming this optimum is closely reached for the HLT1, we assume an efficiency of $\epsilon_{HLT1} = 0.96 \pm 0.03$ for the remainder of this Thesis.[8]

6.2.4 A decision-tree inspired HLT2 selection

The total output from the HLT1 is tuned to be 30kHz, at which speed it is possible to perform partial event reconstruction online in the HLT computing farm.

Ideally $100\,\%$ of offline selected events should be let through the trigger. There is a small loss in efficiency initially due to the simpler reconstruction performed. For this channel $\sim 97\,\%$ of the offline-selected signal candidates were reconstructible in the HLT2. This corresponds to a better than $99\,\%$ HLT2 reconstruction on each of the 4 final state particles. However, the quality with which each of these tracks are reconstructed is much poorer in the HLT2 than offline. To demonstrate this we plot the distribution of $\chi^2_{tr}/n.d.f.$ for signal tracks in the HLT in Fig. 6.8. Offline

[8] The HLT1 efficiency should be high when the events have been passed by the L0 trigger, HLT2 and offline selections.

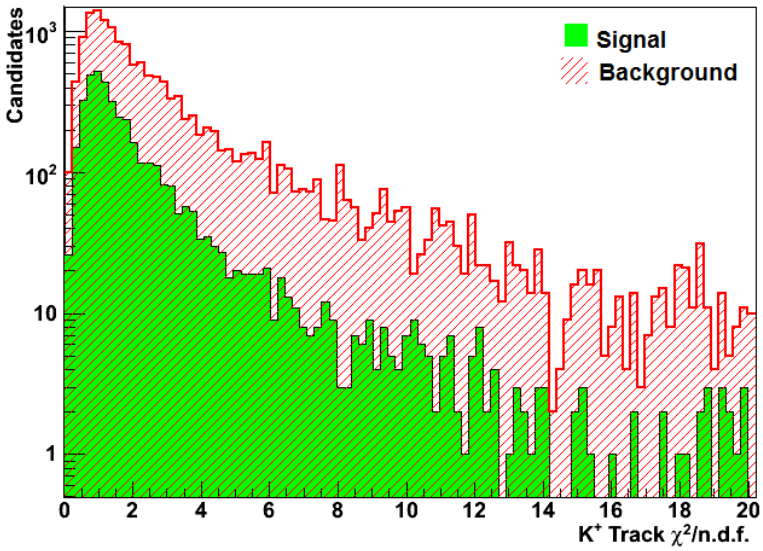

Figure 6.8: Distribution of the track $\chi^2_{tr}/n.d.f.$ in the HLT2 for the negative kaon. Signal is shown in green and background in red from the sample of offline-selected events. Despite an offline cut of $\chi^2_{tr}/n.d.f. < 3.0$ the distribution in the HLT2 extends out to > 100.

a track-quality $\chi^2_{tr}/n.d.f.$-cut of < 3 was employed. In the HLT, however, the tracking performance is much poorer and the distribution of $\chi^2_{tr}/n.d.f.$ for signal tracks extends beyond 100.

Poorer tracking in the HLT2 means the vertices, impact parameters, and distances are reconstructed with lower resolution and poorly calculated errors. This results in lower separation power, as the distributions of background and signal overlap much more than offline. To maintain a high signal efficiency and still remove sufficient background it is necessary to move to a more sophisticated cut-based approach, namely a decision-tree inspired selection.

6.2.4.1 A decision tree

A collection of cuts can be thought of as the selection of a hyper-rectangle in a multi-dimensional space. Most cut-based approaches rely on kinematic variables, e.g. A and B where either the signal or background is peaking, to select regions of signal and remove regions of background, the cuts are usually optimised simultaneously finding, for example $A > a$ and $B > b$ to be optimal, then the cuts will be applied together

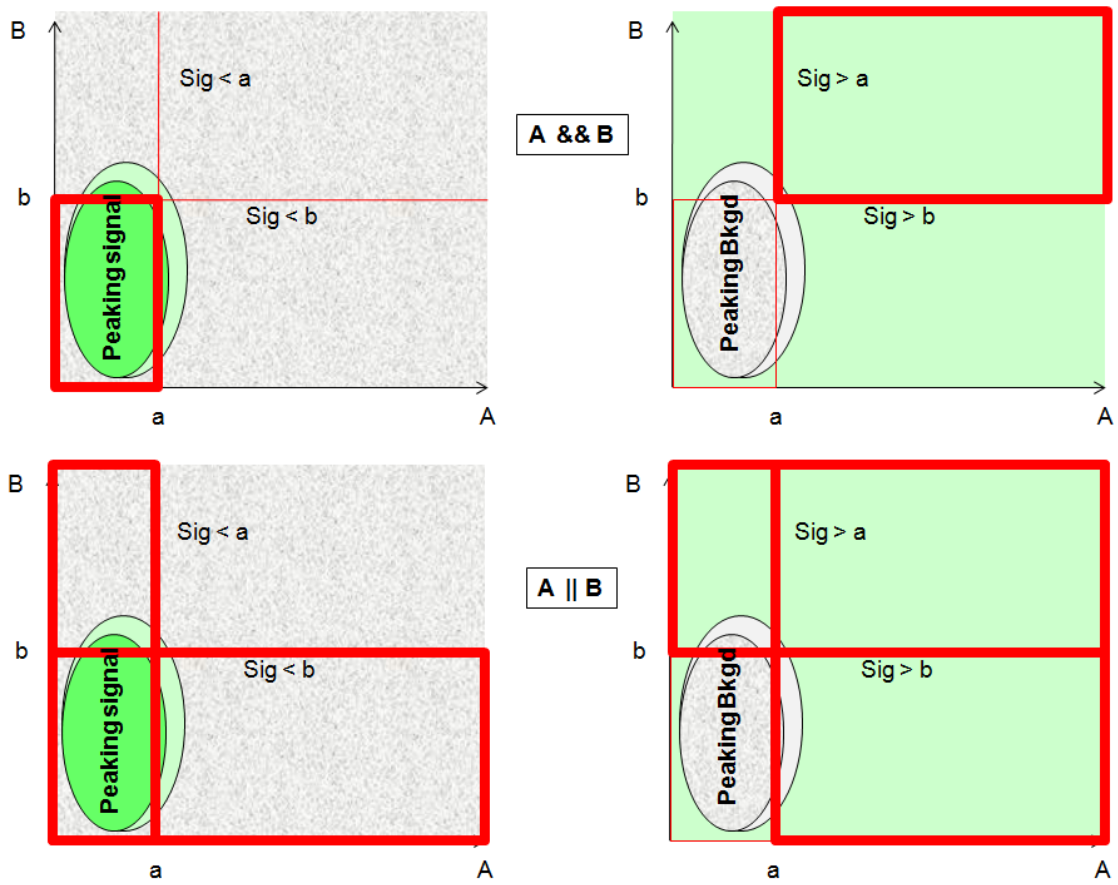

Figure 6.9: A comparison of rectangular cuts. In the top example cuts such as $A > a\ AND\ B > b$ have been employed. Higher signal efficiency with a comparable background rejection can be obtained with $A > a\ OR\ B > b$, shown beneath. Signal in green and background in grey. The red outlined area represents the selected region.

$A > a\ AND\ B > b$. It is possible to improve the signal efficiency and/or reduce the background by also considering cut combinations such as $A > a\ OR\ B > b$. This idea is represented in Fig. 6.9. Additional selection power is gained as we move away from hyper-rectangles to OR-based cuts which form hyper-polygons, or several overlapping hyper-rectangles.

The permutations of OR-based cuts are numerous. A decision tree allows us to find the particular cut permutations with large background suppression and high signal efficiency. An example decision tree is given in Fig. 6.10. At the first step the available data with Monte Carlo truth information are taken, all possible cut variables are ranked by their separation power.[9] The event sample is then separated

[9]We use the ROOT [127] package TMVA and the tools available therein for calculation of the separating power and formation of the decision trees. For more details on TMVA see Ref. [128]

about the point of largest separation, using the variable with the most separating power creating two subsets or 'leaves'. In a rectangular cut-based approach, one of these leaves would be categorised as background, the other as signal, and the background leaf would be discarded, loosing any signal events in that sample. In a decision-tree method the full procedure is repeated on both the resulting data subsets, creating more leaves in the decision 'tree', until a desired purity is reached, no separation is available, or the sample size becomes too small to justify splitting.

Background can then be localised to final leaves with a small signal fraction. The cut string(s) which arrive at all other combinations (i.e. signal) can then be identified. These will be logical combinations of AND and OR cuts with the highest separating power. In the example in Fig. 6.10 a set of cuts is found to filter out a large proportion of the background. Recombining the 'signal' leaves, and restarting the procedure then allows the identification of the next cut string. This process is iterated until no further separation power is available or the desired purity is reached. The aim is to find cuts with a very large signal efficiency, and a much smaller efficiency on background.

6.2.4.2 Optimisation procedure

Optimisation was performed to keep the highest percentage of offline selected events, with the smallest overall rate on L0-selected minimum bias events.[10] Cuts were optimised on a sample of roughly 50 % of the offline selected or L0 events, and evaluated on the full sample to reduce biases from statistical fluctuations.

Initially a set of rectangular cuts were identified with at least 99.9 % signal efficiency. The resulting dataset was then examined in a decision tree to determine a cut string which removed a significant proportion of the background events. This process was then iterated until no further separating power was available.

[10] See Table 6.1

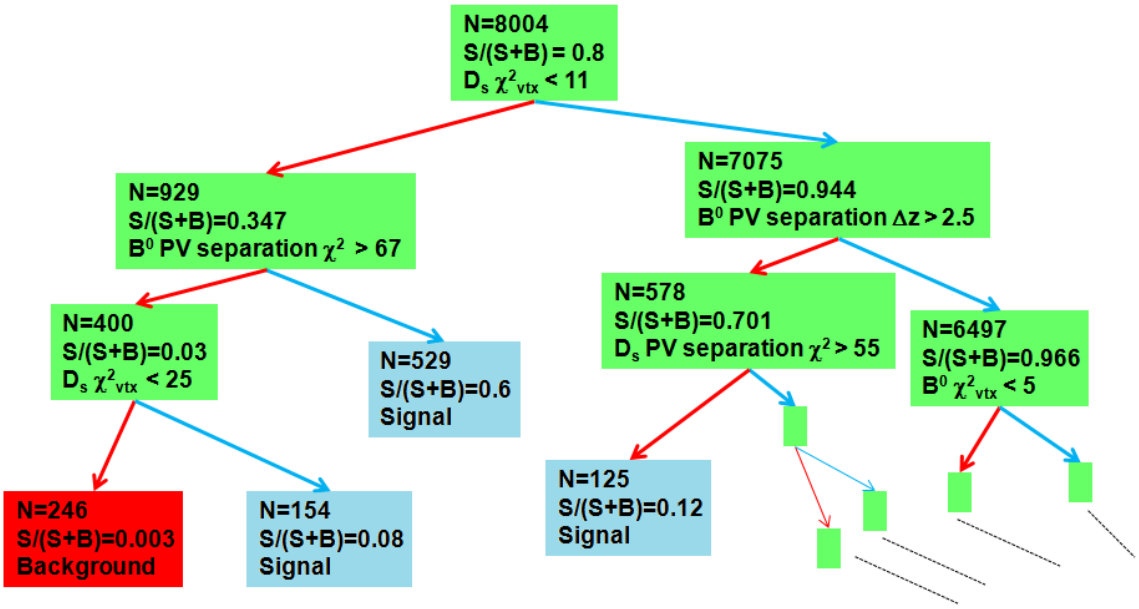

Figure 6.10: An example decision tree for illustration. In this example the final leaves are required to have a purity better than 1 % or a minimum number of 100 events. N=S+B, S and B are the total number of signal and background entries in each set, no weighting is applied to the events at this stage. From this example the cut string $(\chi^2_{vtx}(D_s^{\pm}) < 25 \;||\; B^0 \text{ PV separation } \chi^2 > 67)$ can be identified.

6.2.4.3 HLT2 selection cuts

The following cuts were found[11] :

Charged tracks: A sample of pions, kaons and muons are selected from long charged tracks using kinematic cuts

Hadrons: $P > 2\,\text{GeV}c^{-1}$, $p_T > 500\,\text{MeV}c^{-1}$, IP $> 0.03\,\text{mm}$, $\chi^2_{IP} > 2$.

Muons: $P > 3.9\,\text{GeV}c^{-1}$ and $p_T > 1\,\text{GeV}c^{-1}$.

Selection of charmed mesons: A $D^{\pm}_{(s)}$ vertex is formed from two opposite charged kaons and one charged pion as selected in the previous step which form a vertex with a fit $\chi^2_{vtx} < 125$. Candidate mesons are selected which have:

$p_T > 1.5\,\text{GeV}c^{-1}$, $\cos\theta^r_p > 0.996$, $\Delta z_{PV} > 2\,\text{mm}$, $\chi^2_{PV} > 35$.

mass from $-200\,\text{MeV}c^{-2}$ to $+110\,\text{MeV}c^{-2}$ of the nominal PDG mass.

[11] where IP is an impact parameter, and χ^2_{IP} its significance χ^2 from any PV. Δz_{PV} is the distance in the beam direction between the PV and the decay vertex, and χ^2_{PV} its significance. θ^r_p and other variables are as defined in Table E.2.

Selection of B_q^0 ***candidates***: A B_q^0 vertex is formed from a $D_{(s)}^{\pm}$ and $\mu^{\pm}$ candidate, which form a vertex $\chi^2_{vtx} < 15$ and:

mass from $2.9\,\mathrm{GeV}c^{-2}$ to $5.9\,\mathrm{GeV}c^{-2}$.

$\cos\theta_p^r > 0.9975$, $\Delta z_{D_{(s)}^{\pm}} > 0.25\,\mathrm{mm}$. $\Delta z_{PV} > 0.75\,\mathrm{mm}$, $\chi^2_{PV} > 2$.

Decision-tree based cuts: background is suppressed by demanding:

$\chi^2_{vtx}(D^{\pm}) < 25 \;||\; IP(K^{\pm}) > 0.15$

$\chi^2_{vtx}(D^{\pm}) < 20 \;||\; IP(\pi) > 0.15$

$\Delta z_{PV}(D^{\pm}) > 3.5\,\mathrm{mm} \;||\; \chi^2_{IP}(\pi) > 15$

$p_T(D^{\pm}) > 3.5\,\mathrm{GeVc}^{-1} \;||\; \chi^2_{IP}(\pi) > 90 \;||\; \chi^2_{vtx}(D^{\pm}) < 15$

$p_T(D^{\pm}) > 4\,\mathrm{GeVc}^{-1} \;||\; P_t(\mu) > 2\,\mathrm{GeVc}^{-1} \;||\; \chi^2_{vtx}(D^{\pm}) < 30$

$p_T(B^0) > 3\,\mathrm{GeVc}^{-1} \;||\; \chi^2_{vtx}(D^{\pm}) < 15$

$\chi^2_{PV}(B^0) > 60 \;||\; \chi^2_{vtx}(D^{\pm}) < 10$

$\chi^2_{PV}(D^{\pm}) > 150 \;||\; \chi^2_{vtx}(B^0) < 3$

$\chi^2_{vtx}(B^0) < 3 \;||\; \chi^2_{vtx}(D^{\pm}) < 5 \;||\; \chi^2_{tr}(\mu) < 4$

$\chi^2_{PV}(B^0) > 30 \;||\; \chi^2_{vtx}(D^{\pm}) < 5 \;||\; p_T(\mu) > 2\,\mathrm{GeVc}^{-1}$

6.2.4.4 HLT2 selection results

From the above optimised HLT2 selection, 7,127 from 8,035 B_s^0-events and 7,767 from 8,702 B_d^0-events were selected. This corresponds to an efficiency $\epsilon_{HLT2} = (0.890 \pm 0.002)$. From the 2,898,799 minimum bias events which have passed the L0 trigger 530 events are selected. This corresponds roughly to a trigger rate of 160 Hz in the absence of HLT1. 1,278 candidates are selected in these 530 events, these are categorised based on MC Truth information in Fig. 6.11. The majority (665) of the L0 candidates are ghosts. 8 of the candidates are signal and 356 are from other b-decays. The efficiency of the L0 trigger is unchanged by the HLT2 selection.

Since the 160 Hz rate is too high for the available bandwidth, work on improving the tracking performance of the HLT2 is ongoing.

The largest overlap with other trigger channels occurs for the HLT2 "single muon" selection which selects 31 % of the signal events which were selected by my algorithm.

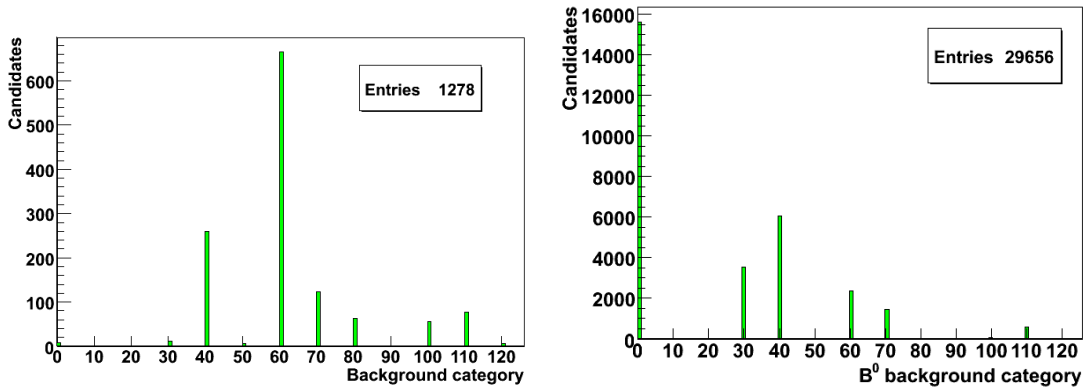

Figure 6.11: MC truth information on HLT2 selected candidates. A histogram of the background category is shown. On the left, for candidates from the L0 minimum bias sample. On the right for candidates from the signal sample. The meaning of the various background categories are discussed in Table E.1.

6.2.5 Event yields

The overall selection efficiency, with L0, HLT1 and HLT2, is calculated as follows:

$$\begin{aligned}
\varepsilon_{tot} =& \epsilon_{geom} \times \epsilon_{sel} \times \epsilon_{HLT2} \times \epsilon_{L0} \times \epsilon_{HLT1} \\
\varepsilon_{tot} =& (0.1895 \pm 0.0003) \times (2.19 \pm 0.02) \times 10^{-2} \\
& \times (0.890 \pm 0.002) \times (0.847 \pm 0.003) \times (0.96 \pm 0.03) \\
\varepsilon_{tot} =& (3.00 \pm 0.10) \times 10^{-3}
\end{aligned} \tag{6.54}$$

The signal event yield for one nominal year is calculated as follows:

$$N = 2 \times \ \sigma_{b\bar{b}} \ \times \int \mathscr{L} dt \times f_b \times BR_{vis} \times \varepsilon_{tot} \tag{6.55}$$

$$N_{B_s} = 2 \times 10^{12} \times 0.1 \times (4.3 \pm 1.5) \times 10^{-3} \times (3.00 \pm 0.10) \times 10^{-3}$$

$$N_{B_s} = (2.58 \pm 0.90) \times 10^{6} \tag{6.56}$$

$$N_{B_d} = 2 \times 10^{12} \times 0.4 \times (6.14 \pm 0.62) \times 10^{-4} \times (3.00 \pm 0.10) \times 10^{-3}$$

$$N_{B_d} = (1.47 \pm 0.16) \times 10^{6} \tag{6.57}$$

where $\sigma_{b\bar{b}} = 500\,\mu$b and $\int \mathscr{L} dt = 2\,\text{fb}^{-1}$. With these optimised selections, the expected annual yield is more than twice what was expected from the DC04 study

[5, 129]. The errors are dominated by the error in the visible branching ratios, with a significant contribution from the error in the expected HLT1 performance. Now that the selections have been optimised we will go on to investigate the systematic effects that influence this analysis.

6.3 Generator study of production asymmetry

At LHC we start with the collisions of two proton beams, which are not CP-symmetric. This produces an unequal number of particles and antiparticles. LHCb covers a region of high rapidity, where these asymmetries are largest. Even species created symmetrically (but not isotropically) in 4π (such as $gg \to b\bar{b}$) may be seen to hadronize asymmetrically within the LHCb acceptance (e.g. $N(b) \neq N(\bar{b})$).

Previous studies of production asymmetry [130, 131, 132] focus on the general production asymmetries at general LHC detectors, commonly examining a subset of heavy-quark species, examining a particular subset of parameters. However, due to the unusual high-rapidity ranges probed by LHCb, different overall asymmetries are expected; additionally asymmetries in the backgrounds and underlying events are important for systematic studies.

An LHCb-specific Monte Carlo generator study was performed, on more than 70M events. The details appear in Ref. [6], which is summarized in Appendix C. The production asymmetry specific to LHCb is determined for many event types and particles. It is shown in Appendix C that the production asymmetry differs between species and is a function of several kinematic variables.

In this section the results of this study are summarized in terms of the application to the measurement of a_{fs} at LHCb.

Table 6.5: Expected production asymmetries, δ_p, for selected particles in the LHCb acceptance.

Particle	PID	$\delta_p \times 1000$	Particle	PID	$\delta_p \times 1000$
$\pi^{\pm}$	± 211	$-(2.16 \pm 0.09)$	$B^{\pm}$	± 521	$-(9.1 \pm 0.8)$
$K^{\pm}$	± 321	$-(8.2 \pm 0.2)$	B_d^0	± 511	$-(3.2 \pm 0.5)$
$D^{\pm}$	± 411	$+(0.45 \pm 0.45)$	B_s^0	± 531	$-(1.5 \pm 0.8)$
D^0	± 421	$+(4.0 \pm 0.8)$	$\mu^{\mp}$	± 13	$+(1.0 \pm 0.9)$
$D_s^{\pm}$	± 431	$-(1.6 \pm 0.8)$			

As in Tables C.3 and C.5, with Tuned PYTHIA.

6.3.1 Application to the study of a_{fs}

It is shown in Sec. 6.2.4 that the events selected by the LHCb trigger and event selections will most likely be dominated by inclusive-$b\bar{b}$ events. The production asymmetries expected are given in Tables C.3 and C.5, of the Appendix, which are collated in Table 6.5. Average production asymmetries are of the order 10^{-3} for neutral B-mesons. It has been shown that the production asymmetries are a function of several kinematic variables, particularly energy, transverse momentum, and pseudo-rapidity. LHCb is the first far-forward experiment examining 14 TeV proton-proton collisions. As such it is likely that Monte Carlo generators will need retuning. The predictions given should therefore be treated as order-of-magnitude estimates which must be measured in data in signal channels.

In comparison with Table 6.5, the production asymmetries from the fully-simulated B_s^0 and B_d^0 signal event cocktail, see Table 6.1 are:

$$\delta_p^i = \frac{\bar{N}}{N} - 1 \tag{6.58}$$

$$\delta_p^d = \frac{260575}{261707} - 1 = -(4.3 \pm 2.8) \times 10^{-3} \tag{6.59}$$

$$\delta_p^s = \frac{187701}{184921} - 1 = (15.0 \pm 3.3) \times 10^{-3} \tag{6.60}$$

The statistical errors for these 800k events are much larger than for the pure generator-level study in Table 6.5. The asymmetries in the B_s^0 events seem to disagree, however, this is attributed to a known bug in this software version affecting

the production percentages.[12] The more precise values from Table 6.5 are adopted throughout this analysis.

In the measurement of a_{fs}, the production asymmetry enters only in the time-dependent component of Eqn. 6.36. Exploiting the precise vertexing and momentum determination of LHCb for a time-dependent analysis the production asymmetry can therefore be separated from the detector and background asymmetries to measure a_{fs}. This method will be discussed further in Sec. 6.6.

6.3.2 Possible measurement of production asymmetries

Currently the most precise determination of production asymmetry arises from the time-dependent measurement of the flavour specific asymmetry itself. Assuming the production asymmetry, $\sim 10^{-3}$, and detector asymmetries, $\sim 10^{-2}$, are very much larger than the flavour specific asymmetries, $\sim 10^{-4}$, the time-dependent analysis can be used in the $B_s^0 \to D_s^{\pm}\pi^{\mp}$ channel to extract the production asymmetry in B_s^0. As is reported in Ref. [106] this allows the measurement of the production asymmetry to a statistical significance of 0.2 % in $2\,\text{fb}^{-1}$. Obviously a simultaneous measurement of a_{fs} and the production asymmetry is not possible through this method. To measure the production asymmetry in data most accurately requires a channel which is not flavour specific and in which the background and detector asymmetries are zero or well-known.

Clearly then, tagged, charge-symmetric, channels such as $B_s^0 \to J/\Psi\phi$ are the best place to measure this parameter, however, they will always suffer from lower statistics than the semileptonic channels used for the most accurate determination of a_{fs}. For the estimation of the overall systematic error in the measurement of a_{fs} a cross-check in such control channels will be important.

[12] The influence of this bug can also be seen in Table C.5

6.4 Simulation of the LHCb detector asymmetry

A detector asymmetry is introduced through a difference in the reconstruction efficiency of charge-conjugated events as in Eqn. 6.29. A generic detector asymmetry can be physical, related to geometry or physics, or unphysical, introduced through software processing. A Monte Carlo study was performed on 5.7M fully reconstructed events, as reported in Appendix D, to predict the level of detector asymmetry in LHCb.

It is asserted, that to control, measure and eliminate, the geometric part of this asymmetry the polarity of the magnet should be reversed often. Providing this removes geometric and tracking asymmetries, the remaining detector asymmetry is repeated for all final state particles in Table 6.6. This is a function of momentum as discussed in Appendix D.

6.4.1 Proposed measurement of detector asymmetries

For measuring the interaction asymmetry for hadrons it is necessary to use a channel where other asymmetries (physics, background, and/or production asymmetries) are zero or are well known. A measurement should be obtained in high statistics, applying the same cuts as those applied in signal channels, to enable re-weighting to the signal distributions. To calculate the detector asymmetry requires calculation of the reconstruction efficiency for each flavour/charge of each hadron.

There are several methods possible for the estimation or direct measurement of the reconstruction efficiency as have been pioneered in colliders at lower energy in cleaner

Table 6.6: Predicted detector asymmetry, δ_c, for final state particles.

Particle	PID	$\delta_c \times 1000$	Particle	PID	$\delta_c \times 1000$
$e^{\mp}$	± 11	$-(0.4 \pm 0.4)$	$\mu^{\mp}$	± 13	$-(0.1 \pm 0.2)$
$p^{\pm}$	± 2212	$-(77.2 \pm 0.4)$	$\pi^{\pm}$	± 211	$-(13.7 \pm 0.1)$
$K^{\pm}$	± 321	$-(32.1 \pm 0.3)$			

environments. In the majority of cases MC and real data are combined. Tracks from Monte Carlo can be added to the data. Or tracks from the data can be added to the MC. This is known as MC embedding. Ideally, though, we would like to perform this measurement with data only, cross-checking with MC. Data methods require over-constrained partially reconstructed channels. BELLE has sucessfully used $D^{*-} \to \bar{D}^0\pi^-$ where $\bar{D}^0 \to \pi^+\pi^- K^0_s$ and $K^0_s \to \pi^+\pi^-$ [133, 134]. The momenta of the pions from the K^0_s-decay can be determined even if one of them is not reconstructed, which permits the direct measurement of track efficiency and detector asymmetry as a function of momentum.

The ideal channel for studying detector asymmetry in LHCb is $B^0_d \to D^{*-}\mu^+\nu_\mu$ where the charm meson decays hadronically, $D^{*-} \to \bar{D}^0\pi^-$, and $\bar{D}^0 \to K\pi\pi\pi$. When only one of the $\bar{D}^0$ daughter hadrons is not reconstructed, this decay is still over-constrained. The flavour of the B^0_d at decay is tagged by the muon charge, and the flavour of the missing hadron is dictated by charge conservation at the tertiary vertex. B-production and physics asymmetries do not affect the measurement.

Assuming the reconstruction of this channel is about half of the efficiency of $B^0_d \to D^{*-}\mu^+\nu_\mu$, $D^{*-} \to \bar{D}^0\pi^-$, $\bar{D}^0 \to K^+\pi^-$ and taking the DC04 selection from Ref. [135], $\sim$9 million selected and triggered events are expected in $2\,\text{fb}^{-1}$ (fully reconstructed). This would potentially provide a detector asymmetry measurement with statistical precision of $\sim 3{\times}10^{-4}$ in $2\,\text{fb}^{-1}$ for either kaons or pions. It is likely that bandwidth requirements will further limit this sample, to a rate similar to $B^0_q \to D^\mp_q\mu^\pm X^0$ presented in Sec. 6.2.

6.4.2 Application to the study of a_{fs}

In hadronic flavour specific decays of the type $B^0_s \to D^\mp_s\pi^\pm$, $D^\mp_s \to K^+K^-\pi^\mp$ there should be little to no detector asymmetry, as the final state is charge symmetric. Second-order detector asymmetries may be introduced through differences in the momentum spectra of the daughter pions.

For decays of the type $B_q^0 \to D_q^{\mp}\mu^{\pm}X^0$, the final state will exhibit an asymmetry:

$$\epsilon_r(f) \propto \epsilon(\mu^+) * \epsilon(\pi^-) \tag{6.61}$$

$$(1+\delta_c^q) = \frac{1}{(1+\delta_c^{\pi})(1+\delta_c^{\mu})} \tag{6.62}$$

$$\begin{aligned}\delta_c^q &\sim -\delta_c^{\pi} - \delta_c^{\mu} \\ &\sim -\delta_c^{\pi} = +(1.37 \pm 0.01) \times 10^{-2}\end{aligned} \tag{6.63}$$

Since $\delta_c^{\mu} \to 0$, providing the magnetic field in LHCb is reversed. See Table D.1. δ_c^{π} is the primary source of pollution in the measurement of A_{fs}.

With the event selection reported in Sec. 6.2 the detector asymmetries are calculated from the MC Truth information to be $\delta_c^s = +(0.1 \pm 2.2) \times 10^{-2}$ and $\delta_c^d = +(2.5 \pm 2.1) \times 10^{-2}$ overall. These agree with each other, and with the expected asymmetry, however, with only a few thousand events selected this has a large statistical error.

Measurement of the pion reconstruction asymmetry as in Sec. 6.4.1 can potentially measure this asymmetry to a good statistical significance, however, it is still likely that the statistical and systematic errors on this measurement will effect the measurement of a_{fs}. The detector asymmetry can, however, be controlled by considering the decays $B_s^0 \to D_s^{\mp}\mu^{\pm}X^0$ and $B_d^0 \to D^{\mp}\mu^{\pm}X^0$ simultaneously, where the $D_s^{\mp}$ and $D^{\mp}$ decay to the same final state $K^-K^+\pi^{\mp}$. In this way the detector asymmetries cancel and the physics asymmetries can be measured. This subtraction method is further discussed in Sec. 6.6.

6.5 Monte Carlo study of asymmetric backgrounds

At LHC production and detection asymmetry will not only be observable in signal modes, but in all particles. This means backgrounds will also be asymmetric. We

define a background asymmetry as:

$$\delta_b^i = \frac{N(\text{Bg in } \bar{f}^i)}{N(\text{Bg in } f^i)} - 1 = \frac{\bar{b}^i}{b^i} - 1$$
$$(1 + \delta_b^i) = (1 + \delta_{c,b}^i)(1 + \delta_{p,b}^i) \tag{6.64}$$

which will be different for each signal mode i, and should be considered different for each background category. Background asymmetry is further discussed in Appendix C. With triggering and selection applied, background is expected to be dominated by inclusive-$b\bar{b}$ events. Table C.3 lists the expected production asymmetry for many particles, which will be modified by the detector asymmetry for the final states examined.

6.5.1 Application to the study of a_{fs}

In the fully hadronic mode, $B_s^0 \to D_s^\pm \pi^\mp$, the final state is charge-symmetric. In this mode the detector asymmetry is expected to closely cancel. The background asymmetry will also be small. Combinatoric background from real $D_s^\pm \pi^\mp$ will still, however, be asymmetric due to the production asymmetry in $D_s^\pm$ and $\pi^\mp$. This will be the dominant source of background asymmetry in this mode and can be measured simply in the B_s^0 mass distribution. Asymmetry in real $D_s^\pm \pi^\mp$ is expected to be $\delta_b^{D_s^\pm \pi^\mp} \sim \delta_p^\pi - \delta_p^{D_s} \sim -(0.6 \pm 1.1) \times 10^{-3}$ from Table C.3.

In the semileptonic modes $B_q^0 \to D_q^\mp \mu^\pm \nu$, all backgrounds are expected to be asymmetric. For example the number of fake muons which result from pion punch-through will be asymmetric due to the pion interaction asymmetry. The asymmetry is also expected to be different for $q = s, d$. The dominant background is expected to be from real $D_q^\pm$ combined with real $\mu^\mp$ in an inclusive-$b\bar{b}$ event. This background would enter with an asymmetry $\delta_b^{D_q^\pm \mu^\mp} \sim -\delta_c^\pi - \delta_p^\mu - \delta_p^{D_q}$. Which is
$\delta_b^{D_s \mu} \sim +(1.34 \pm 0.2) \times 10^{-2}$ and $\delta_b^{D\mu} \sim +(1.00 \pm 0.2) \times 10^{-2}$. The background

asymmetry term in the determination of A_{fs}, from Eqn. 6.40, is then:

$$A_B^s = (2.28 \pm 0.34(stat) \pm 0.80(br)) \times 10^{-3} \quad (6.65)$$

$$A_B^d = (1.84 \pm 0.37(stat) \pm 0.19(br)) \times 10^{-3} \quad (6.66)$$

for use in Sec. 6.6 we note that the difference between these parameters is given by:

$$\Delta A_B^{s,d} = A_B^s - A_B^d = (4.4 \pm 5.0(stat) \pm 8.2(br)) \times 10^{-4} \quad (6.67)$$

From the candidates chosen in the selection which is reported in Sec. 6.2 the background asymmetry is consistent with zero, with a large statistical error. Namely: $\delta_b^s = +0.18 \pm 0.10$ and $\delta_b^d = -0.15 \pm 0.08$. A background sample with 100-times the relative integrated luminosity would be required for a direct comparison.

6.5.2 Fitting for the peaking background

It is important to precisely measure any background asymmetry, as it can bias a_{fs} (as shown in Eqn. 6.40). In the semileptonic modes this is not easy due to the peaking backgrounds, however, it is still possible if the shapes of the signal and the background can be adequately separated in a multidimensional analysis.

To extract the signal and background simultaneously, a two dimensional fit is performed ($D_q^{\pm}$-mass, B_q^0-mass), maximising the log likelihood.

It has been observed, from the Monte Carlo (Fig. 6.7), that the peaking backgrounds are peaking under the $D_q^{\pm}$ mass peaks, but are exponential in the B_q^0-mass distribution. In Sec. 6.2.1 we extend the upper range of the B_q^0-mass cuts to obtain a sideband, which allows us to fit for the peaking background contribution.

Generic shapes are used for signal and background distributions, which are expected from the shapes in the Monte Carlo distributions, phase-space arguments, and

previous experimental fits. The real $D_q^{\pm}$-contributions in the $D_q^{\pm}$-mass spectrum are fit with Crystal Ball functions.[13] The background distribution of $D_q^{\pm}$-masses are fit to second-order Chebychev polynomials. The distribution of B_q^0-masses for signal and background from real b-tracks are fit with Argus functions, all other contributions are fit with an exponential function. There are 21 free parameters.

6.5.2.1 Toy studies

The LHCb Monte Carlo is complex and takes considerable computational time to generate event samples. With the samples that are available it is difficult to assess the reliability of statistical errors in fits for physics parameters. It is similarly difficult to examine correlations, biases, and fit results under a range of input parameters as each would require a separate simulation. Instead the key parameters[14] can be extracted from the full Monte Carlo distribution and used to construct a 'toy' study. Reduced probability distribution functions (pdf) are used to describe the parameters used in the fit model. Generation and fitting to the toy pdf is much faster as a full detector simulation is not required.

To quantify the fit stability and gain confidence over the statistical errors many hundreds of toy experiments are required. We perform a range of toy studies in Sec. 6.6, here we perform a single toy experiment to demonstrate the principle of the fit for the background fractions. In Fig. 6.12 the initial mass pdfs are plotted, with arbitrary initial parameters, from which a simple toy is fitted and generated. A fit to the full Monte Carlo data, and the MC truth information are also shown. In this case the key fit parameters are the extracted number of signal and background events, specifically the peaking backgrounds. There are large statistical errors from the small $b\bar{b}$-inclusive sample available; however, good agreement is obtained.

To demonstrate the statistical errors in this fit, a single toy study with 400k events is shown in Fig. 6.13 generated from the central values of the fit to MC data.

[13] An equally adequate fit is found with a single Gaussian function to each peak.
[14] For example, see Table F.1.

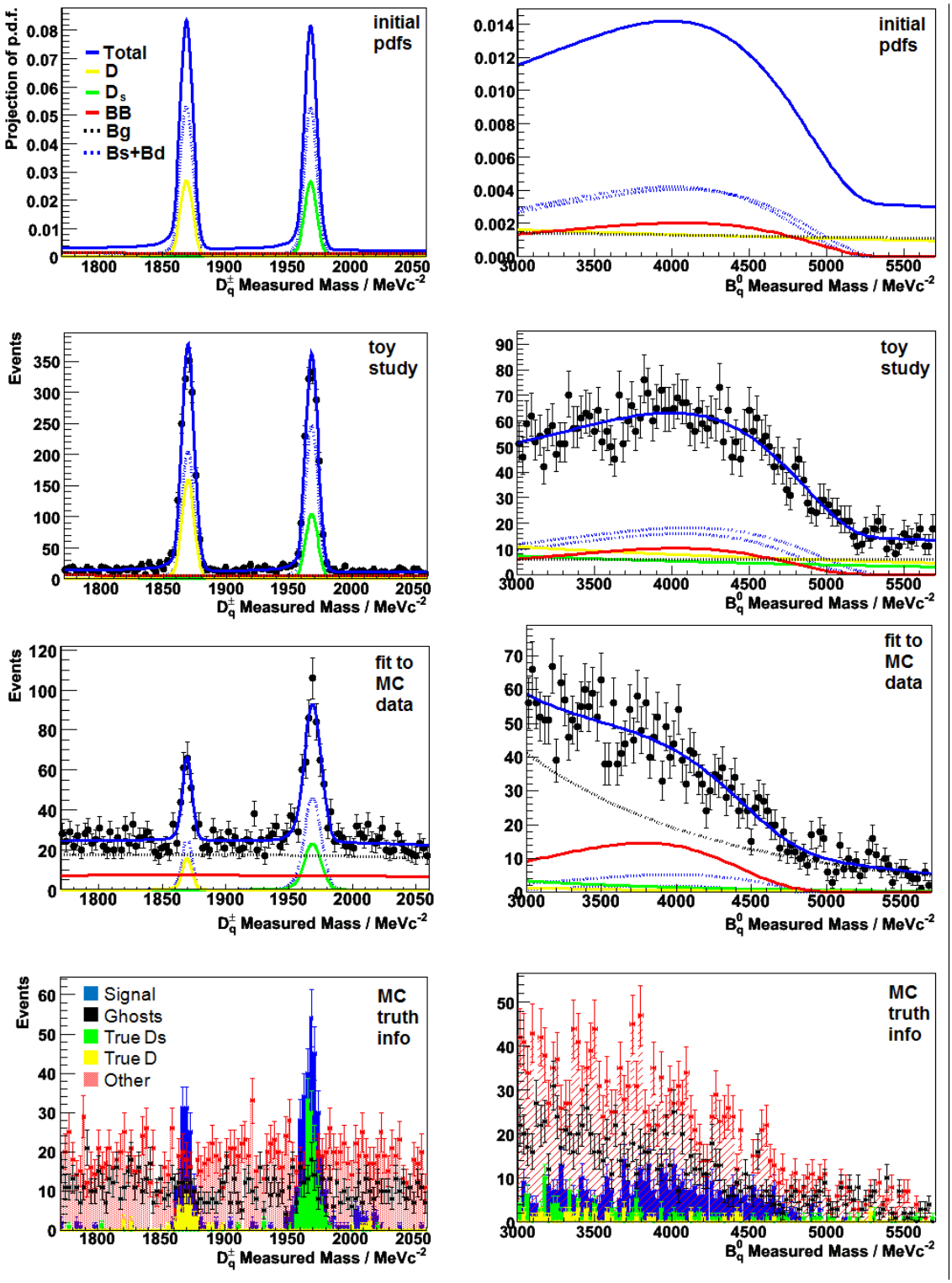

Figure 6.12: Multidimensional fit to extract peaking background in the $b\bar{b}$-sample. Left, the $D_q^{\pm}$-mass spectrum. Right, the B_q^0-mass spectrum. From top to bottom: the initial pdfs, a single toy study, a fit to the full Monte Carlo data, the MC Truth information. The fitted signal and background fractions are consistent with the MC Truth within 1σ.

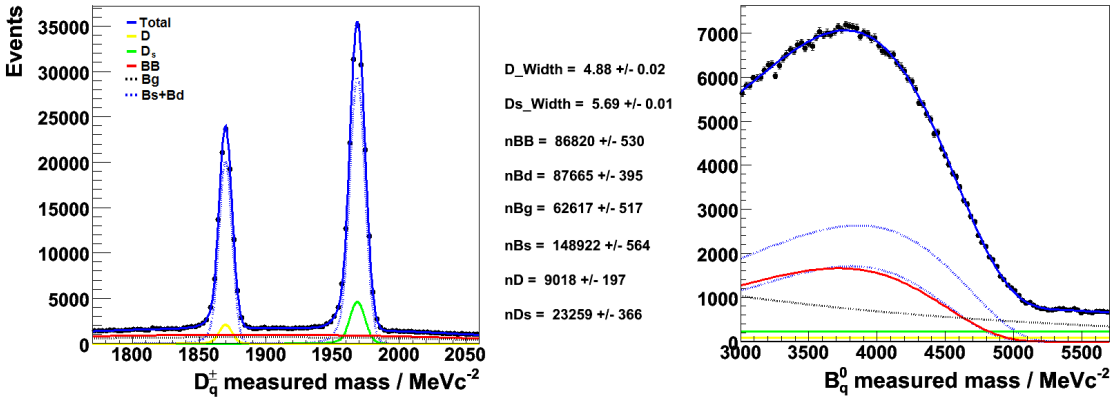

Figure 6.13: Toy study of peaking background, in 400k events. Left, the generation and fit to the $D_q^{\pm}$-mass spectrum. Right, the generation and fit to the B_q^0-mass spectrum. The widths of the two mass peaks, and the fractions of different signal and background types are explicitly written to show the errors. The input and fit values are consistent within 2σ.

6.5.3 Determining the background asymmetry

Fitting simultaneously for the background in the opposite flavours will enable extraction of the background asymmetry from the data. A three dimensional fit is required ($D_q^{\pm}$-mass, B_q^0-mass, final state flavour). This can then be followed by a second three dimensional fit to extract the flavour specific asymmetries ($D_q^{\pm}$-mass, proper time, final state flavour) as in Sec. 6.6. For 400k simulated events in a simple toy study, the statistical errors on the background asymmetry fits are:

$$\frac{\sigma\left(\delta_b^s\right)}{\delta_b^s} = 0.011 \qquad \frac{\sigma\left(\delta_b^d\right)}{\delta_b^d} = 0.010 \tag{6.68}$$

The polluting terms in the measurement of A_{fs}^q, Eqn. 6.40 should also be well-measured, the expected statistical errors are:

$$\frac{\sigma\left(A_B^s\right)}{A_B^s} = 0.015 \qquad \frac{\sigma\left(A_B^d\right)}{A_B^d} = 0.013 \tag{6.69}$$

Fitting for the background asymmetry will get gradually more complicated as new peaking backgrounds are identified. Currently the background types and shapes are not well known and could benefit from further study.

To successfully apply this fit technique to real data we need to reduce the pol-

lution from the background asymmetry as much as possible, which can be done through subtraction of the measurements in two channels: $B_s^0 \to D_s^{\mp}\mu^{\pm}\nu_\mu$ and $B_d^0 \to D^{\mp}\mu^{\pm}\nu_\mu$, as is reported in Sec. 6.6. The remaining background asymmetry will be determined by the difference in A_B^s and A_B^d, Eqns. 6.65 to 6.67, which we have previously introduced as $\Delta A_B^{s,d}$. Due to the small numerical value of this residual asymmetry, order 10^{-4}, its overall statistical error is quantified by:

$$\sigma\left(\Delta A_B^{s,d}\right) \approx 4 \times 10^{-5} \tag{6.70}$$

from the above fit to 400k events, depending on the central values of B/S and δ_b.

The background asymmetries are fitted simultaneously in the extraction of the flavour-specific asymmetries as appears in Sec. 6.6 and Appendix F, where a full selection of toy studies is discussed including the variation of input parameters.

6.6 Subtraction method

Measuring δ_p^q, δ_c^q, and a_{fs}^q from the same untagged channel is not possible. If one uses a control channel to extract δ_c^q a measurement of a_{fs}^q and δ_p^q can then be performed. With the combined selection presented in Sec. 6.2, the most attractive channel to control $B_s^0 \to D_s^{\mp}\mu^{\pm}\nu_\mu X^0$ is $B_d^0 \to D^{\mp}\mu^{\pm}\nu_\mu X^0$ and visa-versa. We restrict the $D_s^{\mp}$ and $D^{\mp}$ decays to the same final state, $D_s^{\mp}, D^{\mp} \to K^+K^-\pi^{\mp}$, so that the detector asymmetry in these two channels will be equal. The remaining asymmetries can then be fitted. The simplest way to see this is to naïvely subtract the two rates.

6.6.1 A naïve subtraction

Let us examine the time-independent part of $A_{fs}^q(t)$ given in Eqn. 6.40 which we will call $A_{fs,t}^{b,q}$. The term $A_{fs,t}^{b,q}$ has no contribution from the production asymmetry or time resolution, but is dependent on the charge asymmetry, the background

asymmetry, and the background to signal ratio B/S:

$$A^{b,q}_{fs,\not{t}} \approx \frac{a^q_{fs}}{2} - \frac{\delta^q_c}{2} + A^q_B \tag{6.71}$$

Measuring simultaneously the flavour-specific asymmetry for both $B^0_s \to D^{\mp}_s(K^+K^-\pi^{\mp})\mu^{\pm}\nu_\mu$ and $B^0_d \to D^{\mp}(K^+K^-\pi^{\mp})\mu^{\pm}\nu_\mu$ now provides a means of removing the error from charge asymmetry. We can measure the quantity:

$$\begin{aligned}\Delta A^{s,d}_{fs} &= A^{b,s}_{fs,\not{t}} - A^{b,d}_{fs,\not{t}} = \frac{\delta^d_c}{2} - \frac{\delta^s_c}{2} + \frac{a^s_{fs}}{2} - \frac{a^d_{fs}}{2} + A^s_B - A^d_B \\ &\approx \frac{a^s_{fs}}{2} - \frac{a^d_{fs}}{2} + \Delta A^{s,d}_B \to \frac{a^s_{fs}}{2} - \frac{a^d_{fs}}{2}\end{aligned} \tag{6.72}$$

From Eqns. 1.36 and 1.37 the SM prediction for this parameter is calculated to be $\Delta A^{s,d}_{fs}|^{SM} = (2.503^{+0.501}_{-0.601}) \times 10^{-4}$, and could be enhanced by an order of magnitude by arbitrary NP contributions. $\Delta A^{s,d}_B$ is expected be small and may be well-measured in the data, using multidimensional techniques, as in Sec. 6.5.2.

6.6.2 Momentum distributions of selected hadrons

A clean cancellation of δ^s_c and δ^d_c requires the pion and kaon momenta distributions in the $D^{\pm}_q$-decays to be equal. If one of these distributions shows a significant difference, a correction may be performed by re-weighting. The momentum distributions for the truth-matched hadron candidates after preselection are given in Fig. 6.14. All the distributions are shown to agree between the two channels. This study should be repeated with real data as it becomes available.

6.6.3 Fit model with the subtraction method.

The fitting package RooFit [136] from within the ROOT [127] data analysis framework is used. The fit model is a product pdf formed from the mass fit model given in Sec. 6.5.2, and a proper time distribution. There are four observable parameters in this multidimensional pdf: the proper time of the B^0_q-decay, the flavour of the

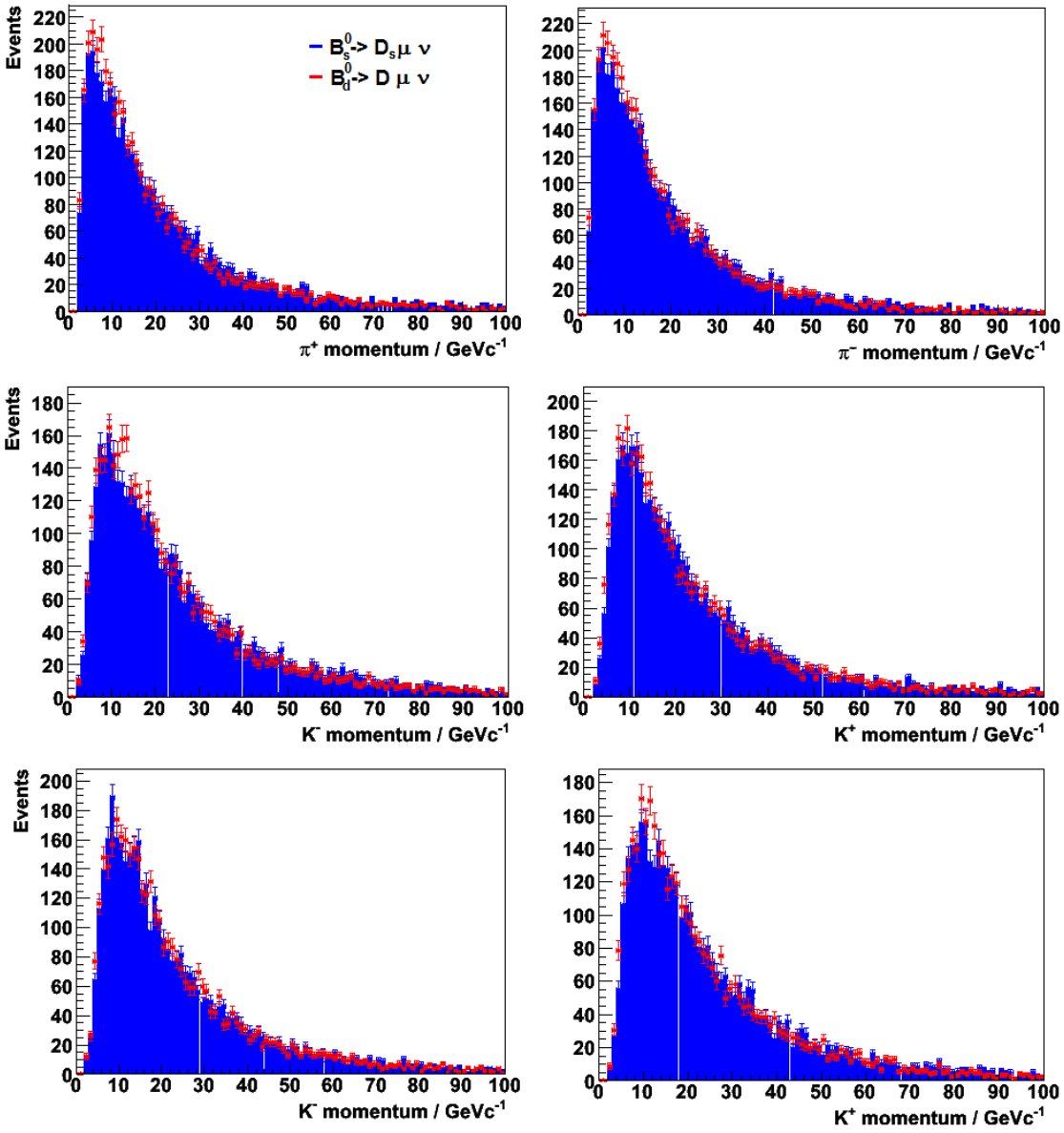

Figure 6.14: Momentum distribution of preselected truth-matched hadron candidates. Top for $\pi^{\pm}$, middle and bottom for $K^{\pm}$, normalised to the same number of events. Left, and right separate charge conjugate decays. The two kaon distributions for each mode are given separately. The distributions in red for B_s^0 decays and in blue for B_d^0 decays are seen to overlap almost exactly.

final state, the B_q^0-mass and the $D_q^{\pm}$-mass.

The proper time distribution is the combination of a decay-rate model, a resolution model and a proper-time acceptance model. The decay-rate pdf and the resolution model are analytically convolved, as given in Eqn. 6.40. The acceptance function is a time-dependent efficiency which is multiplied with the decay rate model.

The fit is performed in two stages. Firstly the mass shapes, background fractions and background asymmetries are directly fitted from the reduced parameter space of the mass distributions and the final state flavour. The shape parameters, asymmetries and fractions are then fixed, allowing the flavour-specific asymmetries to be extracted from a fit to the proper time distributions.[15] We generate the data from the full PDF and fit to two reduced PDFs. Each is a three-dimensional fit: B-mass, D-mass and final state flavour for the first stage, D-mass, proper time and final state flavour for the second stage.

6.6.3.1 Decay rate parameterisation.

We fit directly to the time-dependent rates, $\Gamma(f)$ and $\Gamma(\bar{f})$:

$$\begin{aligned}
\Gamma(f) =& Ne^{-\Gamma t}(1+A_c)\left[(1+a_{fs})\cosh\left(\frac{\Delta\Gamma t}{2}\right)+(2A_p-a_{fs})\cos(\Delta m t)\right] \\
\rightarrow& Ne^{-\Gamma t}\left[(1+A_c+a_{fs})\cosh\left(\frac{\Delta\Gamma t}{2}\right)+(2A_pA_c+2A_p-a_{fs})\cos(\Delta m t)\right] \\
\Gamma(\bar{f}) \rightarrow& Ne^{-\Gamma t}\left[(1-A_c-a_{fs})\cosh\left(\frac{\Delta\Gamma t}{2}\right)+(2A_pA_c+a_{fs}-2A_p)\cos(\Delta m t)\right]
\end{aligned}$$

[15] We are required to perform a two stage fit, as a B-mass constraint is used in the calculation of the proper time distribution.

where N is a normalisation constant and terms of order $a_{fs}\delta_i$ have been ignored. Due to the coupling between a_{fs}, A_c and A_p, the finite statistics and the finite time resolution, a simultaneous fit to these three parameters will not converge. However, this expression can be re-parameterised as:

$$\Gamma(f) = Ne^{-\Gamma t}\left[(1+x_1)\cosh\left(\frac{\Delta\Gamma t}{2}\right) + (x_2+x_3)\cos(\Delta m t)\right] \tag{6.73}$$

$$\Gamma(\bar{f}) = Ne^{-\Gamma t}\left[(1-x_1)\cosh\left(\frac{\Delta\Gamma t}{2}\right) + (x_2-x_3)\cos(\Delta m t)\right] \tag{6.74}$$

$$\text{where: } x_1 = A_c + a_{fs} \qquad x_2 = 2A_cA_p \qquad x_3 = 2A_p - a_{fs} \tag{6.75}$$

The three terms x_1, x_2 and x_3 are manifestly uncorrelated from each other, allowing x_1 to be fitted in the absence of information on x_2 and x_3. Now subtracting x_1 in the two channels gives us the physics quantity we would like to measure:

$$\Delta A_{fs}^{s,d} = \frac{x_1^s}{2} - \frac{x_1^d}{2} \rightarrow \frac{a_{fs}^s}{2} - \frac{a_{fs}^d}{2} \tag{6.76}$$

We can fit for x_1^s and x_1^d independently, or fit for $\Delta A_{fs}^{s,d}$ and either x_1^s or x_1^d. The proper time resolution dilutes the sensitivity to the cosine term, but does not influence the sensitivity to x_1. In this pdf it would also be possible to fit for Γ, $\Delta\Gamma$, and even Δm providing the time resolution is good enough, however they do not influence the $\Delta A_{fs}^{s,d}$ fit, therefore we set them constant in this study and assume they are measured elsewhere. The influence of possible biases resulting from this approach will be investigated in Sec. 6.6.4.3.

6.6.3.2 Proper time acceptance function.

The proper time acceptance function is modelled with a power law of the form:

$$\epsilon_t = N\frac{(C(t-t_0))^P}{1+(C(t-t_0))^P} \tag{6.77}$$

N is a normalisation term, representing the maximum reachable efficiency. C is a term governing the slope and scale of the acceptance function, and P determines its

form. This is identical to what is used in many analyses, e.g. Ref. [5] and Sec. 9.3.2 in Ref. [31]. From these studies we set $C = 1.29\,\mathrm{ps}^{-1}$ and $P = 3$. We use a range of central values for C, to test the fit stability, as described later in this Chapter.

6.6.3.3 Background model.

The background model used is based on MC studies. To be clear, there are a few parameters whose meaning is undefined in the background (for example proper time acceptance and resolution), and there are a few parameters for which the current statistics available from DC06 Monte Carlo production are insufficient to provide a sufficient constraint (such as the proper time distributions of different categories of background). We therefore select generic models for the types of background investigated in Sec. 6.5.2. For all backgrounds we use the same proper time acceptance and resolution as the signal. We apply a B-lifetime to all but the combinatoric background, which is assumed to have a lifetime $\sim 0.1\,\mathrm{ps}$. Peaking and combinatoric backgrounds are each assigned their own background asymmetry, as is discussed in Sec. 6.5. For this toy study we perform experiments with a range of B/S values and a range of central values for the fit parameters.

6.6.4 Toy studies of LHCb sensitivity to $\Delta A_{fs}^{s,d}$

A range of toy studies were performed to investigate the sensitivity to $\Delta A_{fs}^{s,d}$ and the stability of the fit under a range of input parameters. The results are presented here, with further results given in Appendix F where necessary.

The input values for mass shape parameters and background proportions were taken from fits to Monte Carlo data. These parameters can be extracted from the first stage of fitting to the data. The pull distribution of these will be presented in Table F.1 of Appendix F. The input values from physically measured parameters that are kept constant in the fit are given in Table 6.7. In each case it is assumed these parameters will be well measured in other channels or taken from other

Table 6.7: Constant input parameters for toy study that are set constant, taken from Refs. [5, 31, 13].

Name	symbol	value	error	unit
$\boldsymbol{B_d^0}$:				
lifetime	τ_d	1.530	± 0.009	ps
width difference	$\Delta\Gamma_d/\Gamma_d$	0.0	± 0.2	
mass	M_d	5279.4	± 0.3	MeVc^{-2}
mass difference	Δm_d	0.507	± 0.005	ps^{-1}
$\boldsymbol{B_s^0}$:				
lifetime	τ_s	1.425	± 0.041	ps
width difference	$\Delta\Gamma_s/\Gamma_s$	0.069	$^{+0.058}_{-0.062}$	
mass	M_s	5367.5	± 0.6	MeVc^{-2}
mass difference	Δm_s	17.77	± 0.12	ps^{-1}
$\boldsymbol{D_q^{\pm}}$:				
$D^{\pm}$-mass	$M(D^{\pm})$	1869.3	± 0.2	MeVc^{-2}
$D_s^{\pm}$-mass	$M(D_s^{\pm})$	1968.5	± 0.3	MeVc^{-2}
time resolution† :				
signal	$\sigma(\tau)_{sig}$	0.270		ps
background	$\sigma(\tau)_{bg}$	0.500	estimate	ps
comb'l background:				
lifetime‡	τ_{Bg}	0.1	estimate	ps
Acceptance*:				
	t_0	0.0		ps
	C	1.29		ps^{-1}
	P	3.0		

† The time resolution depends on the reconstruction method used, and the missing mass of the reconstructed B-candidate. A few central values were used from 0.12-0.5 ps.

‡ estimate only. A few central values were used from 0.1-3 ps.

* $\epsilon = [C(t-t_0)]^P/[1+\{C(t-t_0)\}^P]$, from the LHCb TDR [31] and Ref. [5].

experiments. Many of these parameters were varied as discussed later in this Chapter. Firstly a toy study was performed with 500 experiments and 1M signal events per experiment at the nominal input values.

6.6.4.1 Nominal fit results.

The nominal input and fit values for the asymmetry parameters are given in Table 6.8, for the 500 experiments performed, each with 1M signal events. Due to the coarse proper time resolution applied, some of the x-parameters cannot be extracted from the nominal fit. The fit and pull distributions of $\Delta A_{fs}^{s,d}$ are given in Figs. 6.15 and 6.16. A Gaussian curve is fitted to the $\Delta A_{fs}^{s,d}$ and pull distribution. The fit is well behaved, the bias of the pull distribution is consistent with zero, and the width is consistent with unity. All other pull distributions, and the correlations

Table 6.8: Input asymmetry parameters for toy study and output from a nominal fit with 500 toys, each with 1M signal events.

Parameter		Input	Output		Scale	Pull / σ	
Name	symbol	value	mean fit value	mean fit error		bias	width
backgrounds:							
comb'l	δ_b^c	$+1.59 \pm 0.2$	$+1.61 \pm 0.49$	0.49 ± 0.04	$\times 10^{-2}$	$+0.051 \pm 0.049$	1.007 ± 0.036
Real $D^{\pm}$	δ_b^d	$+1.00 \pm 0.2$	$+1.09 \pm 0.14$	2.50 ± 0.01	$\times 10^{-2}$	$+0.042 \pm 0.059$	1.217 ± 0.042
Real $D_s^{\pm}$	δ_b^s	$+1.34 \pm 0.2$	$+1.45 \pm 0.09$	1.70 ± 0.01	$\times 10^{-2}$	$+0.069 \pm 0.051$	1.035 ± 0.036
production:							
B_d^0	δ_p^d	-3.2 ± 0.5	---†		$\times 10^{-3}$	---†	
B_s^0	δ_p^s	-1.5 ± 0.8	---†		$\times 10^{-3}$	---†	
detector:	δ_c	$+1.37 \pm 0.01$	---†		$\times 10^{-2}$	---†	
physics:							
B_d^0	a_{fs}^d	$-4.8^{+1.0}_{-1.2}$	---†		$\times 10^{-4}$	---†	
B_s^0	a_{fs}^s	$+2.06 \pm 0.57$	---†		$\times 10^{-5}$	---†	
x_i^q**-parameters**:		(calculated)					
	x_1^d	-7.28	-7.33 ± 0.10	2.131 ± 0.001	$\times 10^{-3}$	-0.020 ± 0.049	1.008 ± 0.035
	x_1^s	-6.78	---†		$\times 10^{-3}$	---†	
	x_2^d	-2.18	---‡		$\times 10^{-5}$	---‡	
	x_2^s	-1.02	---‡		$\times 10^{-5}$	---‡	
	x_3^d	$+3.68$	$+1.76 \pm 0.30$	6.320 ± 0.001	$\times 10^{-3}$	-0.035 ± 0.047	0.978 ± 0.034
	x_3^s	$+1.48$	---‡		$\times 10^{-3}$	---‡	
	$\Delta A_{fs}^{s,d}$	$+2.503^{+0.501}_{-0.601}$	$+2.42 \pm 0.61$	12.69 ± 0.01	$\times 10^{-4}$	-0.006 ± 0.048	0.976 ± 0.036

† this is not a directly fitted parameter. ‡ no sensitivity.

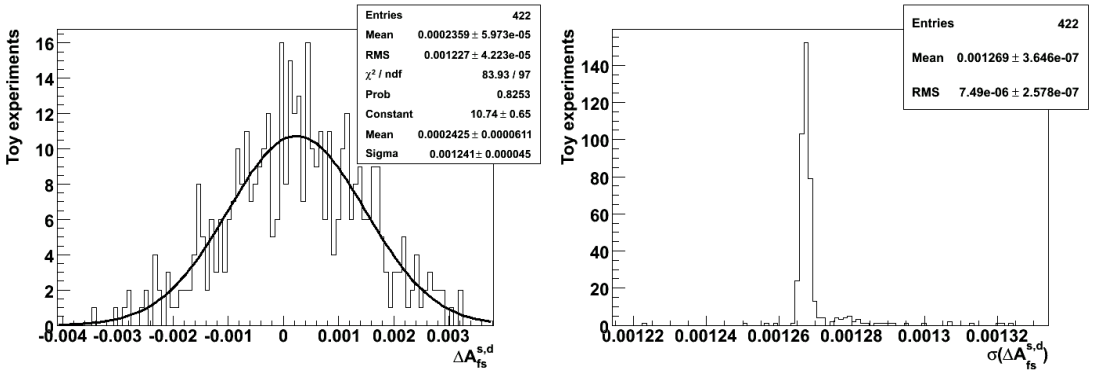

Figure 6.15: Distribution of $\Delta A_{fs}^{s,d}$ in nominal toy study, 500 toys, 1M signal events per toy. Left, the distribution of $\Delta A_{fs}^{s,d}$. A Gaussian curve is fitted to the distribution. The Gaussian mean is consistent with the arithmetic mean, and the Gaussian sigma is consistent with the error returned from the fit. Right, distribution of the error returned from the fit.

between all fit parameters, are discussed in Appendix F. $\Delta A_{fs}^{s,d}$, x_1^d and x_3^d, can be measured in the nominal fit. The measurement of x_3^d can be used as a measurement of the production asymmetry in B_d^0 with a precision of $\sim 6{\times}10^{-3}$, providing a_{fs}^d is ignored. A similar measurement cannot be made of x_3^s as the time resolution of 270 fs is insufficient to resolve the fast Δm_s oscillations.

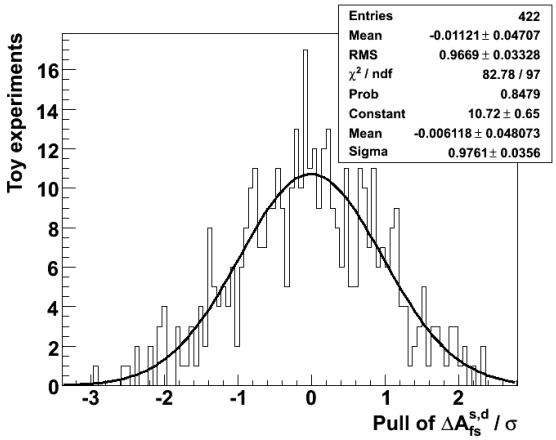

Figure 6.16: Pull distribution of $\Delta A_{fs}^{s,d}$ in nominal toy study, 500 toys, 1M signal events per toy. A Gaussian curve is fitted to the pull distribution. The bias is consistent with zero, and the width is consistent with unity.

6.6.4.2 Stability to parameter variations.

A series of different input parameters were used to test the stability of the fit model. The results of the toy studies are summarized in Table 6.9. The fit results for $\Delta A_{fs}^{s,d}$ are shown in each case to demonstrate the central input value is recovered.

As can be seen in Table 6.9 the variation of most parameters produces no residual bias or change in the fit error. Increasing the background fraction increases the fit error slightly. This should be avoided nevertheless, as new background modes could enter the selection with different asymmetries and shapes. In the case of very large values of a_{fs}^{d}, a significant fit bias is seen that brings $\Delta A_{fs}^{s,d}$ closer to zero. In the expected region of $a_{fs}^{q} \leq 10^{-3}$ (even with large NP contributions) this bias is quite manageable and will contribute a small systematic error. The statistical significance of the $\Delta A_{fs}^{s,d}$ measurement is not improved substantially by better time resolution. However, better resolution allows the fitting of x_3^s. With $\sigma_\tau = 120\,\text{fs}$, x_3^s can be fitted with a statistical precision of $(3.80 \pm 0.01)\times 10^{-2}$ in 1M signal events. We note that this fit model assumes one resolution for all events, in reality the time resolution will be a function of the missing mass taken by the neutrino and the X^0 system [5, 129]. With correct parameterisation and proper time calculation we believe sensitivity to x_3^s can also be achieved in the data [137].

Table 6.9: $\Delta A_{fs}^{s,d}$ fits with various input parameter values. Each study was performed with 500 toys, each with nominally 1M signal events.

Varied parameter			$\Delta A_{fs}^{s,d} \times 1000$			$\Delta A_{fs}^{s,d}$ Pull / σ	
Name	symbol	value	input	mean fit value	mean fit error	bias	width
–None–			$+0.2503$	$+0.242 \pm 0.061$	1.269 ± 0.001	-0.01 ± 0.05	0.976 ± 0.036
Total	B/S	0.1	$+0.2503$	$+0.316 \pm 0.091$	1.220 ± 0.001	$+0.05 \pm 0.07$	0.996 ± 0.063
Background		1	$+0.2503$	$+0.153 \pm 0.069$	1.380 ± 0.003	-0.08 ± 0.05	0.981 ± 0.035
		2	$+0.2503$	$+0.114 \pm 0.087$	1.583 ± 0.001	-0.07 ± 0.06	0.907 ± 0.044
Peaking	B/S	0.5	$+0.2503$	$+0.229 \pm 0.063$	1.267 ± 0.001	-0.01 ± 0.05	1.000 ± 0.035
Background		1	$+0.2503$	-0.002 ± 0.088	1.524 ± 0.008	-0.18 ± 0.05	0.941 ± 0.040
Signal	$\frac{f(B_s^0)}{f(B_d^0)}$	4	$+0.2503$	$+0.285 \pm 0.063$	1.576 ± 0.001	$+0.02 \pm 0.06$	1.040 ± 0.040
Fractions		0.25	$+0.2503$	$+0.228 \pm 0.072$	1.427 ± 0.001	-0.02 ± 0.05	0.974 ± 0.038
Comb'l	τ_{Bg}	1.5 ps	$+0.2503$	$+0.096 \pm 0.061$	1.219 ± 0.002	-0.14 ± 0.05	1.021 ± 0.035
lifetime		3.0 ps	$+0.2503$	$+0.365 \pm 0.053$	1.281 ± 0.002	$+0.08 \pm 0.05$	0.947 ± 0.033
time	$\sigma(\tau)$	0.12 ps	$+0.2503$	$+0.292 \pm 0.063$	1.246 ± 0.001	$+0.02 \pm 0.06$	0.986 ± 0.041
resolution		0.50 ps	$+0.2503$	$+0.342 \pm 0.073$	1.293 ± 0.001	$+0.08 \pm 0.05$	1.000 ± 0.045
Lifetime	$\frac{\Delta\Gamma^{d,s}}{\Gamma^{d,s}}$	+0.1, -0.1	$+0.2503$	$+0.181 \pm 0.086$	1.526 ± 0.005	-0.05 ± 0.06	1.039 ± 0.040
difference		-0.1, +0.1	$+0.2503$	$+0.224 \pm 0.059$	1.261 ± 0.001	-0.02 ± 0.05	0.989 ± 0.035
		-0.1, -0.1	$+0.2503$	$+0.234 \pm 0.075$	1.269 ± 0.001	-0.01 ± 0.06	1.059 ± 0.035
	a_{fs}^s	+0.01	$+5.24$	$+5.188 \pm 0.062$	1.269 ± 0.001	-0.04 ± 0.05	0.978 ± 0.038
		-0.01	-4.96	-4.786 ± 0.066	1.269 ± 0.005	-0.02 ± 0.04	0.893 ± 0.038
	a_{fs}^d	+0.01	-4.99	-4.752 ± 0.066	1.269 ± 0.001	$+0.19 \pm 0.06$	1.064 ± 0.045
		-0.01	$+5.01$	$+4.774 \pm 0.093$	1.267 ± 0.001	-0.19 ± 0.05	1.064 ± 0.033
Background	δ_b^i	$\times$ 10	$+0.2503$	$+0.669 \pm 0.082$	1.268 ± 0.001	$+0.33 \pm 0.07$	1.029 ± 0.051
asymmetries		$\times$ -10	$+0.2503$	$+0.194 \pm 0.075$	1.259 ± 0.002	-0.04 ± 0.06	1.077 ± 0.043
Production	δ_p^i	$\times$ 10	$+0.2503$	$+0.170 \pm 0.066$	1.256 ± 0.003	-0.03 ± 0.03	1.034 ± 0.041
asymmetries		$\times$ -10	$+0.2503$	$+0.265 \pm 0.073$	1.236 ± 0.006	$+0.00 \pm 0.059$	1.005 ± 0.042
Detector	δ_c	+0.05	$+0.2503$	$+0.045 \pm 0.063$	1.269 ± 0.001	$+0.13 \pm 0.05$	0.998 ± 0.036
asymmetry		-0.05	$+0.2503$	-0.074 ± 0.058	1.269 ± 0.001	-0.26 ± 0.05	0.949 ± 0.034
Proper time	C	1.0 ps^{-1}	$+0.2503$	$+0.215 \pm 0.050$	1.204 ± 0.002	-0.03 ± 0.04	0.966 ± 0.034
acceptance		1.5 ps^{-1}	$+0.2503$	$+0.265 \pm 0.052$	1.296 ± 0.001	$+0.01 \pm 0.05$	0.977 ± 0.037

6.6.4.3 Stability to parameter biases.

Fit biases can be directly introduced in two places: from poorly measured parameters taken from control channels and previous experiments (e.g. $\Delta\Gamma_s$), or from biases in the first stage of the fit process that are carried over to the second fit stage (e.g. the fraction of background in the sample). A selection of these parameters were explicitly biased to investigate the influence on the fit of $\Delta A_{fs}^{s,d}$. The results are given in Table 6.10. Here we can see the benefits of the subtraction method. Biases in the background fractions and asymmetries produce very small biases in $\Delta A_{fs}^{s,d}$, up to $\Delta A_B^{s,d}$, which is likely to be of order 10^{-4} (from Sec. 6.5).

6.6.4.4 Scaling with integrated luminosity.

A summary of the sensitivity for different sample sizes is given in Table 6.11. The sensitivity to $\Delta A_{fs}^{s,d}$ scales with the square root of the number of events, as expected. In $2\,\text{fb}^{-1}$ $(4.05 \pm 0.91) \times 10^6$ signal events are expected. Scaling to this event size we expect an sensitivity of $\sigma(2\,\text{fb}^{-1}) = (6.31 \pm 0.71) \times 10^{-4}$ in one nominal year. From the condition in Ref. [114] and Sec. 6.1.3, that the experimental error on a_{fs}^s should be at or below $|\Gamma_{12}^s/M_{12}^s| \approx 5 \times 10^{-3}$, this precision will already place constraints on new physics. Over the lifetime of LHCb $10\,\text{fb}^{-1}$ is expected, which will reduce this error to $\sigma(10\,\text{fb}^{-1}) = (2.82 \pm 0.32) \times 10^{-4}$ which provides sensitivity to moderate new physics contributions in B_s^0-mixing.

Table 6.10: $\Delta A_{fs}^{s,d}$ fits with induced fit biases. Each study was performed with 500 toys, each with 1M signal events.

Biased parameters			$\Delta A_{fs}^{s,d} \times 1000$		$\Delta A_{fs}^{s,d}$ Pull / σ	
Name	symbol	biased value	mean fit value	mean fit error	bias	width
–None–			$+0.242 \pm 0.061$	1.269 ± 0.001	-0.006 ± 0.048	0.976 ± 0.036
Peaking backg'd fractions	$f(D^{\pm})$	0	$+0.144 \pm 0.065$	1.252 ± 0.003	-0.087 ± 0.054	1.037 ± 0.039
	$f(D_s^{\pm})$	0				
background asymmetries	δ_b^d	0	$+0.131 \pm 0.069$	1.269 ± 0.001	-0.097 ± 0.073	1.056 ± 0.040
	δ_b^s	0				
	δ_b^c	0				
lifetime difference	$\frac{\Delta\Gamma_s}{\Gamma_s}$	0	$+0.117 \pm 0.080$	1.251 ± 0.001	-0.114 ± 0.069	1.107 ± 0.052
Proper time bias	t_0	$0.05\,\text{ps}^{-1}$	$+0.139 \pm 0.072$	1.269 ± 0.001	-0.089 ± 0.057	1.057 ± 0.041

For the input parameters without bias, see Tables 6.7 and 6.8.

Table 6.11: $\Delta A_{fs}^{s,d}$ fits with different sample sizes. Each study was performed with 500 toys.

Number of signal	$\Delta A_{fs}^{s,d} \times 1000$		$\Delta A_{fs}^{s,d}$ Pull / σ	
	mean fit value	mean fit error	bias	width
100,000	$+0.044 \pm 0.163$	3.559 ± 0.001	-0.058 ± 0.046	0.953 ± 0.033
200,000	$+0.368 \pm 0.134$	2.835 ± 0.001	$+0.043 \pm 0.047$	0.989 ± 0.034
1,000,000	$+0.242 \pm 0.061$	1.269 ± 0.001	-0.006 ± 0.048	0.976 ± 0.036
2,000,000	$+0.224 \pm 0.070$	0.898 ± 0.001	-0.031 ± 0.063	1.041 ± 0.047

6.7 Summary

We have demonstrated that a precise measurement of flavour specific asymmetries is possible at LHCb, providing the systematic pollutants can be controlled. By performing a time-dependent measurement in $B_s^0 \to D_s^{\mp}\mu^{\pm}\nu_\mu$ and $B_d^0 \to D^{\mp}\mu^{\pm}\nu_\mu$ and fitting simultaneously we have asserted that the production and detector asymmetry can be eliminated allowing for the clean determination of $\Delta A_{fs}^{s,d} = (a_{fs}^s - a_{fs}^d)/2$. In the Standard Model $\Delta A_{fs}^{s,d} = (2.503^{+0.501}_{-0.601}) \times 10^{-4}$. Or alternatively, if the detector asymmetry is well-measured this allows the direct determination of a_{fs}^s and a_{fs}^d. Taking the measured value of $\Delta A_{fs}^{s,d}$ and the precise b-factory measurements of a_{fs}^d can also be used to determine a_{fs}^s, however the current b-factory error of $\sim 5 \times 10^{-3}$ will become the dominant error after only a few weeks of data taking at design luminosity.

Detailed toy studies of the $\Delta A_{fs}^{s,d}$-fit have been performed, demonstrating that the fit is robust under different input parameter sets, robust under the introduction of small biases, and able to extract the background asymmetries from the data. We have shown that if the shapes of the distributions are known and are separable in a multidimensional analysis that the background fractions and asymmetries can be extracted from the data. This manifestly depends on the correctness of the background model. The background model is therefore the single element which would benefit most from further study. To improve the background model specific backgrounds should be generated with the equivalent integrated luminosity of the current signal sample so that their shapes and asymmetries can be accurately predicted. We note, though, that for the measurement of $\Delta A_{fs}^{s,d}$, the background asymmetries are expected to mostly cancel between the two channels, and therefore systematic error contributions from the background model will be small.

With a decision-tree inspired HLT2 selection and a reoptimised offline event selection, $(2.58 \pm 0.90) \times 10^6$ $B_s^0 \to D_s^{\mp}\mu^{\pm}\nu_\mu$ and $(1.47 \pm 0.16) \times 10^6$ $B_d^0 \to D^{\mp}\mu^{\pm}\nu_\mu$ events can be selected in $2\,\text{fb}^{-1}$. The number of events used by DØ to make the current world measurement will be surpassed at LHCb in two days at design LHC luminosity

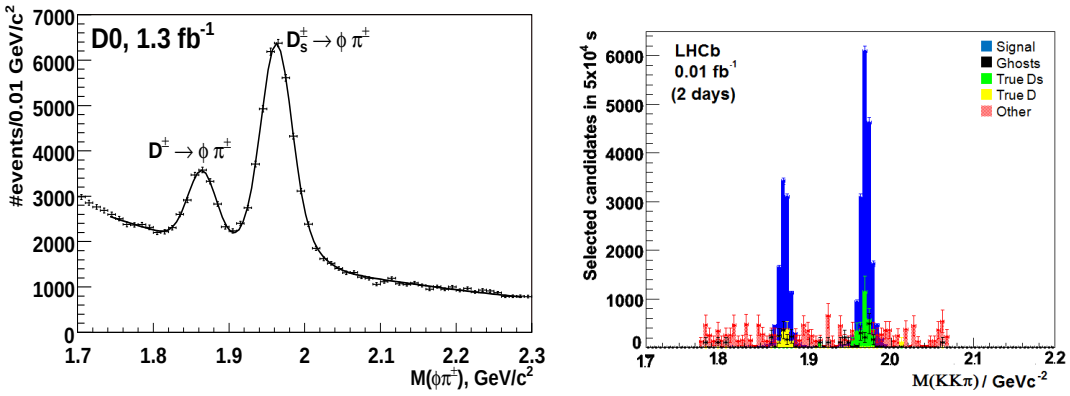

Figure 6.17: Mass distributions of $D_q^{\mp}$-mesons after selection of $B_q^0 \to D_q^{\mp} l^{\pm} \nu_l$-candidates. Left, data for the current world leading measurement by DØ, taken from Ref. [115]. Right, the expectation of LHCb from this Monte Carlo study.

(as shown in Fig. 6.17). LHCb can measure $\Delta A_{fs}^{s,d}$ with a statistical significance of $\sigma(2\,\text{fb}^{-1}) = (6.31 \pm 0.71) \times 10^{-4}$ in one year of data taking. This is reduced to a predicted $\sigma(10\,\text{fb}^{-1}) = (2.82 \pm 0.32) \times 10^{-4}$ in the $10\,\text{fb}^{-1}$ expected over the lifetime of LHCb. This sensitivity allows a measurement down to the SM value, at which level moderate new physics enhancements would be clearly visible.

Chapter 7

Conclusions

The next chapter in particle physics began this year (2008) with the start up of the LHC. Using this next-generation particle accelerator we hope to see the evidence of new physics: a candidate for dark matter, a quantum explanation of gravity, and a reason for the matter-antimatter asymmetry in the universe.

Precise tests of the Standard Model, as performed by LHCb, are in all cases complimentary to the generic resonance searches performed by ATLAS and CMS, and are required for the determination of the form of any new physics. LHCb is *the* precision heavy-flavour experiment in the LHC era.

We have shown that the LHCb RICH is one of the crucial detectors contributing to the precision of LHCb. We have reported on the testing and simulation of the pixel Hybrid Photon Detectors used in the RICH. The full sample of HPDs required for the LHCb RICHes, including spares and replacements, have been produced and fully tested by the LHCb collaboration at two custom photo-detector test facilities. More than 97 % of all devices met or exceeded the specifications. The majority of HPDs exceeded the requirements and/or the specifications in key areas, including the vacuum quality, the inherent dark noise and the pixel chip quality. In particular, the detector QE far exceed expectations, by a relative 27 %, which was verified by LHCb with a purpose-built measurement system. The increased QE was shown to

significantly improve the performance of the LHCb particle identification system, in a full Monte Carlo simulation of the detector.

The simulation of the HPDs in the LHCb Monte Carlo was improved. A more realistic geometric description, including signal-correlated backgrounds from internal reflections was developed. We have shown that, with the extra signal-correlated background of up to 15 %, the degradation to the particle identification performance is minimal.

A key part of LHCb's physics programme will be the measurement of the flavour-specific asymmetry in neutral B-meson mixing. This parameter quantifies CP-violation in the mixing and is very small in the Standard Model, however it is very sensitive to new physics, which can increase the asymmetry by up to two orders of magnitude. We propose a simultaneous measurement in the semileptonic channels $B_s^0 \to D_s^{\mp}\mu^{\pm}\nu_\mu$ and $B_d^0 \to D^{\mp}\mu^{\pm}\nu_\mu$, of the quantity $\Delta A_{fs}^{s,d} \approx (a_{fs}^s - a_{fs}^d)/2$. Crucially, the detector, production, and background asymmetries are fitted from the data, or eliminated from the measurement. In this way LHCb can perform this measurement with small systematic errors. We have performed a range of Monte Carlo toy studies, which show that a statistical precision of $(6.31 \pm 0.71) \times 10^{-4}$ can be reached in $2\,\text{fb}^{-1}$ of data taking. This represents more than an order of magnitude improvement over the current world leading measurement. With this unprecedented precision we can test the Standard Model prediction and hopefully get our first glimpses of new physics in B_s^0-mixing.

Bibliography

[1] R. W. Lambert, "The LHCb pixel hybrid photon detectors," in *Proceedings of the international workshop on New Photon-Detectors*, Kobe, Japan, June 27-29 2007, Proc. of Sci. (**PD07**) 019, 14th February 2008.

[2] R. W. Lambert, "Quantum efficiency of hybrid photon detectors for the LHCb RICH," in *Proceedings of the 10th ICATPP Conference on Astroparticle, Particle, Space Physics, Detectors and Medical Physics Applications*, Villa Olmo, Como, Italy, October 8-12 2007, World Scientific (2008), pp. 85-89. M. Barone *et al.* Eds. ISBN 978-981-281-908-6.

[3] S. Eisenhardt *et al.*, "Quantum efficiency of LHCb RICH pixel hybrid photon detectors," LHCb-note 2008-025 (2008).

[4] A. Augusto Alves *et al.*, LHCb collaboration, *The LHCb detector at LHC*, J. of Instrumentation **3** (2008) pp. S08005.

[5] N. Brook, N. Cottingham, R. W. Lambert, F. Muheim, J. Rademacker, P. Szczypka, Y. Xie, "LHCb's potential to measure flavour-specific CP-asymmetry in semileptonic and hadronic B_s^0 decays," LHCb-note 2007-054 (2008).

[6] R. Lambert and F. Muheim, "Generator study of the production asymmetry in LHCb," LHCb-note 2007-124 (2007).

[7] C. D. Anderson, "The positive electron," Phys. Rev. **43** (1933) pp. 491-494.

[8] R. P. Feynman, "The reason for antiparticles," in *The 1986 Dirac memorial lectures*, R.P. Feynman and S. Weinberg. Cambridge University Press, 1987. ISBN 0-521-34000-4.

[9] C. Jarskog, *Advance series on directions in high energy physics - Vol 3. CP Violation.* World Scientific Pubs., 1989. ISBN 9971505614.

[10] A. D. Sakharov, "Violation of CP invariance, C asymmetry, and baryon asymmetry of the universe," Soviet Physics Journal of Experimental and Theoretical Physics (JETP) **5** (1967) pp. 24-27. Republished in Soviet Physics Uspekhi.

[11] A. B. Carter and A. I. Sanda, "CP violation in B-meson decays," Phys. Rev. D **23** (1981) pp. 1567-1579.

[12] W. N. Cottingham and D. A. Greenwood, *An introduction to the Standard Model of particle physics.* Cambridge University Press, 2003. ISBN 0-521-85249-8.

[13] C. Amsler *et al.*, the Particle Data Group, *Review of particle physics*, Phys. Lett. B **667** no. 1 (2008).

[14] A. Zee, *Quantum field theory, in a nutshell*. Princeton University Press, 2003. ISBN 0-691-01019-6.

[15] M. Longair, *Theoretical concepts in physics*, Cambridge University Press, 2003. ISBN 0-521-52878-X.

[16] M. Gell-Mann, "The Eightfold Way: a theory of strong interaction symmetry," DOE Technical Report TID-12608, March 15, 1961.

[17] I. S. Hughes, *Elementary particles*. Cambridge University Press, 1991. ISBN 0-521-40739-7.

[18] R. Gupta, "Introduction to lattice QCD," in Lectures given at the *LXVIII Les Houches Summer School, Probing the Standard Model of Particle Interactions*, July 28-Sept 5, 1997. hep-lat 9807028v1.

[19] R. D. Peccei and H. R. Quinn, "CP conservation in the presence of pseudoparticles," Phys. Rev. Lett. **38** (1977) pp. 1440-1443.

[20] R. D. Peccei, "The strong CP problem and axions," (2006) hep-ph 0607268v1.

[21] H. Banerjee, D. Chatterjee and P. Mitra, "Is there still a strong CP problem?" (2003) hep-ph 0012284.

[22] N. Cabbibo, "Unitary symmetry and leptonic decays," Phys. Rev. Lett., **10** (1963) pp. 531-533.

[23] M. Kobayashi and T. Maskawa, "CP-Violation in the renormalisable theory of weak interactions," Progress of Theoretical Physics, **49** (1972) pp. 652-657.

[24] Y.-M. Yao *et al.*, the Particle Data Group, *Review of particle physics*, J. Phys. G, **33** no. 1 (2006).

[25] J. H. Christenson, J. W. Cronin, V. L. Fitch, and R. Turlay, "Evidence for the 2π Decay of the K_2^0 Meson," Phys. Rev. Lett., **13** no. 4 (1964) pp. 138-140.

[26] S. W. Herb *et al.*, "Observation of a dimuon resonance at 9.5 GeV in 400-GeV proton-nucleus collisions," Phys. Rev. Lett. **39** (1977) pp. 252-255. Many popular articles also exist, for example see the article by L. Lederman at http://www.symmetrymagazine.org/cms/?pid=1000195.

[27] L. Wolfenstein, "Parametrization of the Kobayashi-Maskawa Matrix," Phys. Rev. Lett. **51** (1983) pp. 1945-1947.

[28] A. J. Buras and M. Lindner, "Quark mixing, CP violation and rare decays after the top quark discovery," Chapter 2 in [138], pp. 66-220, hep-ph 9704376.

[29] R. Fleischer, "Flavour physics and CP Violation," in Lectures presented at the *Central European School in Particle Physics*, Tsakhkadzor, Armenia, 24th August - 6th September, 2003 hep-ph 0405091.

[30] O. Schneider, for the Particle Data Group, "B^0 - $\bar{B}^0$ mixing," in [24], pp. 836-842 (2006), earlier version also available as hep-ex 0405012 v1 (2004).

[31] LHCb collaboration, *LHCb Reoptimised Detector Design and Performance, Technical Design Report 9*, CERN LHCC 2003-030 LHCb, 9th September 2003.

[32] M. Antonelli *et al.*, the FlaviaNet working group, "Precision tests of the Standard Model with leptonic and semileptonic kaon decays," (2008) hep-ph 0801.1817v1.

[33] B. Aubert *et al.*, the BABAR Collaboration, "Improved measurement of CP violation in neutral B decays to $c\bar{c}s$," Phys. Rev. Lett. **99** (2007) pp. 171803, hep-ex 0703021.

[34] K.-F. Chen *et al.*, the BELLE Collaboration, "Observation of time-dependent CP violation in $B0 \to \eta' K^0$ decays and improved measurements of CP asymmetries in $B0 \to \phi K^0$, $K_s^0 K_s^0 K_s^0$ and $B^0 \to J/\psi K^0$ decays," Phys. Rev. Lett. **98** (2007) pp. 131802, hep-ex 0608039.

[35] J. Charles *et al.*, the CKMfitter Group, "CP violation and the CKM matrix: assessing the impact of the asymmetric B factories," Eur. Phys. J. C41, 1-131 (2005) [hep-ph 0406184], updated results and plots available at: http://ckmfitter.in2p3.frF.

[36] M. Bona *et al.*, the UTfit collaboration, "First evidence of new physics in $b \leftrightarrow s$ transitions," hep-ph 0803.0659v1 (2008).

[37] U. Nierste, "CP asymmetry in flavour-specific B decays," hep-ph 0406300 v2 (2006).

[38] A. Lenz, U. Nierste, "Theoretical update of B_s-$\bar{B}_s$ mixing," hep-ph 0612167 v1 (2006).

[39] M. Ciuchini, E. Franco, V. Lubicz, F. Mescia an C. Tarantino, "Lifetime differences and CP violation parameters of neutral B mesons at the next-to-leading order in QCD," hep-ph 0308029 v2 (2003).

[40] C. S. Kim, J. Lee, W. Namgung, "CP violation in the semileptonic B_{l4} ($B \to D\pi l\nu$) decays: A model-independent analysis," Phys. Rev. D, **59** (2003) pp. 114005-1 – 114005-11.

[41] B. Casey, for the DØ collaboration, "Heavy flavor physics winter results," presented at the 40th winter conference *Rencontres De Moriond*, on *Electroweak Interactions and Unified Theories*, 11-18th March 2006. available online through URL http://moriond.in2p3.fr/EW/2006/Transparencies/B.Casey.pdf (2006).

[42] C. S. Kim, J. Lee, W. Namgung, "CP violation in the semileptonic B_{l4} ($B \to D\pi l\nu$) decays: Multi-Higgs-doublet model and scalar-leptoquark models," Phys. Rev. D, **59** (2003) pp. 114006-1 – 114006-7.

[43] M. Okamoto, "Full determination of the CKM matrix using recent results from lattice QCD," in *Proceedings of the 23rd international symposium on Lattice Feild Theory*, Dublin, Ireland, July 2005, hep-lat 0510113.

[44] S. Laplace, Z. Ligeti, Y. Nir and G. Perez, "Implications of the CP asymmetry in semileptonic B decay," hep-ph 0202010 v2 (2002).

[45] M. Beneke, G. Buchalla, A. Lenz and U. Nierste, "CP asymmetry in flavour-specific B decays beyond leading logarithms," hep-ph 0307344 v2 (2003).

[46] Edward Nelson, "Mathematical pearls: a proof of Liouville's Theorem," in *Proceedings of the American Mathematical Society*, **12** (1961) No. 6, pp. 995.

[47] LHC collaboration, *LHC Design Report*, CERN EDMS 0000024513 v. 0, January 2005. Volumes I, II, III (Introductions as CERN EDMS 445892/4, 445913/5, 445760/2, also available through http://ab-div.web.cern.ch/ab-div/Publications/LHC-DesignReport.html). .

[48] ALICE collaboration, *ALICE Technical Proposal*, CERN LHCC 95-71, 15th December 1995 (also available through http://aliceinfo.cern.ch/Collaboration/Documents/TechnicalProposal.html).

[49] J. Ellis *et al.*, the LHC Safety Assessment Group "Review of the safety of LHC collisions," J. Phys. G **35** (2008) pp. 115004, http://lsag.web.cern.ch/lsag/LSAG-Report.pdf.

[50] *The CERN Large Hadron Collider: accelerator and experiments*, J. Inst. **3** (2008) pp. S08001-S08007.

[51] N. Ellis, "B-physics in the LHC experiments," Nucl. Phys. B (proc. suppl.) **93** (2001) pp. 317-323.

[52] K. Aamodt *et al.*, the ALICE collaboration, "The ALICE experiment at the CERN LHC," in Ref. [50] (2008) pp. S08002. .

[53] ATLAS collaboration, *ATLAS Technical Design Report*, CERN LHCC 99-14, 25th May 1999 (also available through http://atlas.web.cern.ch/Atlas/internal/tdr.html). .

[54] G. Aad *et al.*, the ATLAS collaboration, "The ATLAS Experiment at the CERN Large Hadron Collider," in Ref. [50] (2008) pp. S08003. .

[55] CMS collaboration, *CMS Physics, Technical Design Report*, CERN LHCC 2006-001, 02 February 2005 (also available through http://cmsdoc.cern.ch/cms/cpt/tdr/index.html). .

[56] S. Chatrchyan *et al.*, the CMS collaboration, "The CMS experiment at the CERN LHC," in Ref. [50] (2008) pp. S08004. .

[57] LHCf collaboration, *Technical Design Report of the LHCf experiment*, CERN LHCC 2006-004, 07 February 2006. .

[58] O. Adriani *et al.*, the LHCf collaboration, "The LHCf detector at the CERN Large Hadron Collider," in Ref. [50] (2008) pp. S08006. .

[59] TOTEM collaboration, *TOTEM, Technical Design Report*, CERN LHCC 2004-002, 04 March 2004 (also available through http://totemtdr.web.cern.ch/totemtdr/totemtdr24-03-04.pdf). .

[60] G. Anelli *et al.*, the TOTEM collaboration, "The TOTEM Experiment at the CERN Large Hadron Collider," in Ref. [50] (2008) pp. S08007. .

[61] F. Sauli, "Imaging with the Gas Electron Multiplier," Nucl. Instr. and Meth. A **580** (2007) pp. 971.

[62] LHCb collaboration, *LHCb Technical Proposal*, CERN-LHCC-98-004 LHCb, 20th February 1998.

[63] LHCb collaboration, *LHCb VELO, Technical Design Report 5*, CERN LHCC 2001-011 LHCb, 31st May 2001.

[64] LHCb collaboration, *LHCb Inner Tracker, Technical Design Report 8*, CERN-LHCC-2001-040, December 2001.

[65] LHCb collaboration, *LHCb Outer Tracker, Technical Design Report 6*, CERN-LHCC-2001-024, 14th September 2001.

[66] LHCb collaboration, *LHCb Magnet, Technical Design Report 1*, CERN-LHCC-2000-007 LHCb, 7th January 2000.

[67] LHCb collaboration, *LHCb Calorimeters, Technical Design Report 2*, CERN-LHCC-2000-036 LHCb, 6th September 2000.

[68] LHCb collaboration, *LHCb Muon System, Technical Design Report 4*, CERN-LHCC-2001-010 LHCb, 28th May 2000, Addendum 1, CERN-LHCC-2003-002, January 2003, Addendum 2, CERN-LHCC-2005-0012, April 2005.

[69] LHCb collaboration, *LHCb RICH, Technical Design Report 3*, CERN-LHCC-2000-037 LHCb, 7th September 2000.

[70] J. V. Jelley, *Čherenkov radiation and its applications*, Pergamon Press, London, 1958.

[71] T. Bellunato *et al.*, "Cherenkov rings from aerogel detected by four large-area hybrid photodiodes," Nucl. Instr. and Meth. A **504** (2003) pp. 290-293.

[72] A. Carbone, J. Nardulli, S. Pennazzi, A. Sarti and V. Vagnoni, "Charmless charged two-body B decays at LHCb," LHCb-note 2007-059 (2007).

[73] LHCb collaboration, *LHCb Trigger System, Technical Design Report 10*, CERN-LHCC-2003-031, September 2003.

[74] T. Gys, "Production of 500 hybrid photon detectors for the RICH counters of LHCb," in proceedings of *the Fourth Conference on New Developments in Photodetection*, Beaune, France, 19th-24th June 2005, Nucl. Instr. and Meth. A **567** (2006) 1, pp. 176-179.

[75] M. Campbell *et al.*, "A fine pitch bump bonding process compatible with the manufacture of the pixel-HPD's for the LHCb RICH detector," in *Proceedings of the 2004 IEEE Nuclear Science Symposium and Medical Imaging Conference*, Roma, Italy, 16-22 October 2004, Nuclear Science Symposium Conference Record, 2004 IEEE **1**, 16-22 October 2004, pp. 657-661, and IEEE Trans. Nucl. Sc. **53** (2006) 4, pp. 2296-2302.

[76] K. Wyllie, G. Aglieri Rinella, M. Campbell, M. Castro Carballo, T. Gys, S. Jolly, M. Moritz, C. Newby, D. Piedigrossi and L. Somerville, "Silicon detectors and electronics for pixel hybrid photon detectors," in Proceedings of *the 6th International Conference on Large Scale Applications and Radiation Hardness of Semiconductor Detectors*, Florence, Italy, September 29 - October 1, 2003, Nucl. Instr. and Meth. A **530** (2004) 1-2 pp. 82-86.

[77] A. Baldit *et al.*, the NA60 collaboration, "Study of prompt dimuon and charm production with proton and heavy ion beams at the CERN SPS," CERN-SPSC-2000-010 (2000).

[78] LHCb collaboration, Contract with Delft Electronic Products - Photonis, *Supply of Hybrid Photon Detectors for the LHCb Rich Counters*, Contract # F549/PH/LHCb. Appendix 1, T. Gys.

[79] National Instruments LabVIEW, http://www.ni.com/labview/.

[80] N. Kanaya, G. Aglieri-Rinella, T.Gys, D. Piedigrossi, K. Wyllie, "Performance study of hybrid photon detectors for the LHCb RICH," in *Proceedings of the fifth international workshop on Ring Imaging Detectors, RICH 2004*, Playa de Carmen, Yucatan Peninsula, Mexico, 30 November-05 December 2004, Nucl. Instr. and Meth. A **553** (2005) 1-2, pp. 41-45.

[81] W. E. Spicer and A. Herrera-Gomez, "Modern Theory and Applications of Photocathodes," in *Proceedings of the SPIE International Symposium on Optics, Imaging and Instrumentation*, San Diego, CA, July 11-16, 1993, SLAC-PUB-6306, SLAC/SSRL-0042 (1993) pp. 3295-3310.

[82] A. Braem *et al.*, "Highly segmented large-area Hybrid Photodiodes with bialkali photocathodes and enclosed VLSI readout electronics," in proceedings of *the Second Conference on New Developments in Photodetection*, Beaune, France, 21-25th June 1999, Nucl. Instr. and Meth. A **442** (2000) 1, pp. 128-135.

[83] M. Adinolfi, "System test of a three-column LHCb RICH-2 prototype detector," in *Proceedings of the fifth international workshop on Ring Imaging Detectors, RICH 2004*, Playa de Carmen, Yucatan Peninsula, Mexico, 30 November-05 December 2004, Nucl. Instr. and Meth. A **553** (2005) 1-2, pp. 328-332.

[84] T. Gys, N. Kanaya and D. Piedigrossi, "Quantum efficiency measurements of LHCb-RICH pre-series pixel-HPDs," LHCb-note 2007-136 (2007).

[85] T. Gys, X. Le Gouard, A. Papanestis, A. Petrolini, K. Wyllie, "Column Numbering Convention for RICH2," LHCb CERN-EDMS-758769 (2006).

[86] R. W. Lambert, F. Muheim and R. Plackett, "RICH1 Column Mounting Note: Positions and Conventions," LHCb CERN-EDMS-864762 (2007).

[87] R. W. Lambert, K. Wyllie and F. Muheim, "RICH2 Column Mounting Note: Positions and Conventions," LHCb CERN-EDMS-815983 (2007).

[88] K. Wyllie, R. Plackett, "Column Numbering Convention for RICH1," LHCb CERN-EDMS-864727 (2007).

[89] LHCb collaboration, *LHCb Computing, Technical Design Report 11*, CERN-LHCC-2005-019, June 2005.

[90] M. Cattaneo and P. Maley for the LHCb collaboration, *Gaudi: LHCb Data Processing Applications Framework: Users Guide*, http://lhcb-comp.web.cern.ch/lhcb-comp/Frameworks/Gaudi/Gaudi_v9/GUG/GUG.pdf, 2001.

[91] I. Balyaev, G. Corti, S. Easo, W. Pokorski, F. Ranjard and P. Robbe for the LHCb collaboration *Gauss: The LHCb simulation program: Users guide and reference manual*, http://lhcb-comp.web.cern.ch/lhcb-comp/Simulation/Gauss.pdf, 2005.

[92] M. Cattaneo for the LHCb collaboration, *Boole: LHCb digitization program: Users guide and Reference Manual*, http://lhcb-release-area.web.cern.ch/LHCb-release-area/BOOLE/BOOLE_v6r5/doc/Boole.pdf, 2005. .

[93] M. Cattaneo for the LHCb collaboration, *Brunel: LHCb reconstruction program: Users Guide*, http://lhcb-comp.web.cern.ch/lhcb-comp/Reconstruction/BUG.pdf.

[94] For example see: LHCb collaboration, http://lhcb-release-area.web.cern.ch/LHCb-release-area/DOC/davinci/.

[95] For example see: T. Ruf for the LHCb collaboration *Panoramix introduction from a physicist*, http://lhcb-reconstruction.web.cern.ch/lhcb-reconstruction/Panoramix/Panoramix_intro.pdf . .

[96] T. Sjöstrand, S. Mrenna and P. Skands, "PYTHIA 6.4, physics and manual," FERMILAB-PUB-06-052-CD-T, J. H.E.P. **05** (2006) 026, pp. 1-489, hep-ph 0603175.

[97] D. J. Lange, "The EvtGen particle decay simulation package," in *Proceedings of the 7th international conference on B-physics at Hadron Machines, Beauty 2000*, Kibbutz Maagan, Israel, 13-18 September 2000, Nucl. Instr. and Meth. A **462** (2001), pp. 152-155.

[98] For example see: M. Goossens for the CERN application software group, *Geant - Detector Description and Simulation Tool*, http://wwwasd.web.cern.ch/wwwasd/geant/, and http://wwwasdoc.web.cern.ch/wwwasdoc/pdfdir/geant.pdf.

[99] J. Alison *et al.*, the Geant4 collaboration, "Geant4 developments and applications," IEEE Trans. on Nuclear Science **53** no. 1, (2006) pp. 270-278. .

[100] H. Abdelouahed *et al.*, the Geant4 collaboration, "Physics reference manual," http://geant4.web.cern.ch/geant4/ UserDocumentation/UsersGuides/PhysicsReferenceManual/fo/PhysicsReferenceManual.pdf.

[101] S. Easo *et al.*, the LHCb RICH collaboration, "Simulation of LHCb RICH using Geant4," IEEE Trans. on Nuclear Science **52** no. 5, (2005) pp. 1665-1668. .

[102] M. Adinolfi, "System test of a three-column LHCb RICH-2 prototype detector," in *Proceedings of the fifth international workshop on Ring Imaging Detectors, RICH 2004*, Playa de Carmen, Yucatan Peninsula, Mexico, 30 November-05 December 2004, Nucl. Instr. and Meth. A **553** (2005) 1-2, pp. 328-332.

[103] For example see, R. Wiel, "Reflectivity of steel," Nature **159** (1947) pp. 305-305.

[104] S. Hallensleben, S.W. Harmer, P.D. Townsend, "Optical constants for the S20 photocathode. and their application to increasing photomultiplier quantum efficiency," Opt. Comm. **180** (2000) pp. 89-102.

[105] E. H. Darlington, "Backscattering of 10-100keV electrons from thick targets," J. Phys. D: Appl. Phys. **8** (1975) pp. 85-93.

[106] P. Szczypka, "Study of the sensitivity to flavour-specific asymmetries with the LHCb detector," CERN-THESIS-2008-045 (2008).

[107] B. Aubert *et al.*, the BaBar collaboration, "Search for T and CP Violation in B^0-$\bar{B}^0$ Mixing with Inclusive Dilepton Events," hep-ex 0202041 (2002).

[108] E. Nakano *et al.*, the BELLE Collaboration, "Charge asymmetry of same-sign dileptons in B^0 - $\bar{B}^0$ mixing," Phys. Rev. D **73** (2006) pp. 112002, hep-ex 0505017.

[109] Jim Wiss, "Recent results on fully leptonic and semileptonic charm decays," hep-ex 0605030 v4 (2006).

[110] D. E. Jaffe *et al.*, the CLEO Collaboration, "Bounds on the CP asymmetry in like sign dileptons from $B^0\bar{B}^0$ meson decays," Phys. Rev. Lett. **86** (2001) pp. 5000, hep-ex 0101006.

[111] V. M. Abazov *et al.*, the DØ Collaboration, "Measurement of the CP-violation parameter of B^0 mixing and decay with $p\bar{p} \to \mu\mu X$ data," Phys. Rev. D **74** (2006) pp. 092001, hep-ex 0609014.

[112] T. Aaltonen *et al.*, the CDF Collaboration, "Measurement of CP asymmetry in semileptonic B decays," CDF-note 9015, 070816 (2007), available through http://www-cdf.fnal.gov/physics/new/bottom/070816.blessed-acp-bsemil/public-acp-bsemil.ps .

[113] E. Barberio *et al.*, the Heavy Flavor Averaging Group, "Averages of b-hadron properties at the end of 2005," hep-ex 0603003 (2006).

[114] Y. Grossman, Y. Nir and G. Raz, "Constraining the phase of B_s-$\bar{B}_s$ mixing," Phys. Rev. Lett. **97** (2006) pp. 151801-1 – 151801-4. Extended version available online hep-ph 0605028 v3 (2006).

[115] V. M. Abazov *et al.*, the DØ Collaboration, "Measurement of the charge asymmetry in semileptonic B_s decays," Phys. Rev. Lett. **98** (2007) pp. 151801, hep-ex 0701007.

[116] V. M. Abazov *et al.*, the DØ Collaboration, "Combined DØ measurements Constraining the CP-Violating phase & width difference in the B_s system," FERMILAB-PUB-07/044-E (2007), to be published in Phys. Rev. D, hep-ex 0702030.

[117] Z. Ligeti, M. Papucci, and G. Perez, "Implications of the measurement of the $B_s^0\bar{B}_s^0$ mass difference," hep-ph 0604112 v3 (2006).

[118] A. Abulencia *et al.*, the CDF collaboration, "Measurement of the B_s^0-$\bar{B}_s^0$ Oscillation Frequency," Phys. Rev. Lett., **97** (2006) pp. 062003-1 – 062003-7.

[119] G. Corti, L. Fernández, P. Robbe, O. Scheider, "Monte Carlo event type definition rules," LHCb-note 2005-034 (2007).

[120] B. Aubert *et al.*, the BABAR collaboration, "Measurement of the relative branching fractions of $\bar{B} \to D/D^*/D^{**}l^-\bar{\nu}_l$ decays in events with a fully reconstructed B meson," SLAC-PUB-12393 (2007), hep-ex 0703027.

[121] D. Liventsev *et al.*, the BELLE collaboration, "Study of $B \to D^{**}l^+\nu_l$ with full reconstruction tagging," (2008), hep-ex 0711.3252.

[122] K. Abe *et al.*, the BELLE collaboration, "Measurement of the inclusive semileptonic branching fraction of B mesons and $|V_{cb}|$," (2002), hep-ex 0208033.

[123] A. E. Snyder, "Review of exclusive $\bar{B} \to D^{**}l\nu_l$ decays - branching fractions, form factors and $|V_{cb}|$," in *Proceedings of the 8th international workshop on Heavy Quarks and Leptons, HQL06*, Munich, Germany, 16-20th October 2006, hep-ex 0703035.

[124] R. Tesarek, private communication. 9th April 2008. tesarek@fnal.gov.

[125] A. Pérez-Calero, "Muon+Track in HLT," talk at the LHCb T-REC meeting, 7th April 2008.

[126] A. Pérez-Calero, Antinio.Maria.Perez.Calero@cern.ch, private communication, 23rd April 2008.

[127] R. Brun *et al.*, *ROOT: an object-orientated data analysis framework*, http://root.cern.ch.

[128] A. Hoeker *et al.*, *TMVA: toolkit for multivariate data analysis in ROOT*, http://tmva.sourceforge.net, part of the ROOT data analysis framework [127].

[129] O. Leroy, F. Muheim, S. Poss, and Y. Xie, "Selection of $B_s^0 \to D_s^- \mu^+ \nu_\mu$ events in LHCb," LHCb-note 2007-029 (2007).

[130] M. Botlo *et al.*, "Further comments about B-physics in pp interactions," SLAC-PUB-5795 SSCL-538 (1992) pp. 1-56.

[131] E. Norrbin and T. Sjöstrand, "Production and hadronization of heavy quarks," Eur. Phys. J. C. **17** (2000) pp. 137-161.

[132] The Proceedings of the 2000 Workshop on *Standard Model physics (and more) at the LHC*, CERN, Geneva 25th May 1999. G. Altareli and M. L. Mangano eds. CERN-2000-004 (2000).

[133] L. M. Zhang, Z. P. Zhang *et al.*, the BELLE collaboration, "Measurement of D^0-$\bar{D}^0$ mixing in $D^0 \to K_s \pi^+ \pi^-$ decays," Phys. Rev. Lett. **99** (2007) pp. 131803, hep-ex 0704.1000.

[134] P. Koppenburg, Patrick.Koppenburg@cern.ch, private communication, 15th May 2008.

[135] M. Calvi, "Selection of $B_d^0 \to D^{*-} \mu^+ \nu_\mu$ events and flavour tagging studies in LHCb," LHCb-note 2007-036 (2007).

[136] W. Verkerke, D. Kirkby, "The RooFit toolkit for data modeling," in *Proceedings of 2003 conference for computing in High-Energy and Nuclear Physics* (CHEP 03), La Jolla, California, 24-28th Mar 2003, pp. MOLT007. See http://roofit.sourceforge.net, part of the ROOT data analysis framework [127].

[137] For example see the works of K. Lessnoff, "Asymmetry measurements with $B_s^0 \to D_s \mu \nu$ decays," talk at the LHCb-UK meeting, 11th November 2008, CERN, and K. Lessnoff's Thesis, to be submitted.

[138] A. J. Buras and M. Lindner, *Heavy flavours II*, Vol. 15 of *Advanced series on directions in high energy physics*, World Scientific pubs. (1997) ISBN-9810222157.

[139] D. E. Swets, R. W. Lee, R. C. Frank, "Diffusion coefficient of helium in fused quartz," J. Chem. Phys. **34** (1961) pp. 17-22.

[140] J. S. Masaryk and R, M. Fulrath, "Diffusion of helium in fused silica," J. Chem. Phys. **59** (1973) pp. 1198-1199.

[141] R. W. Lee, R. C. Frank, D. E. Swets, "Diffusion of hydrogen and deuterium in fused quartz," J. Chem. Phys. **36** (1962) pp. 1062-1071.

[142] J. F. Shackelford, P. L. Studt, R. M. Fulrath, "Solubility of gases in glass. II. He, Ne and H_2 in fused silica," J. Appl. Phys. **43** (1972) pp. 1619-1626.

[143] P. Brimblecombe, *Air composition and chemistry*, Cambridge University Press, 1995. ISBN 0-521-459729.

[144] E. Kalashnikov, I. Tolstikhin, B. Lehmann and B. Pevzner, "Helium transport along lattice channels in crystalline quartz," J. Phys. Chem. of Solids **64** (2003) 11, pp. 2293-2300.

[145] R. G. Montague, M. F. A. Harrison and A. C. H. Smith, "A measurement of the cross section for ionisation of helium by electron impact using a fast crossed beam technique," J. Phys. B: At. Mol. Phys. **17** (1984) pp. 3295-3310.

[146] L. J. Kieffer and G. H. Dunn, "Electron impact ionization cross-section data for atoms, atomic ions, and diatomic molecules: I. experimental data," Rev. Mod. Phys. **38** (1966) pp. 1 - 35.

[147] E. Norrbin and R. Vogt, Section 5 in Chapter "Bottom production," in [132].

[148] D. Perret-Gallix, V. A. Ilyin and A. E. Pukhov, Section 3 in Chapter "QCD," in [132].

[149] G. Corcella *et al.*, "HERWIG 6.5: an event generator for hadron emission reactions with interferring gluons (including supersymmetric processes)," J. H.E.P. **0101** (2002) 010, hep-ph 0011363.

[150] T. Sjöstrand, P. Z. Skands, "Multiple interactions and the structure of beam remnants," J. H.E.P. **03** (2004) 053, pp. 1-79, hep-ph 0402078.

[151] J. M. Butterworth, J. R. Forshaw, M.H. Seymour, "Multiparton interactions in photoproduction at HERA," CERN-TH-96-82, M-C-TH-96-05, UCL-HEP-96-02, Z.Phys **C72** (1996) pp. 637-646, hep-ph 9601371.

[152] S. Frixione, P. Nason and B. R. Webber, "Matching NLO QCD and parton showers in heavy flavour production," J. H.E.P. **08** (2003) 007, hep-ph 0305252.

[153] K. Lessnoff, "The tuning of pythia for the LHCb, using Gauss," LHCb note 2007-125, 28th Sep 2007.

Appendices

Appendix A

Ion Feedback Effects in Photocurrent Measurements

In the measurement of photocurrent from a vacuum photodetector device, one must consider the effects of ion feedback, which will act to increase the measured current. Measurements of the QE of a photodetector are performed by measuring the photocurrent and are therefore influenced by ion feedback. The HPDs used in the LHCb RICH are such a vacuum photodetector, employing a multi-alkali photocathode, and a large electrostatic potential, as described in Chapter 4. The HPD QE is a key parameter dictating the performance of these devices in the RICH system and is therefore measured for every HPD by the manufacturer, and for a subset of HPDs by LHCb. The QE measurement is reported in Sec. 4.3, where ion feedback effects are seen as an increase in the drawn current from the photocathode for a few atypical HPDs, faking an increased QE. In this Appendix, the ion feedback effects are investigated. A simple model is presented based on electrostatics that agrees with the data gathered and the ion feedback is used to monitor vacuum degradation in the HPDs.

A.1 An introduction to ion feedback

The ion feedback rate is the rate at which residual gas atoms or molecules are ionised by the electrons emitted from the photocathode. As the photoelectrons travel through the vacuum of the tube they may ionise residual gas molecules. The positive ions produced are accelerated towards the photocathode. When these ions impact the photocathode they deposit their energy, which results in the emission of many secondary electrons. The secondary electrons are then accelerated back to the anode, forming a large cluster of hits on the anode. In the standard operational voltage configuration[1], the HPD cross-focuses the electrons producing the highest electron density close to the longitudinal centre, along the cylindrical axis of the HPD (see Fig. 4.1). In this configuration ion feedback has a characteristic delay resulting from the drift time of the ions and it is also known as the afterpulse. The afterpulse rate from ion feedback (IFB) at $-20\,\mathrm{kV}$ is determined from a timing scan at PDTF [1], where the ratio of the peak in delayed large clusters to the peak in the initial prompt signal is measured. The ion feedback probability measures the vacuum quality of the HPD and is measured at PDTF for all HPDs [1].

Mechanisms for the introduction of residual gases, besides initial low vacuum quality, involve diffusion through the quartz window, diffusion through imperfections in the tube body or vacuum seal, and outgassing of the HPD internally. The diffusion rate of a gas is inversely proportional to the square root of its molar mass.[2] Hydrogen and helium gases are therefore the most diffusive [139, 140, 141]. Similarly helium and hydrogen are the most soluble gasses in quartz [142]. Helium is approximately ten times more abundant in dry air than hydrogen[3], and may diffuse readily through crystalline quartz due to the match of the expected atomic spacing to the size of the helium atom [144]. It is expected then, that helium should be the most abundant residual gas in the HPD.

Ion feedback increases the photocurrent drawn from a given light signal, i.e. it

[1] i.e. as used in the RICH system, with -20 kV at the photocathode.
[2] Graham's law, Thomas Graham, 1831.
[3] e.g. see Chapter 1 in [143]

produces a gas gain.[4] For the majority of production HPDs we have shown that our QE values agree with that of DEP (who perform the measurement at a higher voltage) and we know independently that the average ion feedback rate is extremely low from extensive PDTF testing [1], indicating excellent initial vacuum for the majority of production HPDs.

The gain that results from the IFB can be measured at PDTF using the QE measurement system between 0-500 V.[5] This measurement is an independent measurement of the vacuum quality, and/or vacuum degradation over time.

The ionisation cross-section and therefore the gain introduced is closely determined by the energy of the primary electron. For the main pollutant of the vacuum, helium, the cross-section of ionisation reaches a maximum at around 130 V [145]. The ionisation is prohibited below a threshold of 24.6 eV, which corresponds to the first ionisation energy of helium. Helium is, however, the element with the largest first ionisation energy and so any other pollutants would be expected to exhibit lower thresholds if present. Under normal operating conditions, photoelectrons take on a range of different energies, and accelerate towards the anode. There is a 3D spatial distribution of cross-section, secondary electron multiplicity, and therefore a 3D-distribution of ion feedback probability.

We plot the photocurrent versus voltage (LIV) curve for a selection of extreme cases in Fig. A.1, left, to be compared with Fig. 4.11. It is useful to note that the gain is approximately uniform across the HPD wavelength range, and that a measurement at between 20 V and 24.6 V recovers the true QE of the HPD, see Fig. A.1, right. This confirms the main residual gas is likely to be helium, as is further discussed in Sec. A.2.

[4]Quantitatively, the gain, G, here is the total of the induced current divided by the prompt photo-electron current $G = I/I_{pe}$, the single-pass or round-trip gain, g, is then the gain from the first ionisation step $g = 1 + I_{2e}/I_{pe}$.

[5]The electrical configuration and distribution system employed for the QE measurement is different to the standard RICH/PDTF operational configurations, compare Fig. 4.10 with Fig. 4.1.

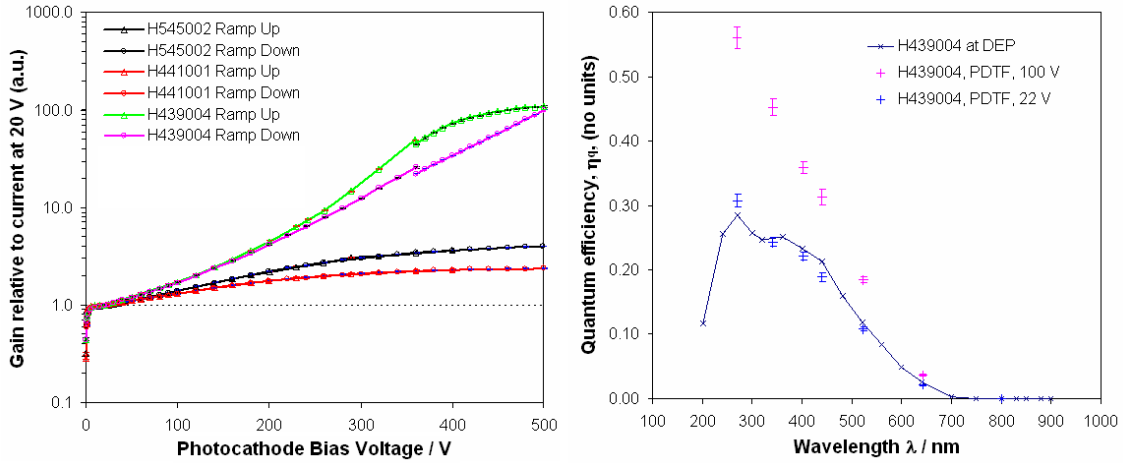

Figure A.1: Atypical extreme cases seen in LIV scans at PDTF. Left, photocurrent measurements with applied Voltage (LIV). The shoulder around 20 V corresponds to a gain of ≤ 1, and an increased gain due to ion feedback is observed with increasing voltage. c.f. Fig. 4.11. H545002 and H441001 show a steady increase in gain due to ion feedback. H439004 shows a large and hysteric gain, which suggests a much more extreme ion feedback effect. Right, gives QE curves for H439004 as measured at different voltages, without correcting for this gain.

A.2 Modelling the ion feedback effect

We model the effects of ion feedback within the HPD from the geometry of the HPD and the cross-section of the electron-helium ionisation interaction given in Ref. [145], Fig. A.3. From Ref. [146] the ion current is related to the cross section through:

$$\frac{I_i}{I_e} = \rho_{He}\ S\ \sigma_T \tag{A.1}$$

$$\frac{I_{2e}}{I_e} = \rho_{He} \int_0^{v_{max}} N_{2e}(v)\ \sigma(v)\ \left(\frac{\partial S(v)}{\partial v}\right)\ dv \tag{A.2}$$

Where v is a voltage, I_i is the ion current, I_e is the electron current, ρ_{He} is the number density of helium within the HPD, σ_T is the total cross-section and S is the length over which the interaction can occur. As there is a three-dimensional distribution of potential within the HPD, and there will be a dependence on the secondary electron multiplicity, N_{2e}, on the voltage of the ion produced when it impacts the photocathode (which will also be v), hence on the position within the HPD that the ionisation occurs $N_{2e}(v)$. The full secondary electron current I_{2e} is then provided by the second expression; where $\delta S(v)$ is the average thickness of a volume within the HPD which subtends a voltage from v to $v + \delta v$, with an

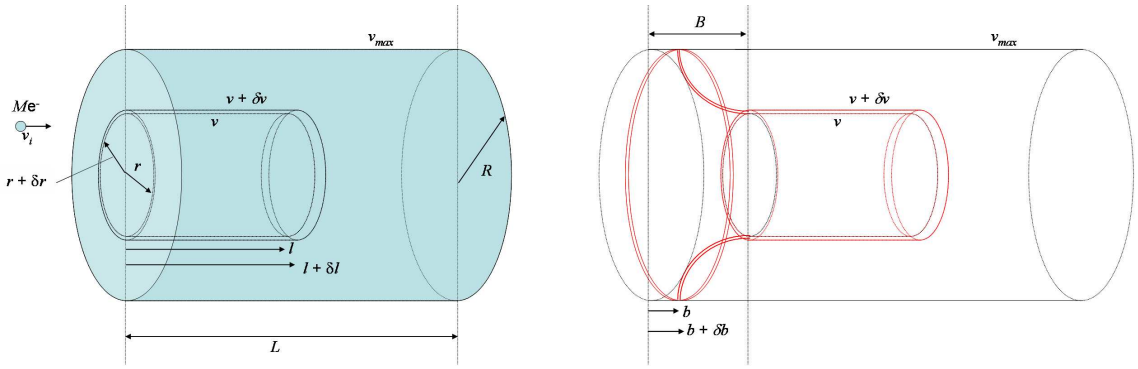

Figure A.2: Modelling the voltage contours within the HPD during the LIV measurement at PDTF. Left, simple model where voltage contours form concentric cups closed at one end. Right, more complex geometric model where voltage contours form concentric trombones, closed at the thin end. The photocathode is on the left in these diagrams. All models are of HPDs length L and radius R which are known HPD dimensions. M is the initial electron flux which begins at a voltage v_i due to the known residual kinetic energy from the photoelectric process. v_{max} is the potential difference between the photocathode and HPD body. B is a highly constrained fit parameter. l, b, v and r are possible integrand choices.

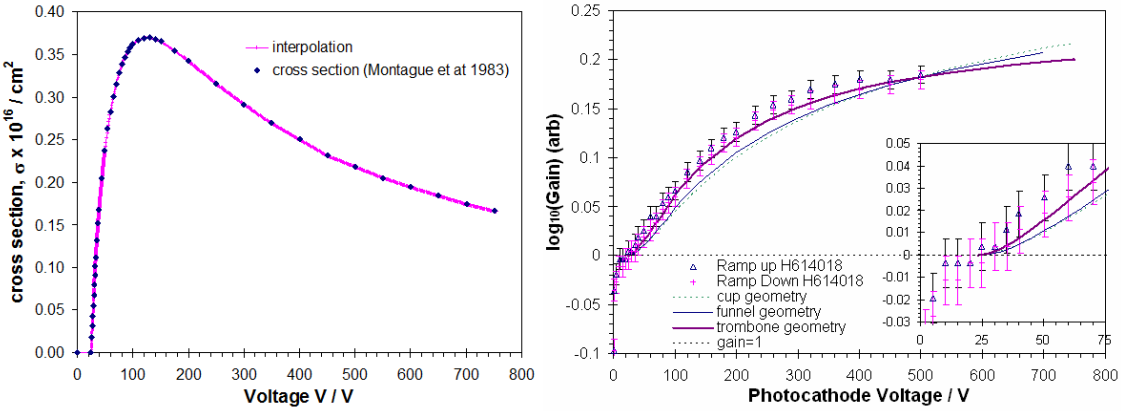

Figure A.3: Left, cross section of ionisation of helium with electrons from [145]. Right, fits to the LIV curve for H614018 measured at PDTF following a simplified geometric description. Inset, magnified around the threshold region. Good agreement is obtained to the threshold and shape of the trombone-like description.

instantaneous cross-section of $\sigma(v)$.

We consider three simplistic models, of concentric cups, concentric funnels and concentric trombones, two of which are shown in Fig. A.2. A full field description was not used, in order to obtain an analytic solution. We assume a linear increase of voltage toward the anode of the HPD $v \propto L$, and a linear increase in secondary electron number with ion impact voltage $N_{2e} \propto v$. We also assume the number of electrons is not sufficiently depleted by the interaction and that the probability of

cascade effects due to feedback from the secondary electrons is minimal, i.e. the ion feedback probability $<< 1$. With these models we fit to the data, with only one free parameter – equivalent to the number density of helium – as a normalisation parameter, and constrain this to the PDTF value of the gain at 500 V, shown in Fig. A.3. We find despite its simplicity the basic trombone model gives a reasonable description of the gain curves obtained. There are disagreements which we attribute to the much simplified geometrical description, additional threshold effects, for example, from the second ionisation of helium, and possible non-linear dependence of the number of secondary electrons on the ion voltage.

The form of the curve, particularly the plateau, is consistent with the presence of helium as the main residual gas, although other gases are not fully ruled out.

A.3 Ion feedback cascade effects

As ion feedback produces gain, avalanche/cascade effects are expected as the round-trip gain approaches unity. Since we know the work function of the photocathode, $\approx$1.5 eV, we can roughly estimate that for the peak interaction voltage of 130 V for helium, the maximum number of secondary electrons will be $\sim$85. Allowing for some absorption and scattering of the electrons by the photocathode, we could guess there should be $\sim$50 electrons emitted per impact. Therefore, if the ion feedback probability approaches $1/50 \approx 2\,\%$ the HPD will build up a continuous emission of electrons from ion feedback, and be no longer useful. From observations of cascade effects in the lab, we conclude this threshold is around 4 %. The average ion feedback percentage as measured at PDTF for the production tubes is much lower than this threshold, at 0.03 % at -20 kV [1]. However, with ions of up to 20 kV energy increased secondary electron multiplicity will obviously be expected. Ion feedback is clearly a key parameter to monitor for the HPDs over the life of the experiment.

Ionisation of residual helium is an extreme case of excitation of the helium atom. Excited helium atoms will relax through the emission of a photon. When this

emission becomes the dominant source of photoelectrons it is known as glow-discharge. In the regime of low ion-feedback the level of light induced from glow-discharge will produce a very small additional photocurrent. Taking the case of an HPD with an imperfect vacuum seal under operation: as the gas density within the HPD rises over time, the ion feedback probability will also rise, increasing the round-trip gain. As the round-trip gain increases, but remains below unity, the HPD will be perfectly useable and the feedback rate of $< 4\,\%$ can be compensated. Abruptly, at the onset of a cascade, the number of primary photo-electrons from the ion-feedback processes and glow-discharge will mask the signal photoelectrons, rendering the HPD insensitive to light. HPDs passing this threshold will be abruptly rendered useless.

We have examined two HPDs at PDTF, which failed under operation at CERN with a characteristic increase in ion feedback over a few weeks. The LIV curves appear as Fig. A.4. Using a geometric progression to model the gain curve, we see that at the point when the round-trip gain approaches unity, that even in the absence of signal light a cascade builds up within these HPDs. The drawn current reaches a maximum which is limited by the $1\,\mathrm{G}\Omega$ series resistor used at PDTF to protect the HPD from damage (see Fig. 4.10). Resistors of a lower value, $150\,\mathrm{M}\Omega$ are employed within the LHCb RICH standard HV distribution system and therefore the continued operation of a degraded HPD in the RICHes will damage the HPD photocathode much quicker. We need to monitor the ion feedback of HPDs closely in RICH 1 and RICH 2 to detect the onset of such vacuum degradation.

A.4 Monitoring the vacuum through monitoring the gain

As shown in the previous sections, we can understand ion feedback as being produced by residual gases in the HPD and that a simplistic model can give us a reasonable approximation to the LIV curves obtained in the presence of ion feedback. We can use the measurement of the LIV curve as a diagnostic tool. This is an independent measure of the vacuum quality.

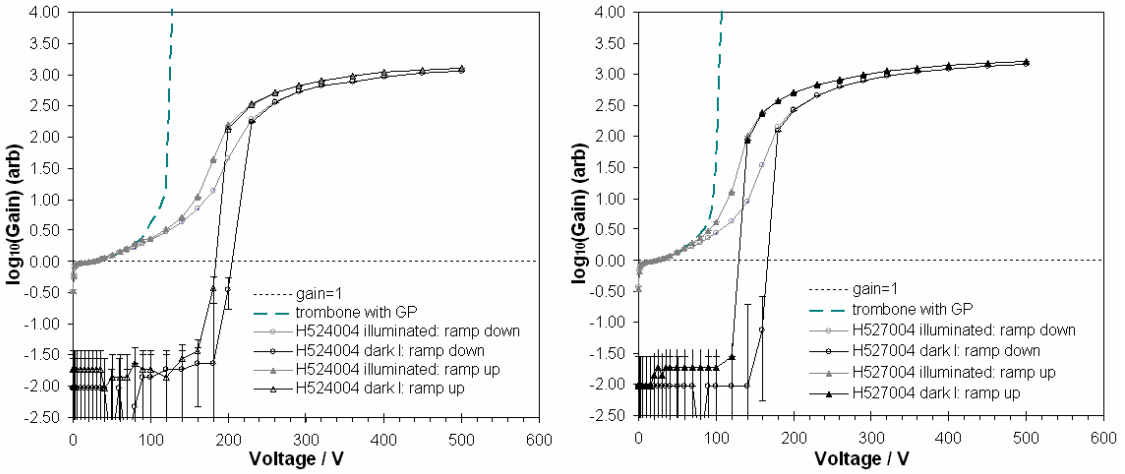

Figure A.4: HPDs with vacuum quality problems removed from the SSB 2 test column. Dark-current and LIV curves are shown from PDTF measurements and compared to the predictions of the previously discussed trombone-like model (Fig. A.2, right), where we describe the build up of the cascade using a geometric progression. Left for H542004. Right for H527004. The dark current resulting from thermionic emission and field effects cascades due to the ion feedback in the HPD as the voltage passes the modeled threshold, where the round-trip gain becomes unity.

It is known that tube vacuum was of lower quality for the preseries HPDs than for the production batches. Due to the necessity to monitor the HPD production, particularly in the early stages and to utilise the HPDs frequently for tests of our LHCb-RICH system, the majority of these preseries HPDs were exposed to ambient atmosphere for several months. As a result of these two factors we would expect to observe accelerated degradation of the vacuum of these preseries HPDs through increasing the level of residual gases, particularly helium. We have measured these effects for the HPDs of the preseries.

In the example case, in Fig. A.1, it is clear that since manufacture and QE testing of the preseries HPD H439004 there has been a large degradation in its vacuum quality, resulting in a large increase in gain as a function of voltage. In this atypical case the gain is extreme and hysteric. This is clearly observed even at low voltages and represents a clear example of the use of this method to identify vacuum degradation.

It is noted that the ion feedback process with the operational primary electron rate, M, of $50\,\mathrm{MHz\,cm^{-2}}$ at the photocathode may remove helium from the HPD over time. Assuming each ion is removed from the vacuum entirely, adsorbing to the photocathode, the decay constant of the helium can be estimated. A

minimum lifetime estimate is obtained by assuming the maximum electron flux of $50\,\mathrm{MHz\,cm^{-2}}$, equal to the maximum hit rate in RICH 1, and the maximum electron-helium cross-section, σ, which peaks at around $\sigma_{max} = (0.37 \pm 0.02) \times 10^{-16}\,\mathrm{cm^2}$ [145]. This is a very low cross section, meaning a large number density of helium is required to produce appreciable ion feedback. Assuming the IFB rate is $\ll 1$ the decay constant of the helium density, λ, is given by $\lambda \approx \sigma_T * M$, which is independent of the magnitude of the number density. A long decay time is expected of $\tau \geq 17\,\mathrm{yrs}$. The time taken will be increased by any additional helium permeation. Under this level of illumination, no observable improvement is expected over the lifetime of LHCb, providing that the IFB rate is $\ll 1$ and other factors, such as cascade effects, do not occur (see Sec. A.3). Under increased illumination and/or in the presence of cascade effects an improvement would be expected.

A.5 Summary

We have demonstrated that the ion feedback effects seen as an increase in the drawn current from the photocathode for a few atypical HPDs, can be understood from first principles. A simple model is presented based on electrostatics that agrees with the data gathered and is consistent with helium being the main pollutant of the HPD vacuum. We have asserted that the ion feedback must be closely monitored in the RICH detectors, and have presented a measurement of the photocurrent as an independent measurement of the ion feedback.

Appendix B

HPD Parameter Distributions Across Baseline Detectors

Many of the HPD parameters measured by DEP and PDTF will directly influence the performance of the LHCb RICH. It is important to consider the distribution of parameters such as HPD quantum efficiencies and HPD dark count across the photon detector planes as the distribution of Cherenkov photons is peaked in the centre of the RICH detectors. With the RICH 1 and RICH 2 detectors now fully populated with HPDs, and mounted in the detector, the distribution of key parameters across the baseline RICHes are presented in this Appendix. The position conventions are defined in Refs. [85, 88], and the column orientation in Refs. [87, 86]. The measurements presented are taken from the DEP and PDTF data which are described in this Thesis in Chapter 4.

B.1 PDTF test results

We adopt a categorisation scheme to qualify HPDs as appears in Table 4.5. HPDs have been mounted preferentially with respect to category, as can be seen in Figs. B.1 and B.2. E-type HPDs have been moved to the edge of columns, to regions of lower

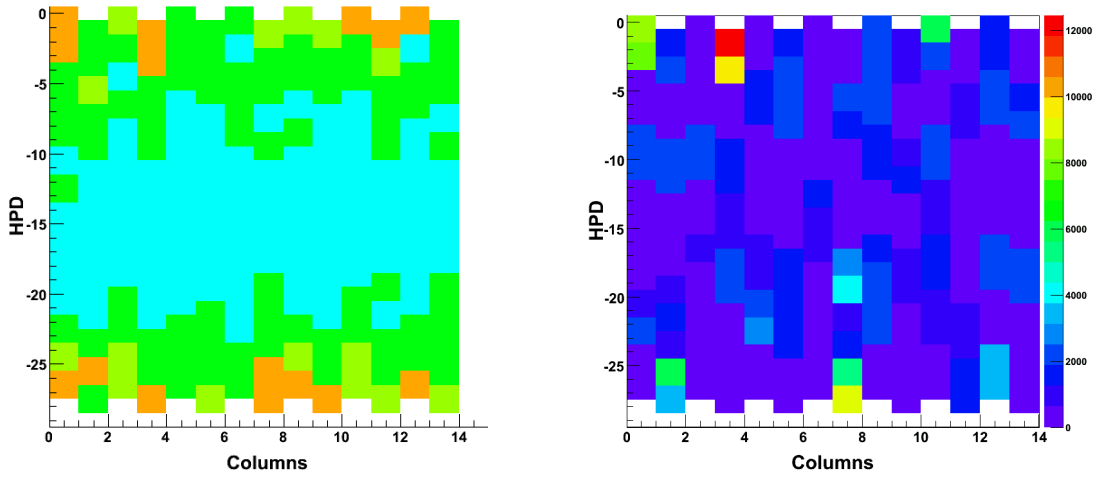

Figure B.1: Left, the categories of HPDs in RICH 1. A+ - Light blue, A - light green, B - dark green, E - amber. Right, leakage currents in nA. Vertical units are 1/2 an HPD, horizontal units are ladders in RICH 1, from left to right is U0-U6, D6-D0, from top-to-bottom in RICH 1.

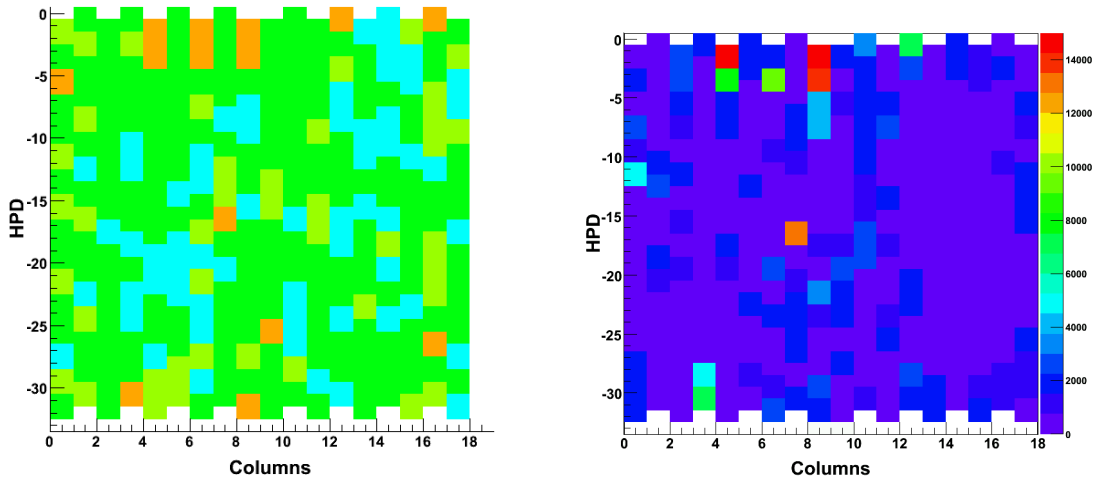

Figure B.2: Left, the categories of HPDs in RICH 2. A+ - Light blue, A - light green, B - dark green, E - amber. Right, leakage currents in nA. Vertical units are 1/2 an HPD, horizontal units are columns in RICH 2, from left to right is from column C0-C8, A0-A8 in RICH 2.

occupancy. As E-type HPDs are each flagged with an issue this procedure removes these flagged HPDs from the highest occupancy regions. HPDs have been grouped together in terms of leakage current to facilitate simpler time alignment. This can also be seen in Figs. B.1 and B.2. The ion feedback percentage and the dark count will be two important factors to monitor during operation of LHCb. Both of these parameters introduce noise in the system which will reduce the pattern recognition

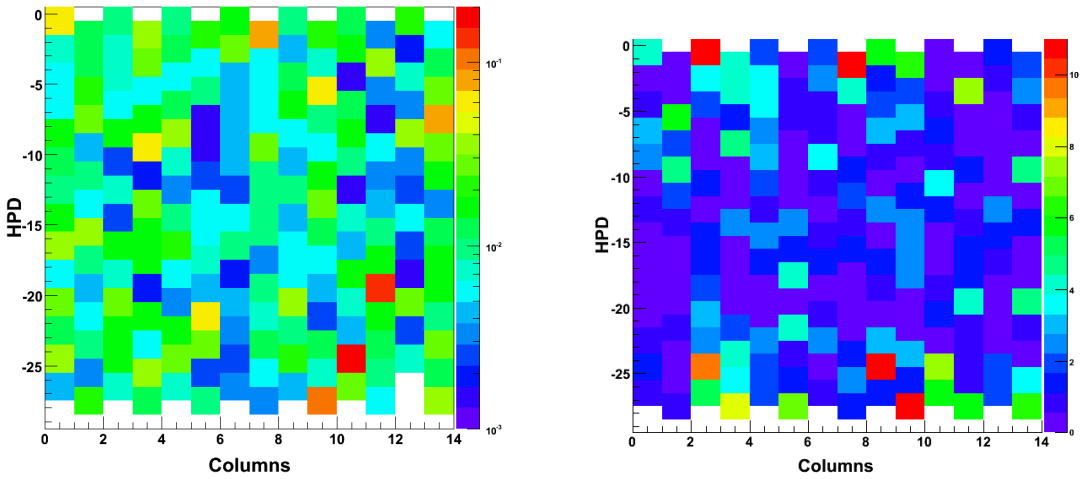

Figure B.3: Left, the distribution of ion feedback percentage in RICH 1. Right, the dark count distribution in kHz cm^{-2}. Vertical units are 1/2 an HPD, horizontal units are ladders in RICH 1, from left to right is U0-U6, D6-D0, from top-to-bottom in RICH 1.

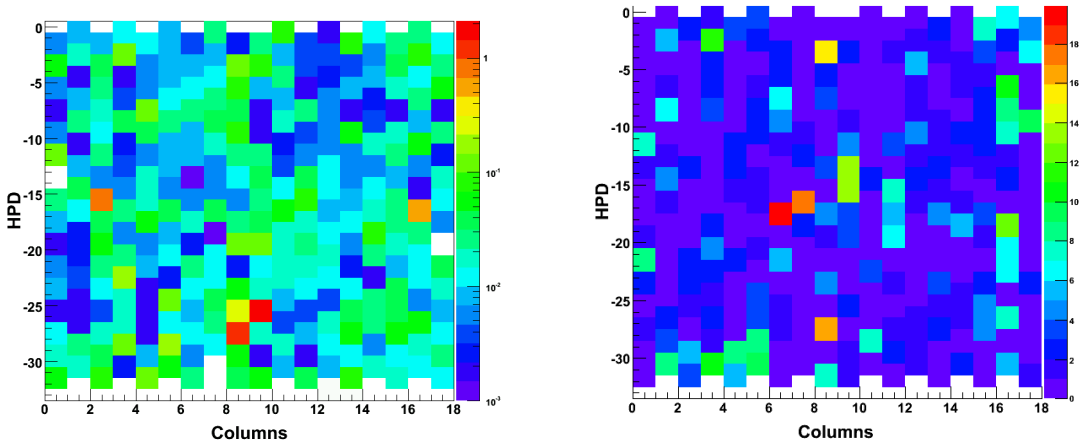

Figure B.4: Left, the distribution of ion feedback percentage in RICH 2. Right, the dark count distribution in kHz cm^{-2}. Vertical units are 1/2 an HPD, horizontal units are columns in RICH 2, from left to right is from column C0-C8, A0-A8 in RICH 2.

performance and either could potentially increase as a function of time. The baseline distribution of these parameters is given in Figs. B.3 and B.4.

B.2 Photon distributions

The expected distribution of Cherenkov photons from $b\bar{b}$-inclusive events from our Monte Carlo simulation are shown in Figs. B.5 and B.6. The distribution of photons

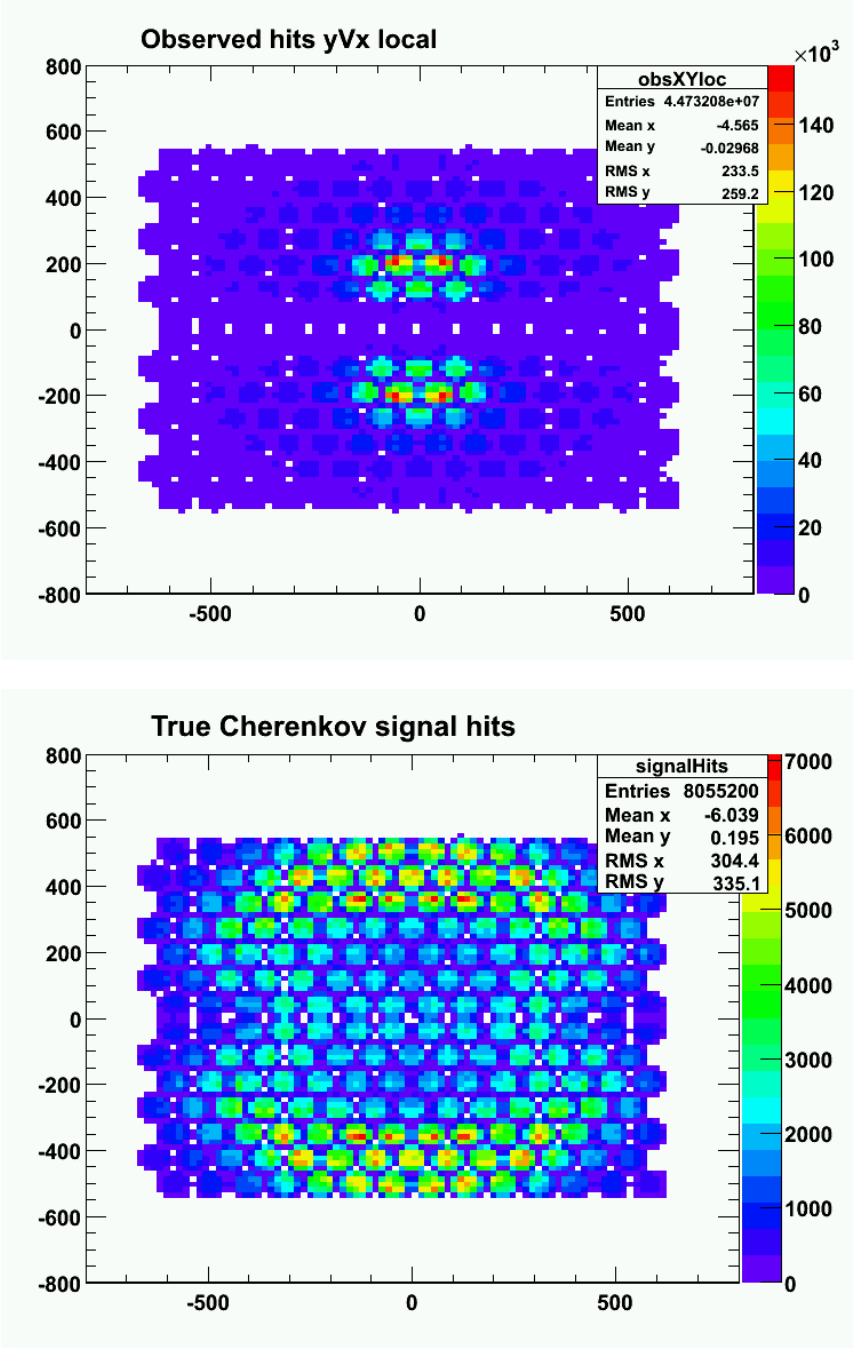

Figure B.5: The simulated distribution of photons in RICH 1, from Monte Carlo simulated $b\bar{b}$-events. The scales and units are arbitrary. The acceptance of individual HPDs can be seen. Top, for all hits. Bottom, true hits from the Aerogel radiator only.

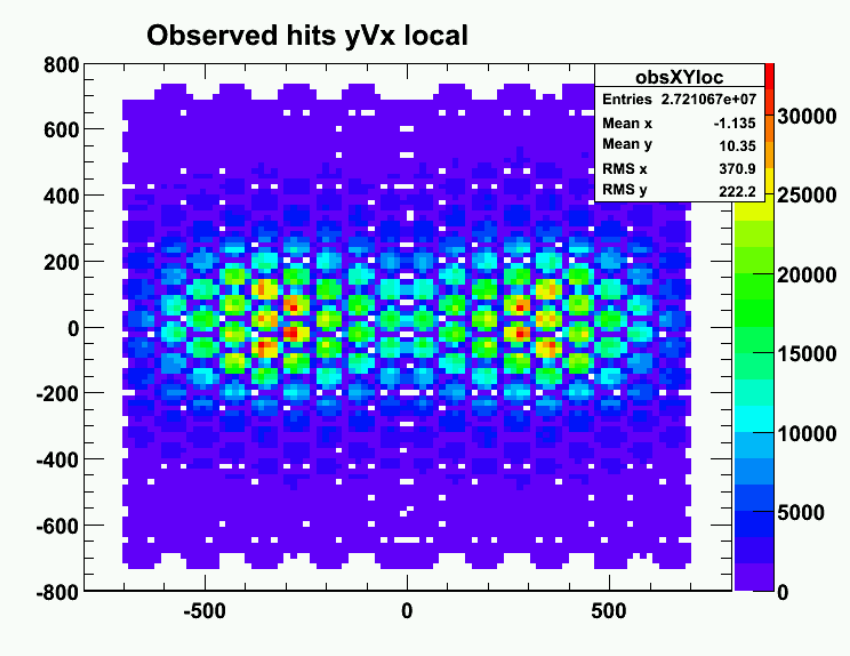

Figure B.6: The simulated distribution of photons in RICH 2, from Monte Carlo simulated $b\bar{b}$-events. The scales and units are arbitrary. The acceptance of individual HPDs can be seen.

is peaked in the central regions in both detectors as the majority of charged particles are produced at low angles to the beam. In RICH 2 the distribution is flatter compared to RICH 1 due to secondaries, material scattering, the effect of the magnet, and the smaller acceptance subtended by RICH 2. It can be seen that in RICH 1 the majority of hits fall on 20 of the 196 HPDs. The distribution of Aerogel photons is much flatter due to their larger Cherenkov angle and lower momentum threshold.

B.3 Quantum efficiency distributions

The distributions of the integrated quantum efficiencies across the baseline detectors are plotted in Figs. B.7, B.8 and B.9. The procedure used to integrate the QE is described in Sec. 4.3.5.2. HPDs in RICH 2 were positioned at random with respect to quantum efficiency, then the columns of HPDs were positioned to equalize the quantum efficiency and the expected occupancy on the left and right of the detector. In RICH 1, where the photon distribution is more decidedly peaked in the central regions, HPDs were specifically orientated with respect to QE to place

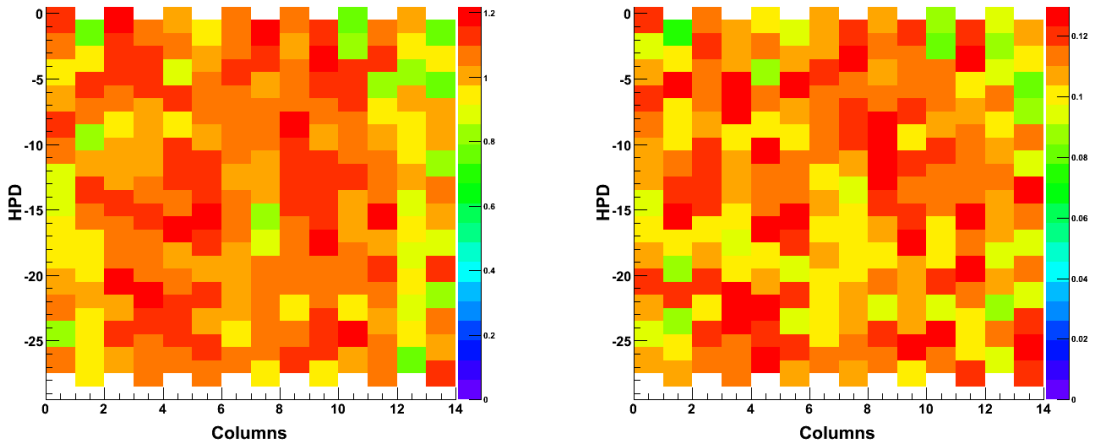

Figure B.7: Integrated QE distributions across RICH 1. Left, over the full wavelength range. Right, weighting for the expected wavelength distribution of photons from the Aerogel radiator. Vertical units are 1/2 an HPD, horizontal units are ladders in RICH 1, from left to right is U0-U6, D6-D0, from top-to-bottom in RICH 1.

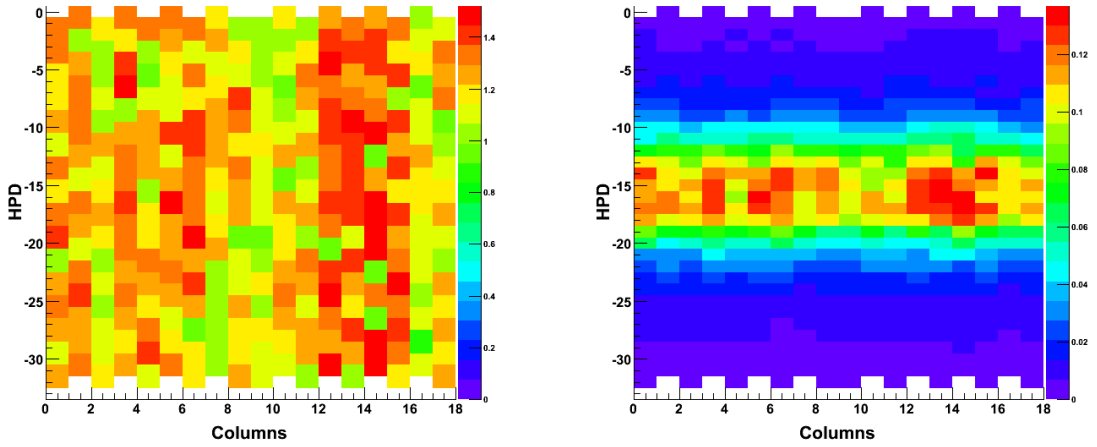

Figure B.8: Left, HPD goodness distributions across RICH 2. Right, the HPD goodness weighted for the average vertical photon occupancy within each column. Vertical units are 1/2 an HPD, horizontal units are columns in RICH 2, from left to right is from column C0-C8, A0-A8 in RICH 2

the highest QE tubes in the regions of highest occupancy, capitalising on the HPD quality. It can be seen that the distribution of overall ΣQE δE in RICH 1 is peaked in the central region (Fig. B.7 left), and that the $\Sigma\mathrm{QE} \times T \times A\,\delta\mathrm{E}$ weighted for Aerogel performance appears flatter (Fig. B.7 right). The procedure for weighting this integral is given in Sec. 4.3.5.2. The chosen distribution of HPDs mimics the distribution of Cherenkov light. Photons from the Aerogel radiator are relatively uniform, and the photons from the gas radiator are highly peaked in the central

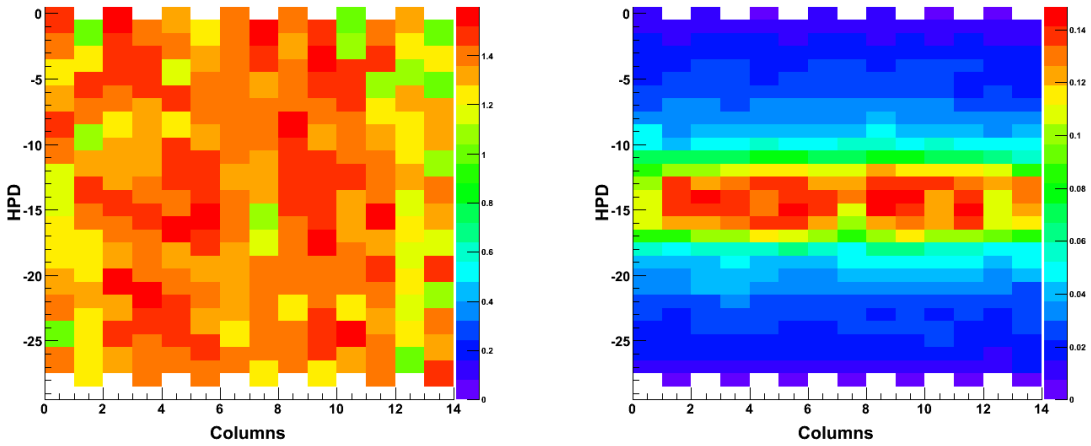

Figure B.9: Left, HPD goodness distributions across RICH 1. Right, the HPD goodness weighted for the average horizontal photon occupancy within each ladder. Vertical units are 1/2 an HPD, horizontal units are ladders in RICH 1, from left to right is U0-U6, D6-D0, from top-to-bottom in RICH 1.

regions. Due to the lack of a strong correlation between the overall integrated QE and the QE weighted for Aerogel performance, our orientation provides good performance in both cases.

For the gas radiators we define a parameter, the 'HPD goodness' which is a relative measure of the overall efficiency of each HPD relative to the expectations from DC06. We weight the integrated quantum efficiency (across the full wavelength range), the number of dead channels and (to a much smaller extent) the HPD dark count, as measured by the PDTFs [1]. Due to the excellent HPD quality, this is highly dominated by the HPD QE.

The HPD goodness convoluted with the overall occupancy of HPDs, in terms of the average photon distribution within each HPD column or ladder (one-dimensionally) as shown in Figs. B.8 and B.9. This plot demonstrates the importance of the central HPDs to the overall performance of the RICH. The anticipated improvement in photon yeilds is described in Sec. 4.3.6. We estimate the increase in the number of recovered photons in RICH 2 to be 22 % and the increase in the number of photons in RICH 1 to be 36 %. This will directly improve the performance of the LHCb particle identification system.

Appendix C

Generator Study of the Production Asymmetry for LHCb

Proton-proton interactions at LHC are not charge symmetric, or CP-symmetric. The resulting production asymmetry is a key systematic to many measurements at LHCb as discussed in 6.1.4. We define a production asymmetry, δ_p^i, for each particle type, i, which we generically expect to be non-zero[1]:

$$\delta_p^i = \frac{\bar{I}}{I} - 1 \tag{C.1}$$

where I and $\bar{I}$ refer to the number of particles and antiparticles produced.

Previous studies of production asymmetry [130, 131, 132] focus on the general production asymmetries at general LHC detectors, commonly examining a subset of heavy-quark species, examining a particular subset of parameters. Due to the unusual high-rapidity ranges probed by LHCb, different overall asymmetries are expected, additionally asymmetries in the backgrounds and underlying events are important for systematic studies.

In this Appendix we summarize an LHCb-specific study of the production asymmetry which is detailed further in Ref. [6] and available on request. In this study

[1] We adopt the convention of Nierste from Ref. [37].

we estimate the production asymmetry in LHCb for many event types and particles comparing the PYTHIA and HERWIG generators. In particular we examine the energy, pseudo-rapidity and transverse momentum dependence crucial to determine whether triggering and signal selections will alter the production asymmetry.

C.1 Phenomenology of asymmetric mechanisms

In this section we discuss phenomenologically the mechanisms which are asymmetric in the production of species following the approach of Refs. [130, 131] and [147].

In our discussion we define the following terms. The hard-scattered products are partons resulting from the perturbative high-energy scattering process (e.g. $gg \to b\bar{b}$). The beam remnant is the collection of quarks and gluons remaining from the two interacting protons. We define the underlying event as any interaction not including the hard scatter.

At LHC we start with the collisions of two proton beams. We expect an overall excess in the production of baryons to anti-baryons and an overall charge asymmetry. We start with an excess of u and d quarks with respect to their antipartners, so would expect produced particles with these constituents to be highly asymmetric. LHCb concentrates on the high-rapidity regions of phase space. LHCb is therefore sensitive to processes which redistribute the particle and antiparticle content as a function of rapidity and transverse momentum. Even species produced symmetrically (such as $gg \to b\bar{b}$) may be asymmetric within the LHCb acceptance (e.g. $N(b) \neq N(\bar{b})$).

Such a mechanism is that of beam drag. The beam remnants, with a high particle content of u and d quarks in particular, propagate close to the kinematic limit of pseudo-rapidity and at a very low transverse momentum. The remnant may exhange momentum with a hard-scattered parton, drawing the hard-scattered product towards the beam, as shown in Fig. C.1. For example, this produces an excess of $\bar{B}^0_d$ compared with B^0_d-mesons at high rapidity [131].

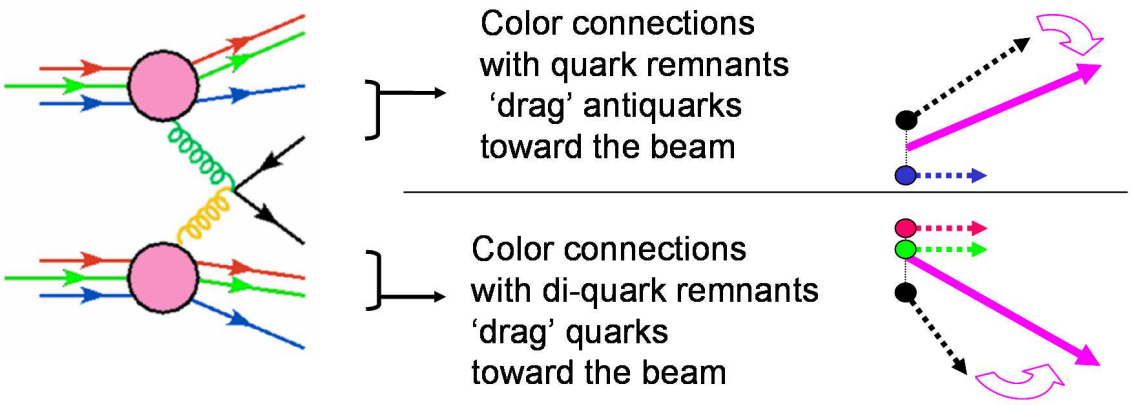

Figure C.1: Simplified cartoon illustration of beam drag. Beam remnants redistribute the proportions of quarks and antiquarks in pseudo-rapidity and transverse momentum, pulling them towards the beam. On the left you see a cartoon of the hard-scattering process, on the right a cartoon of the effect of beam-drag, where the black dotted lines represent the momentum of the hard-scattered parton, the coloured-dotted lines represent the momentum of the beam remnants and the solid pink line represents the resultant momentum.

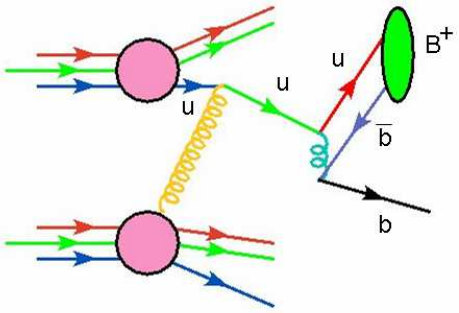

Figure C.2: Scattered valence-quarks, after [131]. Scattered valence quarks directly result in production asymmetries for heavier species. These processes are analogous to deep inelastic scattering: in this cartoon a gluon from the lower proton probes the parton distribution functions in the upper proton.

High-p_T, high-energy, jets produced from a directly scattered valence quark will be biased by the asymmetry in the valence quarks available [131]. This valence-quark scattering is demonstrated in Fig. C.2. For example, this would produce an excess of B_d^0 at high p_T and E.

The final direct mechanism considered here is cluster collapse [147]. Hard-scattered quarks may directly hadronize with beam remnants, or scattered valence quarks as is shown in Fig. C.3. This is the extreme case of beam drag and is also asymmetric. This mechanism enhances the production of leading particle types. For B_d^0-mesons this produces an excess of B_d^0 increasing slowly with rapidity [131].

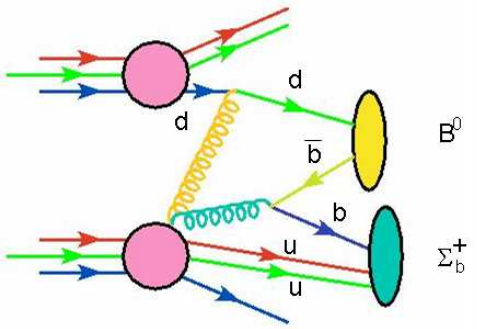

Figure C.3: Cluster collapse, after [131]. Enhances the production of leading particles which directly hadronize with the beam remnants, maintaining flavour content from the beam remnants. Two examples are shown in this cartoon, for the enhancement of B_d^0 and Σ_b^+.

As these mechanisms effect the availability of certain quark species, considering conservation laws, they even produce an asymmetry in species which are unable to directly accept a beam remnant, for example $\bar{B}_s^0$-mesons.

One expects, as found by Ref. [130]:

$$|\delta_p^{B^\pm}| \geq |\delta_p^{B_d^0}| \geq |\delta_p^{B_s^0}| \neq 0 \tag{C.2}$$

As the distribution of beam remnants is highly peaked toward the kinematic limit of pseudo-rapidity and toward zero transverse momentum one expects the production asymmetry to be functions of these two variables, and that LHCb's high-rapidity range will bias the overall asymmetry to larger values compared to central detectors.

These three mechanisms have indeed been investigated separately in Monte Carlo using the PYTHIA generator, for example by Refs. [131] and [147], in good agreement with the theoretical arguments presented.

C.2 Fragmentation in HERWIG and PYTHIA

This study, in essence, could be viewed as a study of fragmentation. Here we refer to fragmentation as the whole set of processes following the hard scatter resulting in observable final state mesons and baryons. Fragmentation is a non-perturbative

process in QCD and is insolvable by direct analytical means. One overcomes this problem by separating the process into a high-energy perturbative part, and a low-energy non-perturbative part. The perturbative part is commonly called 'showering'. The non-perturbative stage is commonly called 'hadronization', 'confinement', and ambiguously also referred to as fragmentation if additional final states particles are created. Confinement is followed by possible immediate decay of heavy, unstable, resonances, which is also a calculable process. Hard scattering and showering can be described well in perturbation theory, by, for example, a matrix-element method, as can the decay process. This leaves the non-perturbative region which one can either parameterise from available data, or provide a more simplistic model with input parameters collected empirically.

We choose to compare two generators, HERWIG and PYTHIA, whose models differ significantly to study the effects on production asymmetry. In the following section we address the differences between these generators which both use the model-centred approach. Covering their fragmentation, their minimum bias methods and their methodology for underlying events. HERWIG and PYTHIA are examples of parton-shower event generators [148].

HERWIG, an event generator for Hadron Emission Reactions With Interfering Gluons, is a Monte Carlo event generator and physics simulator [149], frequently used in high-energy physics experiments. HERWIG 6.510, the most recent version, is written in the Fortran language.

PYTHIA, prolific in high-energy physics experiments, particularly for hadron colliders, is also a Monte Carlo event generator [96]. PYTHIA 6.41 is the most recent version, also written in Fortran.

HERWIG and PYTHIA both use a matrix element calculation to perform hard scattering processes, submit the products to parton showering, fragmentation, confinement and decay.

C.2.1 Minimum Bias

HERWIG and PYTHIA both begin their minimum bias simulations with a parameterisation of the total cross-section. Both generators use a Donnachie-Landshoff fit parameterised in terms of s to an exponent, with the same parameters [148].

In PYTHIA no separation between soft minimum bias and hard scattering processes is made, in both cases a multiple-interaction model is adopted, that is controlled by the minimum transverse momentum permitted in each interaction. In this way there is no realised cut off between hard and soft processes.

In HERWIG a much simpler model based on the UA5 parameterisation of soft collisions is adopted. Only soft collisions are simulated, which is not particularly applicable at LHC energies and luminosities where hard scattering events are much more frequent and are significant in minimum bias samples. This does have the advantage of increased generation speed for minimum bias events. Only u, d, s and small numbers of c are generated.

C.2.2 Fragmentation

Parton showering is essentially the same in the two generators, which employ the DGLAP equations to evolve the partons down to a cut-off energy which approaches the non-perturbative regime. HERWIG performs the showering down to very low energies, essentially exhausting the perturbative regime, allowing showering down to radiation of gluons with twice the mass of the down quark. PYTHIA cuts showering at a higher energy of 1 GeV.

Hadronisation and confinement are treated entirely differently by the two generators, as is characterised in Fig. C.4.

HERWIG takes the selection of shower products within each jet, forces any gluons to decay to light quarks, and performs a colour-clustering, to link quarks/antiquarks, diquarks/antidiquarks, into colour-singlet states. These intermediate clusters are

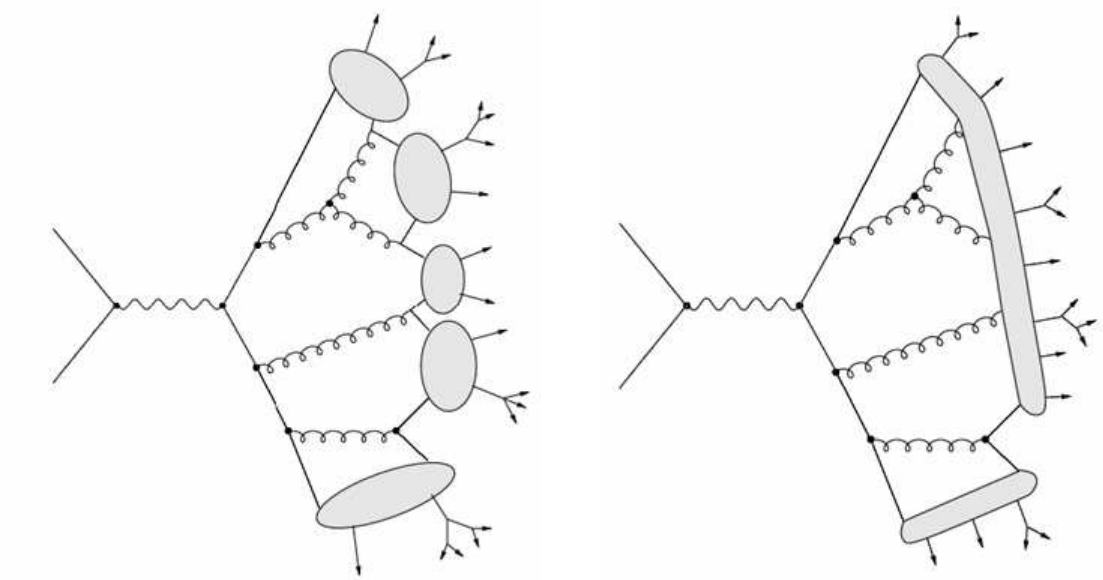

Figure C.4: Fragmentation and hadronization schema for two different models. Left, a cluster model, such as that used in HERWIG, right for a Lund-string model, as used in PYTHIA.

then allowed to decay. If a cluster is too light to decay into two hadrons, it is taken to represent the lightest single hadron of its flavour. A redistribution of four-momenta may then be performed to bring the hadrons on-shell. This is known as the 'clustering' model.

PYTHIA uses the more complicated Lund-string model [96]. At the termination of showering, colour connections are identified between partons in the overall event, which are described by a linearly-increasing confinement potential of $1\,\mathrm{GeV\,fm^{-1}}$ between the partons (including gluons). Fragmentation is allowed when the energy stored in the confinement potential reaches the mass of a quark-antiquark pair which is subsequently pulled from the vacuum. These partons are permitted to tunnel into the neighboring potential wells of the confinement potential. Fragmentation is propagated from one end of the string to the other. It is believed this propagation of probability amplitudes and permission of quantum effects is more theoretically sound than the clustering model.

Clusters in HERWIG are created and then forced to fragment further if their mass is above a tuned cut-off value. As standard this cut is below the threshold for the production of b-baryons. This is expected to have large implications on the

production asymmetry of other b-hadrons. From the discussions in Sec. C.1 it is clear that the baryon production asymmetry is expected to be very large, when the production of baryons is prevented by HERWIG this asymmetry will be redistributed among lighter hadrons. A retuning of the cluster parameters has been performed by the CDF collaboration for the study of b-baryon formation and a similar tuning should be adopted to address this issue at LHCb, although we have not attempted this here.

C.2.3 Underlying event

In the underlying event the unified model adopted by PYTHIA allows for multiple interactions between the partons in the beam hadrons [150]. HERWIG does not allow for multiple interactions, which will significantly change the kinematics and shapes within the underlying event. HERWIG can be used together with the simulation routines, JIMMY [151], though we have not attempted this here, which models underlying interactions based on multiparton interactions, and so is similar to the model used by PYTHIA.

Although both HERWIG and PYTHIA keep the same generator for soft collisions in the underlying event as they have for minimum bias events, interactions between the hard-scattered partons, the underlying event and the beam remnants are handled entirely differently. This is best demonstrated by a direct quote from the PYTHIA manual [96]:

> *"Each incoming beam particle may leave behind a beam remnant, which does not take active part in the initial-state radiation or hard-scattering process. If nothing else, these remnants need to be put together and colour connected to the rest of the event."*

PYTHIA does not intervene in the colour-connection of hard-scattered products to the beam remnants and therefore the underlying event. As intuition would suggest,

the same model is applied to both; therefore beam remnants can effect the jet composition and distribution.

We can compare this with HERWIG [149]:

> *"In hadron-hadron and lepton-hadron collisions there are beam clusters containing the spectators from the incoming hadrons. In the formation of beam clusters, the color connection between the spectators and the initial-state parton showers is cut by the forced emission of a soft quark-antiquark pair. The underlying soft event in a hard hadron-hadron collision is then assumed to be a soft collision between these two beam clusters."*

HERWIG forces the isolation of the beam remnants and the underlying event such that it can more easily be described by the UA5 model.

One can clearly see this treatment will have a large impact on the production asymmetries simulated by the two event generators. The cutting of the colour connection will obviously eliminate the phenomena of beam drag and cluster collapse to first order for the hard-scattered partons. The inclusion of JIMMY to simulate multiple interactions within HERWIG is unlikely to correct for this major issue as a direct separation will then be apparent between any of the products from the interactions and the beam remnant.

C.2.4 The low transverse momentum region

In direct contrast to many other hadron collider experiments LHCb is concentrating on the high-rapidity region, $2.0 \leq \eta \leq 4.9$, benefiting from the large correlated $b\bar{b}$ production at high rapidities. We will heavily exploit the regime of low transverse momentum, and will be influenced by backgrounds in the low-p_T region. In terms of modeling, this is an unusual use case which will heavily test the models used by the event generators.

Multiple interactions are particularly important in the low transverse momentum regime $p_T < 10\,\text{GeV}$ [150]. An adequate desciption of the underlying event may be obtained with the UA5 model, tuned to the observed multiplicity, however hard-scattering at low p_T is also probed by LHCb, typically down to the level of $p_T \sim 5\,\text{GeV}$. The resultant changes in the event shape and flavour distributions due to multiple scattering can no longer be mitigated through simple retuning of the Donnachie-Landshoff fit. PYTHIA as standard or HERWIG with JIMMY are clearly more appropriate for LHCb.

There are additional effects at low transverse momentum from the breakdown of perturbative calculations to leading order. Standard HERWIG and PYTHIA are both leading order (LO) models. That is they employ the LO descriptions of hard scattering (LO matrix elements) and have been historically employed with LO PDFs. There is a systematic problem with LO event generation at low transverse momentum, $p_T < 10\,\text{GeV}$, caused by the low-p_T singularities in the descriptions of parton showering.

Within PYTHIA the singularity is regularised through direct modification of the gluon propagator, which is an approximation valid for low momentum (see Ref. [150] or Sec. 11 in Ref. [96]). Here PYTHIA can no longer be said to be strictly LO, and there is no sound theoretical justification for the modifications performed, however, comparisons with low momentum data from experiment (i.e. UA5 and E735) and subsequent tuning are then possible [150].

In HERWIG no correction is made, and no tuning to low momentum experiment, with obvious large influences on the simulation of low-momentum processes as probed by LHCb. HERWIG can be combined with next-to-leading order (NLO) processes with the routines provided by MC@NLO [152], which we have not attempted here. This is expected to improve the simulation of the low p_T spectrum due to the resummation which is performed.

To summarise, the low-p_T region cannot be well modeled perturbatively. Initial data from LHCb and TOTEM will shed interesting light on the validity of these models.

Table C.1: Event types generated to study production asymmetry.

Event Type	Tuned PYTHIA	Standard PYTHIA	HERWIG	DC06 (PYTHIA)
Minimum Bias	10.5M	10M	10M	0.8M
inclusive $b\bar{b}$	11.6M	1M	11M	26M
B_s^0 or B_d^0	22.3M†	1M†	–	7.0M

† stable B_s^0 and B_d^0

C.3 Generator-level study

To facilitate the prediction of the production asymmetry down to the 10^{-3}-level across several bins in, for example, transverse momentum, tens of millions of events were generated using the LHCb Gauss System. This section reports in an LHCb specific way the study performed and the results obtained. Throughout this study DC06-compatible Gauss version 25r9 was used, with standard DC06 options.

C.3.1 Event types

Table C.1 gives a summary of the dedicated samples generated and used in this study, and compares these to the available DC06 events used as a comparison set. In all cases we study a beam luminosity of $2 \times 10^{32}\,\mathrm{cm}^{-2}\mathrm{s}^{-1}$ with the relative proportion of pileup events allowed.

Standard options were used for the generation of the standard PYTHIA sample. A recent retuning of PYTHIA performed by K. Lessnoff was used as the major sample for this study 'Tuned PYTHIA' [153]. This retuning was expected to improve the event multiplicities and proportion of hadrons, particularly excited B-states in line with current experimental data from CDF and UA5. Any change to the overall multiplicity, and distributions will effectively dilute, or concentrate, the initial beam asymmetry and therefore may alter the production asymmetry.

Inclusive $b\bar{b}$ events were taken from a large inclusive dimuon sample. For the personally generated B_s^0 or B_d^0 samples the B_s^0 or B_d^0 was forced to be stable. This

Table C.2: Production asymmetry, δ_p, in minimum bias events.

Particle	PID	Tuned PYTHIA	Standard PYTHIA	HERWIG	DC06 (PYTHIA)
		$\delta_p * 1000$			
$\pi^{\pm}$	± 211	$-(4.23 \pm 0.16)$	$-(4.12 \pm 0.16)$	$-(1.21 \pm 0.10)$	$-(3.4 \pm 5.6)$
$K^{\pm}$	± 321	$-(17.00 \pm 0.45)$	$-(15.03 \pm 0.45)$	$-(0.08 \pm 0.44)$	$-(15.8 \pm 1.7)$
$D^{\pm}$	± 411	---[1]	---[1]	---[1]	$+(1.2 \pm 28.9)$
D^0	± 421	$+(6.9 \pm 4.6)$	$+(11.6 \pm 4.9)$	$-(3.6 \pm 5.7)$	---[1]
$D_s^{\pm}$	± 431	$-(4.5 \pm 10.2)$	$+(7.8 \pm 10.9)$	NA[2]	$+(15.1 \pm 37.8)$
$B^{\pm}$	± 521	$+(4.4 \pm 13.8)$	$-(1.8 \pm 14.6)$	NA[2]	$+(40.8 \pm 50.8)$
B_d^0	± 511	$-(6.7 \pm 12.6)$	$-(13.7 \pm 13.4)$	NA[2]	$+(82.7 \pm 45.8)$
B_s^0	± 531	$+(7.7 \pm 22.6)$	$+(1.8 \pm 24.2)$	NA[2]	---[1]
$e^{\mp}$	± 11	$-(0.15 \pm 1.33)$	$-(0.46 \pm 1.38)$	$-(0.09 \pm 0.87)$	$+(0.37 \pm 0.50)$
$\mu^{\mp}$	± 13	$-(9.8 \pm 9.5)$	$+(6.9 \pm 10.1)$	$-(8.4 \pm 11.1)$	$+(1.0 \pm 0.9)$

[1] insufficient statistics or no data for this comparison

[2] due to the different nature of HERWIG minimum bias treatment, hard scattering is not observed.

enables simplistic decoupling of the production asymmetry of the signal particles from the production asymmetry of the background (i.e. the many other particles in the signal event). This is quite an important situation to understand and will not be provided as a standard DC06 sample, nor in data.

More than 90M events are used for comparison in this study.

C.3.2 Results

We have found consistently that the tunings of PYTHIA used within this study agree in terms of the production asymmetry, and have found that HERWIG consistently disagrees with the predictions of PYTHIA.

C.3.3 Minimum bias

The minimum bias samples produced give a large kaon and pion sample which can be analysed for production asymmetry, and a smaller charmed hadron and lepton sample for comparison. Typically tens of millions of pions and kaons were are produced from each generator. Table C.2 compares the overall production asymmetry within these samples, where the statistical errors on δ_p are of order 1% or less. We plot the production asymmetry distributions as a function of energy,

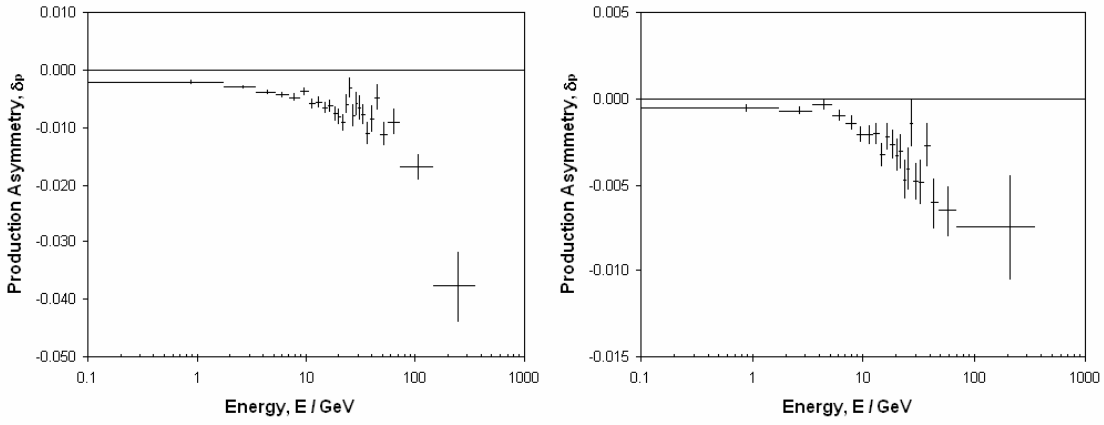

Figure C.5: Minimum bias production asymmetry with energy, $\delta_p(E)$ for charged pions. Left, for Tuned PYTHIA, Right for HERWIG. Event samples shown are given in Table C.1. The trends in the two plots seem to agree, although the production asymmetry in PYTHIA has a larger magnitude.

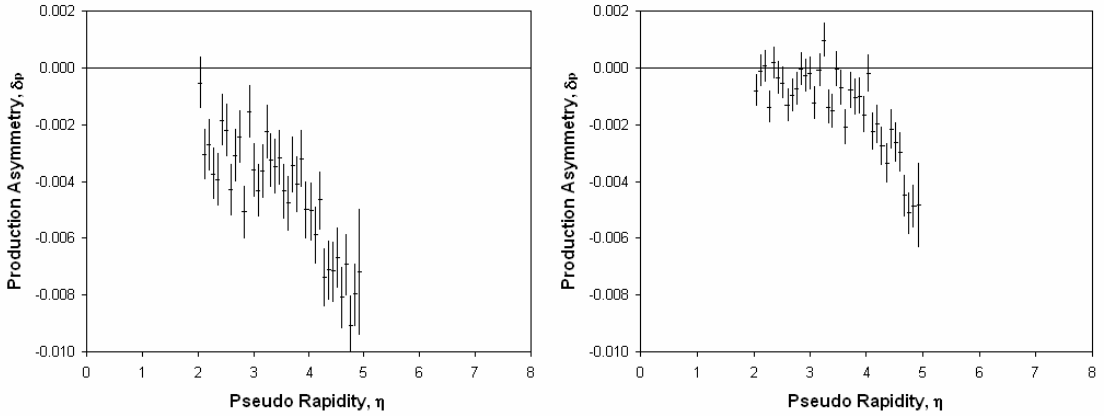

Figure C.6: Minimum bias production asymmetry with pseudorapidity, $\delta_p(\eta)$ for charged pions. Left, for Tuned PYTHIA, Right for HERWIG. Event samples shown are given in Table C.1. The trends in the two plots seem to agree, although PYTHIA produces larger asymmetries in terms of absolute value.

pseudo-rapidity and transverse momentum in Figs. C.5, C.6 and C.7 for charged pions, which displays the typical trends seen in minimum bias samples.

One can discern that PYTHIA seems to predict larger asymmetries than HERWIG. With the exception of pions there are no statistically significant overall asymmetries in HERWIG.

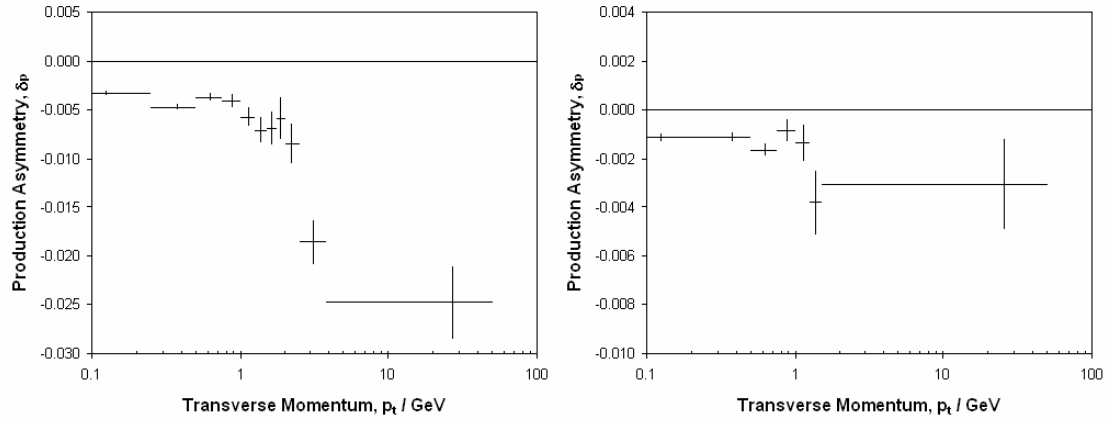

Figure C.7: Minimum bias production asymmetry with transverse momentum, $\delta_p(p_T)$ for charged pions. Left, for Tuned PYTHIA, Right for HERWIG. Event samples shown are given in Table C.1. In this case, no trend is evident for HERWIG, which we attribute to the lack of hard scatter in HERWIG minimum bias events.

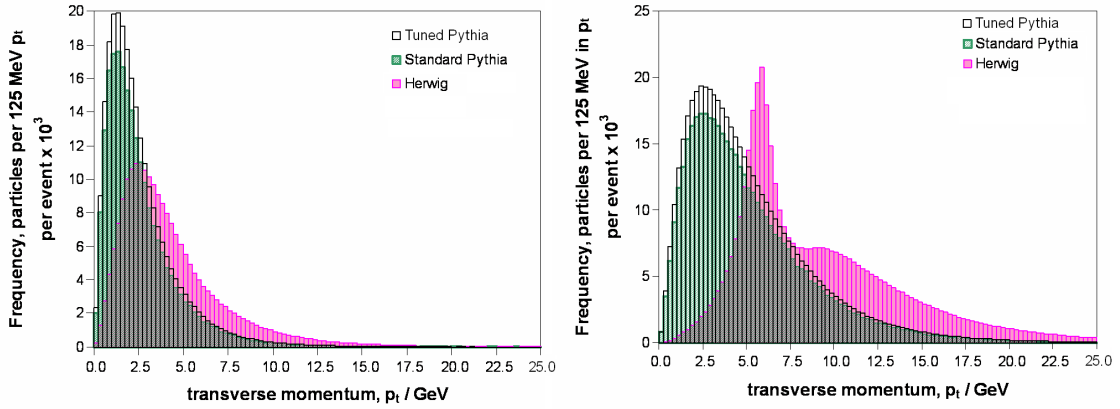

Figure C.8: Transverse momentum distribution of $D_s^{\pm}$ and $B^{\pm}$ in the generated inclusive $b\bar{b}$ samples normalised to the number of events simulated. Left, $D_s^{\pm}$, Right, $B^{\pm}$. Event samples shown are given in Table C.1. The distributions from the three samples are overlaid. HERWIG production of $B^{\pm}$ seems to disagree with PYTHIA.

C.3.4 Inclusive $b\bar{b}$

The inclusive $b\bar{b}$ samples produced give a biased kaon and pion sample, and significant B-meson and leptonic samples which can be analysed for production asymmetry. To indicate the number of particles generated we plot the transverse momentum distribution of $B^{\pm}$ and $D_s^{\pm}$ in Fig. C.8 One can also see considerable differences in these distributions between PYTHIA and HERWIG.

Table C.3 compares the overall production asymmetry within these samples, where

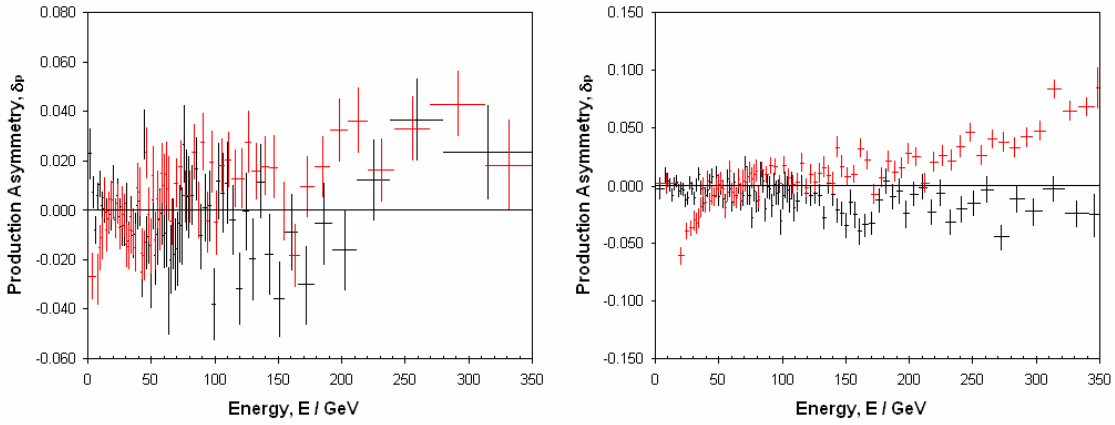

Figure C.9: Inclusive $b\bar{b}$ production asymmetry with energy, $\delta_p(E)$ for Tuned PYTHIA and HERWIG. Left, for $D_s^{\pm}$, Right for $B^{\pm}$. PYTHIA in black and HERWIG in red. Event samples shown are given in Table C.1.

the statistical errors on δ_p are of order 1% or less. Once again we can see a consistent, now very obvious, disagreement between PYTHIA and HERWIG, particularly in the heavy mesons. We plot the distributions of production asymmetry as a function of energy and transverse momentum in Figs. C.9 and C.10 for $B^{\pm}$ and $D_s^{\pm}$, to display the typical trends seen in inclusive $b\bar{b}$ samples.

For the light and charm mesons, such as $D_s^{\pm}$, it seems the two generators agree, save the region of very low transverse momentum and energy, where the perturbative LO calculation as performed numerically by HERWIG is expected to break down. For the heavier mesons, however, such as $B^{\pm}$ the distributions are entirely different. At the very low energy scale or momenta $< 10\,\text{GeV}$ this can again be attributed to

Table C.3: Production asymmetry, δ_p, in inclusive $b\bar{b}$ events.

Particle	PID	Tuned PYTHIA	Standard PYTHIA	HERWIG	DC06 PYTHIA
			$\delta_p * 1000$		
$\pi^{\pm}$	± 211	$-(2.16 \pm 0.09)$	$-(1.8 \pm 0.3)$	$-(0.5 \pm 0.08)$	$-(2.20 \pm 0.07)$
K^{*0}	± 313	---[1]	---[1]	---[1]	$-(5.26 \pm 0.28)$
$K^{\pm}$	± 321	$-(7.73 \pm 0.26)$	$-(7.6 \pm 1.0)$	$+(2.47 \pm 0.25)$	$-(7.18 \pm 0.19)$
$D^{\pm}$	± 411	---[1]	---[1]	---[1]	$+(1.7 \pm 0.6)$
D^0	± 421	$+(4.6 \pm 0.6)$	$+(0.6 \pm 2.4)$	$-(7.2 \pm 0.7)$	$+(3.8 \pm 0.4)$
$D_s^{\pm}$	± 431	$-(1.6 \pm 1.1)$	$+(3.4 \pm 4.3)$	$+(2.8 \pm 1.3)$	$-(1.2 \pm 0.8)$
$B^{\pm}$	± 521	$-(6.5 \pm 0.8)$	$+(0.6 \pm 3.0)$	$+(12.8 \pm 0.9)$	$-(7.2 \pm 0.5)$
B_d^0	± 511	$-(3.2 \pm 0.7)$	$-(1.3 \pm 2.7)$	$+(8.8 \pm 0.8)$	$-(2.7 \pm 0.5)$
B_s^0	± 531	$-(1.9 \pm 1.3)$	$+(0.5 \pm 4.9)$	$-(14.1 \pm 1.5)$	$+(0.6 \pm 0.9)$
$e^{\mp}$	± 11	$+(0.01 \pm 1.17)$	$+(0.9 \pm 2.3)$	$-(0.22 \pm 0.59)$	$-(0.25 \pm 0.49)$
$\mu^{\mp}$	± 13	$+(2.0 \pm 1.2)$	$+(0.9 \pm 2.3)$	$-(3.4 \pm 1.2)$	---[2]

[1] insufficient statistics or no data for this comparison

[2] not presented due to the inherant bias in the sample used.

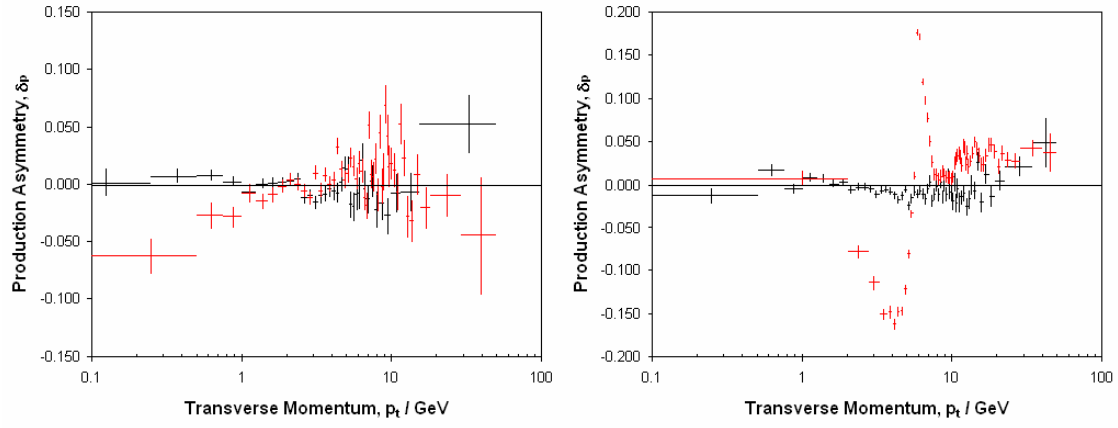

Figure C.10: Inclusive $b\bar{b}$ production asymmetry with transverse momentum, $\delta_p(p_T)$ for Tuned PYTHIA and HERWIG. Left, for $D_s^{\pm}$, right for $B^{\pm}$. PYTHIA in black and HERWIG in red. Event samples shown are given in Table C.1.

Table C.4: Production asymmetry, δ_p, for selected heavy baryons in inclusive-$b\bar{b}$ events.

Particle	PID	DC06 (PYTHIA) $\delta_p * 1000$	Particle	PID	DC06 (PYTHIA) $\delta_p * 1000$
n^0	± 2112	$-(\ 4.9 \pm\ 0.3)$	p^+	± 2212	$-(\ 7.8 \pm\ 0.3)$
Σ^-	± 3112	$-(\ 5.2 \pm\ 1.0)$	Λ^0	± 3122	$-(\ 5.7 \pm\ 0.5)$
Σ^0	± 3212	$-(\ 4.3 \pm\ 1.0)$	Σ^+	± 3222	$-(\ 7.5 \pm\ 1.0)$
χ^-	± 3312	$-(\ 6.1 \pm\ 1.7)$	χ^0	± 3322	$-(\ 3.8 \pm\ 1.7)$
Ω^-	± 3334	$+(\ 4.7 \pm\ 8.7)$	Λ_c^+	± 4122	$-(\ 6.5 \pm\ 1.4)$
Σ_b^-	± 5112	$-(13.4 \pm\ 6.2)$	Λ_b^0	± 5122	$-(\ 4.1 \pm\ 1.5)$
χ_b^-	± 5132	$-(\ 8.3 \pm 5.6)$	Σ_b^0	± 5212	$-(12.3 \pm\ 6.2)$
Σ_b^+	± 5222	$+(\ 1.4 \pm\ 6.2)$	χ_b^0	± 5232	$-(\ 2.7 \pm\ 5.8)$

the failure of the perturbative calculation, the thin peak at around 6 GeV in the p_T cross-section in Fig. C.8 is demonstrably from a production process which provides a very large production asymmetry in the kinematics seen in Fig. C.10.

In the large DC06 sample used here, we can examine the production asymmetry in baryons. The production asymmetry in baryons is expected to be large as the majority are expected to be created through the cluster collapse mechanism, however the beam drag on these baryons will mitigate this effect as it will reduce the number seen by the detector. We display some of the baryonic asymmetries for heavy baryons in Table C.4, from the DC06 B_s^0 and B_d^0 sample. Though statistics are limited we can see the asymmetries up to the order of 10^{-2} (e.g. in $\Sigma_b^{\mp}$-species). The statistics are insufficient to observe any trends with kinematic variables as is

expected from Sec. C.1. Clearly a comparative study of these effects in HERWIG would require retuning of the cluster thresholds to allow the production of b-baryons. These asymmetries should be examined using a signal data set or a large $b\bar{b}$-sample. In real data the asymmetries in baryons should be the largest, although not the easiest to measure. A direct study of these asymmetries in data would presumably be very useful to tune the generators.

Calculating the total b-quark asymmetry in the LHCb acceptance from this large inclusive-$b\bar{b}$ sample, we find $\delta_p(b) = +(3.4 \pm 0.3) \times 10^{-3}$ (DC06 PYTHIA).

C.3.5 B_s^0 or B_d^0

Table C.5 compares the overall production asymmetry within these samples, where the statistical errors on δ_p are of order 1% or less. We would expect significant differences were HERWIG to be compared with these samples in a similar way to the inclusive $b\bar{b}$ samples. We can also see agreement between the asymmetries in Table C.5 for B_d^0 or B_s^0 signal samples and with those in Table C.3 for inclusive $b\bar{b}$. We plot the distributions of production asymmetry as a function of energy and transverse momentum in Figs. C.11 and C.12 for B_d^0 and B_s^0-mesons.

Table C.5: Production asymmetry, δ_p, in B_d^0 or B_s^0 events.

Particle	PID	Tuned PYTHIA	Standard PYTHIA	DC06 B_d^0 (PYTHIA)	DC06 B_s^0 (PYTHIA)
		$\delta_p * 1000$			
$\pi^{\pm}$	± 211	$-(2.27 \pm 0.07)$	$-(2.3 \pm 0.3)$	$-(2.28 \pm 0.14)$	$-(1.85 \pm 0.28)$
$K^{\pm}$	± 321	$-(8.2 \pm 0.2)$	$-(6.4 \pm 0.9)$	$-(7.5 \pm 0.4)$	$-(6.6 \pm 0.7)$
$D^{\pm}$	± 411	- - -	- - -	$+(0.6 \pm 2.2)$	$+(0.45 \pm 0.45)$
D^0	± 421	$+(4.0 \pm 0.8)$	$+(3.8 \pm 2.4)$	$+(4.5 \pm 1.0)$	$+(11.5 \pm 2.1)$
$D_s^{\pm}$	± 431	$-(1.6 \pm 0.8)$	$+(2.2 \pm 3.9)$	$-(4.4 \pm 2.2)$	$-(1.1 \pm 2.0)$
$B^{\pm}$	± 521	$-(9.1 \pm 0.8)$	$-(8.4 \pm 3.9)$	$-(19.0 \pm 2.0)$	$-(3.1 \pm 3.7)$
B_d^0	± 511	$-(3.2 \pm 0.5)$	$-(4.7 \pm 2.2)$	$-(1.1 \pm 0.8)$	$-(13.5 \pm 3.4)$
B_s^0	± 531	$-(1.5 \pm 0.8)$	$-(1.2 \pm 4.0)$	$-(5.9 \pm 3.1)$	$+(2.9 \pm 1.5)$
$e^{\mp}$	± 11	$+(0.37 \pm 0.50)$	$-(2.3 \pm 2.3)$	$+(3.6 \pm 1.1)$	$-(1.7 \pm 2.1)$
$\mu^{\mp}$	± 13	$+(1.0 \pm 0.9)$	$+(3.9 \pm 4.1)$	$-(0.4 \pm 0.8)$	$+(2.8 \pm 2.5)$

insufficient statistics or no data for this comparison

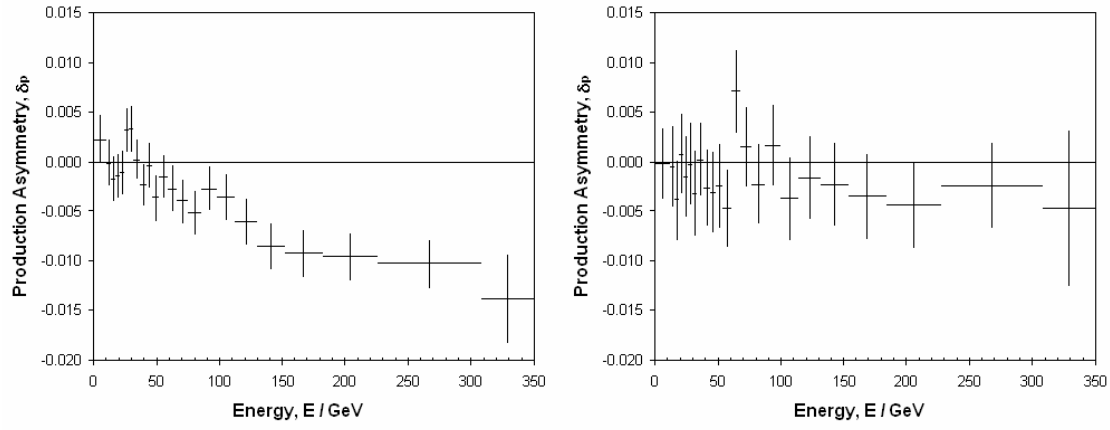

Figure C.11: B_d^0 and B_s^0 production asymmetry with energy, $\delta_p(E)$ with Tuned PYTHIA. Left, for B_d^0 , Right for B_s^0. Histograms are given with variable bin sizes to reflect the varying statistics. Event samples shown are given in Table C.1.

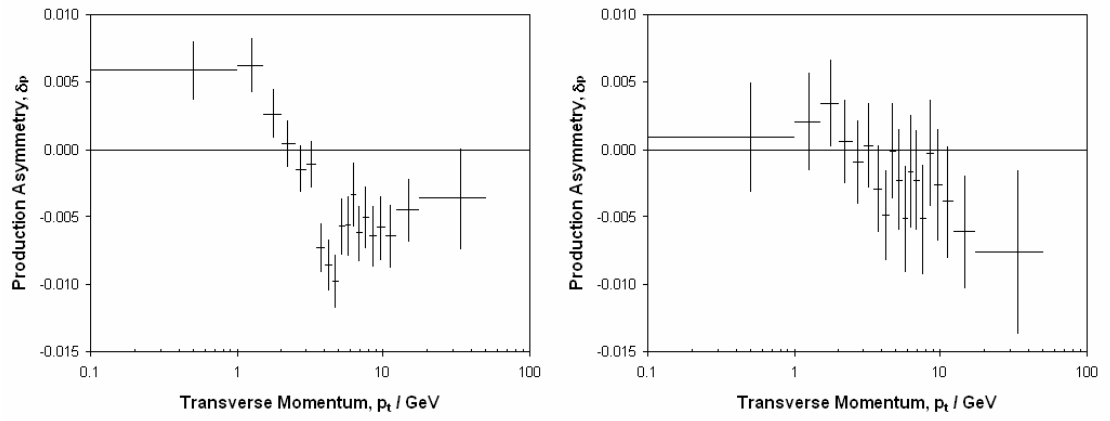

Figure C.12: B_d^0 and B_s^0 production asymmetry with transverse momentum, $\delta_p(p_T)$ with Tuned PYTHIA. Left, for B_d^0 , Right for B_s^0. Histograms are given with variable bin sizes to reflect the varying statistics. Event samples shown are given in Table C.1.

C.4 Discussion

To begin to understand the features in the distributions of the production asymmetry, and the systematic differences between the two generators we must again turn to the nature of the asymmetric hadronization mechanisms included in the two generators studied. The different tunings of the PYTHIA generator used within this study are seen to agree in their predictions of the production asymmetries and their distributions. For all comparisons significant differences between HERWIG and PYTHIA are observed. In some cases these differences are extreme, involving a change of sign and order of magnitude for the predicted overall asymmetry. One

could attribute an overall normalisation change, or slight changes in the variations of this asymmetry, however, the large differences in level of, and the shapes of the production asymmetry are more likely to result from the differences in the models employed, as was described in the introduction.

Luminosity can only affect the production asymmetry slightly. We must assume pile-up events are uncorrelated, hard scatters in multiple interactions do not effect each other due to the separation of the primary vertices. Pile-up interactions will essentially contribute a different background asymmetry. This is one area which would benefit from further study if the luminosity is expected to differ considerably (a factor of ten for example) from the baseline $2 \times 10^{32}\,\mathrm{cm}^{-2}\mathrm{s}^{-1}$ used herein.

Given the limitations of HERWIG seen in this study, it is presumed that the asymmetries quoted by PYTHIA are more reliable estimates. It is clear that there is a significant requirement to perform a study of production asymmetry with signal samples from real data, applying the correct signal cuts. This will require decoupling of the detector asymmetry δ_c by, for example, examining charge-symmetric final states, e.g. $B_s^0 \to J/\Psi(\mu^+\mu^-)\ \phi(K^+K^-)$. Comparing tagged and untagged event samples for CP-Violating phases may also decouple the production asymmetry. Examining time-varying CP-Violation in mixing such as a time-dependent untagged analysis of the flavor specific asymmetry in $B_s^0 \to D_s^{\mp}\pi^{\pm}$ one might extract the production asymmetry as in Ref. [5]. Or alternatively if the detector asymmetry in the sample under investigation is precisely known the production asymmetry may be cleanly extracted. Investigation of these procedures is ongoing.

C.4.1 Summary and outlook

The production asymmetry is of concern and high importance to control our systematics in LHCb for measuring CP-violation. A Monte Carlo study has been performed examining the production asymmetry, δ_p for many different species, in three different event types, comparing the Generators PYTHIA and HERWIG. More than 90M events have been examined of the various types as shown in Table C.1.

We predict a production asymmetry of the order 10^{-3} for B-mesons, and up to 10^{-2} for other particles with recently tuned PYTHIA, see Tables C.2 to C.5. The three different tunings of PYTHIA used in this study agree with each other, however, we observe significant disagreement between PYTHIA and HERWIG, both in the order of magnitude, sign and distributions of production asymmetry. There will be a small contribution to this difference attributed to the differences in the datasets used for tuning, but the majority is attributed to their hadronization models, particularly the way they treat low transverse momentum and the underlying events. We have seen that the standard HERWIG generator is not applicable for the majority of interactions in LHCb, particularly for $p_T < 10\,\text{GeV}$ and should be combined with both JIMMY and MC@NLO, and retuned for the production of b-baryons, to improve predictions for LHCb. Additionally at all energies HERWIG cuts the colour connection between particles from the hard scattering process and the beam remnants, we have seen this has a large effect on the production asymmetry.

Three phenomenological mechanisms, beam drag, cluster collapse and valence quark scattering were introduced as the main sources for production asymmetry. We have seen that we can begin to understand the distributions of asymmetry with energy, transverse momentum, and pseudo-rapidity using these simplified descriptions.

This study provides information on δ_p, not just on particular signal channels, but on a wide variety of backgrounds and the underlying event. These will be particularly useful for persons examining systematic uncertainties in proposed analyses over the coming months.

Appendix D

Simulation of the LHCb Detector Asymmetry

The detector asymmetry is a systematic pollutant to many physics asymmetries we hope to determine at LHCb. Particularly: it will influence all direct CP searches when the final state is not charge symmetric, will mean the tagging efficiency and mistag rate will differ for oppositely charges mesons, and will directly interfere with the measurement of the flavour specific asymmetry.

A detector asymmetry, $\delta_c \neq 0$ is the asymmetry in the reconstruction efficiency of charge-conjugated events of type i:

$$\delta_c^i = \frac{\varepsilon(\bar{f}^i)}{\varepsilon(f^i)} - 1 \tag{D.1}$$

Here f and $\bar{f}$ refer to final state particles and antiparticles respectively, or a collection of particles and the collection of thier charge conjugates. A generic detector asymmetry can separated into several parts:

- Geometric: from the misalignment or inefficiencies in subdetector modules.
- Interaction: charge-conjugate states interact differently with the detector.
- Software biases.

Geometric asymmetry is the most obvious asymmetry at LHCb. Changes in

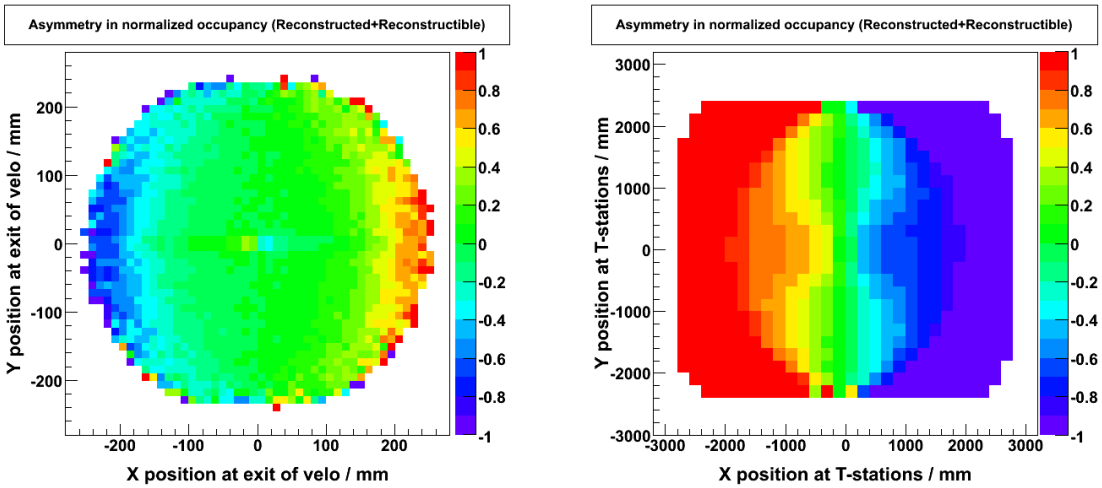

Figure D.1: Asymmetry in muon distributions. The asymmetry in the number of reconstructible muons reconstructed as long tracks is plotted in 2D. Left, for the Velo, right for the T-Stations. Large areas of the T-stations and all downstream detectors are mainly hit by only one charge.

reconstruction efficiencies across the detector would directly produce a detector asymmetry. In Fig. D.1 we plot the asymmetry in the distribution of reconstructed muons given they are reconstructible (as defined in Sec. D.1). In any given magnet polarity, large areas of the T-stations and all subsequent downstream detectors are mainly hit by only one charge from the PV. Misalignments and inefficiencies across the downstream subdetectors would result in asymmetric reconstruction. Any geometric asymmetry cannot be known until calibration and alignment can be performed on a module to module basis, therefore it is not included in the DC06 Monte Carlo. To control, measure and eliminate this asymmetry, the polarity of the magnet should be reversed regularly. Reversing the magnet reverses the bending direction of the particles and inverts the sign of the geometric asymmetry.

An interaction asymmetry is inherently included in the Monte Carlo simulation, which adopts the well-measured PDG values for the cross-sections of the interactions of particles with matter. The cross-sections are very well known for the majority of final state particles. Zero interaction asymmetry is expected for leptons, as they interact electromagnetically with the detector. In the case of hadrons, a significant asymmetry is expected due to the differences in the interaction cross-sections, which are shown for kaons and pions in Fig. D.2.

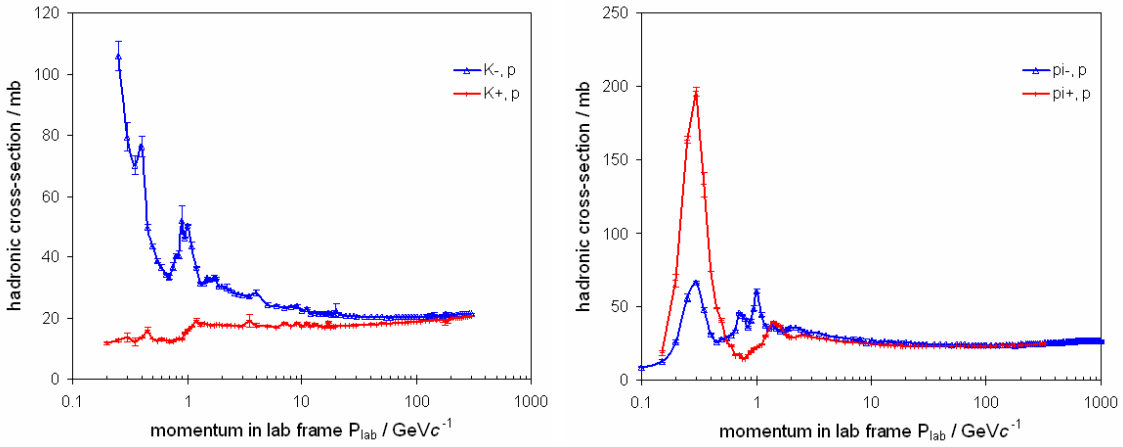

Figure D.2: Cross-section for hadronic interactions with protons, plotted as a function of momentum, from the PDG [24]. Left, for kaons, right for pions.

Computational problems with tracking and reconstruction which result in an asymmetry should be observable in the Monte Carlo, if they exist.

In this Monte Carlo study we examine the resultant detector asymmetries from interactions and tracking to study the level of asymmetry to be expected.

D.1 Simulation study

5.7M fully reconstructed events were used in this study. In order to obtain high statistics in high-momentum leptons two samples were used. Firstly 3.8M events from the $b\bar{b}$-inclusive dimuon sample. In the generation of these events, the b-hadrons were forced to decay semileptonically to muons, providing a large data sample of muons and final state hadrons, with distributions typical of a signal decay. Secondly 1.9M inclusive $J/\Psi \rightarrow e^+e^-$ events, provide a complimentary sample of electrons. These events were generated centrally as part of DC06.[1]

This study was limited to charged long tracks (see Fig. 3.6), which is appropriate for two reasons. Firstly, most analyses are similarly restrictive in track selection. Secondly, charged long tracks have been bent by the magnet and have traversed the

[1]Software versions Gauss v25r10/v25r8, Boole v12r10/v12r10 and Brunel v30r17/v30r14 were used in the generation, and were DaVinci v19r7 was used for the analysis.

downstream tracking stations.

We firstly perform a loose track selection to reduce the influence of secondaries. Tracks are selected from those within the LHCb acceptance which originate within a cylinder 1.5 mm in radius about the beam axis and 25 mm in length about the interaction point. This region is well within the beampipe inside of the VELO. To examine possible edge effects in the VELO and T-stations the acceptance was defined weakly in terms of pseudorapidity, $2.0 < \eta < 4.9$.

Interactions of a particle with the detector determine whether the track produced is able to be reconstructed, i.e. is reconstructible. We define a reconstructability, ϵ_r^j, as the fraction of particles of type j which are reconstructible as long tracks, $\bar{\epsilon}_r^j$ is the equivalent for the charge conjugate of j.

$$\epsilon_r^j = \frac{N(R^{le}, j)}{N(j)} \tag{D.2}$$

where $N(R^{le}, j)$ is the number of reconstructible MC particles of type j and $N(j)$ is the total number of MC particles in the acceptance from near the IP. The efficiency of the tracking for j, ϵ_t^j, and its charge conjugate $\bar{\epsilon}_t^j$ are defined as:

$$\epsilon_t^j = \frac{N(R^d | R^{le}, j)}{N(R^{le}, j)} \tag{D.3}$$

where $N(R^d | R^{le}, j)$ is the number of MC particles reconstructed given they were reconstructible. A track is defined as reconstructible if:

- It is above $1\,\mathrm{GeV}c^{-1}$ in momentum
- It has at least $3\,R$ and $3\,\Phi$ hits in the VELO
- It has at least $1\,x$-plane hit and 1 stereo-plane hit in each of the three T-stations

For each efficiency ϵ_i two quantitative measures of the asymmetry are defined: δ_i,

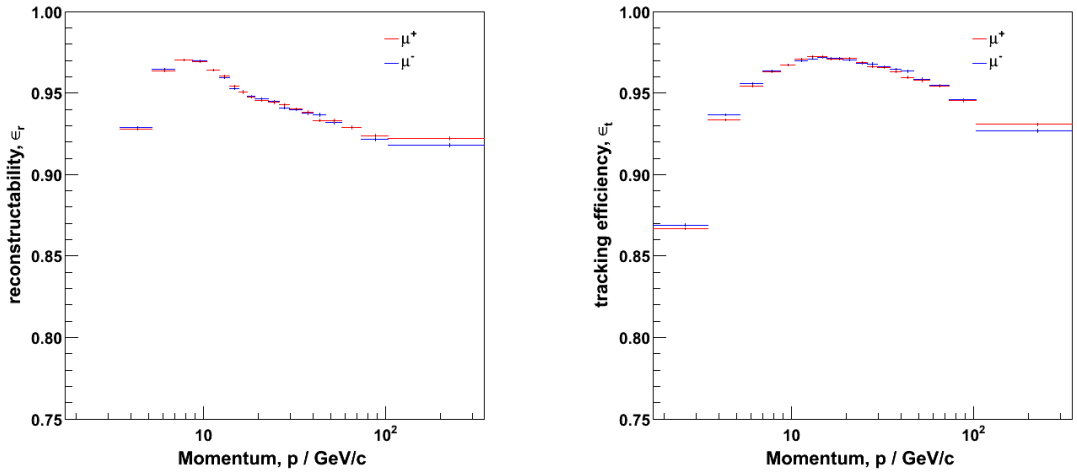

Figure D.3: Reconstruction efficiency, left, and tracking efficiency, right, for muons as a function of momentum.

following the convention of Nierste [37], and a conventional asymmetry, A_i:

$$\delta_i = \frac{\bar{\epsilon}_i}{\epsilon_i} - 1 \qquad A_i = \frac{\epsilon_i - \bar{\epsilon}_i}{\epsilon_i + \bar{\epsilon}_i} \tag{D.4}$$

D.2 Tracking of leptons

The reconstructability, ϵ_r^μ, and tracking efficiency, ϵ_t^μ, of muons are given in Fig. D.3, as a function of momentum. The efficiencies for μ^+ and μ^- are identical within statistical errors, aside from the smallest momentum bin. This is expected for muons, which only interact electromagnetically with the detector. The reconstructability drops as a function of momentum due to my loose track selection, namely that high momentum muons are produced at high rapidities and are less likely to form hits in three VELO modules. The tracking efficiency also drops at higher momentum, partially a knock-on effect of this acceptance, but also because of the tracvk matching process. In the reconstruction process search windows are used to match downstream and upstream tracks, these windows are optimised for tracks of $\sim$10 GeVc^{-1} momentum, the search windows are less efficient for higher momenta.

Using muons we can also examine the left-right symmetry of the tracking. In Fig. D.4

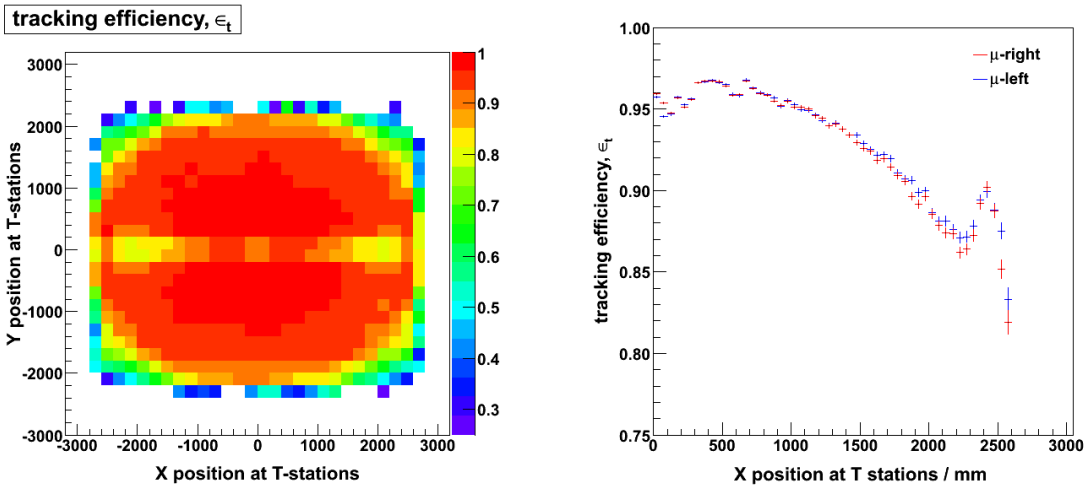

Figure D.4: Muon tracking efficiency as a function of position in the T-stations. Left, a 2D plot. Right, the projection onto the X-axis with positive and negative X overlayed.

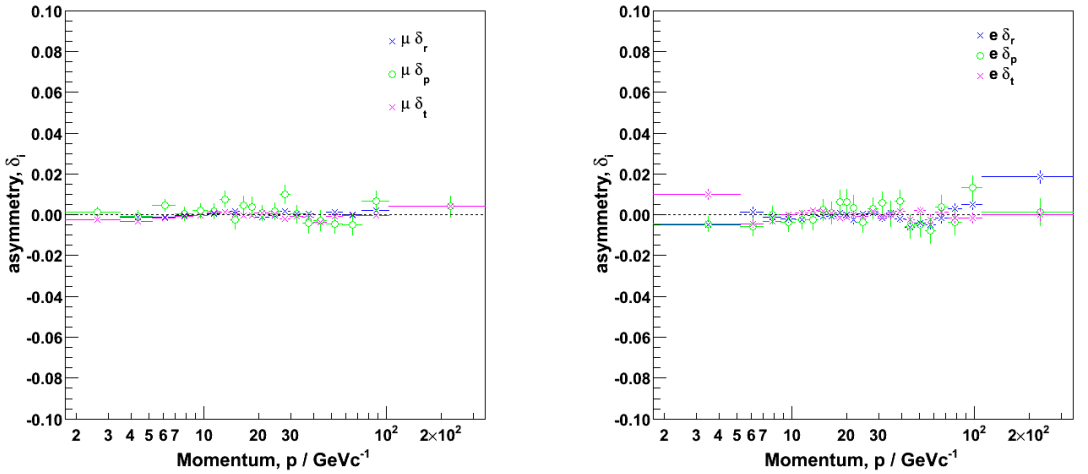

Figure D.5: Asymmetries in the tracking and reconstruction of leptons plotted against momentum. Left, for muons. Right, for electrons. δ_p is the production asymmetry for the selected tracks.

the average tracking efficiency is plotted as a function of the extrapolated track position at the T-stations. The efficiencies for left and right-going muons agree well. The influence of low-momentum muons can be seen in the slight disagreement at larger X position, however, this is eliminated if tighter track selection is made.

Electrons are less ideal for tracking compared to muons. They are not as penetrative, are produced frequently as secondaries and are present in the detector. The asymmetries for muons, δ_c^μ, and electrons, δ_c^e, are show in Fig. D.5. The asymmetries are consistent with zero across the range shown.

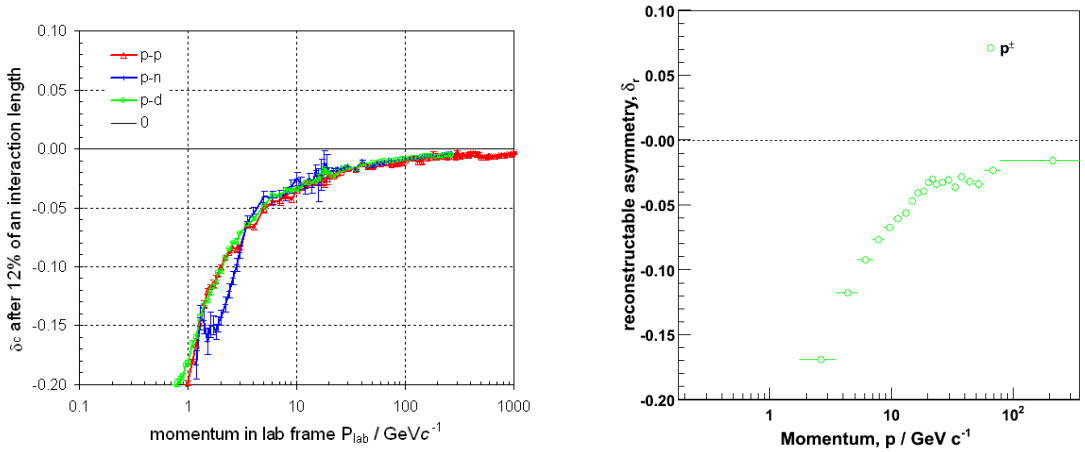

Figure D.6: Proton interaction asymmetry as a function of momentum. Left, the expected detector asymmetry, δ_c, modeled simply from the PDG cross-sections. Right, the reconstruction asymmetry, δ_r, as extracted from the full LHCb simulation.

D.3 Interaction of hadrons

Hadrons interact with the nuclear matter in the detector. The cross-section of these hadronic interactions depends on the flavour and charge of the hadron, whether it is a particle or antiparticle. The cross-section can be significantly different between the two cases, particularly at low energy. This was demonstrated in Fig. D.2 for kaon-proton and pion-proton interactions. Using the PDG cross-section differences it is possible to derive an expected level of detector asymmetry.

From the reoptimised TDR [31] we assume LHCb is a homogeneous isotropic simple hadronic medium subtending 12 % of an interaction length for a hadron of 10 GeVc^{-1} momentum up until the end of the T-stations. Under this very simple approximation the number of hadrons surviving to be reconstructible takes a simple exponential form depending only on the cross-section, which is a function of momentum taken directly from the PDG [24].

In Figs. D.6 to D.8 the asymmetry is plotted as a function of momentum from the PDG, compared with the asymmetry seen in the reconstructibility, δ_r. For the proton, Fig. D.6 the asymmetry from the full simulation matches very well the expected PDG asymmetry. The proton interaction asymmetry is the largest, is

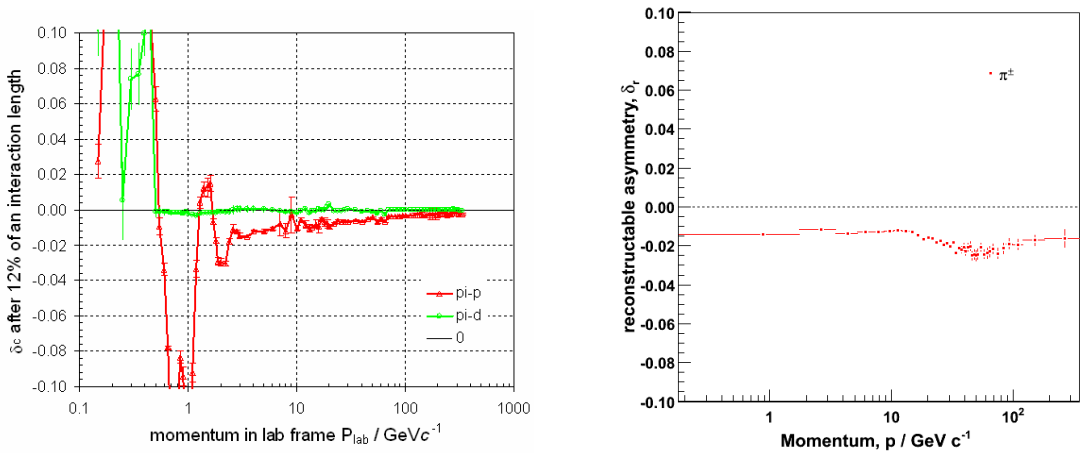

Figure D.7: Pion interaction asymmetry as a function of momentum. Left, the expected detector asymmetry, δ_c, modeled simply from the PDG cross-sections. Right, the reconstruction asymmetry, δ_r, as extracted from the full LHCb simulation.

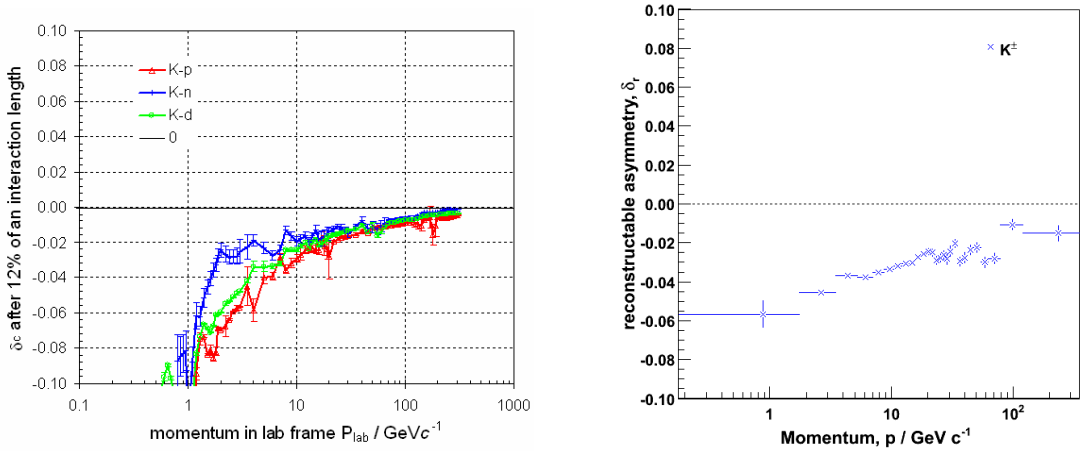

Figure D.8: Kaon interaction asymmetry as a function of momentum. Left, the expected detector asymmetry, δ_c, modeled simply from the PDG cross-sections. Right, the reconstruction asymmetry, δ_r, as extracted from the full LHCb simulation.

negative in δ_r and between $-20\,\%$ and $-2\,\%$, reducing over the momentum range. For pions, Fig. D.7 the asymmetry is much smaller, between $-2\,\%$ and $-1\,\%$, and much flatter in momentum. Kaons are seen to have an asymmetry from $-5\,\%$ and $-2\,\%$, which is less than that expected by the simplistic model adopted.

Table D.1: Detector asymmetry, δ_i, for final state particles.

Particle	PID	reconstructable asymmetry, $\delta_r \times 100$	tracking asymmetry, $\delta_t \times 100$
$p^{\pm}$	± 2212	$-(7.72 \pm 0.04)$	$-(0.07 \pm 0.02)$
$\pi^{\pm}$	± 211	$-(1.37 \pm 0.01)$	$-(0.039 \pm 0.006)$
$K^{\pm}$	± 321	$-(3.21 \pm 0.03)$	$+(0.09 \pm 0.01)$
$e^{\mp}$	± 11	$-(0.04 \pm 0.04)$	$+(0.00 \pm 0.03)$
$\mu^{\mp}$	± 13	$-(0.01 \pm 0.02)$	$-(0.05 \pm 0.02)$

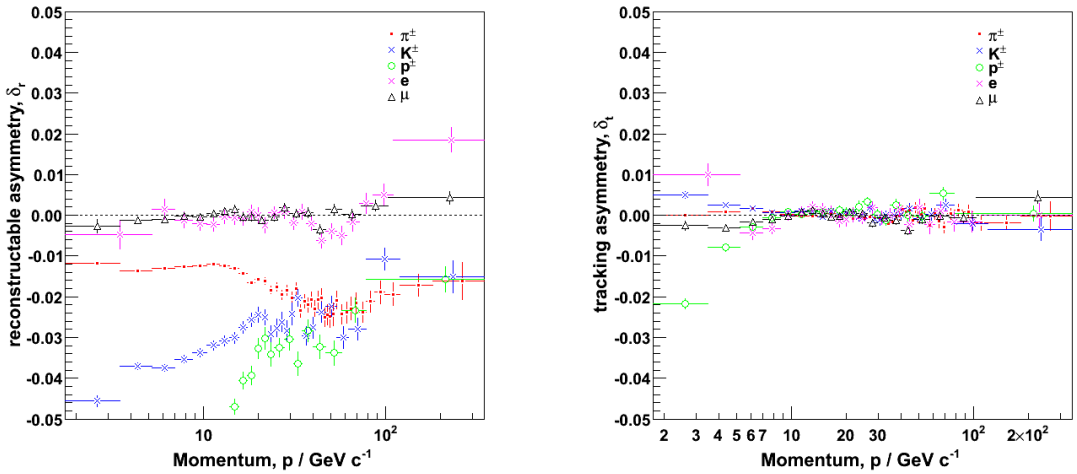

Figure D.9: Tracking and reconstruction asymmetries for final state particles, plotted against momentum. Left, the reconstructible asymmetry as induced by interactions. Right, the tracking asymmetry.

D.4 Summary

The average reconstruction and tracking asymmetries are given in Table D.1 for each particle. They are calculated for tracks between 1.75 and 350 GeVc^{-1} momentum. The tracking asymmetries are all less than 1 per mil. The muon and electron asymmetries are consistent with zero. The other non-zero tracking asymmetries are taken to be induced by second-order effects from the interaction asymmetries, as is clear when we compare the distributions of the asymmetries in Fig. D.9.

Appendix E

Selection of $B_q^0 \to D_q^{(*)\mp}\mu^{\pm}\nu_\mu X^0$ Events

The flavour-specific asymmetry, a_{fs}^q, measures the CP-violating phase in the model-independent Hamiltonian for B_q^0 mixing. In order to make a measurement of this asymmetry in the semileptonic mode a clean sample of decays in the channels $B_s^0 \to D_s^{\mp}\mu^{\pm}\nu_\mu X^0$ and $B_d^0 \to D^{\mp}\mu^{\pm}\nu_\mu X^0$ should be obtained, where both $D_s^{\mp}$ and $D^{\mp}$ decay to $K^+K^-\pi^{\mp}$. These two selections are combined to ensure the detector asymmetries are equal in the two channels, as is required to cleanly extract the parameter ΔA_{fs}^q (as described in Sec. 6.6). The combined offline selection was optimised for this Thesis as discussed in Sec. 6.2.1. A large number of cuts are used for the selection, as summarised in Sec. 6.2. In this Appendix the full cuts are listed, their efficiency and background suppression shown, and the distributions of the underlying parameters graphically represented.

To categorise backgrounds we use MC Truth information and we adopt the convention of LHCb to assign the categories. The categories are explained in Table E.1.

A summary of all cuts is given here in Table E.2, where cuts applied in preselection and in the DC04 selection [129] are compared to the optimised offline (DC06) selection and abbreviations used elsewhere in this Thesis are defined.

The selection code was applied to the event samples given in Table 6.1 added to form a weighted dataset as is described in Sec. 6.2.1.2. The correctly scaled B/S values for each cut not appearing in the preselection are given in Table E.3, ordered by their exclusive B/S reduction. Similarly the results are shown for the L0 selected minimum bias sample in Table E.4. Event numbers presented are scaled to the number of events expected in 5×10^4 seconds.

The distributions of background and signal are given and the optimal cut value shown in Figs. E.1 to E.3.

Table E.1: Standard background categories from MC truth information.

Category	Name	Definition
-1	Undefined	Simple particle, failure in algorithm, N/A or not in the list.
0	Signal	All intermediate resonances reconstructed. All tracks associated with the signal decay.
10	quasi-signal	Intermediate resonances incorrectly reconstructed. All tracks associated with the signal decay.
20	fully-reconstructed physics	All tracks associated with another non-signal decay.
30	reflection	Intermediate resonances incorrectly reconstructed. All tracks associated with a given decay where the mass hypothesis of a daughter is incorrect due to mis-ID.
40	partially-reconstructed physics	All tracks associated with another decay where a few tracks have been missed.
50	low-mass background	Tracks associated with the decay of a particle with much lower mass.
60	ghost	One or more tracks not associated, formed at random from a disparate set of hits in the detector.
70	from PV	No ghosts. One or more tracks came from a PV.
80	all from same PV	All tracks can be associated with the same PV.
100	from different PV	No ghosts. One or more tracks came from a PV. Tracks can be associated with different PVs.
110	$b\bar{b}$	All tracks result from the decay chain of a $b\bar{b}$ pair.
120	$c\bar{c}$	All tracks result from the decay chain of a $c\bar{c}$ pair.
130	uds	All tracks result from the decay chain of particles which are not charmed, and which do not contain a b-quark.

Table E.2: Full list of applied cuts for $B_q^0 \to D_q^{(*)\mp}\mu^{\pm}\nu_\mu X^0$ selection.

Variable	Symbol	Cut type	DC06 presel'n	DC04 sel'n[129]	DC06 sel'n	Unit
Track goodness-of-fit	$\chi^2_{tr}/n.d.f.$	$<$	–	–	3.0	–
Kaon transverse momentum	$p_T(K)$	$>$	300	500	500	MeVc^{-1}
Kaon momentum	$\|p(K)\|$	$>$	2.0	2.0	2.0	GeVc^{-1}
Kaon PID* w.r.t. pion	$\Delta_{LL}(K-\pi)$	$>$	-5.0	-5.0	1.0	–
Kaon PID* w.r.t. proton	$\Delta_{LL}(K-p)$	$>$	-5.0	-3.0	-3.0	–
Kaon PID* w.r.t. muon	$\Delta_{LL}(K-\mu)$	$>$	-5.0	0.0	0.0	–
Kaon ips	ips(K)	$>$	3.0	3.0	3.0	σ
Pion transverse momentum	$p_T(\pi)$	$>$	300.0	500.0	500.0	MeVc^{-1}
Pion momentum	$\|p(\pi)\|$	$>$	2.0	2.0	2.0	GeVc^{-1}
Pion PID* w.r.t Kaon	$\Delta_{LL}(\pi-K)$	$>$	-5.0	-10.0	-5.0	–
Pion ips	ips(π)	$>$	3.0	3.0	3.0	σ
Muon transverse momentum	$p_T(\mu)$	$>$	0.6	1.0	1.0	GeVc^{-1}
Muon PID* w.r.t pion	$\Delta_{LL}(\mu-\pi)$	$>$	-5.0	0.0	0.0	–
Muon PID* w.r.t Kaon	$\Delta_{LL}(\mu-K)$	$>$	-5.0	0.0	0.0	–
Muon PID* w.r.t proton	$\Delta_{LL}(\mu-p)$	$>$	-5.0	0.0	0.0	–
Muon ips	ips(μ)	$>$	2.0	3.0	2.0	σ
D vertex goodness-of-fit	$\chi^2_{vtx}(D)$	$<$	15	10	10	–
D flight distance in beam direction	$\Delta z(D)$	$>$	1.0	1.0	1.0	mm
D ips	ips(D)	$>$	3.0	3.0	3.0	σ
D transverse momentum	$p_T(D)$	$>$	1.5	1.5	1.5	GeVc^{-1}
D measured mass w.r.t.	$M(D)$	$<$	$\pm$200.0	$\pm$200.0	+100.0	MeVc^{-2}
PDG mass of $D_s^{\pm}$	$-M_{PDG}$				-200.0	MeVc^{-2}
$D\mu$ Pointing angle**	$cos\theta_p^r$	$>$	0.995	0.999	0.999	–
B vertex goodness-of-fit	$\chi^2_{vtx}(B)$	$<$	10	5	5	–
B measured mass	$M(B)$	$<$	–	5.4	5.7	GeVc^{-2}
B measured mass	$M(B)$	$>$	2.9	3.0	3.0	GeVc^{-2}

* Calculation of the log likelihood difference between two particle ID hypothesis.
** θ_p^r angle between B flight direction, $\underline{r}$ and direction of $D^{\mp}\mu^{\pm}$ momentum, $\underline{p}$, in the lab frame.

Table E.3: Selection cut effectiveness on weighted signal and background samples after preselection.

Cut	Exclusive			Inclusive		
	S	B	B/S	S	B	B/S
None	58877	483183	8.21	58877	483183	8.21
$\Delta_{LL}(K-\pi) > 1.0$	57026	346727	4.51	55614	250598	4.51
$\chi^2_{tr}/n.d.f. < 3.0$	54143	304280	5.62	51180	166002	3.24
$cos\theta^r_p > 0.999$	57892	354072	6.12	50317	127551	2.53
$M(D) - M_{PDG} < 100.0\,\mathrm{MeV}c^{-2}$	58861	374453	6.36	50314	103931	2.07
$p_T(K) > 500.0\,\mathrm{MeV}c^{-1}$	55658	364954	6.56	45290	65588	1.45
$M(B) < 5.7\,\mathrm{GeV}c^{-2}$	58877	399807	6.79	45290	58253	1.28
$\Delta_{LL}(K-p) > -3.0$	55098	379038	6.87	43944	53169	1.24
$\Delta_{LL}(K-\mu) > 0.0$	57893	406725	7.03	42767	51927	1.21
$\Delta_{LL}(\mu-\pi) > 0.0$	56304	416516	7.40	40980	39961	0.975
$\chi^2_{vtx}(D) < 10.0$	55205	393892	7.14	38578	34463	0.893
$\chi^2_{vtx}(B) < 5.0$	57674	415966	7.21	37862	31717	0.838
$p_T(\mu) > 1.0\,\mathrm{GeV}c^{-1}$	50854	375518	7.38	33076	26615	0.805
$\Delta_{LL}(\mu-K) > 0.0$	58177	444947	7.65	32921	26274	0.798
$\Delta_{LL}(\mu-p) > 0.0$	57816	443479	7.67	32679	26241	0.803
$p_T(\pi) > 500.0\,\mathrm{MeV}c^{-1}$	51120	405417	7.93	28433	22519	0.792
$M(B) > 3.0\,\mathrm{GeV}c^{-2}$	58217	474559	8.15	28159	22024	0.782

Statistical errors of typically 2 % are omitted for clarity. All variables are defined in Table E.2.

Table E.4: Cut effectiveness on samples after preselection, for $\sim 2.9M$ min bias events passing the L0 Trigger.

Cut	Exclusive			Inclusive		
	S	B	B/S	S	B	B/S
None	5	42	8.4	5	42	8.4
$\Delta_{LL}(K-\pi) > 1.0$	5	23	4.6	5	19	3.8
$\chi^2_{tr}/n.d.f. < 3.0$	5	24	4.8	5	8	1.6
$cos\theta^r_p > 0.999^*$	5	36	7.2	5	7	1.4
$M(D) - M_{PDG}(D_s^{\pm}) < 100.0\,\mathrm{GeV}c^{-2}$	5	34	6.8	5	3	0.6
$p_T(K) > 500.0\,\mathrm{MeV}c^{-1}$	5	27	5.4	5	2	0.4
$M(B) < 5700.0\,\mathrm{MeV}c^{-2}$	5	43	8.6	5	2	0.4
$\Delta_{LL}(K-p) > -3.0$	5	31	6.2	5	2	0.4
$\Delta_{LL}(K-\mu) > 0.0$	5	36	7.2	5	2	0.4
$\chi^2_{vtx}(D) < 10.0$	5	33	6.6	5	2	0.4
$\Delta_{LL}(\mu-\pi) > 0.0$	5	31	6.2	5	2	0.4
$\chi^2_{vtx}(B) < 5.0$	5	36	7.2	5	2	0.4
$p_T(\mu) > 1.0\,\mathrm{GeV}c^{-1}$	5	31	6.2	5	2	0.4
$\Delta_{LL}(\mu-K) > 0.0$	5	41	8.2	5	2	0.4
$\Delta_{LL}(\mu-p) > 0.0$	5	38	7.6	5	2	0.4
$p_T(\pi) > 500.0\,\mathrm{MeV}c^{-1}$	4	38	9.5	4	2	0.5
$M(B) > 3000.0\,\mathrm{MeV}c^{-2}$	5	47	9.4	4	2	0.5

Statistical errors are omitted for clarity, Poissonian errors are applicable. All variables are defined in Table E.2.

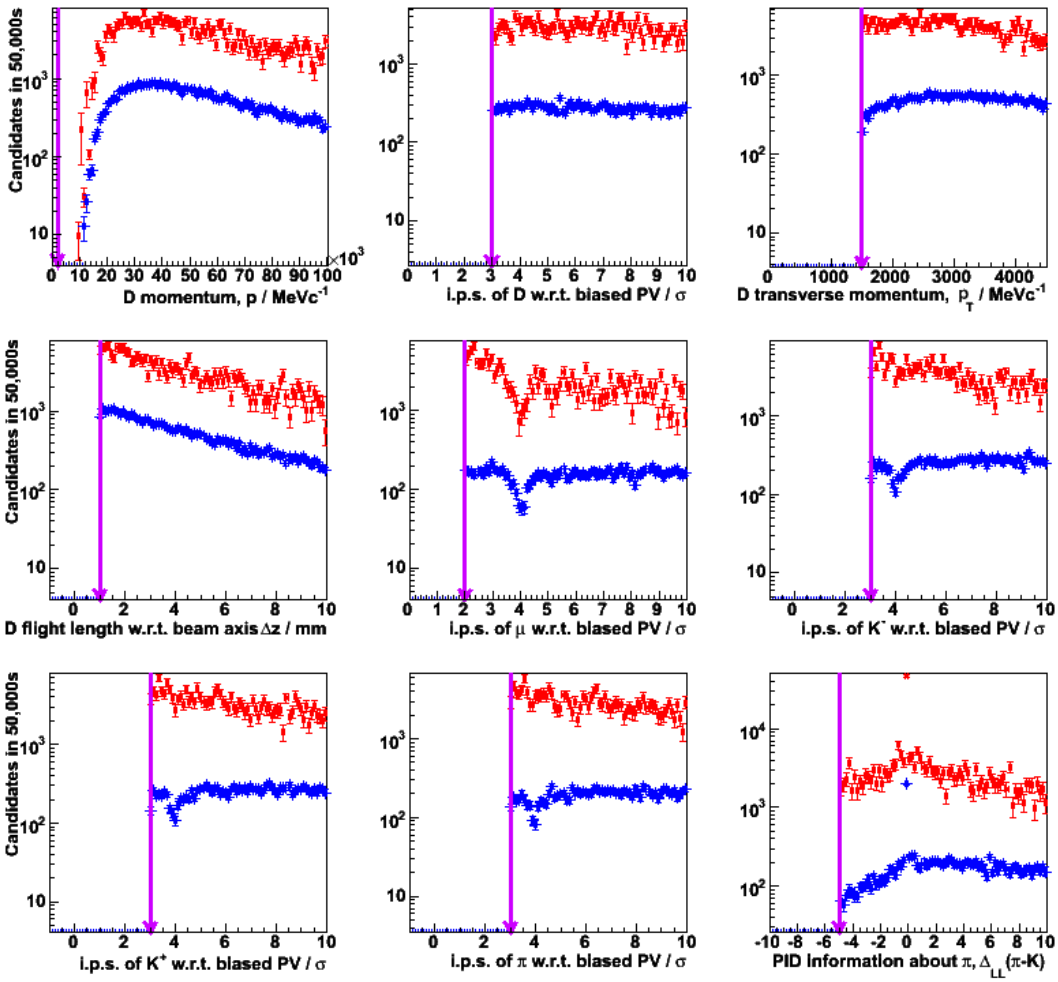

Figure E.1: Preselection cuts in $B_q^0 \to D_q^{(*)\mp}\mu^{\pm}\nu_\mu X^0$. The signal distributions (blue) and background distributions (red) for preselected candidates are shown relative to the cut value (purple arrow), for cuts which are not changed from their values in the preselection. For technical reasons these plots can only be made with preselected data.

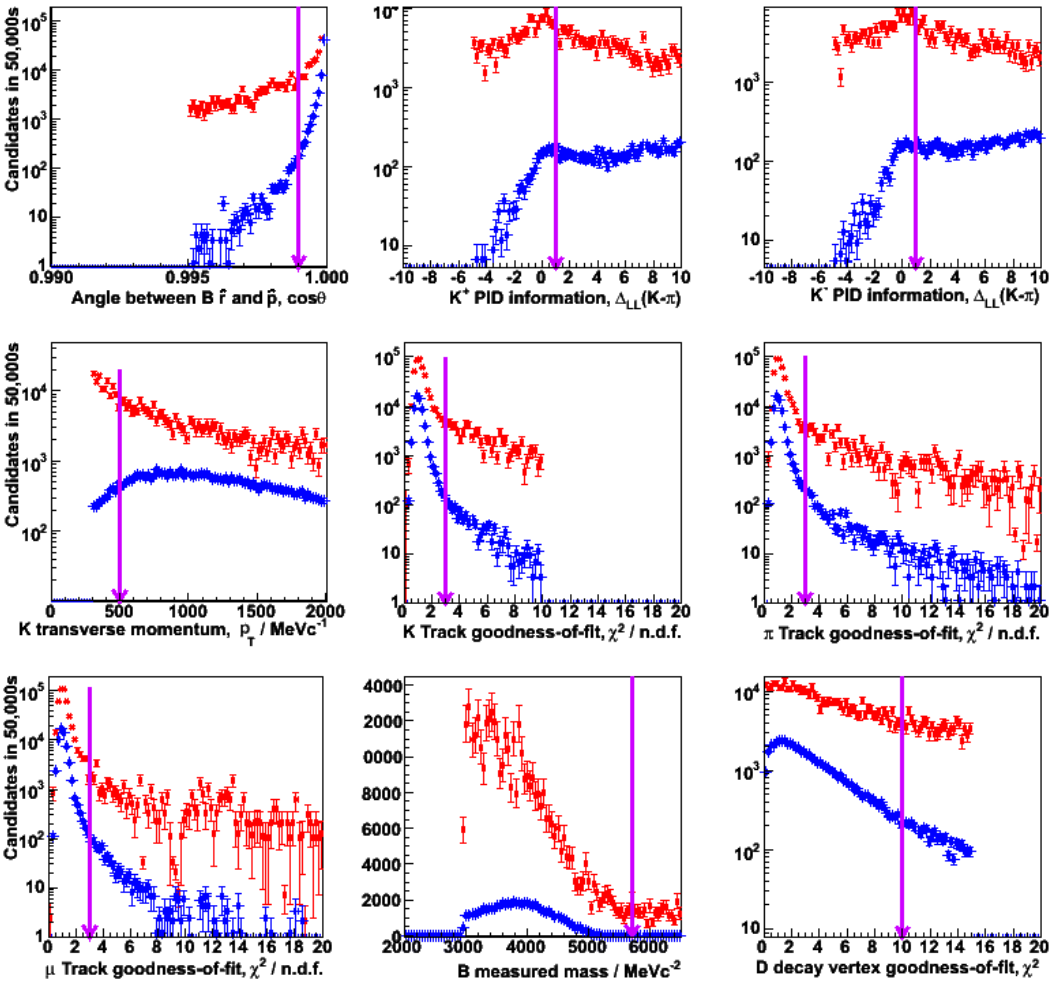

Figure E.2: Selection cuts in $B_q^0 \to D_q^{(*)\mp}\mu^{\pm}\nu_\mu X^0$. The signal distributions (blue) and background distributions (red) for preselected candidates are shown relative to the final selection cut value (purple arrow).

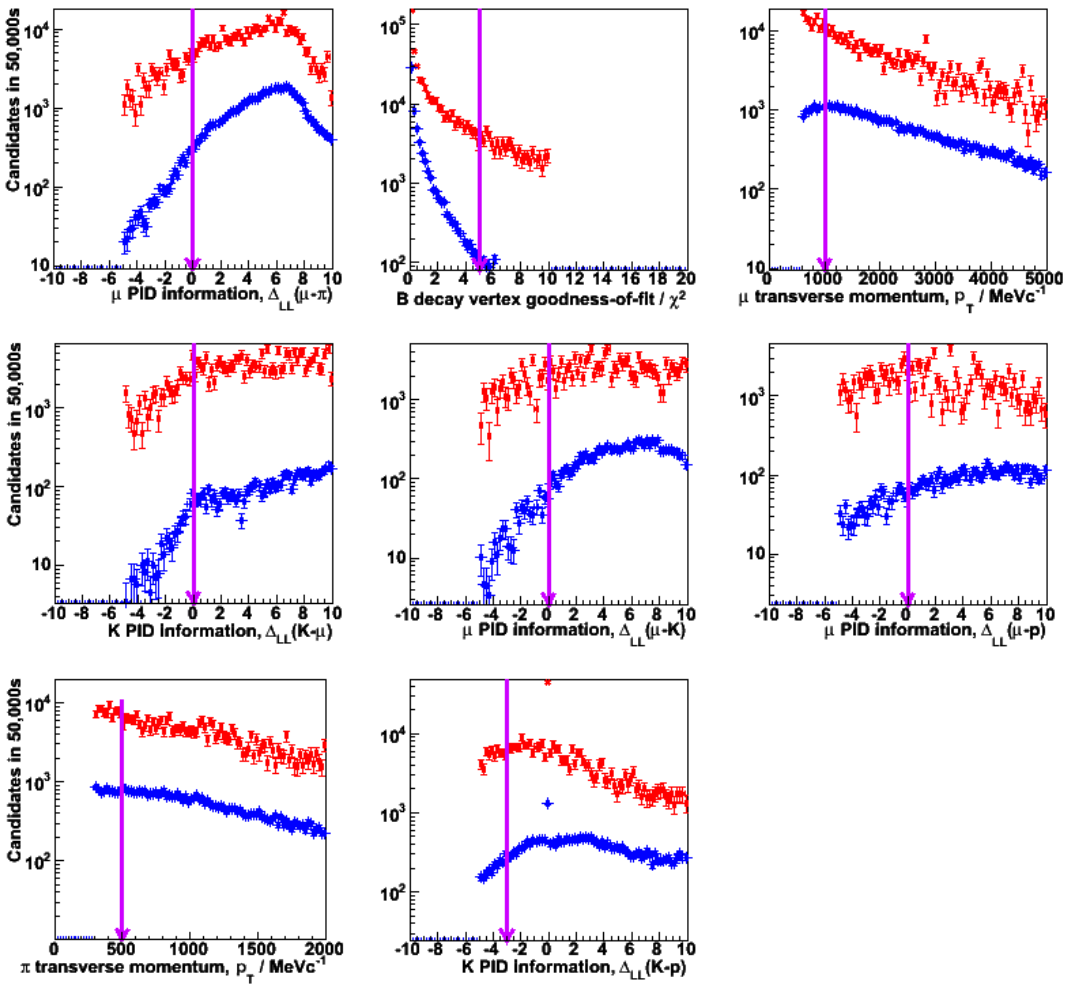

Figure E.3: Selection cuts in $B_q^0 \to D_q^{(*)\mp}\mu^{\pm}\nu_\mu X^0$. The signal distributions (blue) and background distributions (red) for preselected candidates are shown relative to the final selection cut value (purple arrow).

Appendix F

Further Results from Toy Studies of $\Delta A_{fs}^{s,d}$

In this Thesis a novel method is proposed for the simultanous fitting of $B_s^0 \to D_s^{(*)\pm}\mu^{\mp}\nu_{\mu}X^0$ and $B_d^0 \to D^{(*)\pm}\mu^{\mp}\nu_{\mu}X^0$ for the extraction of $\Delta A_{fs}^{s,d} = (a_{fs}^s - a_{fs}^d)/2$. A two-stage fit is performed to extract background ratios and asymmetries from the data and then fit the proper time distribution. This is reported in Sec. 6.6. An extensive toy study was performed using the fitting package RooFit [136]. Further results of this study appear in this Appendix, to compliment the results in Sec. 6.6.

In the first fit stage a three-dimensional fit of the B-mass, D-mass and final state flavour distributions is performed to extract the proportion of backgrounds, fit the mass shapes and extract background asymmetries. This fit is described in Sec. 6.5.2. Input mass shape parameters for the toy study are taken from the fit to fully simulated Monte Carlo data. The background asymmetries are taken from the expectations fully discussed in Appendices C and D. The background proportions are taken from the selection results given in Sec. 6.2 using Monte Carlo truth information. Table F.1 lists the input parameters for mass shapes and the fit result from a nominal toy study, with 500 experiments and 1M signal events per experiment. For other fit parameters see Table 6.8.

Table F.1: Monte Carlo mass shape parameters for toy study, and output from a nominal fit with 500 toys, each with 1M events.

Parameter	Input	Output		Pull / σ	
name	value	mean fit value	mean fit error	bias	width
D-mass parameters					
$D^{\pm}$ peak width /GeVc^{-2}	4.8582	4.858±0.0003	0.00672±0.00007	+0.0167±0.0461	0.94±0.03
$D_s^{\pm}$ peak width /GeVc^{-2}	5.6758	5.676±0.0003	0.00558±0.0006	-0.0371±0.0500	1.02±0.04
Chebychev parameter 1	-0.1544	-0.1542±0.0002	0.00392±0.00004	+0.0766±0.0469	0.96±0.03
Chebychev parameter 2	-0.1830	-0.1830±0.0002	0.00421±0.00004	+0.0186±0.0483	0.99±0.03
B-mass parameters					
Exponential slope /GeV$^{-1}c^2$	-0.00040	-0.00040±0.00001	(1.61±0.03)$\times 10^{-7}$	+0.0119±0.0537	1.10±0.04
for $b\bar{b}$-like background					
Argus p-parameter	5.3263	5.332±0.0074	0.1013±0.0019	+0.0419±0.0761	1.56±0.05
Argus c-parameter	-9.2113	-9.223±0.0181	0.0959±0.0033	-0.0264±0.0743	1.52±0.05
B_s^0-signal					
Argus p-parameter	3.8310	3.831±0.0012	0.0231±0.0003	+0.0095±0.0543	1.11±0.04
Argus c-parameter	-9.6863	-9.6860±0.0042	0.0758±0.0011	+0.0021±0.0561	1.15±0.04
B_d^0-signal					
Argus p-parameter	5.1104	5.111±0.002	0.0323±0.0003	-0.0037±0.0546	1.12±0.04
Argus c-parameter	-9.6863	-9.688±0.004	0.0793±0.0008	-0.0137±0.0550	1.13±0.04
B/S fractions					
B_d^0 signal	0.2713	0.27140±0.00004	0.00080±0.00001	+0.0903±0.0496	1.01±0.04
B_s^0 signal	0.4639	0.4640±0.0001	0.00183±0.00003	+0.0260±0.0536	1.10±0.04
$D^{\pm}$ peaking	0.02856	0.02853±0.00004	0.00071±0.00001	-0.0403±0.0505	1.03±0.04
$D_s^{\pm}$ peaking	0.07375	0.07367±0.00094	0.00178±0.00003	-0.0344±0.0532	1.10±0.04
combinatorial	0.06754	0.06753±0.00008	0.00144±0.00002	+0.0053±0.0560	1.15±0.04
$b\bar{b}$-like	0.0950	–not directly fitted–		–not directly fitted–	

From Table F.1 it can be seen that no parameter is significantly biased in the nominal fit. It also appears that the fit errors on the $b\bar{b}$ Argus parameters are underestimated by 50 %. With 1M signal events, the background fractions can be accurately fitted in this model, with a typical error of 1×10^{-3}. For completeness all pull distributions of fitted parameters are plotted in Figs. F.1 to F.4. Many of the variables used in the fit are highly correlated. For example, the Argus p and c parameters are all close to 100 % negatively correlated with each other within each event category. They are, however, not correlated with $\Delta A_{fs}^{s,d}$, the fit parameter we are trying to measure. The correlation matrix from a typical fit to the mass shapes (the first stage of the combined fit) is given in Table F.2. In the second stage $\Delta A_{fs}^{s,d}$ is 80 % negatively correlated with x_1^d, as expected, and all other correlations are less than 2 %.

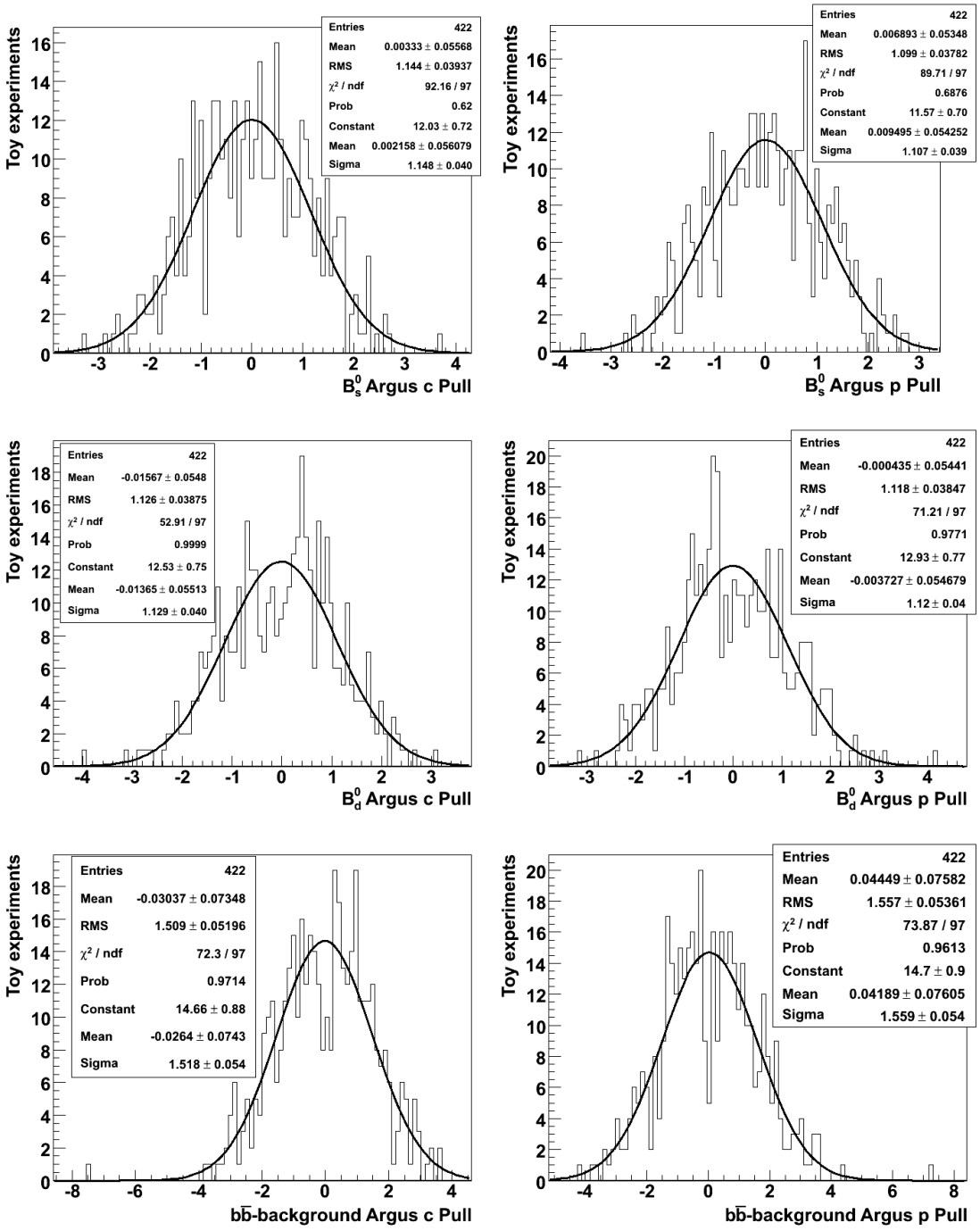

Figure F.1: Pull distributions of fitted Argus parameters. 500 toys, each with 1M signal events. A gaussian is fitted to the distributions in each case.

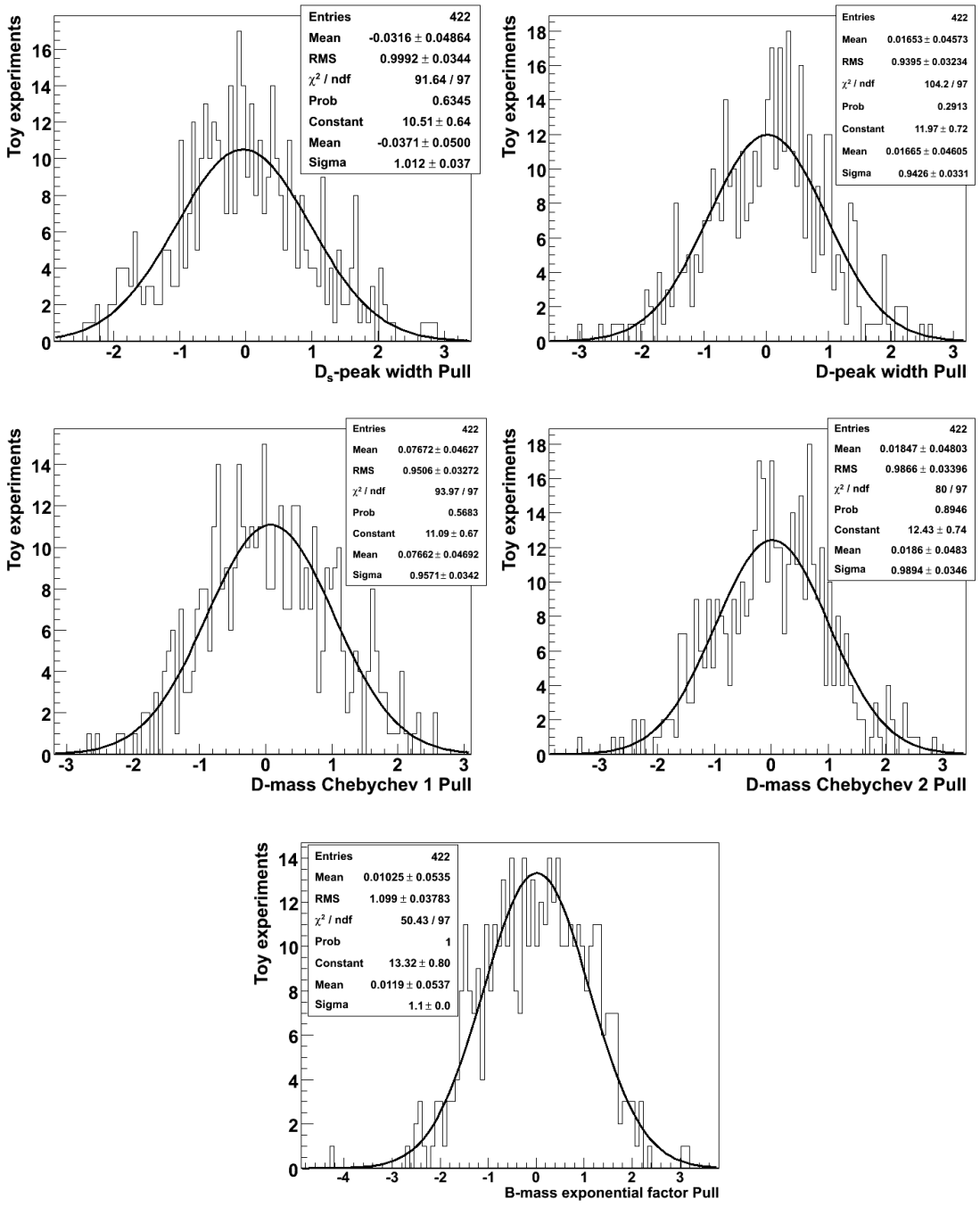

Figure F.2: Pull distributions of fitted mass shape parameters. 500 toys, each with 1M signal events. A gaussian is fitted to the distributions in each case.

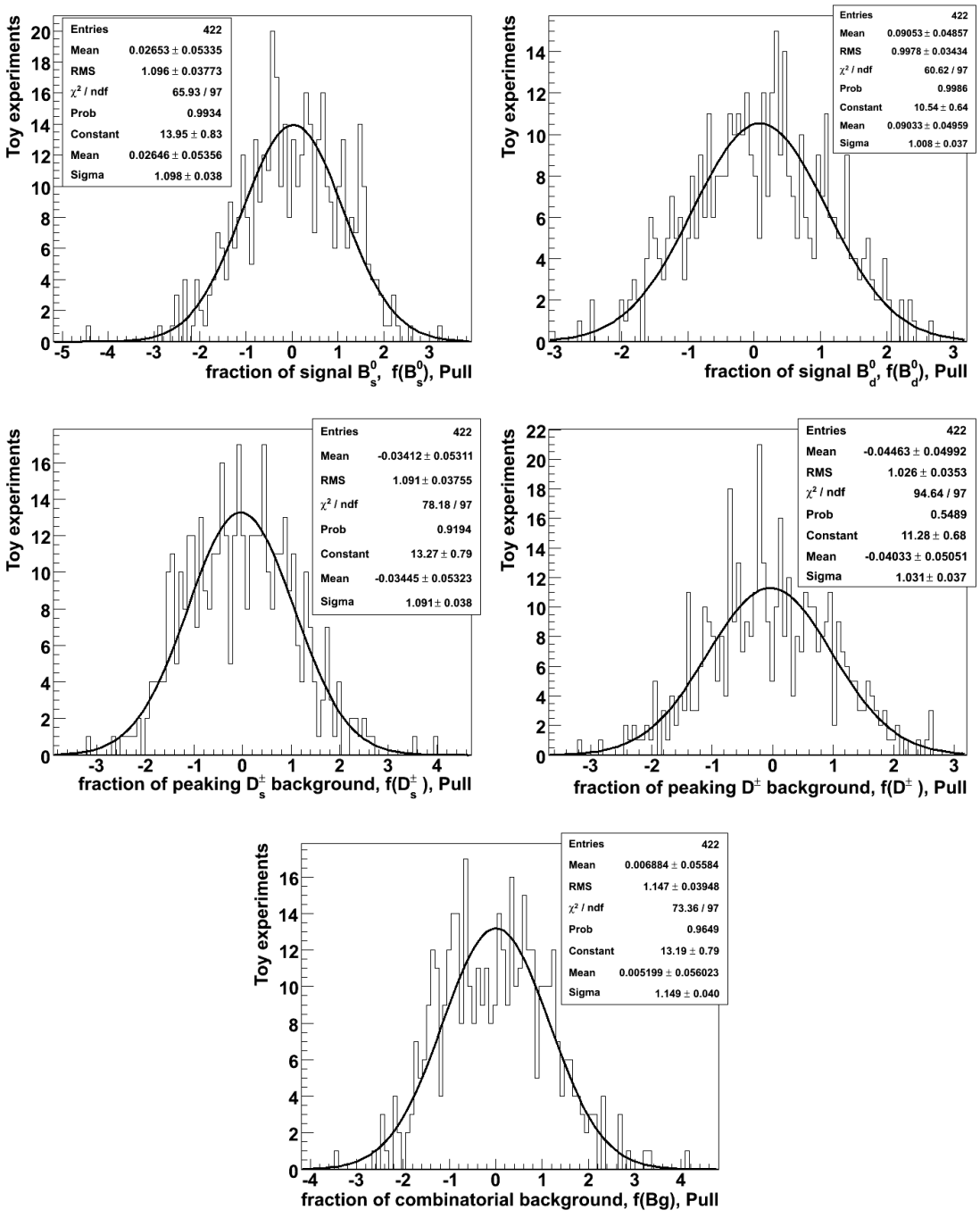

Figure F.3: Pull distributions of fitted background fractions. 500 toys, each with 1M signal events. A gaussian is fitted to the distributions in each case.

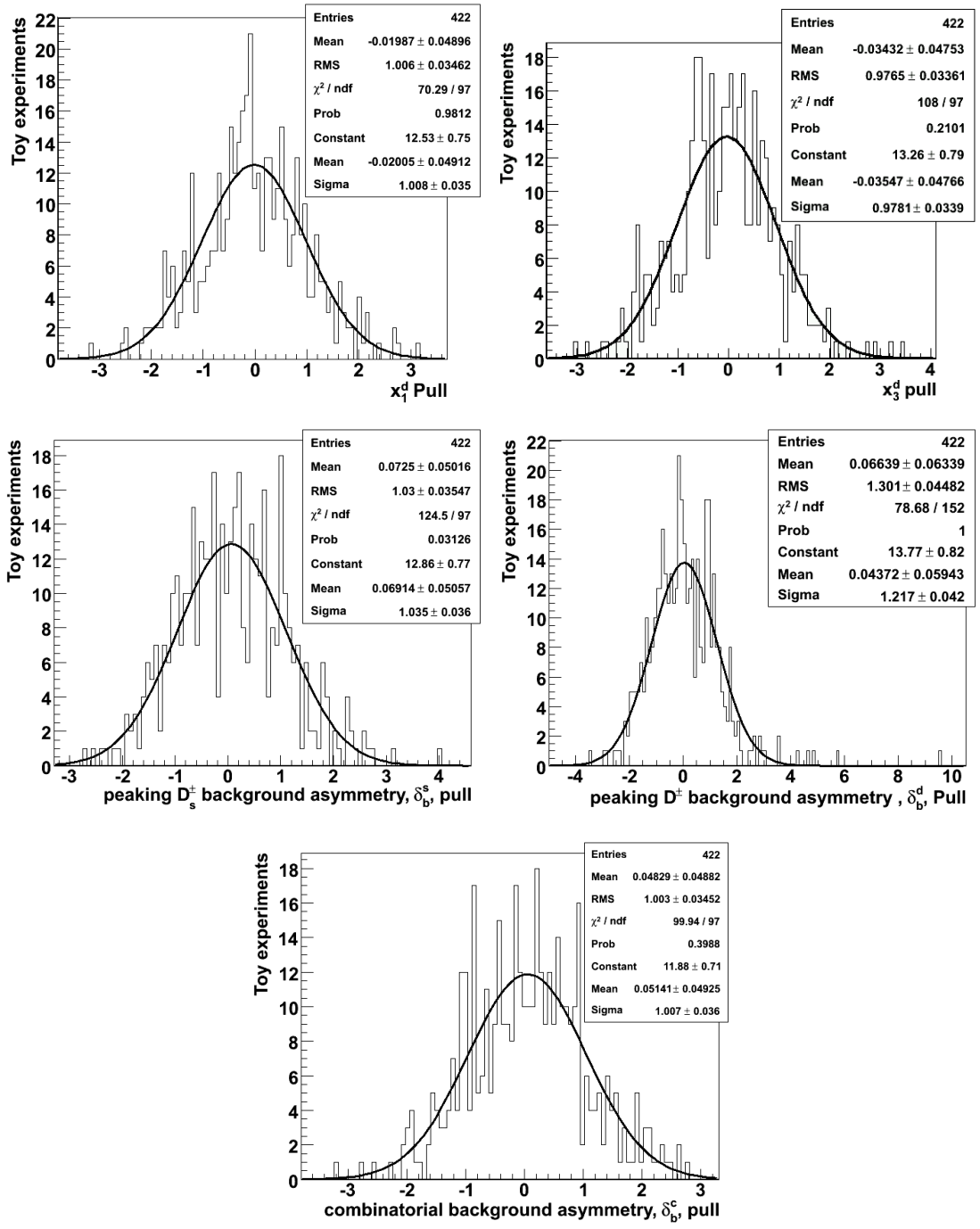

Figure F.4: Pull distributions of fitted asymmetries. 500 toys, each with 1M signal events. A gaussian is fitted to the distributions in each case.

Table F.2: Correlations in a typical fit. 1M signal events.

Parameter		Correlation Matrix																		
No.	Name	1	2	3	4	5	6	7	8	9	10	11	12	13	14	15	16	17	18	19
1	$b\bar{b}$ cAr	1.0	-0.962	0.710	0.351	-0.303	0.623	-0.579	-0.001	0.002	0.002	0.006	-0.003	0.018	0.098	0.597	-0.742	-0.640	-0.640	-0.677
2	$b\bar{b}$ pAr	-0.962	1.0	-0.546	-0.259	0.218	-0.478	0.443	-0.000	-0.000	-0.001	-0.000	0.003	-0.013	-0.075	-0.454	0.606	-0.513	0.487	0.518
3	B exp	0.710	-0.546	1.0	0.536	-0.469	0.891	-0.832	-0.002	0.003	0.002	0.009	-0.005	0.026	0.139	0.852	-0.954	0.952	-0.913	-0.961
4	B_d^0 cAr	0.351	-0.259	0.536	1.0	-0.982	0.478	-0.447	-0.000	0.003	0.004	0.005	-0.003	0.022	0.075	0.560	-0.508	0.511	-0.597	-0.516
5	B_d^0 pAr	-0.303	0.218	-0.469	-0.982	1.0	-0.418	0.391	0.000	-0.003	-0.004	-0.005	0.003	-0.022	-0.065	-0.515	0.444	-0.447	0.549	0.451
6	B_s^0 cAr	0.623	-0.478	0.891	0.478	-0.418	1.0	-0.988	-0.003	0.005	0.003	0.010	-0.004	0.023	0.134	0.758	-0.848	0.912	-0.813	-0.920
7	B_s^0 pAr	-0.579	0.443	-0.832	-0.447	0.391	-0.988	1.0	0.002	-0.004	-0.002	-0.008	0.004	-0.022	-0.127	-0.708	0.793	-0.866	0.760	0.874
8	D Chb1	-0.001	-0.000	-0.002	-0.000	0.000	-0.003	0.002	1.0	-0.065	0.043	-0.072	-0.000	-0.001	0.001	0.008	0.005	-0.009	0.007	-0.002
9	D Chb2	0.002	-0.000	0.003	0.003	-0.003	0.005	-0.004	-0.065	1.0	0.097	0.094	0.000	-0.001	-0.001	0.025	-0.017	0.013	0.009	0.002
10	$D^{\pm}$ Width	0.002	-0.001	0.002	0.004	-0.004	0.003	-0.002	0.043	0.097	1.0	0.021	-0.000	-0.002	0.000	0.039	-0.008	0.004	0.009	-0.001
11	$D_s^{\pm}$ Width	0.006	-0.000	0.009	0.005	-0.005	0.010	-0.008	-0.072	0.094	0.021	1.0	0.001	-0.000	0.000	0.012	-0.017	0.021	-0.006	-0.004
12	d_b^c	-0.003	0.003	-0.005	-0.003	0.003	-0.004	0.004	-0.000	0.000	-0.000	0.001	1.0	-0.038	-0.029	-0.004	0.004	-0.005	0.005	0.005
13	d_b^d	0.018	-0.013	0.026	0.022	-0.022	0.023	-0.022	-0.001	-0.001	-0.002	-0.000	-0.038	1.0	0.005	0.030	-0.023	0.025	-0.032	-0.025
14	d_b^s	0.098	-0.075	0.139	0.075	-0.065	0.134	-0.127	0.001	-0.001	0.000	0.000	-0.029	0.005	1.0	0.119	-0.131	0.141	-0.127	-0.143
15	$f(B_d^0)$	0.597	-0.454	0.852	0.560	-0.515	0.758	-0.708	0.008	0.025	0.039	0.012	-0.004	0.030	0.119	1.0	-0.809	0.778	-0.915	-0.823
16	$f(Bg)$	-0.742	0.606	-0.954	-0.508	0.444	-0.848	0.793	0.005	-0.017	-0.008	-0.017	0.004	-0.023	-0.131	-0.809	1.0	-0.908	0.855	0.909
17	$f(B_s^0)$	0.671	-0.513	0.952	0.511	-0.447	0.912	-0.866	-0.009	0.013	0.004	0.021	-0.005	0.025	0.141	0.778	-0.908	1.0	-0.873	-0.987
18	$f(D^{\pm})$	-0.640	0.487	-0.913	-0.597	0.549	-0.813	0.760	0.007	0.009	0.009	-0.006	0.005	-0.032	-0.127	-0.915	0.855	-0.873	1.0	0.878
19	$f(D_s^{\pm})$	-0.677	0.518	-0.961	-0.516	0.451	-0.920	0.874	-0.002	0.002	-0.001	-0.004	0.005	-0.025	-0.143	-0.823	0.909	-0.987	0.878	1.0

$b\bar{b}$ indicates a parameter of the $b\bar{b}$-like background. B and D indicate parameters governing the combinatorial background B and D mass distributions respectively.
pAr and cAr are the Argus function parameters. Chb1 and Chb2 are the Chebychev coefficients.